University of Southampton

A Numerical Model Study of the Stratocumulus-Topped Marine Boundary Layer

Elizabeth C. Kent

A dissertation submitted in candidature for the degree of Doctor of Philosophy

School of Ocean and Earth Sciences

September 1999

This thesis is the result of work done wholly while in registered postgraduate candidature and has not been submitted for any other degree.

UNIVERSITY OF SOUTHAMPTON

ABSTRACT

FACULTY OF SCIENCE

SCHOOL OF OCEAN AND EARTH SCIENCES

Doctor of Philosophy

A NUMERICAL MODEL STUDY OF THE STRATOCUMULUS-TOPPED MARINE BOUNDARY LAYER

by Elizabeth C. Kent

A one-dimensional model with second order turbulence closure has been developed and used to investigate processes in the cloud-topped marine atmospheric boundary layer. Model developments were required to correctly apply surface flux terms near the sea surface, poor representation of which is common to several models from the recent literature. The improved surface forcing is shown to affect the predicted boundary layer structure. Other developments included the implementation of a fully implicit numerical code, which generated less numerical noise than that originally used in the model, and an improved initialisation procedure. The new model code was then shown to quantitatively reproduce processes in the stratocumulus-topped boundary layer using measurements of atmospheric turbulence from aircraft from the North Sea and the subtropical North Atlantic and North Pacific. The model is robust to changes in the mixing length coefficients used in the turbulence closure and to perturbations in the initial profiles.

The model is used to simulate conditions that occur as winds circulate from the subtropics towards the tradewind regions. The observed transition from a shallow stratocumulus layer to a deeper stratocumulus layer interacting with cumulus clouds beneath is simulated in response to realistic external forcing. The final stages of transition, from cumulus under stratocumulus to shallow cumulus is however not observed in the simulation; possible reasons for this are discussed. The model shows in detail the interaction between the stratocumulus layer and cumulus clouds beneath. The cumulus clouds thicken, moisten and cool the stratocumulus layer and therefore act to maintain the layer, but can also drive entrainment. The peaks in turbulent kinetic energy in the stratocumulus layer which follow cumulus penetrations of the stratocumulus layer can be large enough to directly cause the boundary layer to entrain air from above the boundary layer and grow in height. The entrained air is warmer and drier than the boundary layer air and tends to dissipate the stratocumulus layer. The model is then used to show how the imposed environmental conditions affect processes within the boundary layer. An important model prediction is that cloud top entrainment instability may act to promote mixing between the surface and cloud in deep-decoupled boundary layers. The mixing acts to replenish the cloud liquid water and sustain the cloud. Cloud top entrainment instability has previously been thought to have the capacity to lead to rapid erosion of the cloud, although this has not been observed in practice. This mechanism could help to explain the observed persistence of stratocumulus clouds under these conditions.

LIST OF CONTENTS

LIST OF FIGURES

LIST OF TABLES

ACKNOWLEDGEMENTS

I would like to thank Peter Taylor (JRD) for suggesting the project and Neil Wells (SOES) for agreeing to supervise. David Rogers from Scripps Institution of Oceanography provided the original version of the model and with Xiaohua Yang (also then at Scripps) provided valuable help and support in the early stages. Qiang Fu from Dalhousie University provided the radiation code. Robert Wood from the Meteorological Office Research Flight helped with the interpretation of the aircraft data. Thanks must also go to Scott Woodruff at NOAA/ERL Climate Diagnostics Center and Steven Worley from the Data Support Section at NCAR for providing the COADS cloud and meteorological data. Henry Charnock, George Nurser, Jonathan Sharples, David Smeed and Peter Taylor all provided help and encouragement. Particular thanks must be given to Steven Alderson whose extensive comments on the draft thesis improved the final version immeasurably.

1. INTRODUCTION

1.1 The Occurrence of Stratocumulus-topped Boundary Layers

This study concerns the physical processes which result in the prevalence of stratocumulus-topped boundary layers over the global ocean. The boundary layer will be defined as the region of turbulent mixing in the lower atmosphere. The boundary layer can also be considered to be that part of the troposphere which is affected by processes at the ocean surface and which starts to respond to this forcing within about an hour (Stull 1988). A simple cloudy boundary layer consists of the cloud layer and the layer beneath the cloud, the subcloud layer.

Stratocumulus clouds are low-level clouds often found where a stable layer tops a convective boundary layer. Stratocumulus clouds are distinguished from stratus by the cellular or roll patterns that result from convective processes within the cloud. Boundary layer stratus is usually found at lower levels than stratocumulus and is much more uniform in appearance, often resulting from the development of low-level fog. Large regions of stratocumulus (often referred to as stratocumulus decks) are found where deep convection is suppressed by stable stratification, which reaches to high levels in the atmosphere. This stable stratification limits convection to a shallow boundary layer and a strong inversion is formed both in temperature and humidity. These conditions are often associated with large-scale subsidence found in high-pressure systems and in the high-pressure ridges behind cold fronts (Driedonks and Duynkerke 1989).

Cloud can form if the inversion height is greater than the saturation or lifting condensation level. The latter is defined as the level at which the air is just saturated and contains no liquid water. Once the cloud has formed it is maintained by longwave cooling at the cloud top, a supply of moist buoyant air parcels from below, and by the turbulent entrainment of air from above the inversion which allows the inversion height to be maintained above the saturation level against the effect of subsidence. A supply of moisture through the cloud base is required to maintain the cloud against processes that dissipate liquid water; entrainment of warm, dry air at the cloud top, heating by sensible heat flux originating at the ocean surface and by absorption of shortwave radiation within the cloud.

1.2 The Importance of Stratocumulus

The mean and turbulent structure of the cloud-topped marine atmospheric boundary layer is complex and has only been well sampled in a relatively few experiments. Knowledge

of the boundary layer structure is interesting in its own right, but if this structure could be simply predicted the performance of atmospheric general circulation models (AGCM) could be enhanced. AGCM resolution is presently too coarse to model the cloudy boundary layer well. Predictions of the boundary layer depth to an accuracy better than the AGCM resolution, for example, would allow better definition of the transport of properties from the surface into the higher levels and perhaps improve the AGCM simulation of low clouds, which is often poor.

Stratocumulus have a strong impact on climate (Klein and Hartmann, 1993). Considering the atmosphere-ocean system as a whole, stratocumulus act to cool the system. The shortwave albedo[1] of the cloud top is typically between 0.6 and 0.8, compared with a typical ocean surface value of 0.07 (Payne 1972). Thus much more shortwave radiation is reflected back to space in the presence of stratocumulus compared to clear sky conditions. Clouds therefore act to cool the atmosphere-ocean system at solar wavelengths. This cooling is however compensated by a reduction in longwave cooling as the sea surface emits more longwave than cloud tops which are cooler than the sea surface. This compensation is small for low clouds such as stratocumulus which have cloud tops only slightly cooler than the sea surface temperature (SST) but much larger for high clouds with very cold tops. Thus stratocumulus and other low clouds act to cool the atmosphere-ocean system more than high clouds.

Considering the cloud-topped boundary layer, stratocumulus act to warm the boundary layer as they absorb as well as scatter shortwave. During the daytime the cloud in the boundary layer will warm through solar absorption with only slightly less longwave cooling from the cloud top than from the sea surface. The sea surface receives less heat in the presence of clouds as the main effect is that the absorption and scattering of shortwave radiation at the cloud top reduces the shortwave reaching the sea surface. Longwave cooling of the sea surface is reduced by the presence of low cloud.

The change in net radiative heat input to the atmosphere due to the presence of clouds is known as the cloud radiative forcing. Klein and Hartmann (1993) used satellite-derived cloud and radiation measurements to show that the net radiation is decreased (i.e. less heating) by 1 Wm^{-2} per 1% increase in cloudiness. The global figure for all low cloud is 0.63 Wm^{-2} per 1% increase in cloudiness. Hartmann et al. (1992) show that in the subtropics and midlatitudes the zonal average net radiative forcing by low cloud is larger than for any other satellite-derived cloud type. The global cloud radiative cooling due to low clouds is estimated to be 16 Wm^{-2}, 60% of the total cloud forcing.

---

[1] the fraction of down-welling shortwave radiation reflected

The correct modelling of low-level clouds is thus important for both weather and climate prediction. However, Alekseev et al. (1996) show that there is no consensus from models about the magnitude and mechanisms of the cloud feedback on climate. This is perhaps due to the coarse vertical resolution used in climate simulations (Bushell and Martin 1999).

1.3 Outline of this study

This study uses a one-dimensional model to examine the effect of external forcing on the simulation of the breakup of solid stratocumulus decks to form shallow cumulus. Chapter 2 reviews the present understanding of processes in the atmospheric boundary layer and details some of the experimental campaigns that lead to this understanding. Chapter 3 introduces the equations necessary to describe the atmospheric boundary layer and reviews the main types of models that have been used for atmospheric boundary layer simulation. Chapter 4 describes a one-dimensional Mellor-Yamada type numerical model used in other studies of the atmospheric boundary layer which is here modified to better represent the processes thought to be important in predicting the structure of the boundary layer. Improvements to the model made during this study were required to make the model numerically stable, to correctly force the model at the surface and to conserve heat and water content within the model. In addition numerical code for radiative profile calculation was implemented in order to improve the calculation of radiative heat divergence.

The improvement to the simulation of an idealised boundary layer resulting from the model development is demonstrated in Section 5.1. Sensitivity tests, described in Section 5.2, show the revised version of the model to be stable to changes in the mixing-length coefficients and to changes in the model resolution and time step. Over 200 different model simulations have been performed with most variables changed by an order of magnitude or more, demonstrating the robustness of the new model formulation. In Section 5.3 the model is shown to reproduce aircraft-measured flux profiles when only initialised with mean profiles from atmospheric boundary layer experiments in the North Sea, off the coast of California and near the Azores.

Having demonstrated that the model can reproduce the measured boundary layer structure in several different regions where stratocumulus clouds are found, the model is applied to the problem of stratocumulus to cumulus transition that is an important feature of the trade wind region (Chapter 6). A conceptual model of this transition (Albrecht et al. 1995a) suggests that the breakup of the stratocumulus to form cumulus clouds is driven by the decoupling of the cloud and sub-cloud layers. The validation simulations performed show that

the one-dimensional model developed in this study can simulate decoupled boundary layers and should therefore be able to simulate the transition, unless the organisation of the boundary layer into inhomogeneous regions is an important factor in promoting the transition. Mixed-layer models cannot simulate an inhomogeneous boundary layer although attempts have been made to diagnose decoupling in a mixed layer model (Bretherton and Wyant 1997). Two-layer models (Albrecht 1984 and Wang 1993) have been used to simulate the transition to cumulus but have been criticised for their sensitivity to tuneable model parameters which can radically change the predicted cloud type (Bretherton 1993). The transition has also been simulated with two-dimensional cloud resolving models in a Lagrangian mode (Krueger et al. 1995a,b and Wyant et al. 1997) and with a coarse resolution two-dimensional mesoscale model (Moeng and Arakawa 1980).

In Chapter 6 the one-dimensional model will be used to simulate the Lagrangian evolution of the stratocumulus-topped boundary layer moving from the subtropics towards the tradewind region. The boundary layer is observed to deepen in response to an increasing sea surface temperature imposed to represent observed conditions. The deepening boundary layer first becomes decoupled. When the surface layer has moistened sufficiently due to the surface latent heat flux, small cumulus clouds form at the top of the surface mixed layer which are sufficiently buoyant to rise into the stratocumulus layer above, forming a cumulus-coupled boundary layer. The impact of individual cumulus clouds on the stratocumulus cloud layer is evident in the simulation. The advantage of a one-dimensional model over a large eddy simulation is that the relatively simple, and computationally inexpensive, one-dimensional model allows the impact of the external parameters on the simulation to be investigated with different runs of the model. The effect of differing vertical velocities, properties above the inversion, SST gradients and wind speeds is investigated in Chapter 7. As expected increasing the vertical velocity leads to a shallower boundary layer. The warming and drying effects of the subsidence are however more than offset by the reduction in entrainment warming and drying. Changing the above inversion temperature structure has effects that can be understood in terms of the stability of the lower atmosphere. Drying the atmosphere above the inversion leads to increased mixing between the cloud and surface layer, and thicker cloud, the opposite of current theory which suggests that dry air above the inversion should tend to destabilise and breakup the cloud. Increasing the sea surface temperature gradient and wind speed, and hence the surface fluxes, leads to a deeper boundary layer and thicker cloud. The deeper boundary layer is more likely to become decoupled and so the increased surface fluxes have competing effects, initially to promote decoupling of the surface and cloud layers and then to promote their recoupling with more vigorous cumulus clouds beneath the stratocumulus layer. The results are discussed and conclusions drawn in Chapter 8.

2. THE CLOUDY MARINE ATMOSPHERIC BOUNDARY LAYER

2.1 Introduction

Before attempting to model the cloud-topped marine atmospheric boundary layer it is first necessary to consider the physical processes present. Processes at the ocean surface are described in Section 2.2.1 and the generation of turbulence within the boundary layer in Section 2.2.2. Section 2.2.3 brings together the complex and interrelated processes that occur within the stratocumulus cloud. Radiation within the cloud, turbulence, changes in phase and entrainment are all discussed separately (as far as is possible) before considering their interaction in processes such as cloud top entrainment instability. All these processes need to be included in a model to simulate the cloudy marine atmospheric boundary layer.

Section 2.3.1 describes the regional distribution of stratocumulus clouds calculated from observations of clouds made on merchant ships. The persistence of large regions of stratocumulus clouds over the oceans is demonstrated using observations both from summer and winter. The literature relating to why these stratocumulus clouds persist is reviewed in Section 2.3.2 and conditions related to their dissipation in Section 2.3.3. The climatologically observed evolution from stratocumulus to cumulus clouds in the trade wind regions between the subtropics and the tropics is introduced in Section 2.3.4.

2.2 Physical Processes in the Stratocumulus-topped Marine Boundary Layer

2.2.1 Surface Processes

Under clear skies most of the solar radiation incident at the top of the atmosphere is absorbed in the ocean surface. Some solar radiation is absorbed by water vapour and aerosols within the atmosphere, but most is transmitted and absorbed in the ocean. The ocean is therefore typically warmer than the air in the boundary layer. The sea surface albedo depends on atmospheric transmittance, the angle of the sun, and the roughness of the sea surface (Stull 1988). Payne (1972) measured the oceanic albedo, which is typically 0.06-0.07, and tabulated values as a function of latitude and month for the North Atlantic. In the presence of clouds the solar radiation reaching the sea surface is much reduced, as solar radiation is both reflected at the cloud top and absorbed within the cloud. The sea surface emits longwave radiation as a black body (Liou 1992) and the upward longwave flux at the sea surface therefore strongly depends on the SST. The amount of downward longwave at the sea surface increases in the presence of cloud.

Surface evaporation is the main source of water vapour in the boundary layer, although advection of moister air may also cause humidity to increase. As the sea is usually warmer than the near surface air the transfer of sensible heat is usually from the ocean to the atmosphere. Away from regions of strong sensible heat loss near ocean boundary currents the sensible heat loss is typically 10 Wm^{-2}. Near the sea surface is a region where the turbulent fluxes are assumed to be nearly constant with height. This is the surface layer where the Obukhov length scale defines the height at which buoyant production equals mechanical production (Tennekes, 1973). The turbulent heat and evaporative (latent heat) fluxes depend on the stability of the atmospheric surface layer and are larger in unstable conditions. For a given air-sea temperature and humidity difference the sensible and latent heat fluxes increase with increasing wind speed. The turbulence measurements required to calculate these fluxes are infrequently made over the ocean so bulk parameterisations are often used to estimate these fluxes from mean meteorological variables (e.g. Kent and Taylor 1995). Businger (1973) describes the flux-profile relationships that can be used to calculate the profiles of wind, temperature and humidity in the surface layer. The equations used to describe surface turbulent processes are given in Section 3.2.2.

2.2.2 Turbulent processes and turbulent kinetic energy (TKE)

TKE is a measure of the intensity of turbulence and is a balance between the creation of turbulence, for example due to shear and convection, and its destruction, for example through dissipation to heat and the effects of static stability (Stull 1988). Equations for the terms in the TKE budget are presented in Section 3.2.1.

Buoyancy effects are important at the sea surface, within the cloud and whenever a change of phase occurs. The sensible heat flux at the ocean surface usually acts to warm the lower atmosphere and create a positive buoyancy flux. Processes within the cloud can lead to the generation of TKE, this is discussed in the next section where all the processes within the cloud are discussed.

Nicholls and Leighton (1986) and Nicholls and Turton (1986) describe and model a case study where turbulence throughout the boundary layer is driven by wind shear rather than by buoyancy effects. These conditions usually result in stratus clouds, as it is the convective buoyancy effects that lead to the cellular cloud structure that differentiates stratocumulus from stratus (Garratt 1992). Wind shear is large near the sea surface and may also be large at the inversion, which can lead to entrainment of upper air into the boundary layer.

Integrated vertical turbulent transport is assumed to be zero over the depth of the boundary layer (Stull 1988). The transport usually acts to move TKE from the bottom of the boundary layer towards the top. This transport means that some TKE is dissipated away from its region of generation. TKE is ultimately destroyed by viscous dissipation. Viscous dissipation is most efficient at small scales of turbulence (at frequencies around 1000 Hz) whereas the generation of turbulence occurs mainly at long scales (at frequencies around 0.1 Hz). The large eddy sizes created by buoyancy and shear forces are dynamically unstable and break into smaller eddies creating a cascade of energy from larger to smaller scales (Busch 1973). If the energy spectrum is broad, the frequencies of generation and dissipation are well separated. In between, in the inertial subrange, TKE is transported to higher wave numbers by inertial forces and spatially redistributed by pressure forces. The dissipation rate affects how much TKE remains available for entrainment at the top of the boundary layer.

TKE is redistributed in the boundary layer by static pressure fluctuations. The size of these correlations between pressure changes and TKE is small and hard to measure as they are usually swamped by larger-scale dynamic pressure variations. The pressure correlation term in the TKE budget is usually found as a residual, but it should be remembered that the residual term also includes errors from all the other terms. In stable conditions the pressure correlation terms can lead to the generation of internal waves and therefore to the destruction of TKE by dissipation associated with these motions. In this situation the pressure correlation terms do not simply redistribute the TKE but can actually act to destroy it. Storage and advection of TKE over the oceans are usually both small and therefore ignored (Stull 1988).

2.2.3 Cloud Processes

Four main cloud processes will be described in this section; radiation, changes in phase, the generation of turbulence and turbulently-driven entrainment. All these processes interact, however an attempt will be made to introduce each of them in turn before describing their interaction.

Within the cloud layer the most important effect of radiation is the longwave cooling at the cloud top. In the absence of high cloud the cooling rate is proportional to the difference of the fourth powers of the cloud top and top of the atmosphere temperatures. The net absorption of longwave, and hence the net longwave radiative flux divergence, is confined to a region within about 50 metres of the cloud top (Nicholls 1984, Slingo et al. 1982 a,b). This flux divergence leads to strong local cooling which has a destabilising effect as cooled dense air sinks through the cloud. A weak longwave warming is observed at the cloud base unless the sea surface is colder than the cloud base. This longwave cooling and heating occur both night

and day. During the day, both liquid water and water vapour within the cloud absorb shortwave radiation. Shortwave heating penetrates deeper into the cloud than longwave cooling. The effect of longwave cooling at the cloud top is thus partially offset, but the different vertical profiles of short and longwave absorption and emission can lead to the generation of turbulence even in cases where there is little net heating or cooling within the full cloud layer. Shortwave heating can lead to a decoupling of the cloud and subcloud layers. In a decoupled boundary layer the cloud and the subcloud layer form two separate mixed layers separated by a slightly stable region: mixing in the cloud is driven by radiative processes and mixing in the subcloud layer by shear and buoyancy forcing at the sea surface (Nicholls 1983, Rogers 1983, Nicholls 1984). For this to happen the surface forcing must be insufficient to overcome the slight inversion caused by solar radiative warming of the cloud layer. The cloud layer is thus deprived of moisture as it is cut off from its source at the sea surface, leading to drying (due to entrainment) and thinning (due to the rise in the saturation level) of the cloud layer. The surface layer will moisten as humidity is now only mixed over the subcloud region, and in general will warm. This can lead to convection and the formation of small cumulus clouds beneath the stratocumulus. If the convection in the cumulus clouds is strong enough the cloud and subcloud layers can recouple, although the recoupling may be intermittent and local. The cloud and subcloud layers often recouple in the late afternoon as the effects of solar radiation become less. Observations from the Atlantic Stratocumulus Transition Experiment (ASTEX) show that the decoupling process was inhibited when the amount of solar radiation reaching the boundary layer was reduced by the presence of high level cloud (Albrecht et al. 1995a).

The modelling of radiative transfer in clouds requires knowledge of liquid water content, cloud temperature, cloud surface shape, cloud cover and solar zenith angle amongst other parameters (Stull 1988). In addition, scattering and absorption of short and long wave radiation by spherical water drops of finite size are covered by Mie theory (Liou 1992) which requires knowledge of the size spectrum of the droplets for its exact solution. The treatment of radiative processes in the model used in the present study is described in Section 4.5.

The net cooling or warming of cloud due to the absorption and emission of radiation leads to the evaporation or condensation of cloud liquid water with the associated consumption or release of latent heat. This will tend to offset the change in temperature associated with the radiation. Changes of phase within a cloud can lead to large changes in temperature. An example of lowering of temperature occurs during the evaporation of liquid water when cloudy air is mixed with clear air from above the inversion.

The complex microphysical processes occurring within the cloud are not included in the model used in the present study. They are excluded because of the many additional parameterisations required to explicitly model the microphysics, the need for specification of the distributions of many unknown variables such as aerosol and cloud condensation nuclei (CCN), and the computational expense of such calculations. However some cloud droplet processes are summarised here for completeness following Salby (1996).

Once a water droplet has formed in a cloud its survival depends on the balance between condensation of the surrounding water vapour and evaporation from the drop. The droplet can increase in size by collision with other droplets: large droplets sweep through the cloud volume growing by collecting smaller droplets. As water vapour condenses to form cloud droplets, heat is released, and the cloud temperature rises. Conversely the cloud is cooled if water evaporates from the cloud droplets. The formation of water droplets within the cloud is facilitated by the presence of CCN which are often anthropogenic aerosols such as soluble sulphates. Although a wide range of variability is observed, typical microphysical properties of stratocumulus are: 250 droplets cm^{-3}, a mean droplet radius of 5 μm and a liquid water content of 0.3 gkg^{-1}.

Albrecht (1989) suggests that maritime clouds are more likely than those over land to produce drizzle due to their low concentration of CCN. He argues that the lack of CCN leads to larger drops than where CCN are more abundant, when many more smaller drops are formed. The smaller drops formed when CCN are plentiful are less likely to precipitate out than the large drops in CCN sparse clouds. Thus an increase in the amount of CCN can result in less drizzle and hence higher liquid water content and greater cloudiness. This in turn leads to greater reflectivity (Albrecht et al. 1995b). Cooling due to evaporation of drizzle just below the cloud layer can also cause decoupling of the cloud and subcloud layers independent of solar radiative heating within the cloud layer (Nicholls 1984, Martin et al. 1997).

Turbulence within the cloud layer is usually maintained by longwave cooling at the cloud top. The resulting convection can reach through most of the atmospheric boundary layer (Driedonks and Duynkerke 1989). The longwave warming usually observed at the cloud base also acts to generate turbulence within the cloud. Shortwave radiation acts to suppress turbulence at the cloud top by offsetting the longwave cooling but can also generate turbulence by warming deeper within the cloud. If the turbulence generated at the sea surface is strong, or the cloud base low, surface generated turbulence can be important within the cloud. As mentioned in the previous section any wind shear across the inversion can lead to turbulence within the cloud. Turbulence can be suppressed when very warm air is mixed into the cloud

top during entrainment or at the stable interface at the top of the surface mixed layer in decoupled boundary layers.

Entrainment is the process whereby non-turbulent fluid is engulfed into a turbulent region through a stable interface with minimal transfer of turbulent fluid into the non-turbulent region (Turner 1968). When warm, dry air is entrained at the cloud top, TKE is consumed in order to bring the warm dry air into the cloud, increasing the potential energy of the air. The amount of entrainment depends both on this available kinetic energy (from cloud turbulence produced by wind shear, radiative effects, condensation and surface fluxes for example) and the inversion strength (which defines the amount of potential energy required for the entrainment). The spectra of length and velocity scales of the turbulence are also thought to be important. Entrainment is usually considered to be a mechanism for the dissipation of clouds due to the mixing of warmer, drier air into the cloud. It can however lead to thickening of the cloud if the cloud-top rises more quickly than the base (Randall 1984). The base rises as the lifting condensation level increases with the warming and drying of the boundary layer. If wind shear at the inversion results in Kelvin-Helmholtz instability there is the possibility of entrainment at the cloud top (Stull 1988); although a recent model study has suggested this is not an important mechanism for entrainment (Sullivan et al. 1998).

Insight into the physical mechanisms that determine the entrainment rate has been gained from modelling studies (Sullivan et al. 1998). They suggest that at low Richardson number the motions of thermal plumes are strong enough to fold the inversion and draw warm air into the boundary layer. This folding leads to entrainment and the turbulent mixing of pockets of warm air drawn below the nominal inversion level by strong motions near the plume edge. Lock (1998) uses the results of modelling studies to derive an entrainment parameterisation for cloudy boundary layers (see Section 3.2.3).

Considering these effects together, turbulence within the cloud can lead to entrainment of warm dry air into the boundary layer against buoyancy forces. An entrained parcel of relatively warm dry air is mixed with cloudy air, which can lead to evaporation of cloudy air droplets into the entrained air, causing further cooling. If the entrained air is sufficiently cool and dry to allow large amounts of evaporation, the parcel of dry air can be cooled to such an extent that it sinks through, and even out of, the cloud. The strong downward motion of the air parcel can lead to further entrainment, either by dragging more above inversion air through the inversion with the original air parcel or by the generation of turbulence within the cloud. At a critical ratio of the across inversion temperature and humidity differences this process can be self-sustaining, a process known as cloud top entrainment instability (CTEI). CTEI has the potential to cause large entrainment rates and the breaking up of cloud due to mixing of dry

air into the cloud. There is little consensus however about what the critical values of temperature and humidity differences are that will allow CTEI (Albrecht et al. 1985, Kuo and Schubert 1988, MacVean and Mason 1990). Alternatively, entrainment can lead to suppression of turbulence near the cloud top if the air being entrained is sufficiently warm and moist to form a buoyant stable layer.

2.3 The Persistence of Stratocumulus

2.3.1 Regional Distribution of Marine Stratocumulus

Meteorological reports from Voluntary Observing Ships (VOS) define three categories of stratocumulus (The Met. Office, 1982). Low cloud type 5 is 'stratocumulus not resulting from the spreading out of cumulus' which represents stratocumulus at the top of a convective boundary layer capped by a subsidence inversion. The remaining two classifications of stratocumulus relate to boundary layers in which stratocumulus and cumulus coexist. Low cloud type 8 is 'cumulus and stratocumulus other than that formed from the spreading out of cumulus; the base of the cumulus is at a different level from that of stratocumulus'. This cloud type usually represents small cumulus clouds beneath a stratocumulus layer. Low cloud type 4 is 'stratocumulus formed by the spreading out of cumulus; cumulus may also be present'. This cloud type will often represent deeper cumulus clouds with cloud tops rising into the stratocumulus layer above. Both these cumulus under stratocumulus cloud types can result from decoupling of the cloud and surface layers (see Section 2.2.3) and can be part of the stratocumulus to trade cumulus transition (see Section 2.3.4).

These cloud observations are gathered together in the Comprehensive Ocean Atmosphere Dataset (COADS, Woodruff et al. 1993). COADS contains marine meteorological observations from merchant ships, buoys, platforms and coastal stations. Variables reported include wind speed, SST, air temperature, humidity, surface pressure and cloud types and amounts for low, middle and high clouds. Figure 2.1a shows a solid stratocumulus deck over the midlatitude North Atlantic viewed from above. Figures 2.1b to d show cumulus under stratocumulus from the midlatitude and subtropical North Atlantic. Figures 2.1e and f show scattered small cumulus clouds again from both the midlatitude and subtropical North Atlantic.

Satellite measurements of clouds are more indirect than visual observations. The International Satellite Cloud Climatology Project (ISCCP, Hartmann et al. 1992) characterises cloud cover in seven pressure intervals and with five ranges of visible optical depths. These thirty-five categories are used to produce five radiationally distinct cloud types, high thin, high thick, mid-thin, mid-thick and low cloud. It should be remembered therefore that unlike

the ship-based cloud estimates, ISCCP satellite cloud estimates do not differentiate between cloud types such as stratocumulus and stratus, although cloud structure can be seen on cloud images.

Figures 2.2 and 2.3 show the summer and winter distributions of stratocumulus properties in the North Atlantic and North Pacific respectively calculated between 1980 and 1993 from the COADS version 1a dataset. The proportion of COADS low cloud observations which report types 4, 5 or 8 have been calculated in 2° areas and contoured. The cloud proportions were calculated directly from COADS reports as the cloud atlas of Warren et al. (1988) combines the three stratocumulus types with the two stratus types and with fog into one group. Although this dataset is often used in cloud climatology studies (e.g. Hanson 1991, Klein and Hartmann 1993 and Weaver and Ramanathan 1997) it was felt that it was necessary for the present study to focus on the stratocumulus type separately as the conditions for stratus and fog formation are different from those necessary for stratocumulus formation. In the North Atlantic stratocumulus clouds are most often found to the west of the UK in summer (Figure 2.2a) and there is a strong gradient of fractional stratocumulus occurrence with low fractions to the southwest and high fractions to the northeast. In the winter, although the peak fractional occurrences are lower, the total area where stratocumulus clouds are observed 30% of the time or more is much larger than in the summer, and the strongest gradients are north to south. Figure 2.2b shows the distribution of mean cloud cover for the times when stratocumulus clouds are reported. There is a general tendency for more frequent occurrence of stratocumulus to be associated with more complete cloud cover although there are differences in the patterns between Figure 2.2a and 2.2b. Again the distribution is more zonal in winter. The highest coverage of stratocumulus clouds is found in the summer to the south of Greenland. The smallest cloud cover is found in the western North Atlantic between 20 and 30°N in the summer and between 10 and 20°N in the winter. Figure 2.2c shows the mean cloud base height for times when stratocumulus cloud was observed, in the North Atlantic. The cloud base height is reported in nine intervals between 0 and 2500 metres ranging in thickness from 50 metres at the surface to 500 metres higher up. The resolution is therefore coarse and Figures 2.2c and 2.3c (which shows the cloud base height in the North Pacific) should be interpreted with this in mind. Figure 2.2c does show a fairly coherent pattern with high stratocumulus cloud bases to the west of Africa in both summer and winter and lower cloud bases stretching eastwards from the Gulf Stream region, especially in winter.

In the North Pacific stratocumulus are again more often observed in the east of the basin (Figure 2.3a) particularly to the west of California. The number of reports is low in the tropical Pacific and the cloud variables have not been calculated (see Figures 2.3a-c). In the summer the fractional occurrence of stratocumulus has a strong north-south gradient in the

western Pacific with stratocumulus observed more than 40% of the time in the north and less than 15% of the time in the south. Off the west coast of California percentage occurrences reach over 60%, although 50% is a more typical value. Stratocumulus is observed more often in the eastern than in the western Pacific. As in the North Atlantic the winter distribution is more zonal although the occurrence of stratocumulus off the coast of California is still high. The range of winter occurrences is smaller, with stratocumulus observed about 20% of the time in the south of the region where reports start to become scarce, and over 40% of the time off the Californian coast. Again the cloud cover tends to be more complete when the stratocumulus clouds are frequently observed (Figure 2.3b). Mean cloud cover of more than 6.5 is found in large regions of the north and east Pacific in the summer with smaller cloud cover to the south and west. The cloud cover is much less variable in winter than in summer. The cloud base heights in the North Pacific (Figure 2.3c) are less coherent than in the North Atlantic and the variability noisy.

These stratocumulus cloud distributions can be grouped into three main types. Off the coasts of West Africa (Figure 2.2a) and California (Figure 2.3a) are the subtropical stratocumulus decks. Subtropical stratocumulus decks are also found off the coasts of Peru and Angola (Hanson 1991). These cloud decks occur throughout the year. All these regions are on the east side of the oceanic subtropical high where the trade winds blow from midlatitudes towards the inter-tropical convergence zone. The trade inversion is maintained by subsidence in the descending branch of the Hadley circulation.

The most studied stratocumulus clouds are the subtropical stratocumulus found off the California coast (Figure 2.3a). Early studies summarised by Neiburger et al. (1961) detail the inversion structure in this region. The dissipation of stratiform clouds studied by Neiburger (1944) is ascribed to variation in the inversion height, although the effects of advection and vertical motion are also suggested to be important.

The First ISCCP Regional Experiment (FIRE) Marine Stratocumulus Intensive Field Observations (IFO) took place off the coast of California during June and July 1987 (Albrecht et al. 1988). Its aims were to provide data to help to improve the parameterisation of clouds in general circulation models and to validate cloud retrievals from satellites. Aircraft, ship and satellite data were combined with land based measurements from San Nicholas Island to give measurements from the microscale to the mesoscale. Physical processes investigated were: the factors that affect fractional cloudiness and cloud morphology; the role of CTEI in determining cloud type; factors determining the entrainment rate; diurnal behaviour; the relationship between aerosols and cloud droplet distributions; and the characteristic large scale meteorological environment associated with stratocumulus. It was later concluded however

that a deficiency of FIRE was the inadequate definition of the large-scale fields of temperature, moisture and winds (Albrecht et al., 1995a). Duynkerke and Hignett (1993) and Smith and Kao (1996) model the diurnal variability of the FIRE boundary layer.

While there have been various observational studies of subtropical stratocumulus, midlatitude stratocumulus clouds have been less extensively studied. Regions where the conditions required for stratocumulus development often occur are: the North Sea, the midlatitude North Atlantic and Pacific and near the southern coast of Australia (Klein and Hartmann 1993). Observational studies of midlatitude stratocumulus boundary layers include the Joint Air-Sea Interaction (JASIN) experiment (Pollard et al. 1983) and measurements taken in the North Sea (Nicholls 1984, Nicholls and Leighton 1986). Stratocumulus clouds are also associated with cold air outbreaks, for example in the Gulf Stream and Kuroshio regions and over the Great Lakes.

JASIN took place between July and September 1978 in the area of the North Rockall Trough, an area of 1-2 km deep water off the north west coast of Scotland (Pollard 1978; Pollard et al. 1983). The aim of the experiment was to observe and distinguish between the processes causing mixing in the atmospheric and oceanic boundary layers and relate them to mean properties in the layers, and also to look at momentum and heat budgets and air-sea transfer. An important part of the experiment was to study the interaction of the boundary layer with mesoscale structures. It was also hoped to gather a dataset that would be of use in developing models of both boundary layers. The experiment involved ships, moorings and aircraft with two intensive meteorological phases and ten intensive radiosonde days, and fortuitously coincided with the brief life of the SeaSat satellite.

Guymer et al. (1983) present surface heat budgets for the entire experiment which are complemented by analyses of the boundary layer structure from aircraft measurements (Nicholls et al. 1983; Nicholls 1983) and by boundary layer budgets calculated by Taylor et al. (1983) from the radiosonde profiles. Case studies of the cloud radiative processes are presented by Schmetz et al. (1983) and of atmospheric frontal structure by Taylor and Guymer (1983). Many intercomparisons between the observations from different platforms were made, aircraft overflew buoys and ships and made long, close formation flights to compare systems on the different aircraft. The surface data from ships and buoys were extensively compared (JASIN Field Summary 1979) and the radiosondes used were all of the same type.

The boundary layer during JASIN was near neutral or slightly unstable with small surface fluxes. This meant that small changes in the mean variables could lead to the formation or to the dissipation of clouds (Nicholls et al. 1983). It was noted that coupling

between the cloud and the subcloud layers was weak and intermittent during the aircraft flights, which were always near local noon. The stress profiles from the aircraft decreased to small values near the cloud base (Nicholls et al. 1983) which is at variance with the results of the radiosonde budgets (Taylor et al. 1983) which show the stress extending into the cloud layer. These differences were attributed to sampling effects and the different scales of the two measurement techniques (see discussion following Nicholls et al. 1983).

The other main group of midlatitude stratocumulus measurements were C-130 aircraft measurements of turbulence within stratocumulus and stratus taken over the North Sea (Nicholls 1984, Nicholls and Leighton 1986) which have been extensively modelled (Nicholls 1984, Nicholls and Leighton 1986, Nicholls and Turton 1986, Duynkerke 1989, Ackerman et al. 1995). In JASIN and most of the North Sea flights the surface forcing was weak. When the surface layer is near neutral and surface forcing is weak, intermittent decoupling is often observed. Nicholls (1984) concluded that many factors could increase the tendency of the stratocumulus and subcloud layer to become decoupled. These include smaller buoyancy fluxes at the surface or at the cloud top, evaporation of drizzle beneath the cloud and increased entrainment of warm dry air into the cloud layer.

2.3.2 The Persistence of Stratocumulus Clouds

Section 2.3.1 described some of the regions where stratocumulus clouds are climatologically common. Many observations of these stratocumulus clouds have shown cloud top jumps in humidity and equivalent potential temperature that should be unstable to CTEI (Section 2.2.3). CTEI theories (e.g. Deardorff 1980) suggest that these clouds should rapidly entrain warm dry air and dissipate. Kuo and Schubert (1988) summarise observational data taken in persistent cloud most of which violate the entrainment instability criteria of Deardorff (1980). Most of the data show that these persistent clouds have an increase of liquid water potential temperature (see equation 4.5) of between 5K and 12K across the inversion with 9K being a typical value. Betts (1989) performs an equilibrium energy budget for the convective boundary layer over the ocean. This suggests that for the boundary layer to be in balance with radiatively driven subsidence the mean inversion strength should be 9K. If we therefore take 9K as a typical liquid water potential temperature inversion strength and consider the stability of stratocumulus in different regions as a function of humidity inversion strength. The data presented by Kuo and Schubert (1988) suggests that only midlatitude stratocumulus should be stable to CTEI as they typically have a humidity drop over the inversion of less than 4 gkg^{-1}. Typically the observations of subtropical stratocumulus have humidity jumps across the inversion of between 4 and 8 gkg^{-1} and should not be stable to CTEI. Trade wind cumulus boundary layers are characterised by even larger humidity

inversions, greater than 8 gkg^{-1}. These subtropical stratocumulus and trade cumulus observations suggest that transition from stratocumulus to cumulus occurs with an approximately constant liquid water potential temperature inversion of 9K (perhaps in radiative-convective equilibrium) but with an increasing humidity inversion.

2.3.3 The Breakup of Persistent Stratocumulus

Many observational studies have suggested that an external factor is often present in the breakup of stratocumulus cloud decks. Kloesel (1992) summarises the main external factors as: upward vertical motion ahead of cold fronts crossing stratocumulus regions or in the surface convergence zone ahead of an trough higher in the atmosphere; an increase in subsidence; or changes in the upstream conditions (e.g. offshore warm dry air replacing a maritime air mass). Kloesel (1992) combined FIRE data with satellite observations and model output to study periods of cloud dissipation. Case studies showed clearing resulting from the replacement of marine air with warm dry continental air associated with ridges in the anticyclone and from increased subsidence lowering the inversion to beneath the lifting condensation level.

Kawa and Pearson (1989) use measurements of ozone from the DYCOMS (Dynamics and Chemistry of Marine Stratocumulus) Experiment to calculate entrainment rates for Californian stratocumulus which were found to be largely uncorrelated with variations of boundary layer fluxes. This is suggested to arise from the importance of shortwave divergence in the turbulence budget. Again the breakup and reformation of stratocumulus clouds in this region is found to result from factors external to the boundary layer, such as meteorological disturbances rather than the internal evolution of the boundary layer. This was confirmed by Weaver and Pearson (1990). Brost et al (1982) also attribute changes in cloud amount to changes in the synoptic conditions. Betts and Boers (1990) however suggest that the breakup of stratocumulus to form small cumulus can be predicted from thermodynamics alone. A study of stratocumulus breakup over land (Price 1999) describes two cases where clouds were dissipated by solar radiation, in one case with entrainment enhanced by large wind shear across the inversion.

This section has summarised the conditions leading to the presence or absence of stratocumulus clouds in regions where they are climatologically persistent. The next section will consider the climatologically observed breakup of stratocumulus in the stratocumulus to trade cumulus transition.

2.3.4 The Stratocumulus to Cumulus Transition

The evolution of the subtropical stratocumulus to tropical cumulus clouds was poorly understood until after the ASTEX experiment, which took place in June 1992 in the northeastern Atlantic (Albrecht et al. 1995a). An important part of the experiment were the two Lagrangian experiments where constant level balloons and numerical prediction were used to follow air mass trajectories, which were intensively sampled using aircraft. Particular objectives were the study of the transition of stratocumulus to shallow cumulus including feedback of the effects of transition on the atmosphere and ocean. Mechanisms suggested for the breakup of marine stratocumulus were: CTEI, diurnal decoupling, patchy drizzle, mesoscale variability and circulations and episodic strong subsidence lowering the inversion below the lifting condensation level. ASTEX was designed to discover which of these processes were important in this region. It was also hoped to determine the processes leading to particular cloud types and amounts. Cumulus under stratocumulus was the most commonly observed cloud type during ASTEX.

Following the results of ASTEX Albrecht et al. (1995a) conclude that the breakup of the solid stratocumulus decks is brought about in stages. Initially diurnal decoupling of the cloud and subcloud layers occurs within the shallow boundary layer. As the air moves over warmer sea surfaces and is warmed the inversion strength is decreased allowing the boundary layer to deepen. As the inversion height increases the surface mixing no longer reaches the cloud base even at night and the layers can become permanently decoupled. The stratocumulus layer thins as its moisture supply from the surface is cut off and drier air is entrained at the cloud top. Moisture builds up in the subcloud layer and local recoupling and cumulus convection can occur, either to help maintain the cloud layer by providing moisture or destroy it by enhancing entrainment. As the boundary layer deepens with increasing SST the cloud becomes more broken and convective. The evolution of the boundary layer is shown schematically in Figure 2.4. This picture is complicated by the frequently observed organisation of the low-level cumulus into small mesoscale features feeding on the near-surface moist air, which results in a thicker stratocumulus layer and drizzle.

ASTEX demonstrated the value of the Lagrangian approach to boundary layer measurements (Bretherton and Pincus 1995, Bretherton et al. 1995) with two experiments, one in 'clean' and one in 'dirty' air masses (Albrecht et al. 1995a). The cloud microphysical properties were different in the continental and marine airmasses, with smaller droplets in the 'continental' clouds but with twice the liquid water content and greater reflectivity compared to the 'marine' clouds. An important feature of the ASTEX Lagrangian experiments was the real

time assimilation of soundings from ASTEX into ECMWF and NMC[2] operational analyses, in order to produce high quality regional forecasts for trajectory prediction and mission planning.

Klein et al. (1995) use data from Ocean Weather Ship (OWS) 'N' (30°N, 140°W) to relate the cloudiness at the site to non-local properties using data from VOS. They show that boundary layer cloudiness in this stratocumulus to cumulus transition region of the trade winds reacts to variations in the up-wind SST and upper-air temperatures 24 to 36 hours previously. This is consistent with modelling results. Klein et al. (1995) also conclude, like Klein and Hartmann (1993), that lower tropospheric stability is the best predictor of cloud amount although Norris and Leovy (1994) and Hanson (1991) find strong negative correlations of cloud amount with SST.

2.4 Summary

Many physical processes are important within the cloud-topped boundary layer. Turbulence within the cloud is driven by longwave cooling at the cloud top, which during the daytime is partially compensated by shortwave heating. The vertical distribution of heating and cooling can itself however lead to further instability. Turbulence near the cloud top leads to entrainment of above-inversion air, which supports the boundary layer against subsidence. The presence of large decks of cloud which theoretically violate entrainment instability criteria shows that our understanding of entrainment and cloud processes in general is incomplete. Surface fluxes of buoyancy and momentum mean that the surface layer is often well mixed. If the surface fluxes are weak, decoupling of the cloud and subcloud layer can occur, particularly during the daytime, and a slightly stable region separates the two regions of turbulence.

Detailed observations have been made of subtropical stratocumulus off the coast of California, while the other main subtropical stratocumulus decks are less well studied. JASIN and studies in the North Sea provided valuable insight into midlatitude stratocumulus and the decoupling of cloud and subcloud layers when surface fluxes are weak. Observed dissipation of stratocumulus decks has been linked to mesoscale processes and changes in the subsidence rate rather than to processes internal to the boundary layer like CTEI and decoupling. The stratocumulus to cumulus transition was observed in Lagrangian studies during ASTEX and the cumulus under stratocumulus cloud type was shown to be an intermediate stage in this transition. The driving force for the transition is thought to be the growth of the boundary layer in response to increasing SST.

---

[2] European Centre for Medium-Range Weather Forecasts and National Meteorological Centre (now NCEP, National Centres for Environmental Prediction)

Figure 2.1a Mid latitude stratocumulus in the North Atlantic, viewed from above during JASIN 1972. Photograph by P.M. Saunders.

Figure 2.1b Cumulus under stratocumulus in the midlatitude North Atlantic during JASIN. JASIN photographic collection.

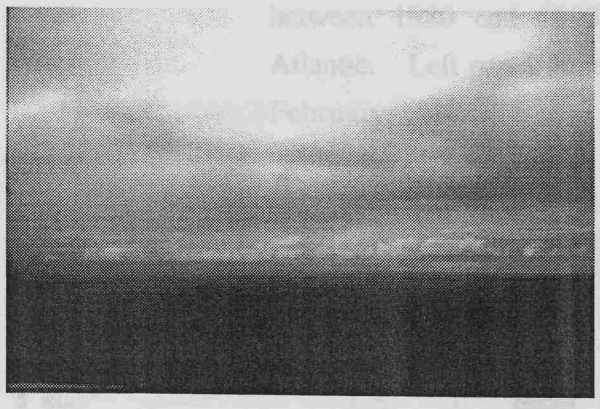

Figure 2.1c Cumulus under stratocumulus in the midlatitude North Atlantic during JASIN. JASIN photographic collection.

Figure 2.1d Cumulus under stratocumulus in the subtropical North Atlantic during ASTEX. Photograph by E.C. Kent.

Figure 2.1e Scattered cumulus in the subtropical North Atlantic during ASTEX. Photograph by E.C. Kent.

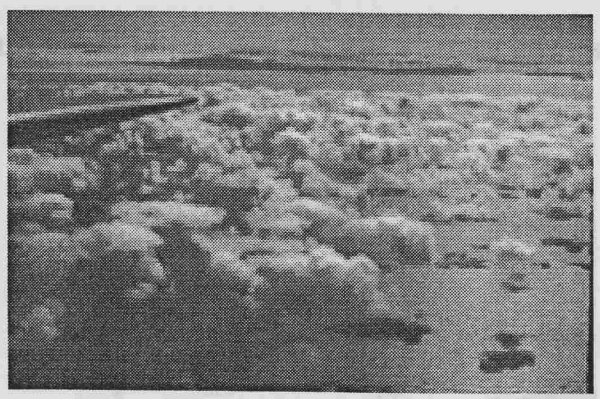

Figure 2.1f Scattered cumulus in the midlatitude North Atlantic during JASIN 1972, viewed from the air. Photograph by P.M. Saunders.

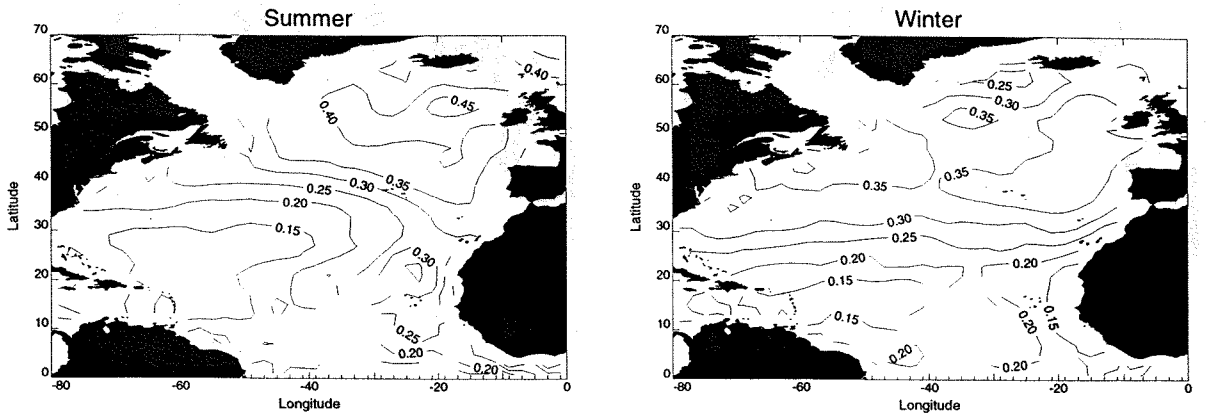

Figure 2.2a Mean proportion of COADS cloud reports with cloud type stratocumulus between 1980 and 1993 calculated from COADS 1a for the North Atlantic. Left panel June-July-August, right panel December-January-February.

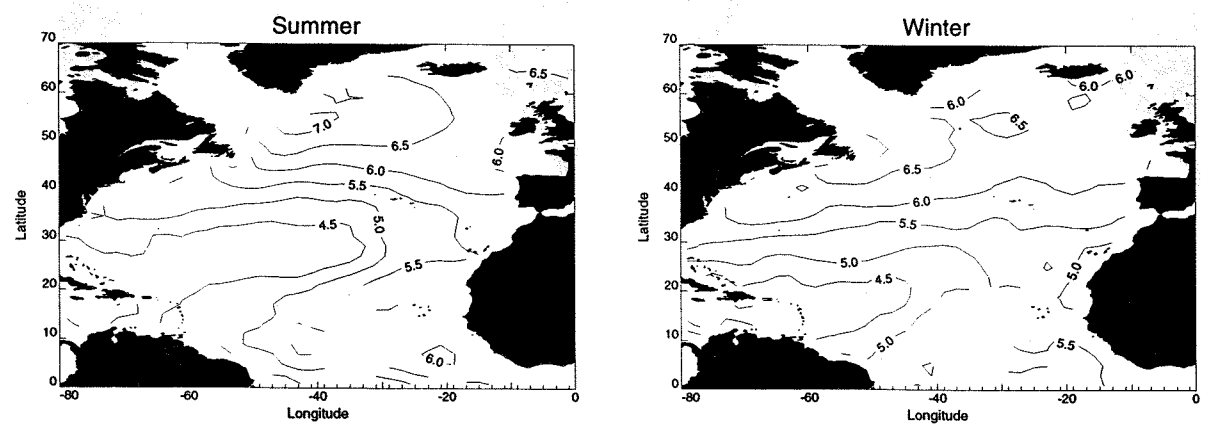

Figure 2.2b As Figure 2.2a but for the cloud cover in octas when stratocumulus clouds are present.

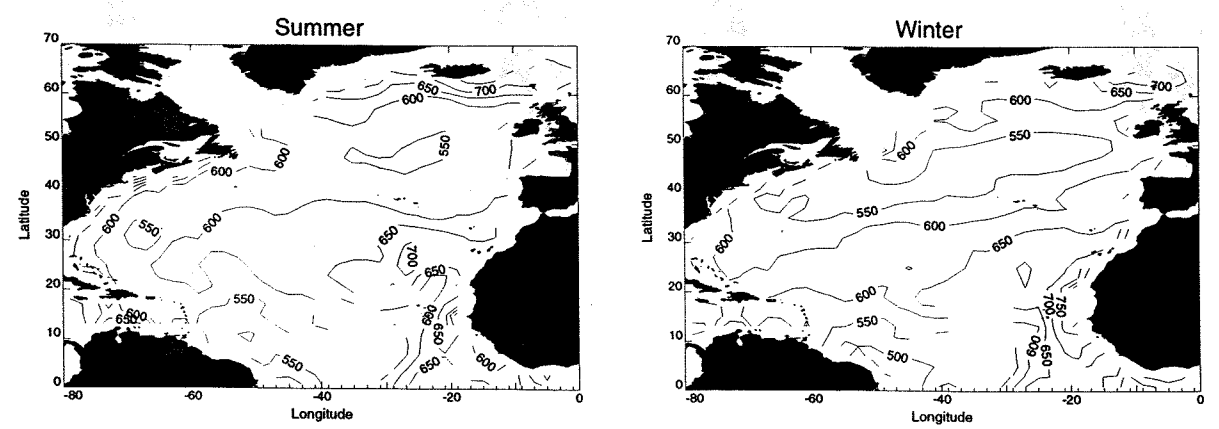

Figure 2.2c As Figure 2.2a but for the cloud base height in metres when stratocumulus clouds are present.

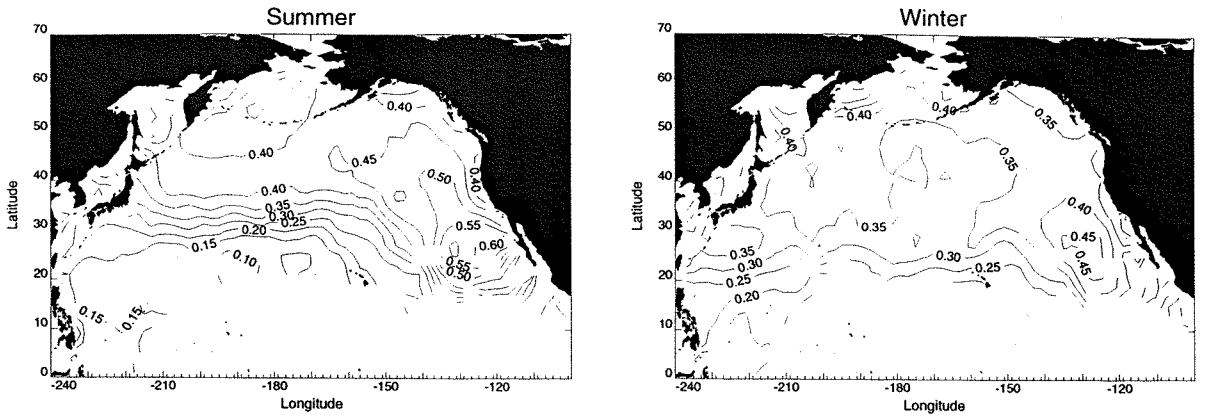

Figure 2.3a Mean proportion of COADS cloud reports with cloud type stratocumulus between 1980 and 1993 calculated from COADS 1a for the North Pacific. Left panel June-July-August, right panel December-January-February.

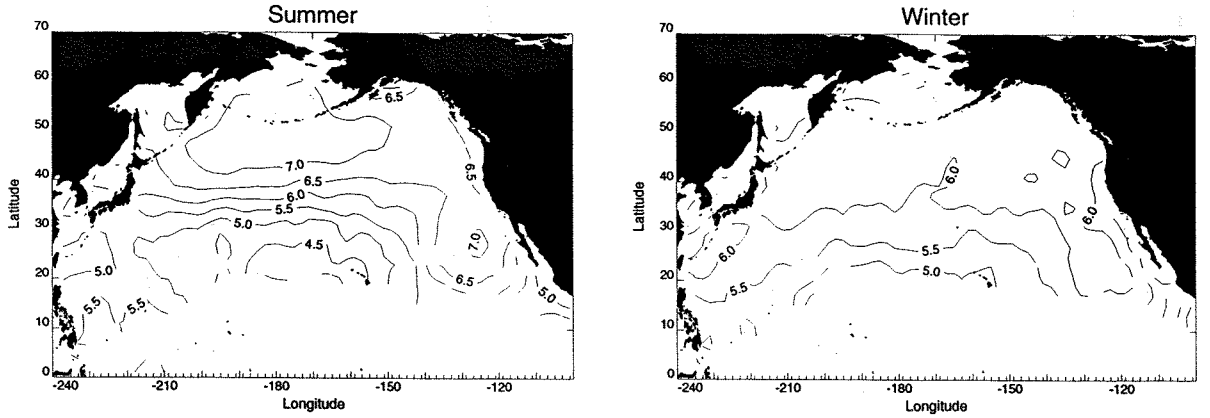

Figure 2.3b As Figure 2.3a but for the cloud cover in octas when stratocumulus clouds are present.

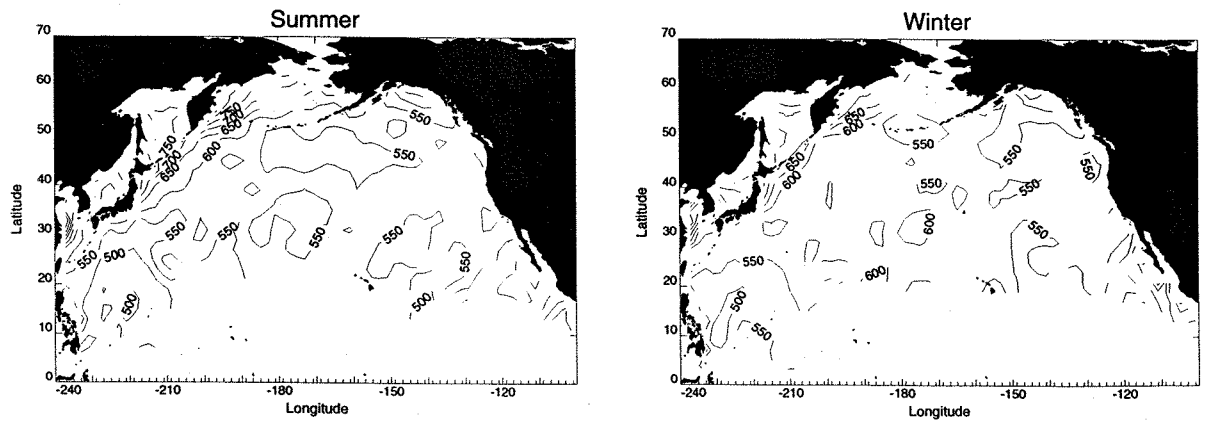

Figure 2.3c As Figure 2.3a but for the cloud base height in metres when stratocumulus clouds are present.

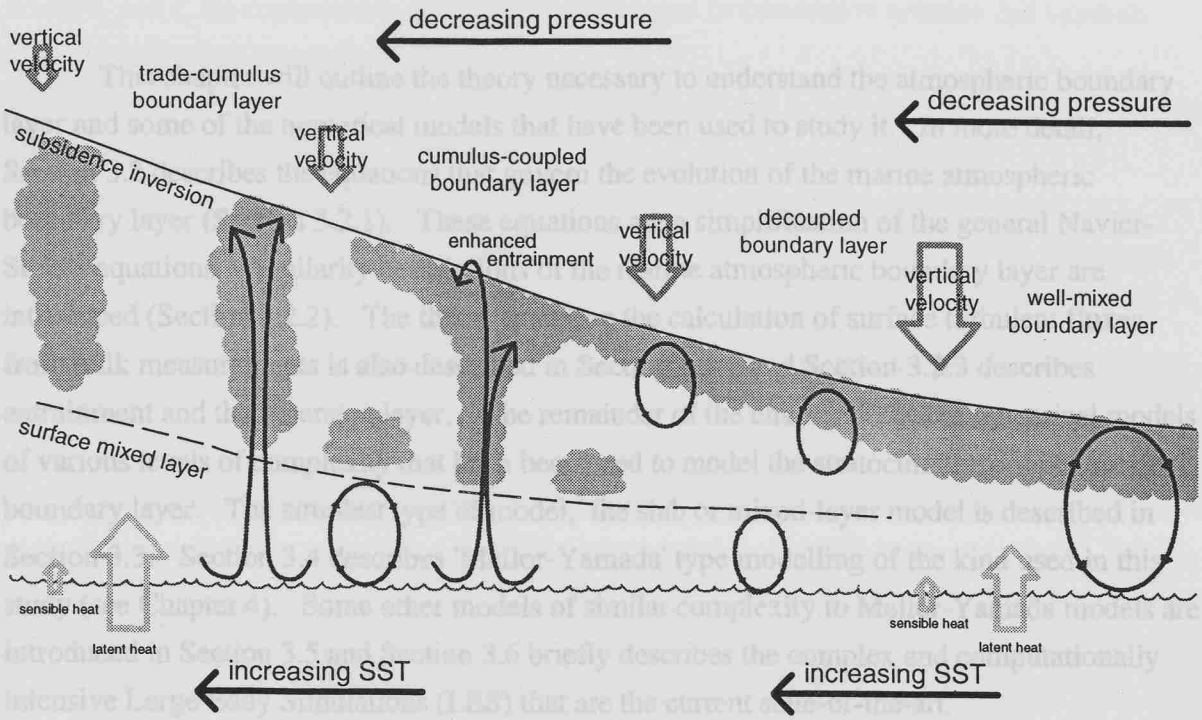

Figure 2.4 Schematic to show the development of the atmospheric boundary layer during the stratocumulus to cumulus transition. Cooler SSTs and high sea surface pressure are on the right of the diagram and represent conditions over the eastern subtropical oceans.

3. ATMOSPHERIC BOUNDARY LAYER THEORY AND MODELLING

3.1 Introduction

This chapter will outline the theory necessary to understand the atmospheric boundary layer and some of the numerical models that have been used to study it. In more detail, Section 3.2 describes the equations that govern the evolution of the marine atmospheric boundary layer (Section 3.2.1). These equations are a simplification of the general Navier-Stokes equations. Similarity descriptions of the marine atmospheric boundary layer are introduced (Section 3.2.2). The theory enabling the calculation of surface turbulent fluxes from bulk measurements is also described in Section 3.2.2 and Section 3.2.3 describes entrainment and the inversion layer. The remainder of the chapter describes numerical models of various levels of complexity that have been used to model the stratocumulus-topped marine boundary layer. The simplest type of model, the slab or mixed-layer model is described in Section 3.3. Section 3.4 describes 'Mellor-Yamada' type modelling of the kind used in this study (see Chapter 4). Some other models of similar complexity to Mellor-Yamada models are introduced in Section 3.5 and Section 3.6 briefly describes the complex and computationally intensive Large Eddy Simulations (LES) that are the current state-of-the-art.

3.2 Equations Describing the Atmospheric Boundary Layer

3.2.1 Equations of Mean Flow in Turbulent Conditions

The assumptions that are necessary to develop the Navier-Stokes equations into a workable set of equations for the atmospheric boundary layer are the Boussinesq approximations appropriate for shallow convection (Busch 1973). These assumptions are: dynamic viscosity and molecular heat conductivity are constant throughout the fluid; fluctuations in pressure, density and temperature are small compared to their mean values; vertical motions are small compared with a scale height (about 8 km, Stull 1988); and that heat generated by viscous stresses can be neglected in the thermodynamic energy equation (Busch 1973). The Boussinesq equations therefore consider viscous, incompressible fluids in which the temperature dependence of density is neglected unless multiplied by the acceleration due to gravity (i.e. in buoyancy terms). This section will summarise the description in Stull (1988) where further details may be found. The approximate equations needed to predict the mean variables including effects of turbulence on mean flow are:

the Continuity equation:

$$\frac{\partial u_i}{\partial x_i} = 0 \qquad \text{where } i = 1,2 \text{ or } 3 \tag{3.1}$$

where u_i and x_i are components of velocity and distance in summation notation (all symbols used are defined in Appendix 1);

the equation of state:

$$p = \rho \Re T_v \tag{3.2}$$

where p is the pressure, ρ is the density of air, $\Re$ is the dry gas constant and T_v is the virtual temperature;

the momentum equations (see equation 3.4.3c in Stull 1988):

$$\underbrace{\frac{\partial u_i}{\partial t}}_{\text{storage}} + \underbrace{u_j \frac{\partial u_i}{\partial x_j}}_{\text{advection}} = \underbrace{-\delta_{i3} g}_{\text{gravity}} + \underbrace{f \in_{ij3} u_j}_{\text{Coriolis}} - \underbrace{\frac{1}{\rho}\frac{\partial p}{\partial x_i}}_{\substack{\text{pressure} \\ \text{gradient}}} + \underbrace{\nu \frac{\partial^2 u_i}{\partial x_j^2}}_{\substack{\text{viscous} \\ \text{stress}}} - \underbrace{\frac{\partial \overline{u_i' u_j'}}{\partial x_j}}_{\substack{\text{divergence of} \\ \text{turbulent} \\ \text{momentum flux}}} \tag{3.3}$$

where t is time, g is acceleration due to gravity, f is the Coriolis parameter and ν is kinematic molecular viscosity. δ_{ij} and $\in_{ijk}$ are the Kronecker delta and alternating direction tensor in summation notation.

The equation for conservation of heat is:

$$\underbrace{\frac{\partial \theta}{\partial t}}_{\text{storage}} + \underbrace{u_j \frac{\partial \theta}{\partial x_j}}_{\text{advection}} = \underbrace{\nu_\theta \frac{\partial^2 \theta}{\partial x_j^2}}_{\text{viscosity}} - \underbrace{\frac{1}{c_p \rho}\frac{\partial R_j}{\partial x_j}}_{\substack{\text{source:} \\ \text{radiation}}} - \underbrace{\frac{LE}{c_p \rho}}_{\substack{\text{source:} \\ \text{latent heat}}} - \underbrace{\frac{\partial \overline{u_j' \theta'}}{\partial x_j}}_{\substack{\text{divergence of} \\ \text{turbulent heat flux}}} \tag{3.4}$$

where θ is potential temperature, ν_θ is the molecular thermal diffusivity, c_p is the specific heat capacity of air, R_j is the jth component of net radiation, L is the latent heat of evaporation of water and E is the evaporation rate. The equation of the conservation of total water content is:

$$\underbrace{\frac{\partial q_t}{\partial t}}_{\text{storage}} + \underbrace{u_j \frac{\partial q_t}{\partial x_j}}_{\text{advection}} = \underbrace{\nu_q \frac{\partial^2 q_t}{\partial x_j^2}}_{\text{viscosity}} - \underbrace{\frac{S_{q_t}}{\rho}}_{\text{source}} - \underbrace{\frac{\partial \overline{u_j' q_t'}}{\partial x_j}}_{\substack{\text{divergence of} \\ \text{turbulent total} \\ \text{water flux}}} \qquad (3.5)$$

where q_t is the total water content, ν_q is the molecular diffusivity of water vapour and S_{qt} is a source term for total water.

Defining the TKE, e, to be $\overline{u'u'} + \overline{v'v'} + \overline{w'w'}$ we can calculate the TKE budget in terms of the velocity variance components. The terms in the TKE budget can be represented in summation notion using Reynolds averaging[3] by:

$$\underbrace{\frac{1}{2}\frac{\partial e}{\partial t}}_{\text{storage}} + \underbrace{u_j \frac{1}{2}\frac{\partial e}{\partial x_j}}_{\text{advection}} = \underbrace{\delta_{i3} \frac{g}{\overline{\theta}_v} \overline{u_i' \theta_v'}}_{\text{buoyancy}} - \underbrace{\overline{u_i' u_j'} \frac{\partial u_i}{\partial x_j}}_{\text{shear}} - \underbrace{\frac{\partial \frac{1}{2}\left(\overline{u_j' e'}\right)}{\partial x_j}}_{\text{transport}} - \underbrace{\frac{1}{\overline{\rho}} \frac{\partial \left(\overline{u_i' p'}\right)}{\partial x_i}}_{\substack{\text{pressure} \\ \text{correlation}}} - \underbrace{\varepsilon}_{\text{dissipation}} \qquad (3.6)$$

where θ_v is the virtual potential temperature and ε the TKE dissipation rate.

In order to split measurements of a quantity into its mean and fluctuating parts and apply the Reynolds averaging techniques required to derive equations like 3.3 to 3.6 we need to consider appropriate time scales for defining the mean (and hence the fluctuating component). This is discussed in detail by Wyngaard (1973) who notes that the averaging time required increases with the order of the term (i.e. it takes longer to accurately define variance or correlation terms than the mean values) and with the measurement height.

3.2.2 Similarity Descriptions of the Atmospheric Boundary Layer

The atmospheric boundary layer is complex and it is usually impossible to fully describe in terms of the basic physical equations. However the boundary layer does show predictable behaviour in many situations and the simplest way to diagnose this behaviour is often by using dimensionless groups of variables. This is known as similarity theory. First it must be decided which variables are important for the particular problem. For example,

---

[3] It is assumed that any variable X can be split into mean (denoted by an overbar) and fluctuating parts (denoted by a dash): $X = \overline{X} + X'$. The covariance between the fluctuating components of X and another variable Y is denoted $\overline{X'Y'}$.

according to Monin-Obukhov similarity (described below), the important variables which give a dimensionless representation of the surface layer turbulence are the buoyancy flux, the surface velocity scale and the height above the surface. These variables are combined into a dimensionless parameter the value of which should indicate the steady state characteristics of turbulence in the surface layer. The relationship of the characteristics of the turbulence to the value of the dimensionless parameter needs to be determined from experiment. Thus the complex nature of the turbulence is described using parameters which are much easier to measure than the turbulence itself.

Above a thin layer at the ocean surface in which viscosity effects are important, the scaling of the near surface layer is often well defined by Monin-Obukhov theory. Monin and Obukhov (1954) suggested that a dimensionless characteristic of turbulence, ζ, must depend only on the surface velocity scale or friction velocity, u_*, the height above the ocean surface, z, $g/\overline{\theta_v}$, and the buoyancy flux, $\left(\overline{w'\theta_v'}\right)_0$. The Obukhov length, L_O, represents the height in the non-neutral surface layer where buoyancy production equals shear production of energy:

$$L_O = -\frac{u_*^3}{\kappa \frac{g}{\overline{\theta_v}} \left(\overline{w'\theta_v'}\right)_0} \qquad (3.7)$$

where κ is the von Karman constant. ζ is then defined as the ratio of the measurement height, z, to L_O. In neutral conditions ζ is zero. In stable conditions the buoyancy is suppressed by stable stratification and ζ becomes large and positive. In highly unstable conditions ζ is large and negative and free-convection occurs. In both very stable and unstable conditions the Monin-Obukhov scaling breaks down and either local or free-convective scaling respectively should be used instead (Garratt 1992). It should be noted that there are different ways of arriving at any particular value of ζ. In unstable conditions large negative values of ζ can be reached with a large heat flux and small u_* or by increasing z (Wyngaard 1973). Thus as height increases in the surface layer conditions become more unstable, while very near the surface (but at heights greater than the roughness length, z_0, see equation 3.8) conditions are close to neutral. Surface scaling should only be used up to heights at which the surface stress is still important and when the height is significantly less than the total boundary layer depth. Surface scaling does not work well for statistics of the horizontal wind speed components as they are sensitive to large eddies which scale with the boundary layer height (Kaimal et al. 1976). Very near the surface (and affecting spectra at scales less than about 1 cm) the Reynolds number independence that allows viscosity and thermal diffusivity to be neglected breaks down (Wyngaard 1973). Through most of the surface layer however the Reynolds number is large enough that these effects are not important.

Free-convective scaling is important near the surface in very unstable conditions. In this regime conditions are not sensitive to the boundary layer height or to L_O, but the height above the surface and the buoyancy flux are still important. Free-convective velocity and temperature scales can be defined which depend on the height and the buoyancy flux (Shaw 1990, Holtslag and Nieuwstadt 1986). In very stable conditions turbulence at the surface is intermittent. There is no satisfactory scaling in this very stable regime (Shaw 1990).

Using Monin-Obukhov theory to define the characteristic behaviour of the turbulence as a function of stability in terms of ζ, we now describe the profiles of momentum, temperature and humidity in the neutral atmosphere and how these neutral profiles are modified in non-neutral conditions. This has been described by Kraus and Businger (1994) and here we summarise their work. Close to the surface the wind speed can only depend on u_* and the height above the surface. Dimensional considerations lead to:

$$\frac{\partial U}{\partial z} = \frac{u_*}{\kappa(z + z_0)} \tag{3.8}$$

where U is the total wind speed and z_0 accounts for finite U at the sea surface. This equation can be integrated to give a logarithmic wind profile. Similar expressions can be found for temperature and humidity. These neutral profiles can be modified for non-neutral conditions by the inclusion of a dimensionless gradient in the gradient equation (Businger et al. 1971, Businger 1973). The dimensionless gradients of temperature (ϕ_t), humidity (ϕ_q) and momentum (ϕ_m) are functions only of ζ and need to be found empirically from experimental data:

$$\begin{aligned}
\frac{\partial U}{\partial z} &= \left(\frac{u_*}{\kappa z}\right)\phi_m(\zeta) \\
\frac{\partial \theta}{\partial z} &= \left(\frac{\theta_*}{\kappa z}\right)\phi_t(\zeta) \\
\frac{\partial q_t}{\partial z} &= \left(\frac{q_*}{\kappa z}\right)\phi_q(\zeta)
\end{aligned} \tag{3.9}$$

when z_0 is much smaller than z.

u_*, θ_* (the surface potential temperature scale) and q_* (the surface humidity scale) are calculated from the surface fluxes of momentum, heat and water:

$$u_*^2 = \overline{w'u'}$$
$$u_*\theta_* = -\overline{w'\theta'}$$
$$u_*q_* = -\overline{w'q'} \qquad (3.10)$$

the empirical functions used to approximate ϕ_m and ϕ_t in the present study are (Dyer 1974):

$$\left.\begin{aligned}\phi_m &= (1-16\zeta)^{-1/4}\\ \phi_t &= (1-16\zeta)^{-1/2}\end{aligned}\right\} \quad \text{unstable}$$
$$\phi_m = \phi_t = 1+5\zeta \qquad \text{stable} \qquad (3.11)$$

The humidity gradient is poorly known and is usually assumed to be the same as the temperature gradient. The gradient relations (equations 3.9) are then integrated to give temperature, humidity and wind profiles:

$$\frac{U-U_0}{u_*} = \frac{1}{\kappa}\left(\ln\frac{z+z_0}{z_0} - \Psi_m\right)$$

$$\frac{\theta-\theta_0}{\theta_*} = \frac{1}{\kappa}\left(\ln\frac{z+z_t}{z_t} - \Psi_t\right)$$

$$\frac{q-q_0}{q_*} = \frac{1}{\kappa}\left(\ln\frac{z+z_q}{z_q} - \Psi_q\right) \qquad (3.12)$$

where θ_0 and q_0 are surface values of θ and q (the specific humidity), z_t and z_q are the roughness lengths for temperature and humidity respectively accounting for the effects of molecular diffusion in the interfacial sublayer (Liu et al. 1979) and the stability functions (Ψ_t, Ψ_q and Ψ_m for temperature, humidity and momentum respectively, Paulson 1970) are:

$$\Psi_m(\zeta<0) = 2\ln\left[\tfrac{1}{2}\left(1+\phi_m^{-1}\right)\right] + 2\ln\left[\tfrac{1}{2}\left(1+\phi_m^{-2}\right)\right] - 2\tan^{-1}\left(\phi_m^{-1}\right) + \pi/2$$
$$\Psi_{t,q}(\zeta<0) = 2\ln\left[\tfrac{1}{2}\left(1+\phi_m^{-2}\right)\right]$$
$$\Psi_{m,t,q}(\zeta>0) = -7\zeta \qquad (3.13)$$

Once the flux profile relationships have been established the surface fluxes can be determined from measurements at a fixed height, say 10 metres, and knowledge of the SST.

This is done using bulk transfer coefficients (equations 3.14) which are found by comparing measurements of the fluxes (from the eddy correlation, profile or dissipation techniques) with mean parameters (see, for example, Large and Pond 1981; 1982).

$$\tau = \rho u_*^2 = \rho C_D U^2$$
$$H_{sen} = -\rho c_p u_* \theta_* = \rho c_p C_T U(\theta_0 - \theta)$$
$$H_{lat} = -L u_* q_* = L C_E U(q_0 - q) \qquad (3.14)$$

where τ is the wind stress, C_D the drag coefficient, H_{sen} the sensible heat flux, C_T the transfer coefficient for sensible heat, H_{lat} the latent heat flux and C_E the transfer coefficient for latent heat. Different values for the neutral values of these coefficients (denoted C_{DN}, C_{TN} and C_{EN}) have been suggested. The Smith (1980; 1988) coefficients are based on good quality open ocean data and Smith et al. (1992) used data from the southern North Sea. The values of the transfer coefficients can be calculated from equations 3.10 to 3.14.

3.2.3 The Inversion and Entrainment

The rate of turbulence-driven entrainment (see Section 2.2.3) across the inversion in stratocumulus conditions is not easy to determine. Lilly (1968, see Section 3.3.1) realised that the warm dry air entrained into the cloud layer could sink through the cloud if evaporative cooling of the entrained air was large enough. This would generate further turbulence and lead to more entrainment and rapid drying out of the cloud layer (CTEI, see Section 2.2.3). Deardorff (1980) refined Lilly's (1968) original criterion for this instability:

$$\Delta_i \theta_e < k \frac{L}{c_p} \Delta_i q_t \qquad (3.15)$$

where θ_e is the equivalent potential temperature, Δ_i denotes a change in a parameter across the inversion and the value of k is about 0.23. MacVean and Mason (1990) consider the theoretical criterion for self-sustaining instability, an instability which once started requires no further external energy input. They concluded that the value of k in equation 3.15 was about 0.7.

Albrecht et al. (1985) extended the instability criteria to include the ratio of cloudy to clear air in the region of mixing. If the volume of clear air being entrained is large then it is unlikely that sufficient cloudy air will be available to mix and the instability will therefore not

occur. By considering the final liquid water content of two air parcels of different properties and masses mixing they arrive at an expression for the onset of instability:

$$\chi < \frac{(1+\gamma_s)q_{liq\,max}}{\gamma_s c_p \Delta_i\theta - L\Delta_i q_v} \tag{3.16}$$

where χ is the fraction of cloudy air in the mixed parcel, q_v is the water vapour mixing ratio, $q_{liq\,max}$ is the maximum in-cloud liquid water content and γ_s is given by:

$$\gamma_s = \frac{L}{c_p}\frac{\partial q_s}{\partial T} \tag{3.17}$$[4]

Nicholls and Turton (1986) compare entrainment rates from mixed layer theory with aircraft observations and note that all of the parameterisations underestimate the measured entrainment rate. They also realised the importance of the proportions of cloudy and dry air being mixed. Kuo and Schubert (1988) extended this mixing fraction approach.

Siems et al. (1990) combine numerical simulations with laboratory and field measurements to study buoyancy-reversing systems such as those liable to CTEI. In a buoyancy-reversing system a lighter fluid stably overlies a denser fluid but some mixtures of these two fluids are denser than either fluid alone. They define a parameter D, the ratio of the density difference between the mixed fluid and the denser unmixed fluid to the density difference between the unmixed layers. They conclude that 'explosive entrainment' (i.e. CTEI) does not occur until D is greater than 1.3. This is a much more stringent condition than others suggested and leads to the conclusion that persistent stratocumulus decks with an observed density ratio between 0 and 0.2 should indeed be stable. They conclude that CTEI is unlikely to be the cause of the transition of stratocumulus to cumulus but that evaporatively induced entrainment, in conjunction with other processes, can enhance cloud and surface layer decoupling, an important feature of the transition.

In a series of papers Lock and MacVean (1999a,b; Lock 1998) use the results of a LES model to derive equations for the parameterisation of entrainment by varying the forcing. They conclude (Lock and MacVean 1999a) that only in the case of surface heating acting alone

---

4 $\frac{\partial q_s}{\partial T}$, the change in saturation specific humidity with temperature can be calculated from the Clausius-Clapeyron relationship, see e.g. Stull (1988).

is the entrainment flux simply related to the surface flux (i.e. the entrainment flux is about 20% of the surface flux, see Section 3.3 on slab models). They find that entrainment rates due to surface forcing and radiative forcing at the cloud top act independently and that radiative cooling promotes deepening of the boundary layer both directly (through cooling in the inversion layer) and indirectly (through entrainment from radiatively generated turbulence). Their experiments neglect effects due to evaporation and condensation by considering a dust cloud. These effects were later included by Lock and MacVean (1999b) who found that entrainment rates driven by buoyancy-reversal were strongly dependent on the cloud depth and liquid water content. Lock (1998) summarises these results to give a parameterisation of the entrainment rate for the shear-free, convective, stratocumulus-topped boundary layer. The entrainment rate depends on; the surface buoyancy flux, the net radiative divergence, the inversion jumps in equivalent potential temperature and humidity, the maximum in-cloud liquid water and the boundary and cloud layer depths.

3.3 Mixed-layer Models

3.3.1 The Lilly (1968) Mixed-layer Model

Lilly (1968) introduced a slab-type model to simulate features of a radiatively active turbulent cloud layer over the sea under a strong subsidence inversion. He considered both wet and dry clouds (i.e. aerosol clouds, such as a cloud of smoke, in which there are no phase changes). For the wet clouds, he thought that the wet-bulb potential temperature must increase upwards in the inversion for the cloud to be stable to CTEI. In his model the potential temperature and total water are constant through the mixed layer, which can contain both clear air and cloud. The mixed layer is capped by an inversion. The height of the cloud base depends on the difference of the surface humidity from its saturation value. All processes within the cloud are assumed to occur in saturated conditions. The change in mixed layer humidity and potential temperature with time depends on the differences between the surface fluxes and the cloud top fluxes and the depth of the mixed layer. The depth of the mixed layer in turn depends on the vertical velocity, cloud top fluxes (including net outward radiation) and the inversion jumps of temperature and humidity. Entrainment of air from above the inversion into the turbulent mixed layer is controlled by subsidence, fluxes, pressure, temperature and the geometry of the mixed and cloud layers. As the model contains no dynamics, assumptions are required to estimate the energy budget and hence the entrainment. TKE is produced by the surface turbulent fluxes. Closure of the energy budget follows Ball (1960) by assuming a partition of the buoyancy flux into a part that produces TKE and a part that dissipates TKE. Assumptions about the ratio of production to dissipation lead to 'maximum' and 'minimum' entrainment conditions. The minimum entrainment condition covers all cases

where the turbulent fluxes are everywhere positive. This occurs when there is no entrainment; when there is free entrainment into a neutral layer (which is rapid and the term minimum entrainment is misleading, Deardorff 1976); or when there is encroachment (the growing of the mixed layer resulting from the thermodynamics of the heating). If the maximum entrainment condition is used all the TKE is assumed to be available for entrainment.

Although Lilly's model has often been used for boundary-layer simulation, many modifications have been suggested, mostly involving the entrainment conditions, the treatment of radiation and the positioning of processes within the constraints of the slab-like distributions. These are discussed briefly in the following sections.

3.3.2 The Treatment of Entrainment and Radiation

In the model of Lilly (1968) the radiative flux divergence is assumed to occur at the cloud top and is assumed to drive entrainment directly. Deardorff (1976) refined this by assuming that some of the radiative divergence occurs within the cloud and some at the top. This is justified by considering the model to represent average conditions over some horizontal area in which there is small-scale variation in the cloud top height. He noted that penetration of cloud hummocks into the inversion region ensures that some of the cooling occurs within the region of (horizontally averaged) large vertical temperature gradient. In this case some of the entrainment is modelled directly and some is turbulently driven within the cloud. Kahn and Businger (1979) place all the radiative cooling within the cloud layer. This approach is supported by Randall (1980). He notes that whilst the amount of cooling happening within the horizontally averaged inversion depth depends on the ratio of this depth to the depth of the region of strong longwave cooling, at any single location, all of the cooling occurs in the turbulent region. These different assumptions of Lilly (1968), Deardorff (1976) and Kahn and Businger (1979) lead to different amounts of entrainment and therefore different steady-state solutions. These different assumptions are included in the models by interpolating between minimum and maximum entrainment conditions and adjusting the fraction of radiative flux divergence occurring in the mixed layer. Randall (1980) asserts that the conclusion of early studies (e.g. Lilly 1968) that the mixed-layer structure was insensitive to the entrainment assumptions made, is valid only when the depth of the radiatively cooled layer at the cloud top is assumed small. The sensitivity of the boundary layer structure to entrainment assumptions increases as the depth of cooling increases.

Deardorff and Businger (1980) show that the slab-model implementation of Schubert et al. (1979) does not adequately allow for the effect of the radiative divergence near the cloud top on the heat flux, although the radiative divergence does act to change the mean temperature.

The contribution of cloud-top cooling to the turbulent entrainment is therefore missed. This is addressed in the model of Stage and Businger (1981 a,b) and further developed by Rogers et al. (1984).

Another area of contention is energy transport, which is not explicitly modelled in this type of model. The amount of entrainment will be different if redistribution of energy is allowed. If energy redistribution is allowed, the slab-model boundary layer can remain well mixed even if there is a region of negative buoyancy flux. It is clear that some transport of energy occurs and this transport is limited by the work required to overcome buoyancy. Turton and Nicholls (1987) model diurnal decoupling using a multiple-mixed layer model in which the decoupling of mixed layers is achieved by explicitly limiting the amount of energy redistribution that is allowed (see Section 3.3.4).

3.3.3 Steady-state Relationships Derived from Mixed-layer Models

Schubert (1976) used a version of Lilly's (1968) mixed layer model to look at the dependence of the steady-state solution on the vertical velocity due to large-scale divergence, sea-surface temperature and entrainment assumptions. He shows that the cloud top and base are lower for smaller SSTs largely resulting from encroachment conditions (see Stull 1988). Lower cloud heights also occur when divergence and hence subsidence rates are larger. The cloud top height increases with entrainment although the cloud thickness is unaffected by the fraction of TKE available for entrainment. Similar results are presented by Schubert et al. (1979) and also Kraus and Schaller (1978) who go on to simulate steady-state characteristics of boundary layers in the trade winds, off the west coast of California, over the Norwegian Sea and over the Arctic Ocean. Hanson (1987) uses mixed layer theory to analytically predict the change in height of the atmospheric boundary layer in response to changing SST.

3.3.4 Multiple Mixed-layer Models

Turton and Nicholls (1987) used a model with multiple mixed layers to simulate the diurnal variability of stratocumulus. The height at which decoupling occurs is predicted by determining whether the TKE is large enough to mix properties through any regions of negative buoyancy. The relative vertical locations of processes that stabilise and destabilise the boundary layer need to be taken into account. This is equivalent to imposing a limit on the work that can be done against buoyancy to redistribute properties. They conclude that the tendency for layers to decouple is enhanced by increased solar absorption in the cloud and by small sea surface buoyancy fluxes, but that other factors are important, such as the geometry

of the boundary layer (the ratio of the subcloud to the mixed layer depth which is related to the large scale divergence).

Another type of bulk model with multiple mixed layers is the Albrecht cumulus model (Albrecht 1984, Bretherton 1993, Wang 1993). These models consist of a surface mixed layer with a small stable layer at the top of this mixed layer then a cloud layer with gradients in temperature and humidity in this cloud layer. Above the cloud layer is an inversion layer with jumps in temperature and humidity. Fluxes into the cloud layer are assumed to be 20% of the surface fluxes and crucial to these models is the cumulus parameterisation required to define the processes, mean profiles and fluxes within the cloud layer. This parameterisation is based on an entraining plume model of cumulus convection. The air entering the cloud layer at the cloud base is assumed to have the same properties as the mixed layer air and is modified on ascent by lateral entrainment of cloud-environment air (Bretherton 1993). Each updraft plume is assumed to exist for constant time. At the end of its lifetime the plume detrains all its air into the cloud environment. The plumes are further assumed to occupy a constant fraction of the cloud layer at all heights. The convective fluxes within the cloud are defined in terms of a cloud mass flux multiplied by cloud-environment differences in properties. Albrecht (1984) took a plume lifetime to be 20 minutes and the fraction of cloud containing updrafts to be 0.02. This defines the mass flux per unit height and can be used to define a timescale on which the whole cloud layer is replenished with updraft air, one third of a day for the values taken by Albrecht (1984).

Once the mass flux has been obtained it is necessary to calculate the cloud-environment differences in temperature and humidity. The closure assumption uses the average difference in buoyancy between the cloud and environment over the whole cloud layer. This buoyancy difference is defined in terms of the lateral entrainment and constrained to be a fraction of the buoyancy difference expected if there was no entrainment. Albrecht (1984) chose the fraction to be a half and then adjusts the lateral entrainment rate to give a buoyancy contrast of 0.5 K. Wang (1993) defines this fractional difference between plume and cloud layer buoyancy in terms of the buoyancy contrast if no lateral entrainment occurred, then tunes this parameterisation to best simulate both stratocumulus and cumulus boundary layers. Bretherton (1993) shows that these different assumptions lead to very different cloud fractions and boundary layer structure. He also notes that observations and our current understanding of the cloudy boundary layer cannot suggest which type of parameterisation is correct.

3.3.5 Drawbacks of Mixed-layer Models

The amount of discussion on the radiation profile and prediction of entrainment rates in the literature illustrates the shortcomings of mixed-layer modelling of the boundary layer. Whilst all of the authors would accept that liquid water within the turbulent cloud is the cause of the radiative cooling, there is disagreement on the best way to include this distributed cooling within the framework of a slab model. None of the models adequately treat shortwave heating (and most neglect it). The shortwave heating is distributed over a thicker layer than the longwave cooling and this is hard to incorporate into slab-type models. Slab models are therefore unable to adequately model diurnal variability and effects such as decoupling of the cloud and subcloud layer. Turton and Nicholls (1987) did however develop a multiple-mixed layer model to simulate such effects.

3.4 Mellor-Yamada Type Models

3.4.1 Introduction

Mellor (1973) developed a model that has been used for atmospheric, oceanic, benthic, coastal and general engineering applications (Nurser 1996). Prognostic equations for the Reynolds stresses, scalar fluxes and variances are used. Closure assumptions include Kolmogorov (1942) energy dissipation, down gradient transfer, and Rotta's (1951) 'return to isotropy' hypothesis in which it is assumed that the pressure correlation term acts to make the turbulence more isotropic. A hierarchy of models can be developed with varying levels of complexity (Mellor and Yamada 1974).

3.4.2 The Different Levels of Complexity

Systematically neglecting the more anisotropic terms in the most complex set of equations, known as level 4, leads to more practical models of lower level, designated 3, 2 and 1. The level 4 and 3 models are too complicated to apply to the atmosphere and the level 1 model produces unrealistic results (Mellor and Yamada 1974). Mellor and Yamada (1974) therefore define a level 2.5 model that includes the most important features of the level 3 model and performs better than the level 2 model. The range of model complexity between levels 3 and 2 is:

Level 3: The level 3 model explicitly solves equations for TKE and the variance and covariance of momentum, temperature and humidity. The mixing length, which represents

the mean distance which an air-parcel travels before it mixes completely with its environment (or the length scale of the eddies which dominate the mixing), is also a prognostic variable.

Level 2: In the basic level 2 model the time derivative, advective and diffusion terms are neglected in the TKE equation giving a local balance between shear and buoyancy production and dissipation. The mixing length is prescribed, often using the diagnostic formula of Blackadar (1962).

Models of Intermediate complexity, levels 2.5 and 2.2: The level 2.5 model includes the time change, advection and diffusion of TKE but neglects equivalent terms in the prognostic equations for the variance and covariance of the scalar variables. For example, the temperature variance reduces to a diagnostic variable. In the full level 2.5 model the mixing length is a prognostic variable. The mixing length equation includes the time derivative, and the advection and diffusion terms. If an algebraic formulation for the mixing length is used (for example that of Blackadar 1962) the level of the model is decreased. Koracin and Rogers (1990) experimented with both the prognostic and diagnostic forms of the mixing length and found that the prognostic form could give unrealistic values, particularly within the cloud layer. They therefore used a diagnostic form for the majority of their modelling. This level of complexity has been described as level 2.2 (Simpson et al. 1996).

3.4.3 Marine Atmospheric Mellor-Yamada Type Model Studies

The original derivation of this type of model was for simulations of conditions over a cooling pond (Yamada 1978,1979). Yamada and Mellor (1979) coupled a cloud model to a level 2.5 model to simulate cumulus in the trade wind region. Mean profiles were well reproduced, although turbulence data was not available for comparison with results. Yamada and Kao (1986) modelled the fair weather marine boundary layer. Their simulations agreed with observations and with the large eddy simulation of Nicholls et al. (1982). In particular the components of the TKE budget were well modelled. Tjernström and Koracin (1995) modelled a decoupled stratocumulus-topped marine boundary layer from the FIRE IFO, again with reasonable results. Koracin and Rogers (1990) and Rogers and Koracin (1992) investigate the effects of surface forcing on the marine atmosphere, although no observations are shown for comparison. They use models ranging in complexity from level 2 to level 2.5.

3.4.4 Drawbacks of Mellor-Yamada Type Models

Nurser (1996) summarises the weaknesses of this type of model. These weaknesses are usually determined by comparison with large eddy simulations (see Section 3.6). Free

convection is poorly simulated by this type of model as the assumptions on which the parameterisations are based cease to be valid. The Mellor-Yamada scheme does not differentiate between 'top down' and 'bottom up' diffusion. This can be important in boundary layers in which the vertical velocity distribution is strongly skewed, for example in strong cumulus convection with narrow regions of strong updraughts and broader regions of weaker descent. Neither free convection nor strongly skewed vertical velocities are found in the stratocumulus boundary layer and conditions of organised convection could not be simulated with a one-dimensional model anyway. Also correlations between scalar quantities and buoyancy are neglected. Comparisons with observations suggest that the turbulent kinetic energy is not well modelled in the Mellor-Yamada scheme.

3.5 Other Higher-order Models

Bougeault (1985) used a one-dimensional numerical model solving for mean values and both second and third order correlations of boundary layer variables to investigate the importance of the stratocumulus diurnal cycle. The model reproduced realistic profiles of variables in the boundary layer using only the large-scale information from JASIN for initialisation. His numerical experiments suggested that the decoupling of the cloud and subcloud layers with cumuli beneath the stratocumulus, was not a steady state solution but a transient due to a time lag for the boundary layer to adapt to the varying solar heating. If daytime conditions were maintained there was a tendency to form a lower solid cloud deck. He also concluded that the cloud top height was determined largely by the nighttime conditions when the turbulent mixing was most active.

Chen and Cotton (1987) modelled Californian stratocumulus using a one-dimensional model with explicit cloud microphysics such as partial condensation and drizzle. They note a 15-20 minute periodicity in cloud top entrainment rates, which they attribute to drizzle processes and shear, changing either of these altered the period of the changes.

Duynkerke and Driedonks (1988) modelled an example of shear driven stratus from the North Sea. Their model based the exchange coefficients on the TKE budget. Good agreement was found with observations although the liquid water amount was over predicted. The model did not contain a drizzle mechanism and could not therefore lose liquid water through precipitation, which was observed at the time.

Ackerman et al. (1995) used a model with complex cloud microphysics to simulate North Sea data, again using the TKE budget for turbulence closure (the same dataset is simulated in the present study, see Section 5.3.1). Their simulation does not show the

observed daytime decoupling of the cloud and subcloud layers. However they note the importance of the cloud droplet size distribution, infrared scattering, the effect of radiative divergence on droplet condensational growth and the subsidence rate on the boundary layer structure.

Krueger et al. (1995 a,b) used a two-dimensional eddy-resolving model to simulate the stratocumulus to cumulus transition. The large eddies in their model are described using anelastic equations and the subgrid scale turbulence closure uses third order moments. A bulk microphysics parameterisation is used but drizzle is omitted from their simulations. The radiation scheme used with this model is the same at that used in the present study. They suggest that intermediate stages in the evolution are a deep stratus-topped boundary layer then a 'cumulus under stratocumulus' boundary layer. The cloud ensemble model explicitly resolved the convective circulations and parameterised the small subgrid scale eddies with third-moment closure. It was also computationally inexpensive. The simulations used diurnally averaged solar radiation indicating that the diurnal cycle was not essential for the transition. The simulated boundary layer depth and mixing ratio were sensitive to the above-inversion structure.

Wyant et al. (1997) also simulate the stratocumulus to cumulus transition with a two-dimensional eddy-resolving model. They use a first-order subgrid scale turbulence closure scheme with Richardson number eddy viscosities. They use a bulk radiation scheme but include parameterisations for the microphysics which includes the effect of drizzle. They confirm the conclusions of Albrecht et al. (1995a) on the nature of the transition. Increasing SST leads to increased latent heat flux and boundary layer depth, which induces decoupling. Initially, diurnal decoupling of the cloud and subcloud layers occurs. As the SST increases further intermittent cumulus clouds detrain into the stratocumulus layer which eventually dissipates as the cumulus convection becomes stronger and the entrainment of above inversion air increases. In the final stages the simulation shows characteristics of trade cumulus. Diurnal variations in solar radiation modulate the fractional cloudiness but do not affect the stages in cloud development.

3.6 Large Eddy Simulations

LES of turbulent processes are a compromise between the higher-order models described in the previous sections and an explicit simulation of all scales of motion. A local spatial filter is applied to the equations to separate large and small-scale motions. An explicit simulation of the large-scale turbulent motions is made and a turbulence closure model used to represent the unresolved small-scale motions. Ideally the cut off is within the inertial subrange

and small-scale motions act only to dissipate the turbulence energy. The problem is that in practice, near boundaries and regions of static stability, the turbulence scales can become smaller than the filter scale and the results in these regions depend only on the form of the turbulence closure, known as the subfilter model (Mason 1994). Different subfilter closures are used (Lesieur and Métais 1996, Mason 1994).

Mason (1994) notes that the results of large eddy simulations that pass convergence criteria (where the model output converges as the resolution and scale of the filter operation decreases) are often treated as data without experimental support. However, deficiencies due to the poor resolution of scales near boundaries and stable regions should be a general problem and validation of a few key cases with experimental data rather than all situations should suffice (Mason 1994). Nurser (1996) suggests that the results of large eddy simulations can be used to test and improve the output of models such as those described in the previous sections. The use of LES results to test and develop entrainment parameterisations has been mentioned in Section 3.2.3, other examples include Moeng et al. (1999) and vanZanten et al. (1999). Bechtold and Siebesma (1998) use a LES model to investigate Gaussian cloud parameterisation (see Section 4.5.1) often used in LES and other types of models.

However, large eddy simulations of the stratocumulus-topped boundary layer are computationally intensive due to the large range of scales required (a few kilometres for boundary layer depth, a few metres for the inversion region and several kilometres horizontally to include the largest eddies, Derbyshire and Kershaw 1993). This means that many studies are run at resolutions which are too coarse to resolve important processes (e.g. Stevens and Bretherton 1999). Running a model at coarse resolution means the closure scheme becomes relatively more important. Some LES of the stratocumulus-topped boundary layer use Richardson number closure (a balance between shear and buoyancy) which is lower level closure than is used in most Mellor-Yamada type models, for example the model used in the present study. Additionally radiation schemes are also computationally expensive and simplified schemes are often used (e.g. Lock 1998). This means that whilst LES has the potential to produce the best results, in practice the compromises required to reduce computational expense mean that this may not always be the case. For example, Bechtold et al. (1996) present a comparison of LES and other models for the FIRE boundary layer. The results from the different LES show wide scatter and the surface fluxes are in all cases larger than those that would be expected from surface layer theory, in one case by a factor of four.

3.7 Summary

The Navier-Stokes equations suitable for the description of atmospheric mean flow in turbulent conditions are introduced. The Boussinesq approximations reduce these Navier-Stokes equations to a form suitable for the study of shallow convective processes in the atmospheric boundary layer. The terms in the TKE budget are also introduced. The boundary layer is often described in terms of dimensionless groups of variables using similarity theory. Monin-Obukhov similarity theory is widely applicable in the atmospheric boundary layer and can be used with the flux-profile relations to determine the effect of atmospheric stability on the surface fluxes of sensible and latent heat.

Modelling of the marine atmospheric boundary layer has evolved from simple analytic slab models, through turbulence closure of different orders to the most sophisticated and computationally intensive large eddy simulations. LES of the stratocumulus-topped boundary layer is currently limited as the range of scales required to characterise the boundary layer is large and is at the limit of current computing power.

Mixed-layer models do not contain sufficient physics to model the stratocumulus-topped boundary layer with its tendency to become intermittently stratified rather than well mixed. LES models are computationally expensive and it is not presently possible to study the impact of changing forcing and profiles for many different cases. This leaves second-order models of which the Mellor-Yamada type has been frequently used to study the stratocumulus-topped, clear, small cumulus and trade cumulus boundary layers. A one-dimensional model of this type is simple enough to enable isolation and understanding of processes within the boundary layer but contains enough physics to model the boundary layer reasonably well in many situations. A Mellor-Yamada type model is described in the following chapter along with details of the model development that has taken place as part of this study.

4. THE NUMERICAL MODEL

4.1 Introduction

This chapter will describe the one-dimensional model used to simulate the atmospheric boundary layer and how it has been developed during the course of this study. Section 4.2 explains the choice of the particular model used and Section 4.3 gives the equations to be solved. The parameterisations and assumptions required to solve these equations (the turbulence closure scheme) are described in Section 4.4 and the treatment of cloud and radiation in Section 4.5. Section 4.6 describes the numerical method chosen to approximate these equations. Section 4.7 presents the equations in finite difference form as used in the model including the boundary conditions. Section 4.8 summarises the model highlighting the modifications that have been made. Again all symbols are defined in Appendix 1.

4.2 Choice of the Underlying Mellor-Yamada Type Model

The model used in this study is one-dimensional and based on that of Koracin and Rogers (1990) and Rogers and Koracin (1992), hereafter KR, who modified a model by Yamada (1978, hereafter Y78) by adding radiative processes and reducing the three-dimensional code to one-dimension. Equations are solved for the evolution of mean profiles of temperature, humidity, wind speed components and TKE (Section 4.3). The variance and covariances of these variables are parameterised (Section 4.4). The turbulence closure scheme (Section 4.4) uses eddy mixing coefficients for momentum, heat and water which are calculated following Y78. The variance and covariance of the momentum, total water content and liquid water potential temperature are also diagnosed using equations defined by Y78. Simplification to the model described by Y78 is made by using a diagnostic rather than prognostic form for the mixing length (Blackadar 1962). The model is therefore second order and level 2.2 (see Section 3.4.2). The cloud and liquid water amounts are calculated from the Gaussian Cloud Model relations (Sommeria and Deardorff 1977; Mellor 1977, Section 4.5.1). The radiation scheme is that of Fu (1991) and uses the delta-four-stream approximation (Sections 4.5.3 and 4.5.4).

This Mellor-Yamada type model formulation is thought to be appropriate for the modelling of stratocumulus-topped boundary layers (Koracin and Rogers 1990). The assumptions on which the model is based will break down under conditions of free convection or when convection is organised. Neither of these conditions should apply in the stratocumulus or shallow cumulus boundary layer. As the model is one-dimensional it cannot be used in regions of strong horizontal inhomogeneity without applying additional empirical

forcing terms. This has not been done in the present study. The model will be used in this study to simulate a Lagrangian evolution of the boundary layer with prescribed SST and vertical velocity.

During the course of this study another one-dimensional model was implemented, the UK Meteorological Office Single Column Model (Lean 1992). It was not found possible to realistically simulate the stratocumulus topped boundary layer with this model. The recent results of Bushell and Martin (1999) use an updated version of this model but come to a similar conclusion. They attribute part of the failure to realistically simulate the cloudy boundary layer to the vertical resolution. Increasing the resolution of this model however deteriorates the performance of the convective adjustment scheme (A. Grant, pers. comm.). In the present study the vertical resolution of the Single Column Model was increased but this did not lead to improved simulations. It was concluded that the Single Column Model was optimised for coarse vertical resolution and therefore it was not used further in this study.

4.3 Equations to be Solved

Equations 3.3-3.6 can be written in one-dimension as equations 4.1 and 4.2 for the wind speed components u and v; as equation 4.6 for liquid water potential temperature, as equation 4.8 for total water content and as equation 4.10 for TKE:

$$\frac{\partial u}{\partial t} + w\frac{\partial u}{\partial z} = f\left(v - v_g\right) + \frac{\partial}{\partial z}\left(K_m \frac{\partial u}{\partial z}\right) \tag{4.1}$$

$$\frac{\partial v}{\partial t} + w\frac{\partial v}{\partial z} = -f\left(u - u_g\right) + \frac{\partial}{\partial z}\left(K_m \frac{\partial v}{\partial z}\right) \tag{4.2}$$

where u and v are the north and east components of wind speed respectively, u_g and v_g are likewise the north and east components of the geostrophic wind speed, w is the vertical wind speed. The viscosity term is neglected, the pressure gradient and Coriolis forces have been combined using:

$$fu_g = -\frac{1}{\rho}\frac{\partial p}{\partial y}; \qquad fv_g = \frac{1}{\rho}\frac{\partial p}{\partial x} \tag{4.3}$$

and the divergence term has been parameterised using an eddy mixing coefficient, K_m:

$$\overline{u'w'} = -K_m \frac{\partial u}{\partial z}; \qquad \overline{v'w'} = -K_m \frac{\partial v}{\partial z} \tag{4.4}$$

The heat equation is written in terms of liquid water potential temperature (θ_l). θ_l is conserved during changes of phase of water. It is therefore particularly suited for use as the thermodynamic variable in cloudy boundary layers as temperature changes due to the consumption and release of latent heat within the cloud are already accounted for. A latent heat source term is therefore not required:

$$\theta_l \approx \theta \exp\left(-\frac{L q_l}{c_p T}\right) \tag{4.5}$$

$$\frac{\partial \theta_l}{\partial t} + w\frac{\partial \theta_l}{\partial z} = \frac{\partial}{\partial z}\left(K_h \frac{\partial \theta_l}{\partial z}\right) + \sigma_r \tag{4.6}$$

where q_l is the liquid water mixing ratio and σ_r is the radiation heat source term (heating rate). The divergence of temperature is parameterised using an eddy mixing coefficient for temperature, K_h:

$$-\overline{w'\theta_l'} = K_h \frac{\partial \theta_l}{\partial z} \tag{4.7}$$

Similarly the total water content (q_t) equation (3.5) is rewritten:

$$\frac{\partial q_t}{\partial t} + w\frac{\partial q_t}{\partial z} = \frac{\partial}{\partial z}\left(K_q \frac{\partial q_t}{\partial z}\right) \tag{4.8}$$

where it is assumed there are no sources of q_t within the model (only a flux from the sea surface) and the divergence of q_t is parameterised by:

$$-\overline{w'q_t'} = K_q \frac{\partial q_t}{\partial z} \tag{4.9}$$

where K_q is the eddy mixing coefficient for humidity. It should be noted that both KR and Y78 use the same values for the eddy mixing coefficients for both heat and humidity (i.e. $K_h = K_q$). In the present study it was found necessary to differentiate between the two coefficients, see Section 4.7.2.

The TKE equation (3.6) is rewritten:

$$\frac{1}{2}\frac{\partial e}{\partial t}+\frac{1}{2}w\frac{\partial e}{\partial z}=\frac{1}{2}\frac{\partial}{\partial z}\left(K_e\frac{\partial e}{\partial z}\right)-K_m\left(\frac{\partial U}{\partial z}\right)^2+\beta g\overline{w'\theta_v'}+\varepsilon \qquad (4.10)$$

where the divergence of TKE is parameterised using an eddy mixing coefficient, K_e, (equation 4.11), the shear production of TKE by equation 4.4, and β is the thermal expansion coefficient ($=1/\overline{\theta_v}$).

$$\overline{w'e'}=K_e\frac{\partial e}{\partial z} \qquad (4.11)$$

As the model is one-dimensional the vertical velocity cannot be found from the continuity equation (3.1) and has to therefore be imposed. The form taken for the vertical velocity profile is a constant, prescribed, value above the inversion level, linearly reducing below the inversion layer to zero at the sea surface. The vertical velocity profile thus changes as the inversion level changes. The prescribed value is usually negative to represent subsidence conditions. This is thought to be a reasonable representation of the vertical velocity profile in the conditions associated with stratocumulus (P.K. Taylor, pers. comm. from analysis of data from JASIN).

4.4 Turbulence Closure

4.4.1 Turbulence Closure Scheme

The reduction of complexity of the turbulence model from level 4 to level 2.2 (Section 3.4.2) means that most of the variances and covariances in the model are parameterised rather than explicitly modelled. This section will describe the parameterisations and approximations required to arrive at a set of equations which are general enough to be useful but simple enough to incorporate into a numerical model (Mellor and Yamada 1974). Five constants are introduced which multiply the mixing length in these parameterisations and are described in Section 4.4.2. The full Reynolds stress model equations that describe the level 4 model are (Stull 1988, equation 4.4.1a):

$$\underbrace{\frac{\partial \overline{u_i' u_k'}}{\partial t}}_{\text{storage}} + \underbrace{u_j \frac{\partial \overline{u_i' u_k'}}{\partial x_j}}_{\text{advection}} = \underbrace{-\overline{u_i' u_j'} \frac{\partial u_k}{\partial x_j} - \overline{u_k' u_j'} \frac{\partial u_i}{\partial x_j}}_{\text{shear production}} - \underbrace{\frac{\partial \overline{u_j' u_i' u_k'}}{\partial x_j}}_{\text{turbulent diffusion}}$$

$$+\underbrace{g\beta\left(\delta_{k3} \overline{u_i' \theta_v'} + \delta_{i3} \overline{u_k' \theta_v'}\right)}_{\text{buoyant production}} + \underbrace{f\left(\in_{kj3} \overline{u_i' u_j'} + \in_{ij3} \overline{u_k' u_j'}\right)}_{\text{Coriolis}}$$

$$-\left(\frac{1}{\overline{\rho}}\right)\left(\underbrace{\frac{\partial \overline{p' u_k'}}{\partial x_i} + \frac{\partial \overline{p' u_i'}}{\partial x_k}}_{\text{pressure diffusion}} - \underbrace{\overline{p'\left(\frac{\partial u_i'}{\partial x_k} + \frac{\partial u_k'}{\partial x_i}\right)}}_{\text{return-to-isotropy}}\right) + \underbrace{\frac{\nu \partial^2 \left(\overline{u_i' u_k'}\right)}{\partial x_j^2}}_{\substack{\text{molecular diffusion} \\ \text{(viscous flux)}}} - \underbrace{\frac{2\nu \overline{\partial u_i' \partial u_k'}}{\partial x_j \partial x_j}}_{\text{viscous dissipation}} \tag{4.12}$$

Scaling arguments based on the magnitude of the terms in 4.12 suggest that the Coriolis, pressure diffusion and molecular diffusion contributions to the momentum flux can be neglected in the boundary layer (Stull 1988). If some commonly used parameterisations are applied (following Mellor 1973): Rotta's (1951) hypothesis models the pressure-strain correlation of the return-to-isotropy term:

$$\overline{\frac{p'}{\rho}\left(\frac{\partial u_i'}{\partial x_k} + \frac{\partial u_k'}{\partial x_i}\right)} = -\frac{e^{1/2}}{3A_1 \ell}\left(\overline{u_i' u_k'} - \frac{\delta_{ik}}{3} e\right) + ce\left(\frac{\partial u_i}{\partial x_k} + \frac{\partial u_k}{\partial x_i}\right) \tag{4.13}$$

where A_1 and c are empirical constants to be derived from experimental data and ℓ is the mixing length (Section 4.4.2). Kolmogorov's (1942) hypothesis allows the viscous dissipation to be modelled:

$$\frac{2\nu \overline{\partial u_i' \partial u_k'}}{\partial x_j \partial x_j} = \frac{2}{3} \frac{e^{3/2}}{B_1 \ell} \delta_{ik} \tag{4.14}$$

where B_1 is a constant (see Section 4.4.2). The triple correlation product is parameterised using equation 4.15 (Mellor 1973; Donaldson 1973):

$$\overline{u_j' u_i' u_k'} = -e^{1/2} \lambda \left(\frac{\partial \overline{u_i' u_k'}}{\partial x_j} + \frac{\partial \overline{u_i' u_j'}}{\partial x_k} + \frac{\partial \overline{u_k' u_j'}}{\partial x_i}\right) \tag{4.15}$$

where λ is a mixing length parameter. These approximations and parameterisations reduce equation 4.12 to:

$$\underbrace{\frac{\partial \overline{u_i' u_k'}}{\partial t}}_{\text{storage}} + \underbrace{u_j \frac{\partial \overline{u_i' u_k'}}{\partial x_j}}_{\text{advection}} = \underbrace{-\overline{u_i' u_j'} \frac{\partial u_k}{\partial x_j} - \overline{u_k' u_j'} \frac{\partial u_i}{\partial x_j}}_{\text{shear production}} -$$

$$\underbrace{\frac{\partial}{\partial x_j}\left(e^{1/2} \lambda \left(\frac{\partial \overline{u_i' u_k'}}{\partial x_j} + \frac{\partial \overline{u_i' u_j'}}{\partial x_k} + \frac{\partial \overline{u_k' u_j'}}{\partial x_i} \right) \right)}_{\text{turbulent diffusion}} + \underbrace{g\beta\left(\delta_{k3} \overline{u_i' \theta_v'} + \delta_{i3} \overline{u_k' \theta_v'} \right)}_{\text{buoyant production}}$$

$$+ \underbrace{\left(-\frac{e^{1/2}}{3A_1 \ell} \left(\overline{u_i' u_k'} - \frac{\delta_{ik}}{3} e \right) + ce \left(\frac{\partial u_i}{\partial x_k} + \frac{\partial u_k}{\partial x_i} \right) \right)}_{\text{return-to-isotropy}} - \underbrace{\frac{2}{3} \frac{e^{3/2}}{B_1 \ell} \delta_{ik}}_{\text{viscous dissipation}} \tag{4.16}$$

We now neglect the storage, advection and turbulent diffusion terms in 4.16 (following Mellor 1973) to give an expression for the flux:

$$\overline{u_i' u_k'} = \frac{\delta_{ik} e}{3} + \frac{3A_1 \ell}{e^{1/2}} \left(\underbrace{-\overline{u_i' u_j'} \frac{\partial u_k}{\partial x_j} - \overline{u_k' u_j'} \frac{\partial u_i}{\partial x_j}}_{\text{shear production}} + \underbrace{g\beta\left(\delta_{k3} \overline{u_i' \theta_v'} + \delta_{i3} \overline{u_k' \theta_v'} \right)}_{\text{buoyant production}} \right.$$

$$\left. + ce \left(\frac{\partial u_i}{\partial x_k} + \frac{\partial u_k}{\partial x_i} \right) - \underbrace{\frac{2}{3} \left(-\overline{u_m' u_n'} \frac{\partial u_m}{\partial x_n} + g\beta \delta_{m3} \overline{u_m' \theta_v'} \right) \delta_{ik}}_{\text{viscous dissipation}} \right) \tag{4.17}$$

where the production of TKE (due to shear and buoyancy effects) has been balanced with the dissipation, i.e.:

$$\frac{e^{3/2}}{B_1 \ell} = -\overline{u_m' u_n'} \frac{\partial u_m}{\partial x_n} + g\beta \delta_{m3} \overline{u_m' \theta_v'} \tag{4.18}$$

Neglecting the horizontal gradients of the mean flow and the vertical gradient of the vertical velocity, the equations for the velocity variances and covariances can be written explicitly from 4.17 (Mellor and Yamada 1982):

$$\overline{u'u'} = \frac{e}{3} + \frac{A_1 \ell}{e^{1/2}} \left(-4\overline{w'u'} \frac{\partial u}{\partial z} + 2\overline{w'v'} \frac{\partial v}{\partial z} - 2\beta g \overline{w'\theta_v'} \right) \tag{4.19}$$

$$\overline{v'v'} = \frac{e}{3} + \frac{A_1 \ell}{e^{1/2}} \left(2\overline{w'u'} \frac{\partial u}{\partial z} - 4\overline{w'v'} \frac{\partial v}{\partial z} - 2\beta g \overline{w'\theta_v'} \right) \tag{4.20}$$

$$\overline{w'w'} = \frac{e}{3} + \frac{A_1 \ell}{e^{1/2}}\left(2\overline{w'u'}\frac{\partial u}{\partial z} + 2\overline{w'v'}\frac{\partial v}{\partial z} + 4\beta g\overline{w'\theta_v'}\right) \tag{4.21}$$

$$\overline{w'u'} = \frac{3A_1 \ell}{e^{1/2}}\left(-\left(\overline{w'w'} - ce\right)\frac{\partial u}{\partial z} + \beta g\overline{u'\theta_v'}\right) \tag{4.22}$$

$$\overline{w'v'} = \frac{3A_1 \ell}{e^{1/2}}\left(-\left(\overline{w'w'} - ce\right)\frac{\partial v}{\partial z} + \beta g\overline{v'\theta_v'}\right) \tag{4.23}$$

Starting from the prognostic equation for temperature flux (e.g. equation 4.4.3a, Stull 1988) and again neglecting the storage, advection and diffusion terms gives:

$$\overline{u'\theta_l'} = \frac{3A_2 \ell}{e^{1/2}}\left[-\overline{u'w'}\frac{\partial \theta_l}{\partial z} - \overline{w'\theta_l'}\frac{\partial u}{\partial z}\right] \tag{4.24}$$

$$\overline{v'\theta_l'} = \frac{3A_2 \ell}{e^{1/2}}\left[-\overline{v'w'}\frac{\partial \theta_l}{\partial z} - \overline{w'\theta_l'}\frac{\partial v}{\partial z}\right] \tag{4.25}$$

$$\overline{w'\theta_l'} = \frac{3A_2 \ell}{e^{1/2}}\left[-\overline{w'w'}\frac{\partial \theta_l}{\partial z} + \beta g\overline{\theta_l'\theta_v'}\right] \tag{4.26}$$

where we have parameterised the pressure-temperature correlation term similarly to equation 4.13:

$$\overline{\frac{p'}{\bar{\rho}}\frac{\partial \theta_l'}{\partial x_i}} = -\frac{e^{1/2}}{3A_2 \ell}\overline{u_i'\theta_l'} \tag{4.27}$$

where A_2 is also a mixing length coefficient (see Section 4.4.2). Analogously to equation 4.14 the dissipation of temperature variance is given by:

$$2\nu_\theta \overline{\frac{\partial \theta_l \partial \theta_l}{\partial x_j \partial x_j}} = 2\frac{e^{1/2}}{B_2 \ell}\overline{\theta_l'\theta_l'} \tag{4.28}$$

B_2 is a mixing length coefficient which relates to the dissipation of temperature and humidity variance in a similar manner to B_1 for the TKE.

Equations of exactly the same form as 4.24-4.26 can be derived for total water fluxes (starting from equation 4.4.2a in Stull 1988). Away from the free convective limit the θ_l variance is found by neglecting the time change and advection of the variance and thus balancing the production and dissipation of θ_l variance (Mellor and Yamada 1982):

$$\overline{\theta_l'\theta_l'} = -\frac{B_2 \ell}{e^{1/2}} \overline{w'\theta_l'} \frac{\partial \theta_l}{\partial z} \tag{4.29}$$

and similarly for the variance of q_t:

$$\overline{q_t'q_t'} = -\frac{B_2 \ell}{e^{1/2}} \overline{w'q_t'} \frac{\partial q_t}{\partial z} \tag{4.30}$$

The drawback of using θ_l as the temperature variable is that it complicates the calculation of virtual potential temperature, since to evaluate fluxes of virtual potential temperature we need to know the liquid water content. The liquid water calculation is part of the cloud parameterisation described in Section 4.5.1. Following Y78 we relate the virtual potential temperature to θ_l:

$$\begin{aligned} \theta_v &= (1 + 0.61 q_t - 1.61 q_l)\theta \\ &= (1 + 0.61 q_t - 1.61 q_l)\left(\theta_l + \frac{\theta}{T}\frac{L}{c_p} q_l\right) \end{aligned} \tag{4.31}$$

The calculation of virtual potential temperature fluxes and covariances are described in Appendix 2 following Yamada and Mellor (1979).

Rearranging equation 4.22 to be in the form of equation 4.4 and substituting for the covariance terms yields, after much substitution and algebra, an equation for the eddy mixing coefficient for momentum:

$$K_m = \frac{l_1 e^{3/2}\left[(1-3c_1)e + 3l_2\{(\Lambda_2 - 3l_2) - 3c(4l_1 + \Lambda_2)\}g\tilde{S}\right]}{\left[e^2 + 6l_1^2 e\left|\frac{\partial U}{\partial z}\right|^2 + 3l_1 l_2 g\tilde{S}\left\{6l_1(\Lambda_2 - 3l_2)\left|\frac{\partial U}{\partial z}\right|^2 + \left(7 + \frac{B_2}{A_1}\right)e + 9l_2(4l_1 + \Lambda_2)g\tilde{S}\right\}\right]} \tag{4.32}$$

likewise rearranging equation 4.26 to be in the form of equation 4.7 gives the eddy mixing coefficient for heat:

$$K_h = \frac{l_2\left[e^{3/2} - 6l_1K_m\left|\frac{\partial U}{\partial z}\right|^2\right]}{\left[e + 3l_2(4l_1 + \Lambda_2)g\tilde{S}\right]} \tag{4.33}$$

and the eddy mixing coefficient for TKE is parameterised following Y78:

$$K_e = 0.2\ell e^{1/2} \tag{4.34}$$

where $\tilde{S}$ is a stability parameter (Appendix 2, equation A2.9) and $l_1 = \ell A_1$, $l_2 = \ell A_2$, $\Lambda_1 = \ell B_1$ and $\Lambda_2 = \ell B_2$.

4.4.2 Mixing Lengths

The Mellor-Yamada type model contains the assumption that the four length scales required for turbulence closure are proportional to a master length scale. The four constants of proportionality (A_1, A_2, B_1 and B_2) are derived from experimental results (Mellor 1973; Mellor and Yamada 1977). The model results are more sensitive to the values of these constants than to the formulation of the master mixing length itself (Mellor and Yamada 1977). This relative insensitivity to the master length scale itself is borne out by the numerical experiments of Koracin and Rogers (1990) who conclude that a simple empirical formulation of the master length scale works as well as a prognostic formulation. The master mixing length in the model is thus calculated following Blackadar (1962):

$$\ell = \frac{\kappa(z + z_0)}{(1 + \kappa(z + z_0)/\lambda_b)} \tag{4.35}$$

where

$$\lambda_b = 0.03u_*/f \tag{4.36}$$

There is a further parameter, c, (equation 4.13) to be defined. These five experimentally-derived constants are found from turbulence measurements made in neutral conditions. Although the values are found from neutral data, Mellor (1973) retrieves the stability-dependent flux profile relations (e.g. Kraus and Businger 1994) from a model containing this type of turbulence closure. Three of the constants (A_1, B_1 and c) relate the TKE to the components of the turbulent flow and are not independent. $B_1\ell$ is the dissipation length scale and A_1 and c the energy redistribution parameters based on Rotta's energy

redistribution hypothesis (equation 4.13). The other two constants (A_2 and B_2) relate to thermal properties and require knowledge of the turbulent Prandtl number ($Pr_t = K_m/K_h$) and the ratio of velocity to temperature variance dissipation.

Near solid boundaries flow is near neutral (see Section 3.2.2), the turbulent TKE flux disappears and a balance between shear production and dissipation can be assumed. In these conditions measurements of $\overline{u'u'}$, $\overline{v'v'}$, $\overline{w'w'}$ and u_*^2 can give values for A_1, B_1 and c. Noting that near the boundary the mixing length must scale with the distance from the boundary (i.e. $\ell \sim \kappa z$). Assuming surface shear and dissipation balance and using equation 3.9 to eliminate the velocity gradient in neutral conditions (Nurser 1996):

$$-\overline{u'w'}\frac{\partial u}{\partial z} \equiv \frac{u_*^3}{\ell} = \varepsilon \equiv \frac{e^{3/2}}{B_1 \ell} \tag{4.37}$$

Giving:

$$B_1 \equiv \left(\frac{e^{1/2}}{u_*}\right)^3 \tag{4.38}$$

Thus the constant B_1 can be found from experimental measurements of TKE and surface stress. The observed range of the ratio of u_*^2 to TKE is 0.16 to 0.17. For constants A_1 and c we start with equation 4.17 (but retain the form for the viscous dissipation from equation 4.16) and again neglect storage, advection and turbulent diffusion and additionally neglect buoyancy terms:

$$\overline{u_i'u_k'} = \frac{\delta_{ik}e}{3} + \frac{3A_1\ell}{e^{1/2}}\left(-\overline{u_i'u_j'}\frac{\partial u_k}{\partial x_j} - \overline{u_k'u_j'}\frac{\partial u_i}{\partial x_j} + ce\left(\frac{\partial u_i}{\partial x_k} + \frac{\partial u_k}{\partial x_i}\right) - \frac{2}{3}\frac{e^{3/2}}{B_1\ell}\delta_{ik}\right) \tag{4.39}$$

Taking u in the along-wind direction and hence v = 0 (in this section only) we assume that the cross-wind turbulence is isotropic and a constant fraction of the turbulence in the along-wind direction. Defining $\overline{v'v'}/e = \overline{w'w'}/e = \gamma$ and rearranging equation 4.39 to be in this form we find:

$$\gamma = \frac{1}{3} - \frac{2A_1}{B_1} \tag{4.40}$$

which, as expected, gives:

$$\frac{\overline{u'u'}}{e} = 1 - 2\gamma \tag{4.41}$$

We now know values for B_1 and γ allowing A_1 to be calculated. Considering now equation 4.22, using $\overline{u'w'} = u_*^2$ and equation 4.37 we find:

$$c = \gamma - \frac{1}{3A_1 B_1^{1/3}} \tag{4.42}$$

allowing c to be calculated from the known values of A_1 and B_1. Mellor (1973) reviews the experimental values of γ which range from 0.15 - 0.28, although 0.2 is the more likely lower limit[5].

The turbulent Prandtl number is then used to relate the temperature transport to the turbulence parameters already defined to give a value for A_2 using equations 4.4, 4.7 and 4.26:

$$Pr_t \equiv \frac{K_m}{K_h} = \frac{A_1}{A_2}\frac{\gamma - c}{\gamma} \tag{4.43}$$

The ratio of the velocity and temperature dissipation (normalised by the TKE and velocity variance respectively) gives the ratio of B_1 to B_2 and hence the final constant, B_2. Similarity theory gives this ratio to be 2/3 (Hinze 1975). Experimental values range from 0.61 to 0.66 (Mellor and Yamada 1977). The sensitivity of the model to the values of these constants is evaluated and discussed in Section 5.2.1.

4.5 Clouds and Radiation

4.5.1 The Gaussian Cloud Model Relations

The subgrid-scale cloud and liquid water parameterisation used is the Gaussian cloud model (GCM). This is appropriate for non-precipitating clouds and was developed by Sommeria and Deardorff (1977) and Mellor (1977). If such a parameterisation is not used

---

[5] The values of the two cross-wind components (v and w) are expected to be equal ($\overline{v'v'} = \overline{w'w'} = \gamma e$). In the measurements that gave $\gamma = 0.15$ these components were dissimilar (Mellor and Yamada 1982) and the results were not used.

then a cloud fraction cannot be calculated; the grid-cell is either saturated with cloud fraction 1 or unsaturated with cloud fraction 0. The GCM conceptually divides each grid-cell (or in this case, level) into a number of sub-cells with a normal distribution of θ_l and q_t, with the mean of each distribution being the level mean. The spread of each distribution depends on the turbulence energy and the gradient of the variable at that level. The cloud cover in a particular grid level is the proportion of the sub-cells that would be saturated assuming this joint distribution of θ_l and q_t. Parameterising fractional cloud cover can be particularly important near cloud boundaries and in the initial stages of cloud growth and becomes more important as the grid size increases. The grid size must not however be so large that the distributions cannot be considered normal. The parameterisation gives both the cloud cover fraction and the liquid water content.

The cloud fraction, r, is calculated by determining the integral over all values of temperature and humidity of the Gaussian bi-normal distribution for the temperature and humidity in all cases where the total water content is greater than the saturation value (q_{sat}):

$$r = \int_{-\infty}^{\infty}\int_{-\infty}^{\infty} H(q_t - q_{sat})G(\theta_l, q_t)\,d\theta_l\,dq_t \tag{4.44}$$

where H represents a Heaviside function and G a Gaussian bi-normal distribution.

A similar expression can be derived for the liquid water mixing ratio by weighting the integral expression in equation 4.44 by q_t - q_{sat} for all values where q_t is saturated:

$$q_l = \int_{-\infty}^{\infty}\int_{-\infty}^{\infty} (q_t - q_{sat})H(q_t - q_{sat})G(\theta_l, q_t)\,d\theta_l\,dq_t \tag{4.45}$$

which can be expanded in a Taylor series to give expressions for the integrals (Mellor 1977):

$$r = \frac{1}{2}\left[1 + \mathrm{erf}\left\{\frac{a(q_t - q_{sat})}{2\sqrt{2}\sigma_s}\right\}\right] \tag{4.46}$$

$$q_l = ar(q_t - q_{sat}) + \frac{2\sigma_s}{\sqrt{2\pi}}\exp\left(-\frac{a^2(q_t - q_{sat})^2}{8\sigma_s^2}\right) \tag{4.47}$$

where:

$$a = \left[1 + \frac{\partial q_{sat}}{\partial T} \frac{L}{c_p} \right]^{-1} \tag{4.48}$$

and $\partial q_{sat}/\partial T$ can be evaluated at the temperature T from the Clausius-Clapeyron relation. The variance of the difference of q_t from q_{sat} is denoted σ_s^2 and can be written as (Yamada and Mellor 1979):

$$\sigma_s^2 = \frac{1}{4}\left(a^2 \overline{q_t' q_t'} - 2ab\overline{q_t' \theta_l'} + b^2 \overline{\theta_l' \theta_l'} \right) \tag{4.49}$$

where:

$$b = a \frac{T}{\theta} \frac{\partial q_{sat}}{\partial T} \tag{4.50}$$

and σ_s^2 can be parameterised as (Y78):

$$\sigma_s^2 = \frac{B_2 \ell}{4e^{1/2}} K_h \left(b \frac{\partial \theta_l}{\partial z} - a \frac{\partial q_t}{\partial z} \right)^2 \tag{4.51}$$

the quantity $a(q_t - q_{sat})/2\sigma_s$ is known as the normalised saturation deficit.

When σ_s is small the GCM reverts to a simple condensation model containing only the mean quantities. The performance of this cloud parameterisation is discussed in Section 6.3.4.

4.5.2 Correlated k-distribution Method

The radiative transfer of longwave radiation is computationally intensive when calculated on a line-by-line basis: it has been estimated that half a million points are necessary to properly resolve the absorption bands for CO_2 and O_3 (Liou 1992). One of the most efficient approximations for the computation of infrared radiative transfer is the k-distribution method. This involves grouping the spectral lines by absorption coefficient (k) rather than by wave number. This leads to a more smoothly varying distribution, which can be represented by a cumulative probability function for the absorption coefficient. The latter function can be accurately represented by a few points.

To extend the k-distribution method to an inhomogenous atmosphere it must be assumed that the cumulative probability of scattering is independent of temperature and pressure. The effect of pressure broadening on the absorption lines is accounted for following Lacis and Olinas (1991). The method is accurate to 1% compared with calculations that treat each absorption line separately.

4.5.3 Delta-Four-Stream Scheme

The delta-four-stream approximation was developed by Cuzzi et al. (1982) and has been implemented by Liou et al. (1988). When scattering by cloud and aerosol particles is considered, the phase function (the angular distribution of the scattered intensity) is strongly peaked in the forward direction. It can be modelled by considering the forward scattered radiation as unscattered and parameterising the intensity of the forward scattered beam as a delta-function. Scattering in other directions is then considered using a scaled-down intensity for the main beam. Once the large forward-scattered peak is accounted for, the remainder of the phase function is more smoothly varying and the angular distribution can be considered in a number of directions, known as streams. The two-stream approximation, accounting only for hemispheric asymmetry, is computationally simple but can give inaccurate results (Cuzzi et al. 1982). The four-stream approximation can be solved analytically and gives a better representation of the phase function and hence also angle-integrated properties.

The approximation is good to 5% or better, except at very low sun zenith angles (where absolute values are small), and is well suited to radiative transfer parameterisations involving flux and heating calculations in aerosol and cloudy atmospheres (Liou et al. 1988).

4.5.4 Model Implementation

The radiation parameterisation used in the model was developed by Fu (1991). 18 radiative bands are considered: 12 longwave and 6 solar. The radiative transfer scheme is based on the delta-four-stream approximation (Liou et al. 1988, see above), which Fu applied to an inhomogeneous atmosphere by assuming continuity of diffuse intensities at the boundaries of homogenous layers. This delta-four-stream parameterisation was also extended to infrared bands. The treatment of scattering, absorption and emission processes are self-consistent throughout the spectrum. The computation time increases linearly with the number of levels used. The absorption due to H_2O, CO_2, O_3, CH_4, and N_2O has been considered by using the correlated k-distribution approach (see Section 4.5.2).

For cloud models in which high vertical resolution is required, the cloud sublayers may be optically thin and cannot be considered as blackbodies in the thermal infrared region. Moreover, scattering can be important in clouds in the 8-13 μm region. The Fu (1991) scheme for radiative transfer can efficiently and accurately compute the detailed vertical structure of the heating rate profile within clouds.

Compared with line-by-line calculations under clear-sky conditions, the errors in heating rates computed by the delta-four-stream scheme with the correlated k-distribution approach are less than about 0.05 K day^{-1}. The errors in radiative fluxes are less than about 1 Wm^{-2} (Krueger et al. 1995a).

The single-scattering properties of water clouds, including extinction coefficient, single-scattering albedo and asymmetry factor, have been parameterised by using the same procedures in both the solar and infrared regions. Stephens (1978) used Mie theory to calculate the single scattering properties of eight observed water clouds and tabulated them as a function of wavelength from 0.3 to 200 μm. These tables have been interpolated and weighted with the solar irradiance and the Planck function (at T = 273 K) to obtain average properties for bands in the solar and infrared.

To implement the radiation code, additional levels have to be specified above the model domain. The temperature and water content of these levels are taken from Anderson et al. (1986).

4.6 Choice of a Numerical Scheme and Solution Procedure

This section describes the steps that are necessary to produce finite difference forms of the equations described in the previous sections. Y78 used a version of a three-dimensional Alternating Direction Implicit (ADI) scheme converted to one-dimension by KR. This proved to be unstable and required smoothing terms (see Richtmyer and Morton 1967). It is not necessary to use a scheme as complex as ADI for this one-dimensional problem so a more straightforward and stable numerical scheme will be used. The scheme chosen for implementation in this study uses centred differencing in the vertical, a forward timestep and fully implicit vertical diffusion. The solution of the numerical equations results in a tri-diagonal matrix, which is solved using a standard numerical technique.

Equations 4.1, 4.2, 4.6, 4.8 and 4.10 can be expressed in the general form (Y78):

$$\frac{\partial \Phi}{\partial t} = \left[\frac{\partial}{\partial z}\left(K_z \frac{\partial \Phi}{\partial z} \right) - w \frac{\partial \Phi}{\partial z} \right] - \Gamma \Phi + \Pi \tag{4.52}$$

where Φ represents any of the prognostic variables and K_z the appropriate eddy mixing coefficient (K_m, K_h, K_e or K_q). Only the TKE equation has a dissipation term (Γ in equation 4.52). The forcing or source term (Π in equation 4.52) represents radiative terms in the θ_l equation, geostrophic forcing in the equations for the wind speed components and buoyancy and shear production in the TKE equation. Use of q_t as the humidity variable means that no humidity source term is required. The parameterisations for Γ and Π in each of the equations are given in Section 4.7.1 (Table 4.1).

Again following Y78 a finite difference version of equation 4.52 which relates values at the current time step, n, (contained in the term DD_k below) to those at the next timestep, n+1, (contained in the terms AA_k, BB_k and CC_k below) can be written in the form:

$$-AA_k \Phi_{k-1}^{n+1} + BB_k \Phi_k^{n+1} - CC_k \Phi_{k+1}^{n+1} = DD_k \tag{4.53}$$

where all the variables are defined at levels k=1,2,3.....k_{max}. Values for the eddy mixing coefficients are defined at the mid-points, k=1$\frac{1}{2}$,2$\frac{1}{2}$,3$\frac{1}{2}$ .... $k_{max-\frac{1}{2}}$.

We now deviate from Y78 and expand each of the terms using a forward time step and centred spatial gradients (rather than using ADI) to give:

$$AA_k = \frac{\Delta t}{\frac{1}{2}(z_{k+1} - z_{k-1})}\left(\frac{K_{k-1/2}}{z_k - z_{k-1}} - \frac{w_k}{2} \right) \tag{4.54}$$

$$BB_k = 1 + AA_k + CC_k + \Gamma \Delta t \tag{4.55}$$

$$CC_k = \frac{\Delta t}{\frac{1}{2}(z_{k+1} - z_{k-1})}\left(\frac{K_{k+1/2}}{z_{k+1} - z_k} + \frac{w_k}{2} \right) \tag{4.56}$$

$$DD_k = \Phi_k^n + \Pi_k \Delta t \tag{4.57}$$

where AA_k, BB_k, CC_k, and DD_k form elements of a tri-diagonal matrix and can be solved using direct substitution following Richtmyer and Morton (1967) with solution:

$$\Phi_k^{n+1} = EE_k \Phi_{k+1}^n + FF_k \tag{4.58}$$

where:

$$EE_k = \frac{CC_k}{BB_k - AA_k EE_{k-1}} \tag{4.59}$$

$$FF_k = \frac{DD_k + AA_k FF_{k-1}}{BB_k - AA_k EE_{k-1}} \tag{4.60}$$

Values for the prognostic variables in the level adjacent to the sea surface are calculated using Monin-Obukhov theory. The calculation procedure is described in Section 4.7.2.

Figure 4.1 shows the output of a simulation with idealised input profiles for the KR code and Figure 4.2 the output of the same simulation for the new model. The KR code output is much noisier than the new model output despite the simplicity of the input profiles. In particular the flux profiles are highly variable. The ability of the new model to represent conditions in the marine atmospheric boundary layer will be demonstrated in Section 5.

4.7 Finite Difference Formulation

4.7.1 Forcing and Dissipation Terms

Comparison of equation 4.55 with equations 4.1, 4.2, 4.6, 4.8 and 4.10 gives the values for the dissipation (Γ) and forcing (Π) terms for each of the variables (Table 4.1). The components of the initial wind profile are set to be the same as the geostrophic components used to force the wind (see Section 4.7.3). The calculation of solar and longwave heating rates is described in Section 4.5.4.

4.7.2 Boundary Conditions

Following Y78 values of EE_2 and FF_2 are defined using the flux profile relations (Table 4.2). When the KR code was implemented it was found that the fluxes of heat, water and buoyancy in the main body of the model were poorly matched to their surface values calculated from surface layer theory. Coupling of the surface fluxes to the main body of the model has been achieved as follows. The surface fluxes and the flux gradients are calculated using surface layer theory (Section 3.2.2). A constant flux layer was then assumed so the fluxes at level 2 (i.e. the first level above the sea surface) are assumed equal to the surface fluxes. Next

the implied K_m and K_h are calculated for the surface layer (k=1 $\frac{1}{2}$) and k=2 $\frac{1}{2}$ from the surface fluxes and the gradients of temperature and momentum in these layers (i.e. from a rearrangement of equations 4.4 and 4.7). K_m and K_h at level k=3 $\frac{1}{2}$ are found by interpolation between their level 2 $\frac{1}{2}$ (surface) and level 4 $\frac{1}{2}$ (main body of model) values. This ensures that the 'observed' surface fluxes are used to force the model interior as the coefficients AA_2 reduce to the surface forcing for each variable (equation 4.53). It should be noted that poor model surface forcing is not restricted to the KR code. In a recent study Wyant et al. (1997) found it necessary to partition the surface fluxes between the three lowest model layers to 'ensure efficient vertical transfer of surface fluxes'. Discontinuities of fluxes near the surface can been seen in the results of LES simulation presented by Moeng et al. (1996) and Bechtold et al. (1996).

A separate mixing coefficient for the total water content (K_q) was found to be required. This is necessary for the water budget of the model to balance. K_q is the same as K_h in the main body of the model but is matched to the humidity flux at the surface. The surface level parameterisation uses either the scheme of Smith (1980, 1988) for open ocean conditions or the HEXOS formulation (Smith et al. 1992) for coastal regions. The improvement in the flux profiles resulting from a combination of the coupling of the surface fluxes to the main body of the model and the revised numerical scheme is shown in Figures 4.3 and 4.4 Figure 4.3 shows the heat, buoyancy and total water fluxes from the KR code and the new model. The poor surface matching can be seen for each of the fluxes in the KR code output (black circles) and the improved matching in the new model (open squares). The improved method of flux matching also impacts on fluxes in the model interior, in particular the total water flux profile is much more realistic in the revised code. Figure 4.4 compares the old and new model output to aircraft buoyancy flux measurements made in the North Sea (see Section 5.3.1). The buoyancy flux from the old code is very noisy and the surface flux about half of the flux just above the surface. The shape of the buoyancy flux profile from the new model simulation agrees both qualitatively with the shape suggested by the observations and falls within the range of variability sampled by the observations at most heights. The revised numerical scheme and flux profile matching have therefore improved the stability and performance of the model and made a significant contribution to the ability of the model to realistically simulate the atmospheric boundary layer.

At the top of the model domain the gradients of the wind speed components, total water content and TKE are set to zero. The gradient of θ_l is defined using a prescribed lapse rate.

4.7.3 Prescription of Variables and Model Initialisation

This section describes the parameters that need to be prescribed in order to run the model and the initialisation of variables that cannot be immediately calculated from the input profiles.

The first group of initialisation variables required relate to the size of the model domain and the location and timing of the model run. We set the number of model levels (level thickness and model domain height), the level at which the inversion occurs (required to impose the initial vertical velocity profile, see Section 4.3) the model time step and the number of seconds between calculation of the radiational forcing (the most computationally expensive part of the model) and between writing output data (the output data are averaged over the period between successive data outputs). We then define the latitude and longitude of the simulation, the start time and the length of the simulation.

The next group of variables are physical parameters that are usually known. These comprise the surface pressure, SST, the vertical gradient of θ_l above the inversion and the rate of increase of SST.

The final group of variables are physical parameters that are not well known: the relative humidity at the sea surface; the sea surface albedo; the average cloud water droplet size and the vertical velocity. In theory these are parameters that can be measured, in practice the measurements are difficult to make and often not available. We appeal to the literature to make the best estimates of these parameters.

The initial profiles of height, θ_l, q_t, the wind speed components and concentration of CO_2 are read from a file. We assume the wind speed profile initially is geostrophic and that the geostrophic wind remains constant throughout the simulation. The geostrophic winds could be altered to reflect any changes in the large scale pressure gradient but this has not been done in the present study. This means that geostrophic forcing only occurs when the wind profiles deviate from their original values. This in effect limits geostrophic forcing to the boundary layer where the profiles are modified by the effects of friction. The mixing ratio in the lowest model level is set to the 95% of the saturation value at the sea surface temperature. Pressures are calculated by integrating the weight of dry air and water vapour in the model upward from the prescribed sea surface pressure (following Y78). This requires using the virtual temperature for the level below that for which the pressure is being calculated. The resulting error is small: using an iteration instead makes a negligible difference. The temperature and the virtual temperature are then calculated at the current level using the now

known pressure. Surface similarity theory (see Section 3.2.2) is used to calculate initial surface parameters from the profile data. The initial kinetic energy profile is set up to decrease linearly from a surface value (Y78, value FF_2 in Table 4.2) to a small but non-zero value at the inversion. The first two iterations are calculated using eddy mixing coefficients calculated from the TKE; the radiation code is not called until the third iteration. This initialisation procedure was implemented to avoid large changes to the profiles in the first few timesteps which could arise when forcing terms were calculated from profiles that had not yet been correctly calculated.

Modifications from the KR code reduced the number of variables prescribed during the initialisation by more than half. This was made possible by the careful reordering of the initialisation procedure. For example in the KR code initial values for surface parameters such as u_* were required. If the value prescribed was too large then unrealistic mixing occurs in the first few timesteps, which could impact on the remainder of the simulation. The revised code calculates initial values where possible rather than relying on a large number of prescribed variables. This also makes the model easier to set up and run.

4.8 Summary

A one-dimensional Mellor-Yamada type model has been implemented. Following Yamada (1978) and Koracin and Rogers (1990) the model solves equations for the evolution of θ_l, q_t wind components and TKE. The variances and covariances of these variables are parameterised using mixing length theory. Liquid water content is calculated using the Gaussian cloud model relations.

Improvements have been made to the model which result in more stable and physical simulations than the KR code. Writing and implementing an implicit centred difference numerical scheme allowed smoothing terms to be removed from the model formulation and the use of a wider range of time steps and grid spacing. Revision was also required to better couple the surface fluxes to the model interior. Without this modification the surface fluxes did not correctly force the model, usually resulting in overestimation of surface turbulence. A sophisticated radiation scheme (Fu 1991) was obtained and implemented and the initialisation procedure refined.

Variable	Eddy-mixing coefficient	Γ	Π
u	K_m	0	$f\,(v-v_g)$
v	K_m	0	$-f\,(u-u_g)$
θ_l	K_h	0	σ_r (= sw + lw)
q_t	K_q	0	0
TKE	K_m	$\frac{2e}{B_1\ell}$	$K_m\left(\frac{\partial U}{\partial z}\right)^2 + 2g\beta\overline{w'\theta_v'}$

Table 4.1 Dissipation and forcing terms in the finite difference equation 4.55 for each of the variables u and v components of wind speed, θ_l, q_t and TKE. The terms are derived from equations 4.1, 4.2, 4.6, 4.10 and 4.12.

Variable	EE_2	FF_2
u	$\frac{\ln\left(\frac{z_1+z_0}{z_0}\right)-\Psi_m(\zeta_1)}{\ln\left(\frac{z_2+z_0}{z_0}\right)-\Psi_m(\zeta_2)}$	0
v	$\frac{\ln\left(\frac{z_1+z_0}{z_0}\right)-\Psi_m(\zeta_1)}{\ln\left(\frac{z_2+z_0}{z_0}\right)-\Psi_m(\zeta_2)}$	0
θ_l	$\frac{\ln\left(\frac{z_1+z_{0t}}{z_{0t}}\right)-\Psi_t(\zeta_1)}{\ln\left(\frac{z_2+z_{0t}}{z_{0t}}\right)-\Psi_t(\zeta_2)}$	$1-E_2$
$\mathbf{q_t}$	$\frac{\ln\left(\frac{z_1+z_{0q}}{z_{0q}}\right)-\Psi_q(\zeta_1)}{\ln\left(\frac{z_2+z_{0q}}{z_{0q}}\right)-\Psi_q(\zeta_2)}$	$1-E_2$
TKE	0	$B_1^{2/3}u_*^2(\Phi_m-\zeta_1)^{2/3}$

Table 4.2 - Lower Bound Values E_2 and F_2 (equations 4.59 and 4.60) by Prognostic Variable

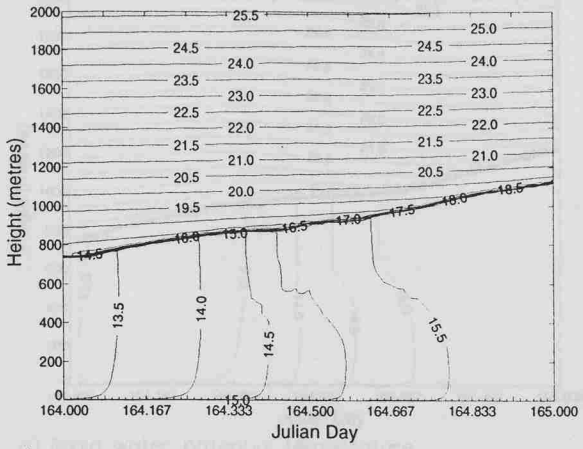

a) liquid water potential temperature

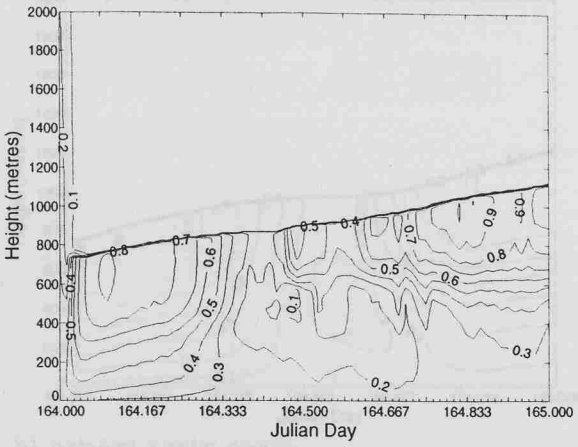

b) turbulent kinetic energy

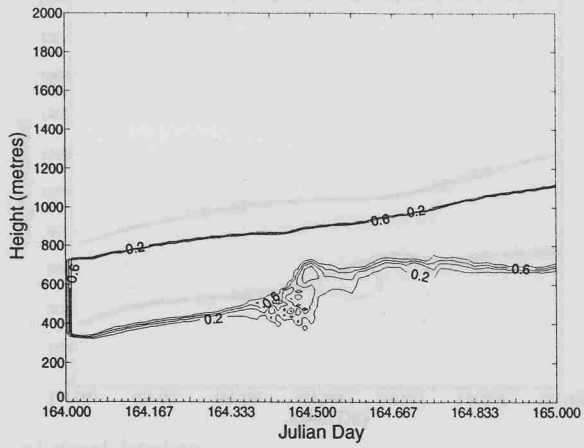

c) cloud fraction

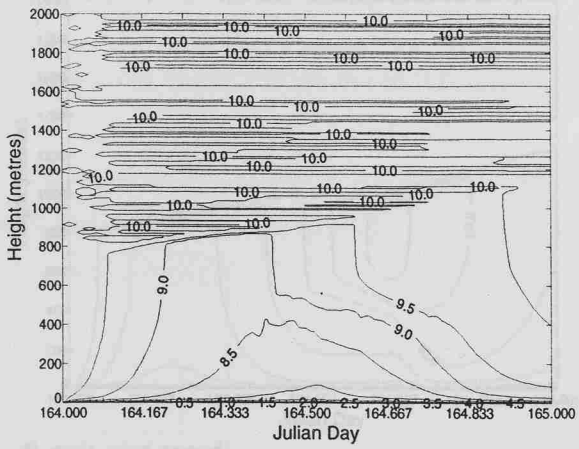

d) east wind speed

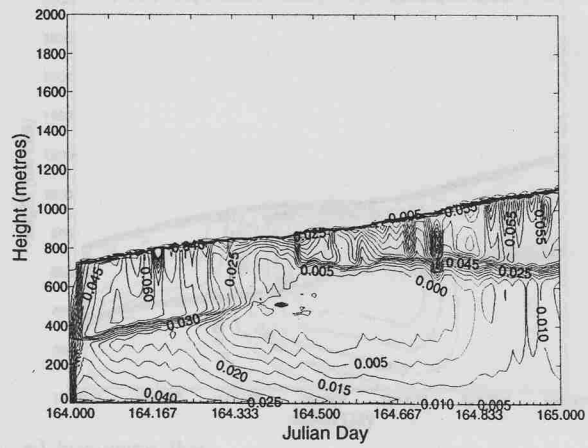

e) buoyancy flux

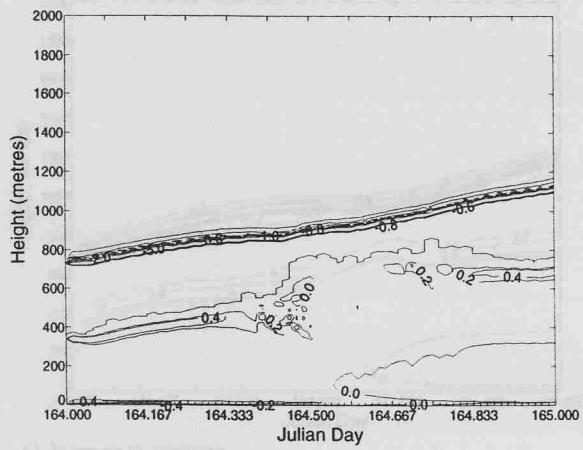

f) longwave cooling

Figure 4.1 Output of an idealised boundary layer simulation using the KR model code. a) θ_l (°C), b) TKE (m^2s^{-2}), c) cloud fraction, d) east wind speed component (ms^{-1}), e) buoyancy flux (Kms^{-1}), f) longwave cooling (°C h^{-1}).

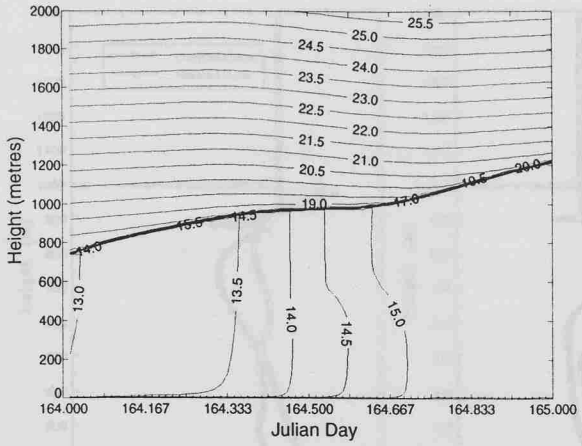

a) liquid water potential temperature

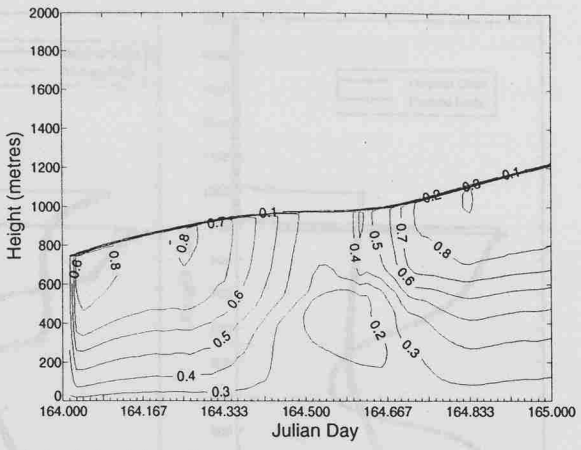

b) turbulent kinetic energy

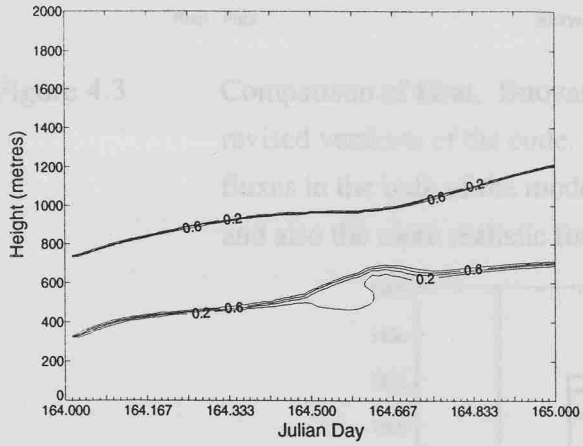

c) cloud fraction

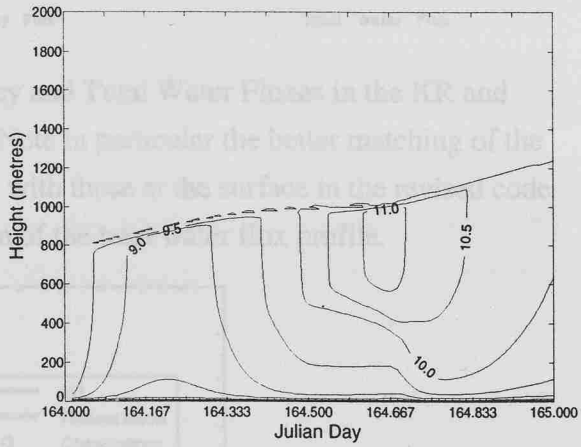

d) east wind speed

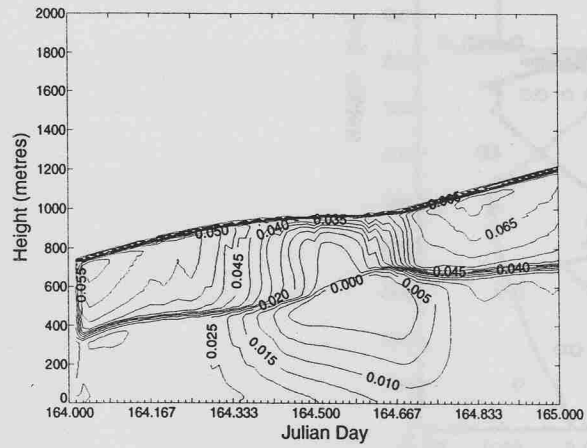

e) buoyancy flux

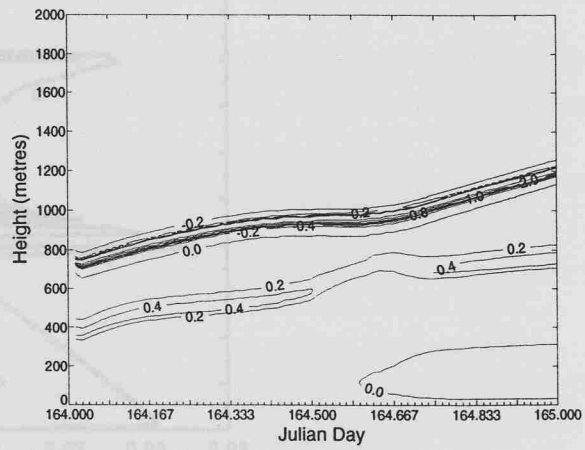

f) longwave cooling

Figure 4.2 As Figure 4.1 but for the revised model code.

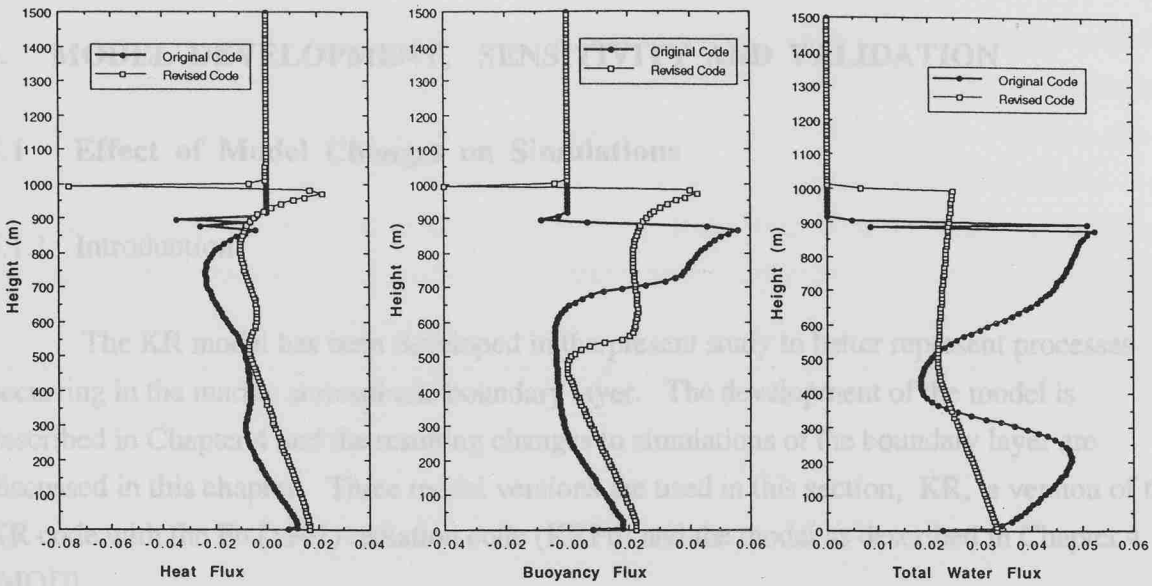

Figure 4.3 Comparison of Heat, Buoyancy and Total Water Fluxes in the KR and revised versions of the code. Note in particular the better matching of the fluxes in the bulk of the model with those at the surface in the revised code and also the more realistic form of the total water flux profile.

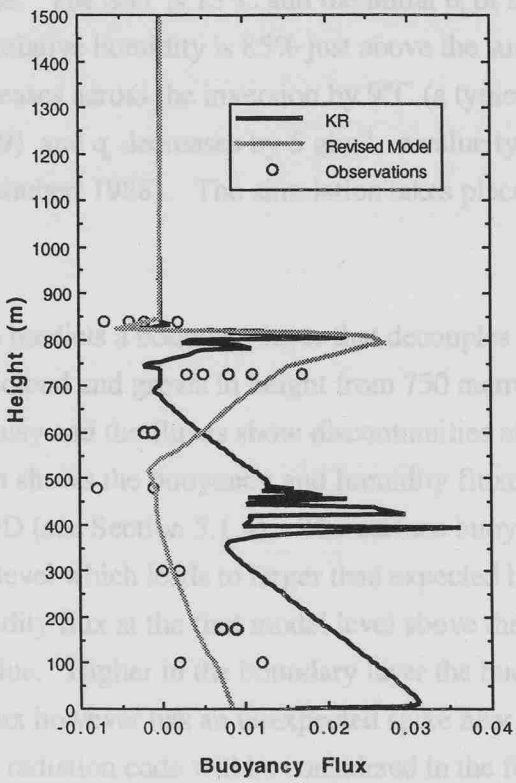

Figure 4.4 Comparison of Buoyancy Flux in KR and the new versions of code with aircraft observations for North Sea simulation (see Section 5.3.1).

5. MODEL DEVELOPMENT, SENSITIVITY AND VALIDATION

5.1 Effect of Model Changes on Simulations

5.1.1 Introduction

The KR model has been developed in the present study to better represent processes occurring in the marine atmospheric boundary layer. The development of the model is described in Chapter 4 and the resulting changes to simulations of the boundary layer are discussed in this chapter. Three model versions are used in this section, KR, a version of the KR code with the Fu (1991) radiation code (KRFu) and the model as described in Chapter 4 (MOD).

5.1.2 Simulation with the Original Model Version

These changes will be illustrated using a one-day simulation of a boundary layer with the following characteristics. The SST is 15°C and the initial θ_l of the well-mixed boundary layer is 13°C. The initial relative humidity is 85% just above the surface and the inversion is at 750 metres height. θ_l increases across the inversion by 9°C (a typical value: Kuo and Schubert 1988, Betts 1989) and q_t decreases by 5 gkg^{-1}, a value typical for midlatitude stratocumulus (Kuo and Schubert 1988). The simulation takes place at 30°N, 30°W in mid June.

The KR simulation predicts a boundary layer that decouples during the day in response to solar heating within the cloud and grows in height from 750 metres to just over 1000 metres. Some of the profiles are noisy and the fluxes show discontinuities at the surface. This is shown in Figure 5.1 which shows the buoyancy and humidity fluxes for KR, KRFu (see Section 5.1.3) and for MOD (see Section 5.1.4). The surface buoyancy flux in KR is about half that at the first model level which leads to larger than expected buoyancy fluxes in the subcloud layer. The humidity flux at the first model level above the surface is about 30% greater than the surface value. Higher in the boundary layer the buoyancy flux profile looks realistic. The humidity flux however has an unexpected spike near the inversion. The deficiencies in the original radiation code will be considered in the following section.

5.1.3 Effect of the New Radiation Scheme

The radiation scheme in the original version of the model is described by Rogers and Koracin (1992). The longwave radiation is calculated using the clear sky formulation of

Sasamori (1968), who used empirical formulae to approximate the temperature dependency of the mean absorption coefficients tabulated by Yamamoto (1952). The absorption coefficients depend on the effective path lengths of water vapour, carbon dioxide and ozone. Within the cloud the absorptivity is calculated from the liquid water path. The shortwave radiation is calculated using a two-stream approximation (see, e.g. Liou 1992) which considers only forward and backward scattering with an asymmetry function that gives their relative strengths. Stephens et al. (1984), who developed the parameterisation, admit that a delta-two-stream approximation (Section 4.5.3) is more accurate but chose the two-stream approximation for simplicity. Two shortwave bands are considered (0.3 μm to 0.75 μm and 0.75 μm to 4.0 μm) and scattering is assumed conservative in the first band and non-conservative in the second. The scattering variables are tuned to agree with theoretical calculations. In the cloud, solar radiation is calculated from bulk parameters following Hanson and Derr (1987) using integrated liquid water content and solar zenith angle. The cloud is assumed well mixed and no account can be taken of any layer structure within the cloud. Both the long and shortwave parameterisation schemes were designed to be computationally efficient with the sacrifice of some accuracy.

In contrast, the radiation code of Fu (1991) uses 18 bands for the radiation (12 longwave and 6 solar), uses a delta-four-stream approximation (Section 4.5.3), and is used in the current radiation programmes for CERES (clouds and the earth's radiant energy system), ARM (atmospheric radiation measurement) and GEWEX (the global energy and water cycle experiment). It should therefore give a better representation of radiative processes in the cloudy atmosphere than the much-simplified scheme in the KR model version.

The most striking difference between the simulations with different radiation codes is the thickness of the cloud and the increased liquid water content. Whilst KR shows strong decoupling of the cloud and subcloud layers with cumulus under a much-thinned stratocumulus layer near midday, KRFu produces a more solid, thicker cloud with no signs of decoupling in the mean profiles. The reasons for this can be seen in Figure 5.2 which compares the shortwave and longwave heating and cooling profiles for KR and KRFu. The bulk solar scheme (KR) can be seen to predict solar heating penetrating much deeper into the cloud than the Fu (1991) scheme. In the bulk solar scheme the extinction depth is assumed exponential whatever the distribution of the liquid water within the cloud, whereas Fu (1991) allows for the amount of liquid water in each model level. In this case the amount of solar absorption is overestimated in KR. The longwave cooling at the cloud top is much smaller in the bulk scheme than that predicted by Fu. The KRFu simulation has more TKE generated by the longwave radiation than KR as the longwave cooling in KRFu is stronger. However less TKE is generated by the shortwave radiation in the KRFu scheme and these combine to give

similar radiatively generated TKE values in the cloud, although the effect of the longwave cooling is slightly greater giving a slightly higher incloud TKE. Differences in both the shortwave and longwave distributions in the cloud lead to the boundary layer in the KR simulation being much warmer, having less liquid water and less cloud. The boundary layer in the KRFu simulation is almost 1°C cooler but has slightly more total water, partly due to decoupling reducing the surface total water flux in the KR simulation.

The updating of the radiation code therefore strongly impacts on both the mean and turbulence structure of the test simulation and leads to changes in the heat and water budgets of the boundary layer. The bulk radiation scheme also produces very noisy evolutions of the longwave cooling and shortwave heating profiles, particularly when the structure of the boundary layer is decoupled.

5.1.4 Effect of the New Numerical Scheme and Surface Flux Matching

The results from the previous section will now be compared with those from a simulation with the version of the model described in Chapter 4 (MOD). The changes to the model that are expected to have an impact on the simulation are the use of a new numerical scheme and the matching of the flux profiles to their surface values. The numerical scheme and the method used to match the flux profiles were described in Sections 4.6 and 4.7. Again there are very noticeable differences caused by the change to the model formulation from KRFu to MOD. The boundary layer growth, which is similar in KR and KRFu is much reduced in the simulation with MOD. The inversion height increases by about 50 metres over the one-day simulation compared to about 250 metres in both KR and KRFu. The turbulent kinetic energy within the cloud is about a third smaller in the cloud in MOD during the night, and during the day the surface and incloud turbulence are decoupled. The subcloud fluxes are smaller, since the values predicted from Monin-Obukhov theory are up to 50% smaller than the fluxes in the subcloud layer for unmatched profiles (KR code, Figure 5.1). These smaller surface fluxes lead to smaller fluxes in the cloud and hence less turbulence and entrainment. The unrealistic spikes in the total water flux near the inversion in the KR code were traced to an inconsistency in the calculation of this flux compared with the heat and buoyancy fluxes. The incorrect value did not impact on other model calculations. As the initial profiles for this idealised simulation are well mixed the simulation is expected to predict a fairly smooth evolution of the boundary layer. The model profiles MOD are much smoother than predicted by KR and KRFu. This is without the time-step averaging that was required in the original model version for numerical stability.

The MOD code therefore predicts more physically realistic flux profiles than KRFu and the implicit numerical scheme used does not create noise in the simulation. The changes impact significantly on the prediction of boundary layer structure and the model will be tested against measurements from boundary layer experiments to ensure that the model fluxes are quantitatively as well as qualitatively reasonable (see Section 5.3).

5.1.5 Summary of the Effects of Model Changes

The radiation code used in the original version of the model (version KR) was computationally simple but better radiative transfer schemes are now available. Updating the code reduced the depth of shortwave heating within the cloud and predicted stronger longwave cooling at the cloud top (version KRFu). The boundary layer was thus cooler, with more liquid water and thicker cloud. Matching the fluxes to their surface values (version MOD) had a strong effect in this simulation as the values in the first two levels in the KR code were up to 50% different from each other. In MOD the subcloud fluxes were reduced to match the surface fluxes and the turbulence within the whole boundary layer was reduced, as was the entrainment rate. Simulation with MOD gave flux profiles that were more physically reasonable than the KR code. The revised numerical scheme was less noisy. The next section demonstrates the robustness of the MOD code.

5.2 Model Sensitivity

5.2.1 Sensitivity to the Mixing Length Coefficients

Section 4.4.2 described the four mixing length constants that multiply the master length scale. The sensitivity of the model to variations in these constants is investigated using laboratory observations (summarised by Mellor 1973 and Mellor and Yamada 1977) to guide the choice of reasonable maximum and minimum values. As the mixing length constants are not all independent, the range of variability in the five parameters can be determined using nine model runs. The sensitivity to these length scale constants was investigated using an idealised atmosphere with the following characteristics. The boundary layer was 800 metres thick, well mixed in temperature ($\theta_l = 8°C$) and humidity ($q_t = 8$ gkg^{-1}) with cloud occupying the top 200 metres beneath a 4°C $\theta_l$and 6 gkg^{-1} q_t inversion. The θ_l gradient above the inversion is 0.006 Km^{-1}. The wind speed is a constant 8 ms^{-1}. These values lead to a simulation in which both radiative and surface forcing are important. The results of the different runs are compared at midday after 12 hours of simulation. The simulation takes place at 40°N, 40°W in mid July. The time step used was 5 seconds and the vertical resolution was 10 metres.

The laboratory experiments reviewed by Mellor (1973) and Mellor and Yamada (1977) were used to define the likely variation in the mixing length constants. All the values used in this section are from these two references. Values used by Y78 will be referred to as the standard values. Estimates of B_1 (equation 4.38) vary from 14.3 to 16.6, the standard value is the upper limit of 16.6. The range of B_1 chosen in this sensitivity study is 14.3 to 18.9 which extends the error limit to give 16.6 as the central value. This gives wider than observed limits for the variation. Changes to the constant B_1 will change the TKE dissipation rate for a given momentum stress value. As B_1 increases (with A_1, A_2 and B_2 constant but γ varying proportionally, equation 4.40) the dissipation increases and hence the amount of TKE at a particular stress value will decrease. However if γ is kept constant then changing the value of B_1 will also change A_1 and the impact will be more complicated. The reported variation in γ was 0.15 to 0.28. As noted in Section 4.4.2 the 0.15 value is suspect and the range of γ will therefore be taken to be 0.20 to 0.28. The standard value is 0.22. Increasing γ will increase the transfer between the different components of momentum. Knowing B_1 and γ allows calculation of both A_1 and c (equations 4.40 and 4.42). Using the standard values of B_1 = 16.6 and $\gamma = 0.22$ gives $A_1 = 0.92$ and $c = 0.08$. Holding B_1 at the standard value A_1 ranges from 0.44 ($\gamma = 0.28$) to 1.11 ($\gamma = 0.2$) and c ranges from -0.01 ($\gamma = 0.28$) to 0.10 ($\gamma = 0.2$).

Calculation of A_2 requires knowledge of a turbulent Prandtl number (Pr_t, equation 4.43) which ranges from 0.70 to 0.85 in the experiments reviewed (the standard value is 0.8). Changing Pr_t within this range changes A_2 between 0.69 and 0.84 (the standard value is 0.74). Increasing Pr_t (larger A_2) will lead to increased mixing of both temperature and humidity. Table 5.1 however shows that a lower value of A_2 (0.58) is obtained with γ =0.28 and Pr_t = 0.8. B_2/B_1 is the ratio of TKE to temperature dissipation (R_{diss}) and estimates range from 0.61 to 0.67 (Mellor and Yamada 1977, Hinze 1975). The standard value is 0.61 so we take a range from 0.56 to 0.67 to span the standard value. Altering R_{diss} with B_1 constant means B_2 then ranges from 9.3 to 11.0 (the standard value is 10.1) which are again wide limits compared to the range from 9.5 to 10.5 suggested by Mellor and Yamada (1977). Larger changes to B_2 however arise with R_{diss} constant and B_1 varying (8.7 - 11.5, see Table 5.1). These values and ranges are summarised in Table 5.1. Figures 5.3a-c show the sensitivity of the simulations to changes in the mixing lengths using the values from Table 5.1.

The most significant change in the model output arises from increasing γ from 0.22 to 0.28 (compare the black line for the standard run with the green line in Figures 5.3a-c). The boundary layer is 0.2 gkg^{-1} drier at the cloud top and the average in-cloud liquid water content is reduced by 30%. In addition the cloud is 30 metres thinner compared to the standard run. The surface stress is reduced by 20% and the surface heat and water fluxes by a maximum of 11%. Boundary layer average TKE is only 12% lower than in the standard run despite the

average eddy mixing coefficient being a third as much as its standard value. The reduced liquid water content and reduced cloud thickness lead to a 17% reduction in the peak solar heating and a 12% reduction in the peak longwave cooling.

Decreasing γ to 0.20 (red line) has the opposite effect but changes are smaller. The boundary layer average TKE decreases by 3% and the boundary layer is 0.5 gkg^{-1} drier than the standard case. Average liquid water content increases by 12% leading to an increase in solar heating of 3%. Increasing B_1 decreases the amount of TKE dissipation. The run with $B_1 = 18.9$ (dark blue line) therefore has the maximum boundary layer average TKE, 10% larger than the standard run. $B_1 = 14.3$ (light blue line) decreases the boundary layer average TKE by 10%. Changes to Pr_t do not strongly affect the mean boundary layer parameters but increasing Pr_t to 0.85 increases the mean heat flux by 6% and decreasing Pr_t to 0.70 decreases the mean heat flux by 11% although mean heat flux values are already small.

Interactions within the cloud-topped boundary layer are non-linear due mainly to the interactions between fluxes, liquid water and radiation. For example, although the simulations for $\gamma = 0.28$ and $B_1 = 14.3$ (the green and light blue lines respectively) have similar boundary layer average TKE the cloud thicknesses are about 50 metres different (Figure 5.3a). The difference in cloud thickness impacts on the shape of the TKE profile (Figure 5.3b) through the radiative fluxes (Figure 5.3c).

Whilst the impact of changing each of the coefficients could have been better isolated by using, for example, a dry boundary layer or no radiative processes, the aim of this sensitivity study was to show the impact of changing these parameters on the simulation of stratocumulus. In the case study both surface forcing and cloud forcing are equally important and it is hoped that we have demonstrated the impact of changing the mixing length coefficients on our simulations. Table 5.2 gives an estimate of the total measurement and sampling errors for aircraft measured boundary layer fluxes. The changes in mixing length coefficients lead to changes of order or smaller than the measurement errors, and where the effects can be isolated have predictable effects. Profiles of all the model prognostic variables are shown in Figure 5.3.

5.2.2 Sensitivity to Model Resolution and Time Step

The effect of the vertical resolution and time step on the model output were tested with the same data as used in Section 5.2.1. The results presented in Section 5.2.1 had a time step of 5 seconds and a vertical resolution of 10 metres. Figure 5.4 shows the results of changing the timestep to values between 1 second and 45 seconds with a constant grid spacing of 10

metres. The subset of variables plotted in this figure was chosen to show the largest differences caused by the change in timestep. The profiles are all similar in form although the simulations with time steps of 20 seconds (light blue line) and particularly 45 seconds (pink line) are showing some differences from the other simulations. The model is behaving consistently for time steps between 1 and 10 seconds (see Figure 5.4). Apart from the 45 second timestep simulation the prognostic variables are little changed by any of the different time steps. The peak boundary layer TKE changes by less than 5% in these five simulations. As the TKE and liquid water content are linked by the Gaussian cloud model relations changes in the TKE affect the liquid water content which varies by a maximum of 7% between the different simulations (again ignoring the 45 second time step simulation). The peak longwave cooling is altered by a maximum of 12% and the peak shortwave heating by 13%. These values are all within the range of the observational uncertainties for these variables (see Table 5.2). Cloud peak fluxes vary by less than 5% between those simulations with time steps of 10 seconds or less and the surface fluxes by a smaller amount.

Whilst changing the time step will affect the accuracy of the simulation, changing the vertical resolution changes the shape of the profiles and will therefore have a stronger impact on the simulations. It is therefore not just the accuracy of the numerical code at a particular resolution that is being checked but also determining the resolution required to properly reproduce the vertical placement of processes. For example, Roach et al. (1982) show that the thickness of the inversion at the stratocumulus cloud top can be less than 10 metres. Resolution coarser than this may impact on processes near the inversion, for example the simulation of the entrainment rate. The net longwave flux divergence occurs within about 50 metres of the cloud top (Slingo et al. 1982a) so the resolution will determine how this divergence is distributed within the cloud. Figure 5.5 shows the effect of changing the grid spacing between 1 metre and 50 metres with a constant time step of 5 seconds. Output is shown averaged in 50 metre ranges to allow comparison. The 50 metre resolution simulation is qualitatively the same as the others but the boundary layer growth is more than 100 metres lower and this run will be ignored in the discussion that follows. For the other runs the depth of the mixed layer varies by 50 metres. Peak TKE changes by less than 13%, peak liquid water content by less than 5%. The average longwave cooling varies by 13% and the shortwave heating by 11%. The boundary layer average buoyancy and water fluxes change by less than 13%; the average heat flux is small so percentage changes are large although absolute changes are small.

The model simulations are therefore stable to changes in the timestep between 1 second and 20 seconds and changes in the vertical resolution between 2 and 20 metres within the accuracy of observations of each quantity given in Table 5.2.

5.2.3 Sensitivity to Initial Conditions

It is important that the model results are not critically dependent on the initial profiles. Small variation in the initial profiles should produce changes that differ in small and predictable ways from the original. This was tested by changing the initial inversion height by ± 20 metres, the initial θ_l profile by ± 0.2°C, the initial wind speed profile by ± 10% and the initial q_t profile by ± 0.2 gkg^{-1} from those used in the previous section. The results of these simulations are shown in Figure 5.6. All the profiles are broadly similar; differences are predictable and are discussed below.

The varying of inversion height has the largest effect on the radiation profiles (beyond the simple effects of geometry on the initialisation profiles) due to the increase or decrease in the cloud thickness and integrated liquid water content. The changes in the radiative fluxes are within 10% of their values in the standard run. Varying the initial temperature profiles has a small but observable effect on the boundary layer height. A uniform decrease in temperature (and hence an increase in the surface fluxes as the SST is kept constant) results in a cooler boundary layer with an inversion about 10 metres higher than the standard run. An increase in temperature has the opposite effect. Humidity is slightly higher (lower) overall in the higher (lower) temperature run. Varying the initial temperature profile affects the cloud amount and liquid water content in a small and predictable way. Fluxes and turbulent kinetic energy are a slightly greater magnitude in the decreased temperature run and peak values below the cloud are slightly displaced due to the small change in boundary layer height. Changes in the radiation profiles cancel to give almost identical shortwave heating and longwave cooling profiles (although displaced by order 10 metres in the vertical). Varying the initial wind profile has little effect on the thermal and moisture structure profiles, although the increased in-cloud TKE (with increased wind speed) leads to slightly larger liquid water content as a direct result of the Gaussian cloud model (and the opposite for decreased wind speed). The stress profiles are directly affected as expected and the TKE is higher in the higher wind speed case. Surface heat, buoyancy and water fluxes are increased (decreased) by the increase (decrease) in wind speed. The in-cloud fluxes are affected in the opposite way with increasing wind speed leading to a decreased in-cloud peak flux. The peak longwave cooling and shortwave heating rates are increased as a direct result of the change in liquid water content. Changes to the humidity profile have an effect on the inversion height. Increasing the humidity increases the inversion height. The cloud is thus thickened since the increased humidity also lowers the saturation height. The opposite happens with a decrease in humidity. Integrated liquid water contents are thus increased as the humidity increases. The sub-cloud TKE is increased with decreasing humidity due to the increase in buoyancy flux but the in-cloud TKE is decreased.

These differences are small. The radiative fluxes are again affected by the change in liquid water content in a predictable manner.

5.2.4 Summary of Model Sensitivity Tests

Simulations of an idealised, well-mixed, stratocumulus topped boundary layer have been performed which demonstrate that the model is robust to changes in the Mellor-Yamada mixing length coefficients, to the grid spacing, the time step and to perturbations in the initialisation conditions.

The choice of ranges for the mixing length coefficients were guided by laboratory measurements from the literature and, where effects could be isolated, resulted in predictable changes to the simulation, although the non-linear nature of the system means that differences were in the main hard to isolate. Differences in the liquid water content strongly feed back on the boundary layer due to the interaction with radiation which meant that changes due to the coefficients A_2 and B_2 were particularly hard to isolate. Maximum differences to the prognostic variables were typically less than 2% although in some cases differences of 10 to 20% were found. Changes in the coefficients γ, associated with the redistribution of energy between the u, v and w components, and B_1, which changes the TKE dissipation rate have the largest impact on the boundary layer although in no case is the structure of the boundary layer significantly changed by the use of different coefficients. The standard values for the mixing length coefficients will therefore be used following Y78.

Changes to the model time step and vertical grid size have been investigated and the model will be run with a time step of 5 seconds and a grid size of 10 metres or less. A fine vertical resolution is required to correctly simulate the generation of turbulence by radiation within the cloud. Two- and three-dimensional models typically use resolutions between 25 and 100 metres and the simulation of stratocumulus entrainment has been shown to be affected by the coarse vertical resolution in LES (Stevens and Bretherton 1999). Perturbations to the initial profiles of θ_l, q_t and wind speed have predictable effects on the simulations as does changing the boundary layer depth. The results of the sensitivity analyses show that the simulations are robust. Changes to the Mellor-Yamada turbulence closure formulation and perturbations to the initialisation profiles can however create changes to the fluxes of order 20%.

5.3 Model Validation

5.3.1 North Sea Case Study

The data used for this validation study were from instrumented aircraft observations (the C130 of the Meteorological Research Flight) in the North Sea taken in 1982 (Nicholls 1984, Nicholls and Leighton 1986, Nicholls and Turton 1986). The data have been modelled in the past (Nicholls 1984, Ackerman et al. 1995 and Duynkerke and Driedonks 1988). The data used here are from Flight 526 which took place on 22nd July 1982 in the North Sea off the Yorkshire coast centred on 54°20'N, 01°36'E. The winds in the region were from the north resulting from an almost stationary anticyclone centred west of Ireland. The data are derived from a series of horizontal sections and slow rate of climb vertical soundings through the boundary layer. The flight pattern was mainly 'L-shaped' with a nominal side length of 60 km. This provides a time-series measurement long enough that any systematic underestimation of the low frequency component of the fluxes should be small (R. Wood[6], personal communication). The cloud observed was thick, uniform stratocumulus covering much of the North Sea. No upper cloud was observed and the area was fairly horizontally homogenous. Some drizzle was observed. Cloud top was at 830m ± 40m and cloud base at 380m ± 80m. The SST was between 15 and 17°C and the surface pressure 1025 mb. See Nicholls (1984) for more details. The model SST was set at 17 °C, the maximum subsidence at -0.001 ms^{-1} at the inversion height. The time step was 5 seconds, the grid spacing 5 metres and the radiation was calculated every 5 minutes. The model was run for 2 hours, starting at 10 am and the results presented are for a 15 minute average value from 11:45 to 12:00. Note that Nicholls (1984) adjusts the results of his radiation calculations to local noon. The cloud droplet radius is set to 9 μm, the sea surface albedo to 0.06 and the temperature lapse rate above the model domain to 0.01 $°Cm^{-1}$. Figure 5.7 shows the results of the model simulation at noon with the observations overplotted where available.

The wind profiles are little different from the initialisation profiles apart from near the surface where the logarithmic form assumed by the model is apparent (Figure 5.7a). Wind speed is reduced slightly in the lower 400m with a small (order 0.1 ms^{-1}) transfer from the v component (northward) to the u component (eastward). θ_l shows little change in the lower 400m, in the cloud layer however there is a heating of about 0.4°C below the inversion which is a result of cloud shortwave heating which is distributed through the cloud layer by a downwards heat flux in the upper portion of the cloud (Figure 5.7b). q_t shows moistening

---

[6] Meteorological Office Research Flight, Farnborough, UK

from the surface: an increase of 0.2 gkg^{-1} is seen up to about 400m (Figure 5.7c). At 100m q_t is about 0.4 gkg^{-1} higher than the initialisation profile. The modelled profile of TKE is of comparable size to the observations (open circles) although values are underestimated at the cloud base (Figure 5.7d). Error bars are 25% of the mean TKE (R. Wood, pers. comm. based on Mann and Lenschow 1994) and represent the random component of the uncertainty. Table 5.2 summarises the error estimates and their sources for all variables. The modelled TKE shows a distinct minimum at the base of the solid cloud layer, in this simulation about 450 metres, in this simulation there is broken cloud below the solid cloud layer the base of which agrees well with the observed cloud base at 380 metres (with a range of ± 80 m). This is consistent with the reported decoupling between the cloud and the subcloud layer, but the observations show higher values through the entire cloud layer (which is in the mean thicker than that modelled). Above the boundary layer the observations show TKE but in the model the TKE drops to zero at the inversion. The source for the observed TKE is not clear. The model thus simulates the observed TKE fairly well considering this is supposed to be a weakness of the Mellor-Yamada formulation.

The modelled boundary layer structure confirms the suggestion of Nicholls (1984) that conditions in the stratified boundary layer were likely to lead to the surface mixed layer moistening and cumulus clouds forming at its top, resulting in cumulus rising into the stratocumulus layer (Figure 5.7e). In the present simulation the liquid water profile decreased slightly more rapidly with height than the observed values, consistent with the modelled cloud base being higher than the observed average (Figure 5.7f). Peak liquid water values are about 20% too high although the vertically integrated value is within the expected error range since the liquid water content falls off faster in the model than in the observations.

Both the upward and downward components of the longwave radiation are modelled reasonably well above the inversion and cloud layer (Figure 5.7g). Values below the cloud are about 10 Wm^{-2} higher than the observations. As both the upwelling and downwelling components are biased by similar amounts the net longwave heating rate is modelled within the estimated 25% error (Figure 5.7i). The longwave warming observed at the cloud base is however misplaced in the model due to the higher cloud base.

The shortwave decrease in the cloud is less well modelled (Figure 5.7h). Although the upwelling and down welling shortwave radiation are within the expected error both above the cloud and in the sub cloud layer, the penetration of shortwave into the cloud is not as deep as in the observations, leading to larger shortwave heating near the cloud top. This is consistent with the cloud liquid water being too high at the cloud top and falling off too quickly within the cloud. The shortwave heating rate is too high by more than the expected 25% error (Figure

5.7i). This concentration of heating near the cloud top reduces the risk of the potential destabilisation of the cloud by radiation processes, as the effect of the longwave cooling at the cloud top is reduced by the large shortwave heating, and the shortwave heating does not reach as deep into the cloud, reducing the buoyancy flux. This is probably the reason for the low TKE modelled in the cloud layer. To get the radiation profiles correct the model has to correctly predict the amount of liquid water in the cloud. Because of the Gaussian cloud model relationship between the amount of cloud and the turbulent kinetic energy the radiative heating and cooling depends not only on the mean profiles of prognostic variables but also on the predicted energetics. That the radiation profiles are modelled reasonably means the model as a whole must be working well.

The buoyancy flux is positive at the surface due to the warm SST and the evaporation (Figure 5.7j). The surface value is about 0.008 Kms^{-1} (about 18 Wm^{-2}). The flux decreases approximately linearly to zero near the cloud base. The buoyancy flux increases in the cloud layer due to the destabilising effect of the radiative heating and cooling. There is a slightly negative buoyancy flux at the cloud top due to the entrainment of warmer air into the cloud layer. The modelled values of buoyancy flux match the observed values well. The total water flux is positive throughout the model domain, with maxima at the sea surface and the cloud top (Figure 5.7k). The modelled water flux is well modelled and is within the range of the observations at all levels. The heat flux is also well modelled, although there is a possibility that the fluxes near the cloud top are too high (Figure 5.7l).

5.3.2 Comparison with GCSS Simulations

The GEWEX Cloud System Study (GCSS) workshop compared the output of six one-dimensional models of the atmospheric boundary layer with 10 LES models (Bechtold et al. 1996, Moeng et al. 1996). The data used for the comparative simulations was based on FIRE data (see Section 2.3.1) and represents an idealised nighttime case with low surface heating and little wind shear. The model was run with the same initialisation profiles and parameters as those presented by Bechtold et al. (1996). Figure 5.8 shows the output of the model and the range of the LES simulations for TKE (Figure 5.8a), liquid water content (Figure 5.8b), buoyancy (Figure 5.8d) and humidity (Figure 5.8e) fluxes, and wind stress (Figure 5.8f). The radiative cooling rate is compared with the output of the one-dimensional models (Figure 5.8c) since no LES output is given by Bechtold et al. (1996). Except for the latent heat flux profiles all lie within or very close to the range of the LES output. Differences are seen in the latent heat flux profiles (Figure 5.8e) where the one-dimensional model output is below the minimum predicted by any of the LES models. It should be noted however that the range of surface latent heat fluxes predicted by the LES models is significantly greater than the

approximately 20 Wm-2 expected from a bulk-formula type calculation. The mean LES surface latent heat fluxes range from 30-80 Wm-2 much higher than would be expected from boundary layer theory. Neither paper discusses reasons for this. The surface water flux predicted in the current simulation seems more realistic than that produced by the LES. It is then not perhaps surprising that the peak in-cloud water fluxes are also low. It should also be noted that the simulation of, for example, TKE in two-dimensional cloud resolving models compared in the above studies was particularly poor and much worse than the present one-dimensional simulation.

The overall agreement between the model and LES simulations is therefore reasonable although in this case the solar radiation simulation has not been tested.

5.3.3 ASTEX First Lagrangian Experiment

Data from the start of the first Lagrangian experiment of ASTEX (see Section 2.3.4) was simulated as further model validation. The mean and turbulence quantities were obtained from Stephan de Roode at the University of Utrecht Web Site[7]. deRoode and Duynkerke (1996) describe the measurements. Flight 3 was chosen as the most suitable dataset for simulation of the stratocumulus-topped boundary layer (Flights 1 and 4 showed a stable temperature gradient throughout the boundary layer, Flight 2 did not contain many measurements and Flight 5 was in the trade cumulus regime).

Figure 5.9 shows the output from the simulation and the boundary layer turbulence measurements from the NCAR Electra aircraft. The error bars are again from Table 5.2 as none are provided with the data. No radiation measurements are provided for this dataset. The turbulent kinetic energy values are slightly lower than the limit of the error bars at the lowest measurement layer and at the lower limit of the error bars at 100 metres (Figure 5.9a). At higher levels and within the cloud the simulated TKE is close to the lower measurements and well within the limits set by the error bars. The in-cloud liquid water content is well simulated at the cloud top but decreases too rapidly within the cloud, reaching zero just below 500 metres, whereas the measurements show liquid water is still present at 450 metres (Figure 5.9b). The buoyancy flux is well simulated too, with most of the simulation (except for one low flux measurement within the cloud layer) close to the measurements (Figure 5.9c). Like the liquid water content the buoyancy flux reduces too quickly deeper within the cloud layer. The inversion height in the model is about 20 metres above the measurements (if the peak water

---

[7] http://www.fys.ruu.nl/~roode/ASTEX.html

flux measurements are assumed to occur just below the inversion) which makes the buoyancy flux simulation in this region of high flux gradient fall outside the observation error bars, but the simulation is realistic. The same is true for the total water flux with realistic in-cloud peak values slightly above the measurements (Figure 5.9d). Zero water fluxes observed at 600 metres height are not seen in the simulation but the near surface water flux is within the error bounds of the measurements. Like the buoyancy flux, the heat flux is well simulated (excepting the one incloud measurement noted above, Figure 5.9e).

5.3.4 Summary of Model Validation

The model has been shown to give physically sensible results in simulations of stratocumulus in a variety of regions. In particular the flux profiles agree well with aircraft measurements of the same quantities. Liquid water contents however may be too high near the cloud top and decrease too rapidly within the cloud. The radiative fluxes have not been well tested. The validation simulations however show that the main features of boundary layer structure can be reproduced with this model and that predicted fluxes and TKE are of the correct order. As the simulations have been initialised with idealised versions of the measured profiles some differences might be expected. It should be noted that measurement of fluxes within the atmospheric boundary layer is difficult and the observations contain large errors. Horizontal inhomogeneities can cause large variability.

It should also be noted that much larger, three-dimensional LES models which represent the current state-of-the-art in atmospheric boundary layer modelling show large scatter between different models when simulating the same cases (e.g. the GCSS simulations, Bechtold et al. 1996). The model used in the present study produces output within the range of the LES results, is not computationally intensive, and can be used to investigate impacts of changes in forcing on the boundary layer in a way which is not yet possible with LES models.

5.4 Summary

Changes to the model formulation made during this study were shown to impact on the simulations of the boundary layer (Section 5.1). The use of a sophisticated radiation scheme reduced the amount of decoupling in an idealised boundary layer compared to the KR code since the resulting longwave radiation was stronger. Matching the boundary layer fluxes to their surface values resulted in smaller subcloud layer fluxes which lead to smaller incloud fluxes, less turbulence and hence smaller entrainment rates and boundary layer heights. The KR version of the model predicted flux profiles that were unphysical: the revised version

predicts more physically reasonable profiles. Changes to the numerical scheme resulted in less noisy simulations.

The revised version of the model has been demonstrated to be stable to changes in the mixing length coefficients (Section 5.2.1), the model vertical resolution and time step (Section 5.2.2) and the initial conditions (Section 5.2.3). In addition the model has been shown to well simulate stratocumulus-topped boundary layers in the North Sea (Section 5.3.1), in the North Pacific off the coast of California (Section 5.3.2) and in the North Atlantic near the Azores (Section 5.3.3).

Colour line	Parameters	A_1	A_2	B_1	B_2	c
black	standard ($\gamma = 0.22$)	0.92	0.74	16.6	10.1	0.08
red	$\gamma = 0.20$	1.11	0.82	16.6	10.1	0.08
green	$\gamma = 0.28$	0.44	0.58	16.6	10.1	-0.01
blue	B_1=18.9 ($\gamma = 0.22$)	1.05	0.70	18.9	11.5	0.10
light blue	B_1=14.3 ($\gamma = 0.22$)	0.79	0.77	14.3	8.7	0.05
pink	$Pr_t = 0.70$	0.92	0.84	16.6	10.1	0.08
yellow	$Pr_t = 0.85$	0.92	0.69	16.6	10.1	0.08
orange	$R_{diss} = 0.56$	0.92	0.74	16.6	11.0	0.08
bluegreen	$R_{diss} = 0.67$	0.92	0.74	16.6	9.3	0.08

Table 5.1: Values of Mixing Length Coefficients (A_1, A_2, B_1, B_2 and c) used in Sensitivity Study. Colours Refer to Lines in Figures 5.3a-c.

Variable	Error	Source
turbulent kinetic energy	25%	RW
liquid water content	20%	RW
Longwave flux	10 Wm^{-2}	RW
Shortwave flux	Maximum of 3% and 20 Wm^{-2}	RW, N84
Radiative heating rate	25%	RW
Heat flux	Maximum of 20% and 2 Wm^{-2}	RW, ECK
Humidity flux	Maximum of 20% and 2 Wm^{-2}	RW, ECK
Buoyancy flux	Maximum of 30% and 3 Wm^{-2}	RW, ECK

Table 5.2: Errors in Aircraft Data. Sources are RW (R. Wood, Met. Research Flight, pers. comm.), N84 (Nicholls 1984), ECK (the flux error has been given an absolute limit of 2 Wm^{-2} to prevent the error becoming near zero at small mean flux values. The buoyancy flux has been assigned a larger minimum error of 3Wm^{-2} as this flux contains errors in both the heat and water components of the flux).

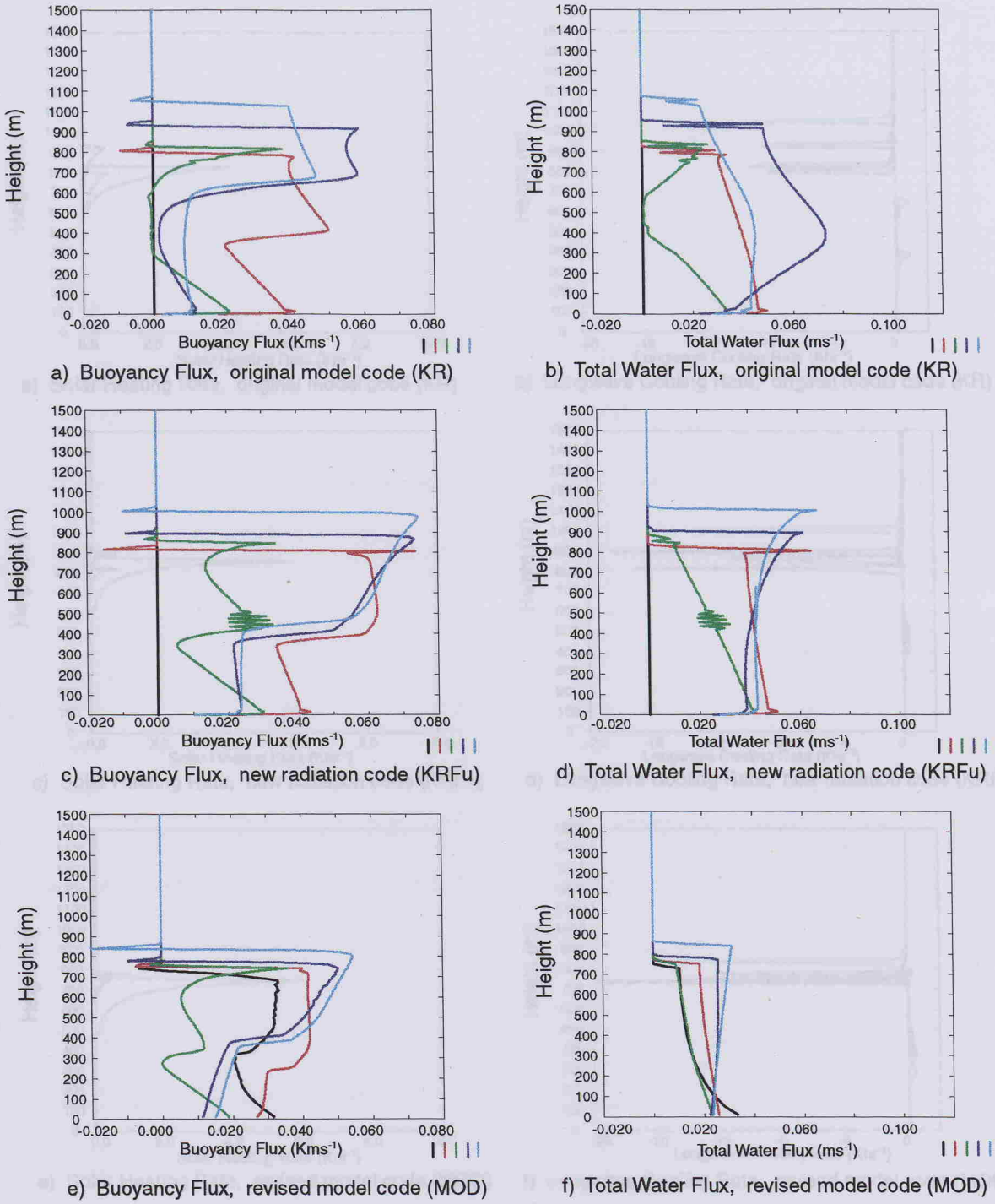

Figure 5.1 Comparison of buoyancy fluxes (Kms^{-1}, left panel) and humidity fluxes (ms^{-1}, right panel) from the original model code (top), from the original model code but with the Fu (1991) radiation code (centre) and for the revised version of the model (lower) plotted as a function of height in metres. Black lines represent output at initialisation, red lines at 0600h, green at 1200h, blue at 1800h and light blue at 2400h.

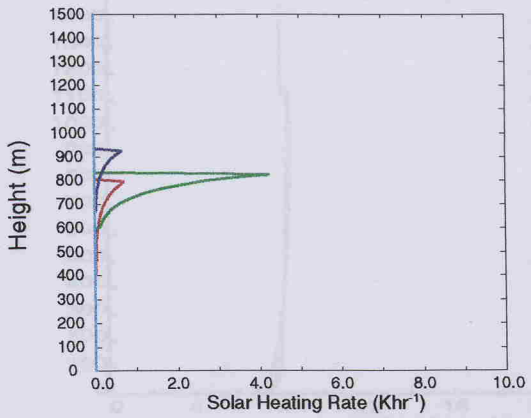

a) Solar Heating Rate, original model code (KR)

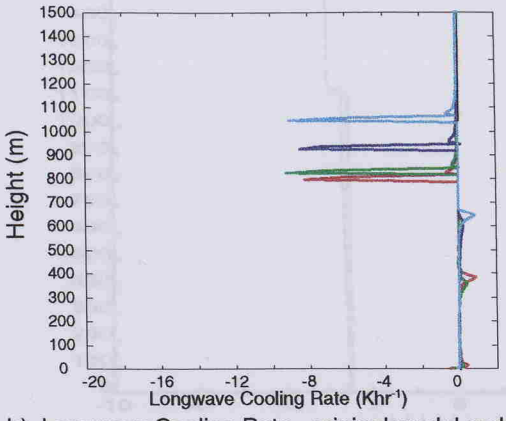

b) Longwave Cooling Rate, original model code (KR)

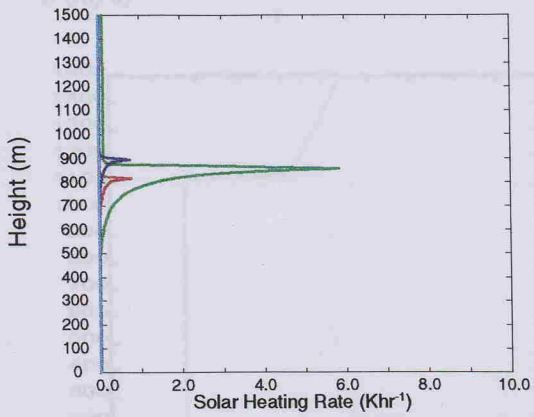

c) Solar Heating Rate, new radiation code (KRFu)

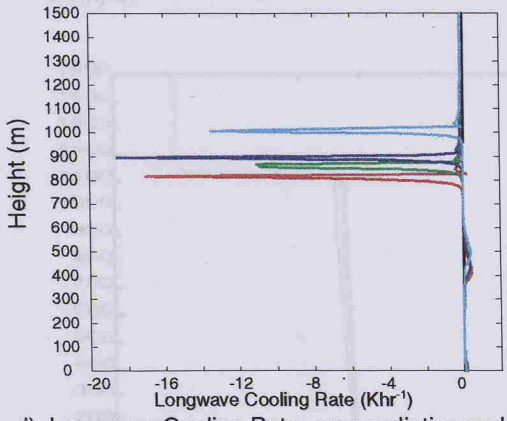

d) Longwave Cooling Rate, new radiation code (KRFu)

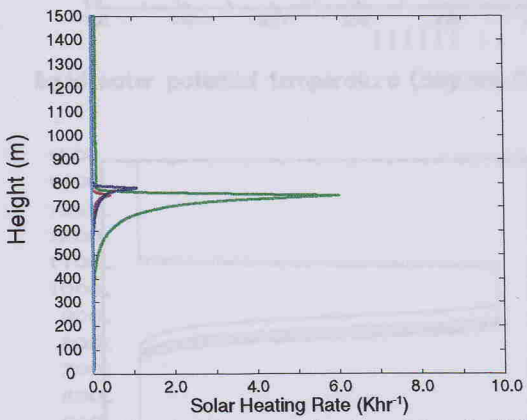

e) Solar Heating Rate, revised model code (MOD)

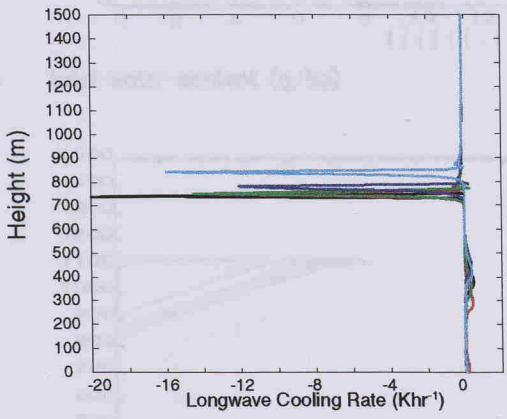

f) Longwave Cooling Rate, revised model code (MOD)

Figure 5.2 Comparison of solar heating rate (Khr^{-1}, left panel) and longwave cooling rate (Khr^{-1}, right panel) from the original model code (top), from the original model code but with the Fu (1991) radiation code (centre) and for the revised version of the model (lower) plotted as a function of height in metres. Black lines represent output at initialisation, red lines at 0600h, green at 1200h, blue at 1800h and light blue at 2400h.

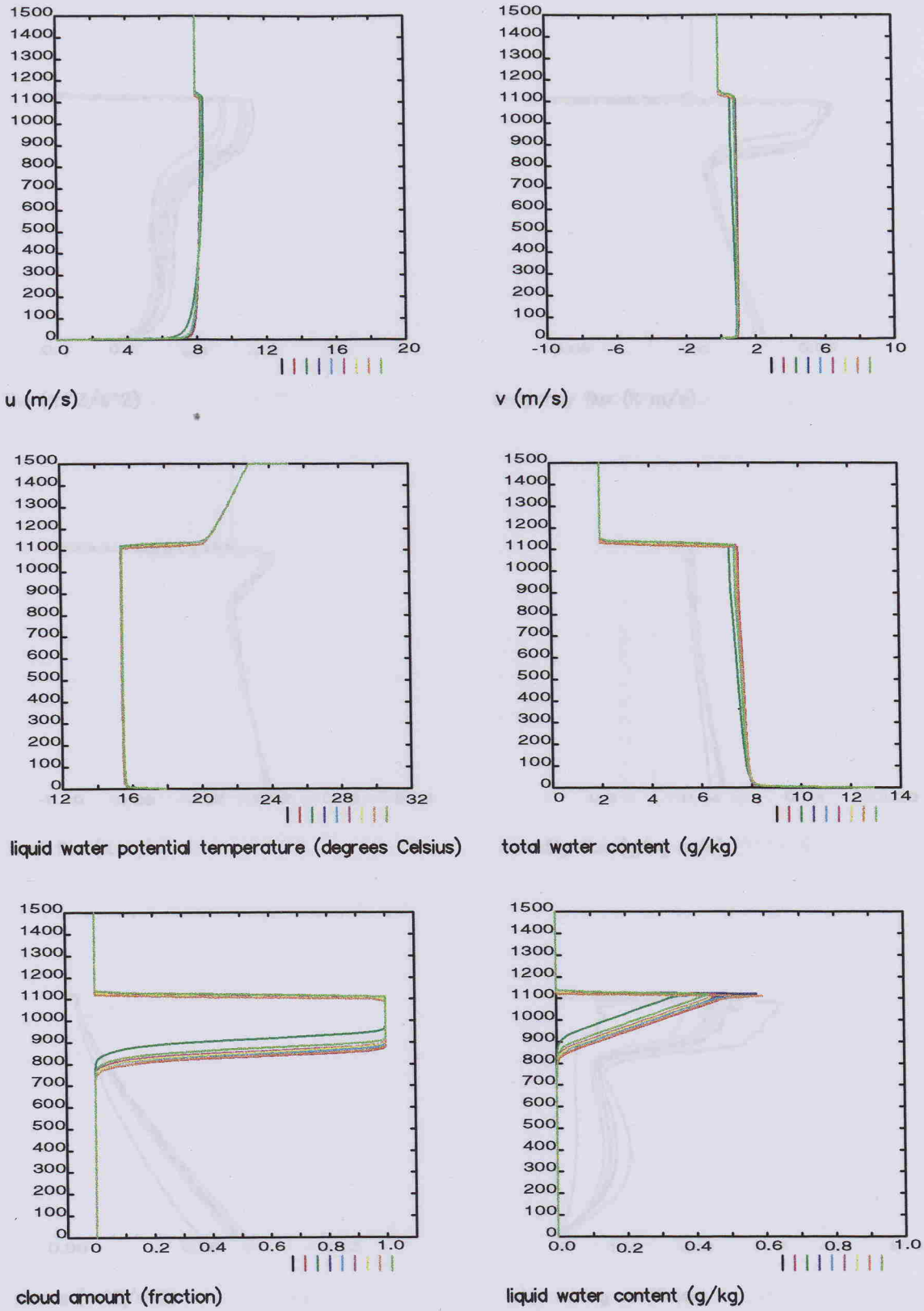

Figure 5.3a Model output showing effect of different mixing length coefficients on the profiles. Black (standard), red (γ=0.20), green (γ=0.28), blue (B_1=18.9), light blue (B_1=14.3), pink (Pr_t=0.70), yellow (Pr_t=0.85), orange (R_{diss}=0.56), bluegreen (R_{diss}=0.67).

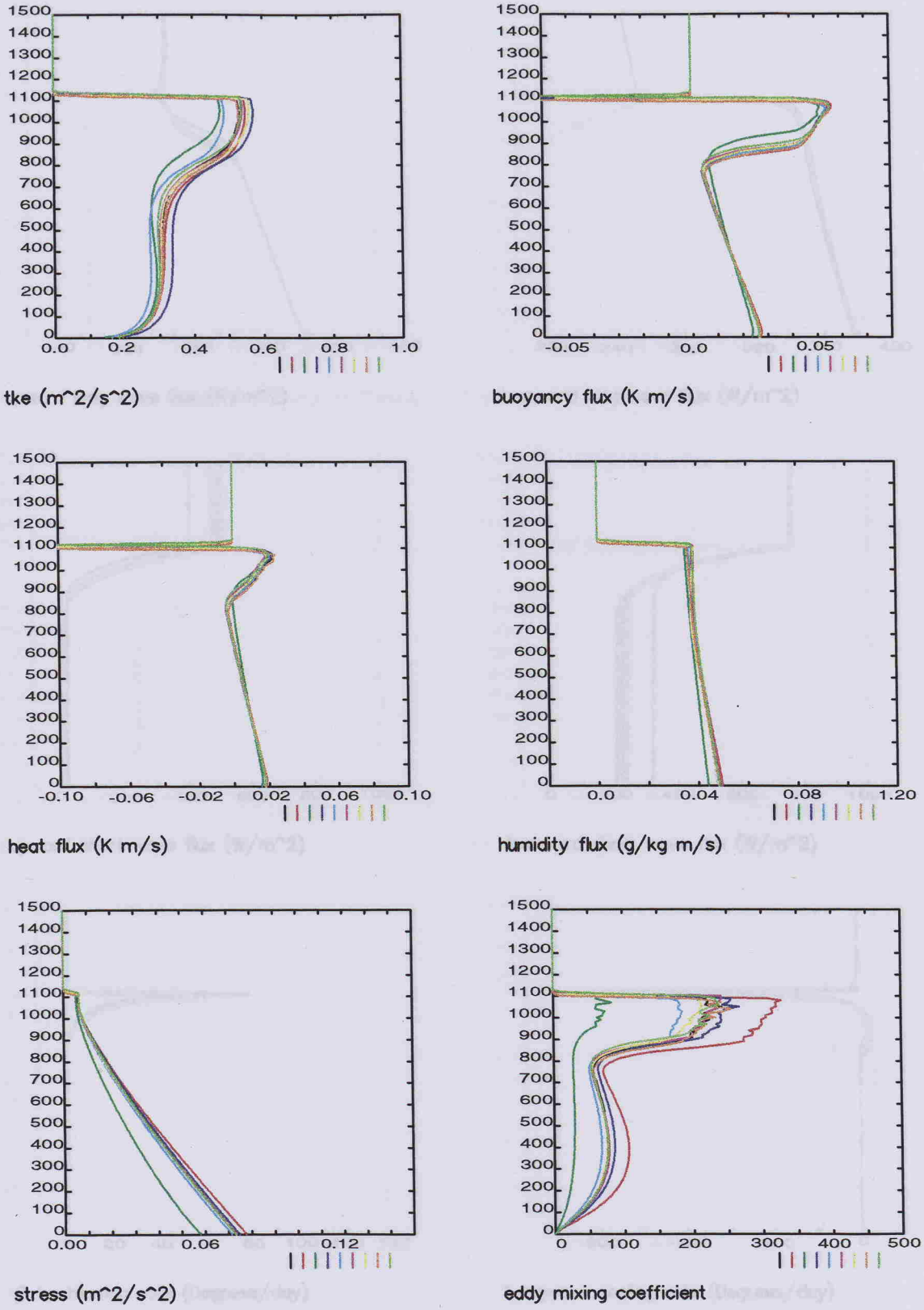

Figure 5.3b Model output showing effect of different mixing length coefficients on the profiles. Lines as Figure 5.3a.

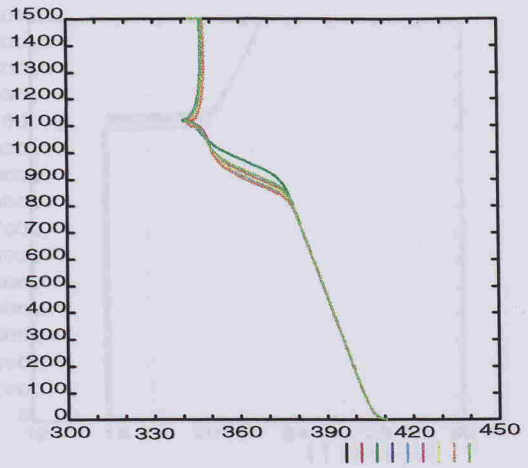

upward long wave flux (W/m^2)

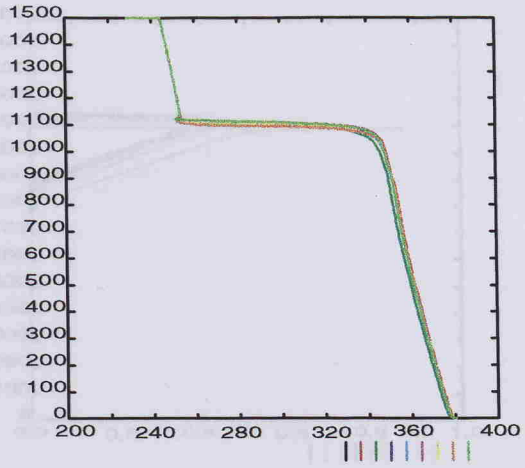

downward long wave flux (W/m^2)

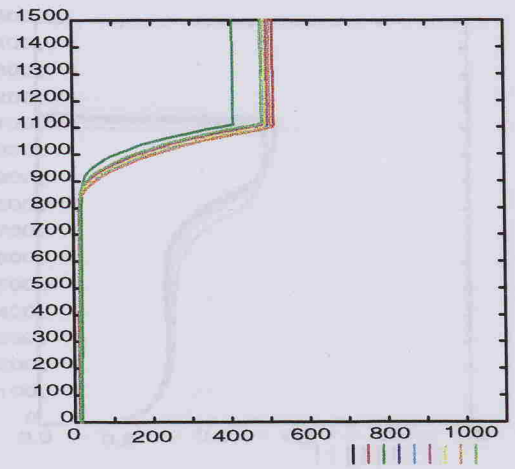

upward short wave flux (W/m^2)

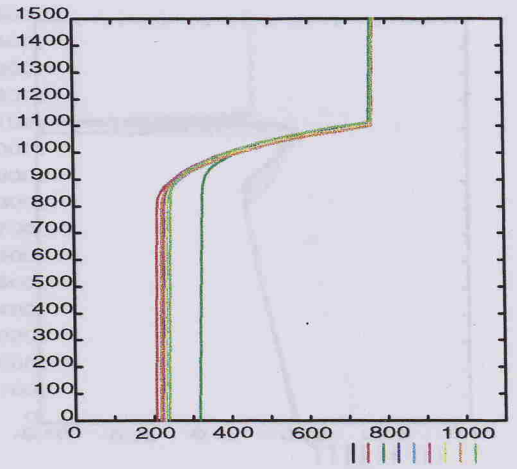

downward short wave flux (W/m^2)

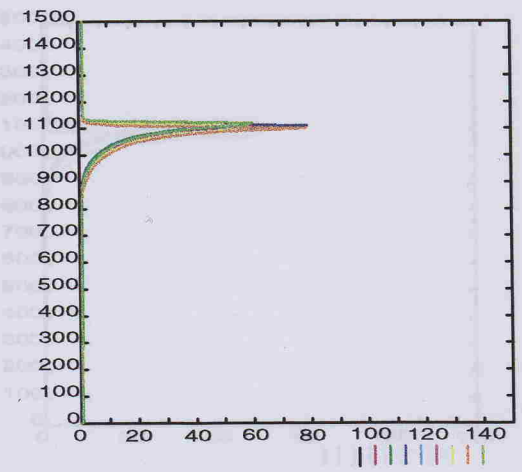

Solar heating rate (Degrees/day)

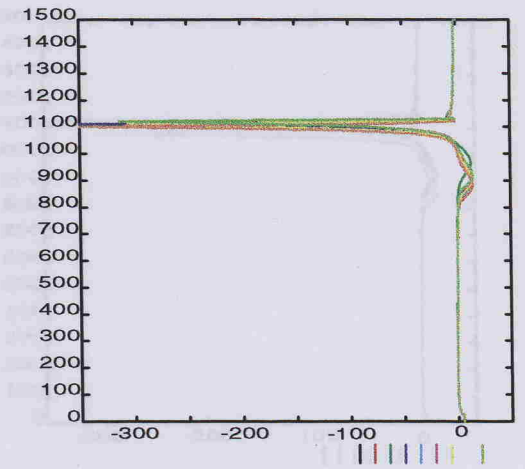

Longwave cooling rate (Degrees/day)

Figure 5.3c Model output showing effect of different mixing length coefficients on the profiles. Lines as Figure 5.3a.

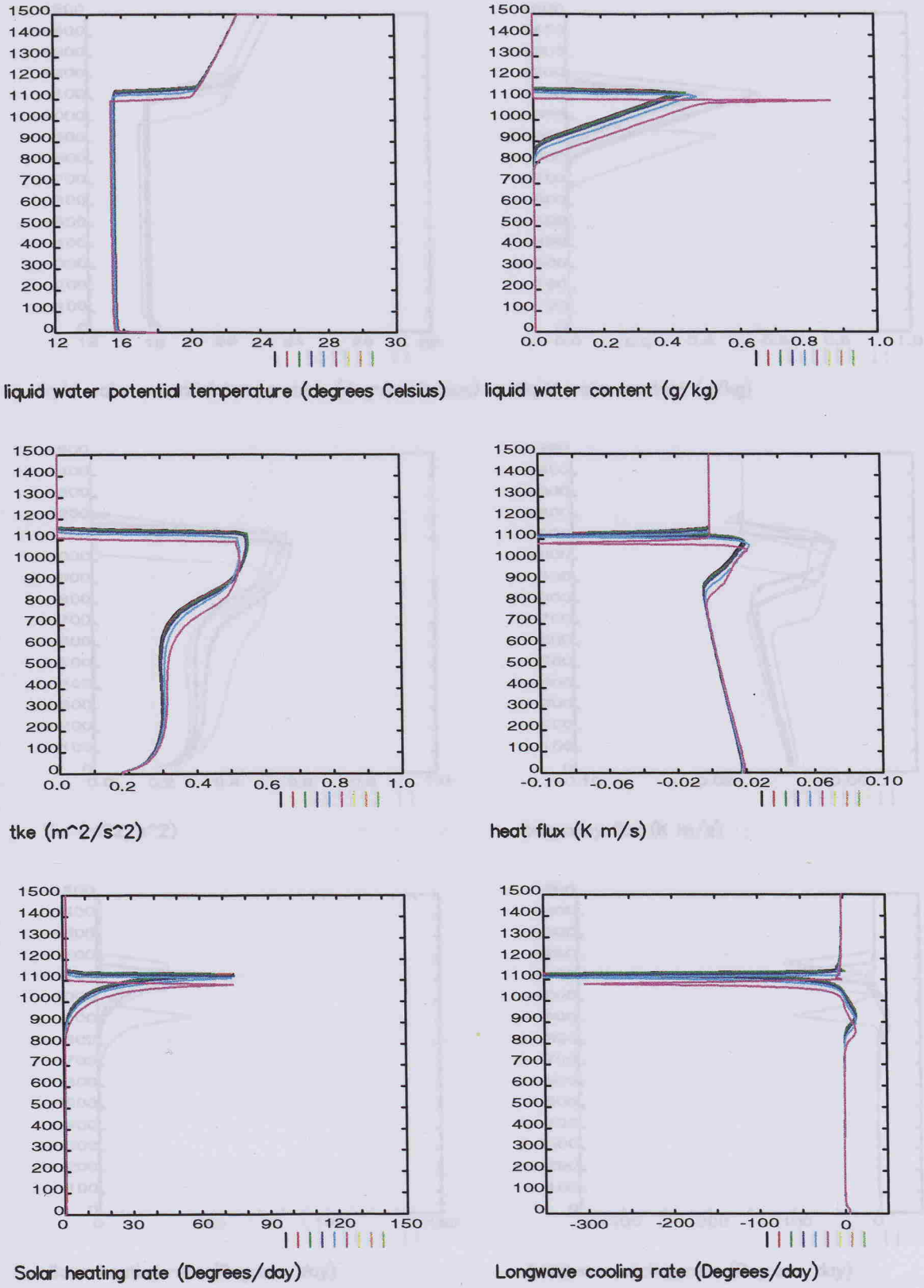

Figure 5.4 Model output showing effect of different time steps, $\Delta z = 10m$.

black $\Delta t = 1sec$, red $\Delta t = 2sec$, green $\Delta t = 5sec$, blue $\Delta t = 10$ sec, light blue $\Delta t = 20sec$, pink $\Delta t = 45sec$.

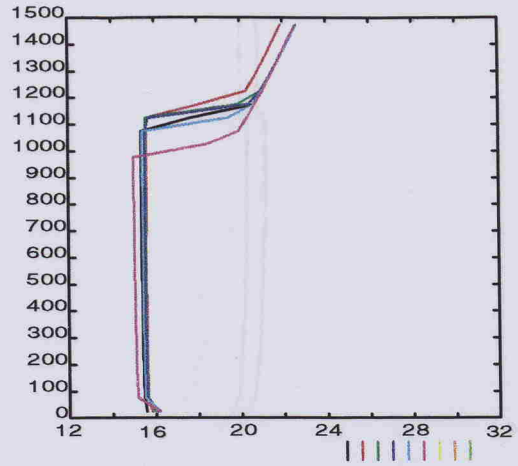

liquid water potential temperature (degrees Celsius)

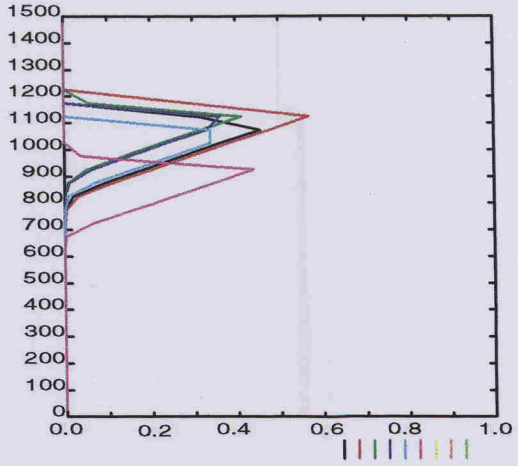

liquid water content (g/kg)

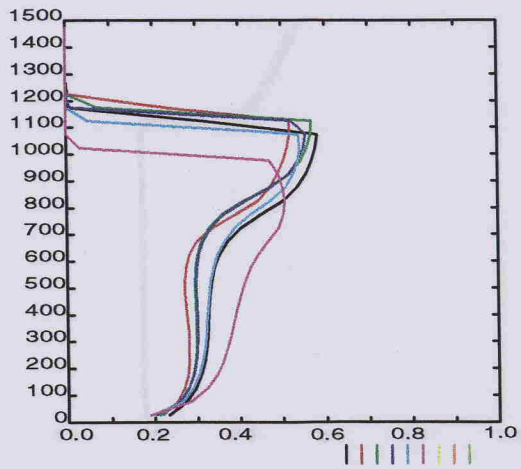

tke (m^2/s^2)

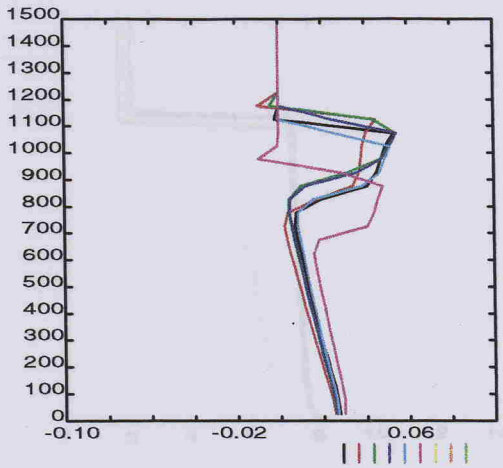

buoyancy flux (K m/s)

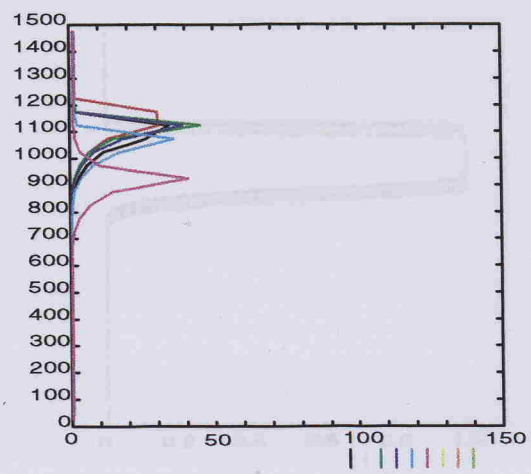

Solar heating rate (Degrees/day)

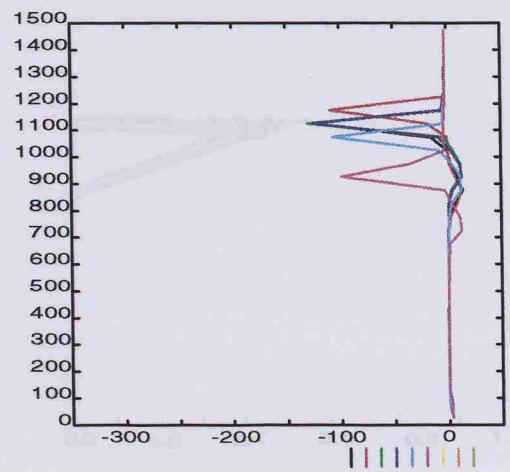

Longwave cooling rate (Degrees/day)

Figure 5.5 Model output showing effect of different grid spacing $\Delta t = 5$sec. black $\Delta z = 1$m, red $\Delta z = 2$m, green $\Delta z = 5$m, blue $\Delta z = 10$m, light blue $\Delta z = 20$m, pink $\Delta z = 50$m.

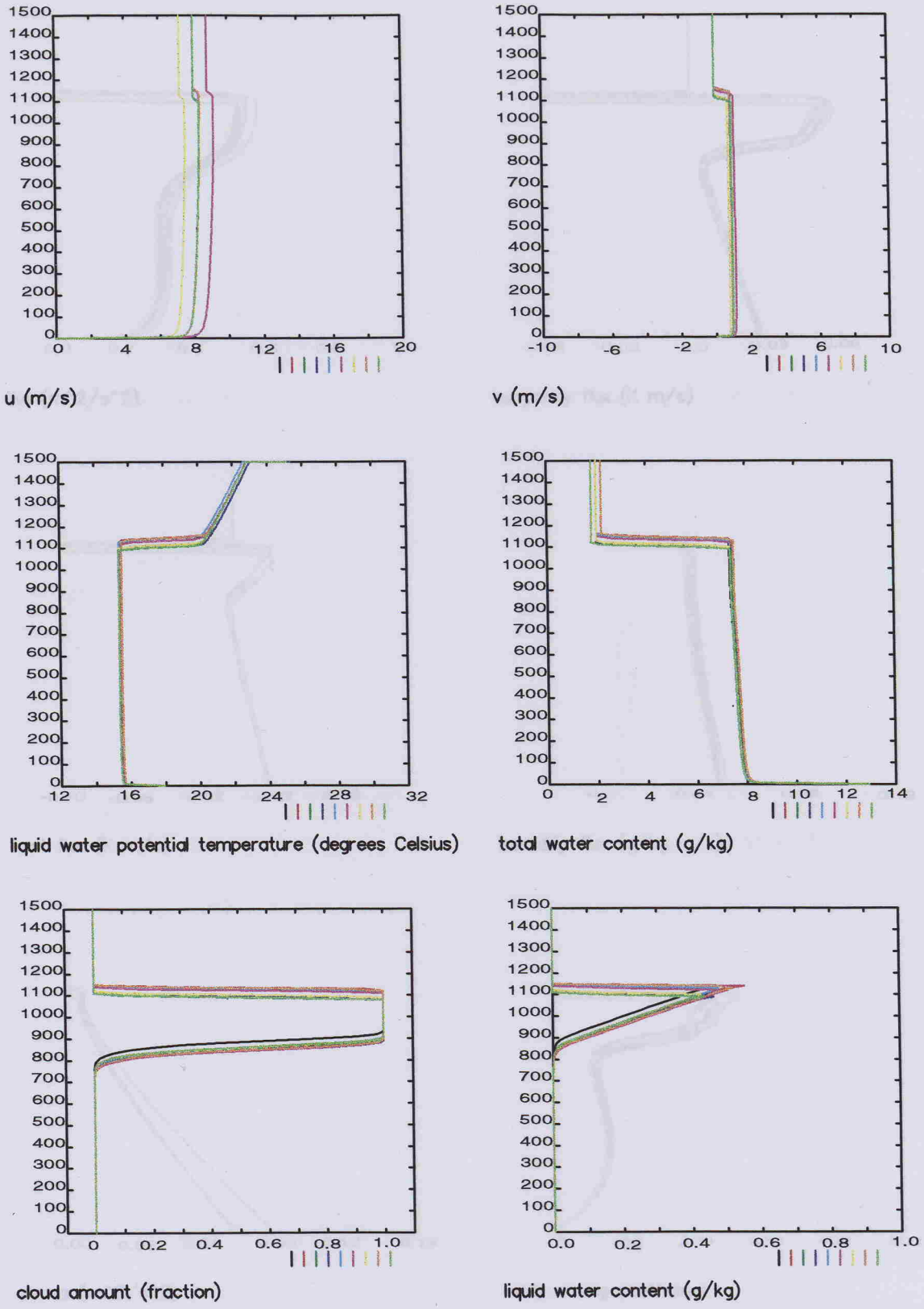

Figure 5.6a Model output showing effect of different initial conditions on the profiles. Black(standard), red (inversion height+20m), green (inversion height-20 m), blue (θ_l+0.2°C), light blue (θ_l-0.2°C), pink (wind speed+10%), yellow (wind speed-10%), orange (q_t + 0.2 gkg^{-1}), bluegreen (q_t - 0.2 gkg^{-1}).

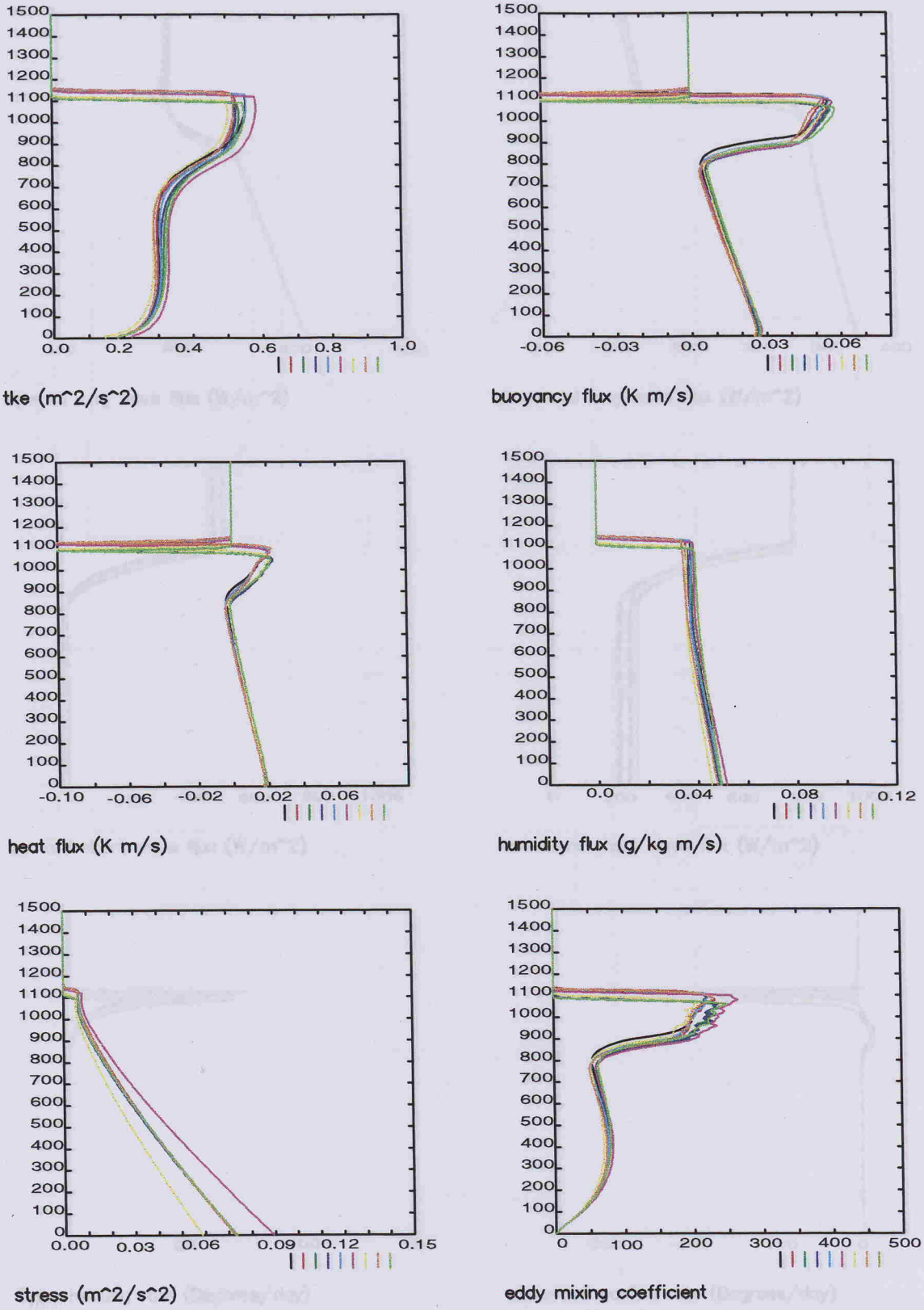

Figure 5.6b Model output showing effect of different initial conditions on the profiles. Black (standard), red (inversion height+20m), green (inversion height-20m), blue (θ_l+0.2°C), light blue (θ_l-0.2°C), pink (wind speed+10%), yellow (wind speed-10%), orange (q_t + 0.2 gkg^{-1}), bluegreen (q_t - 0.2 gkg^{-1}).

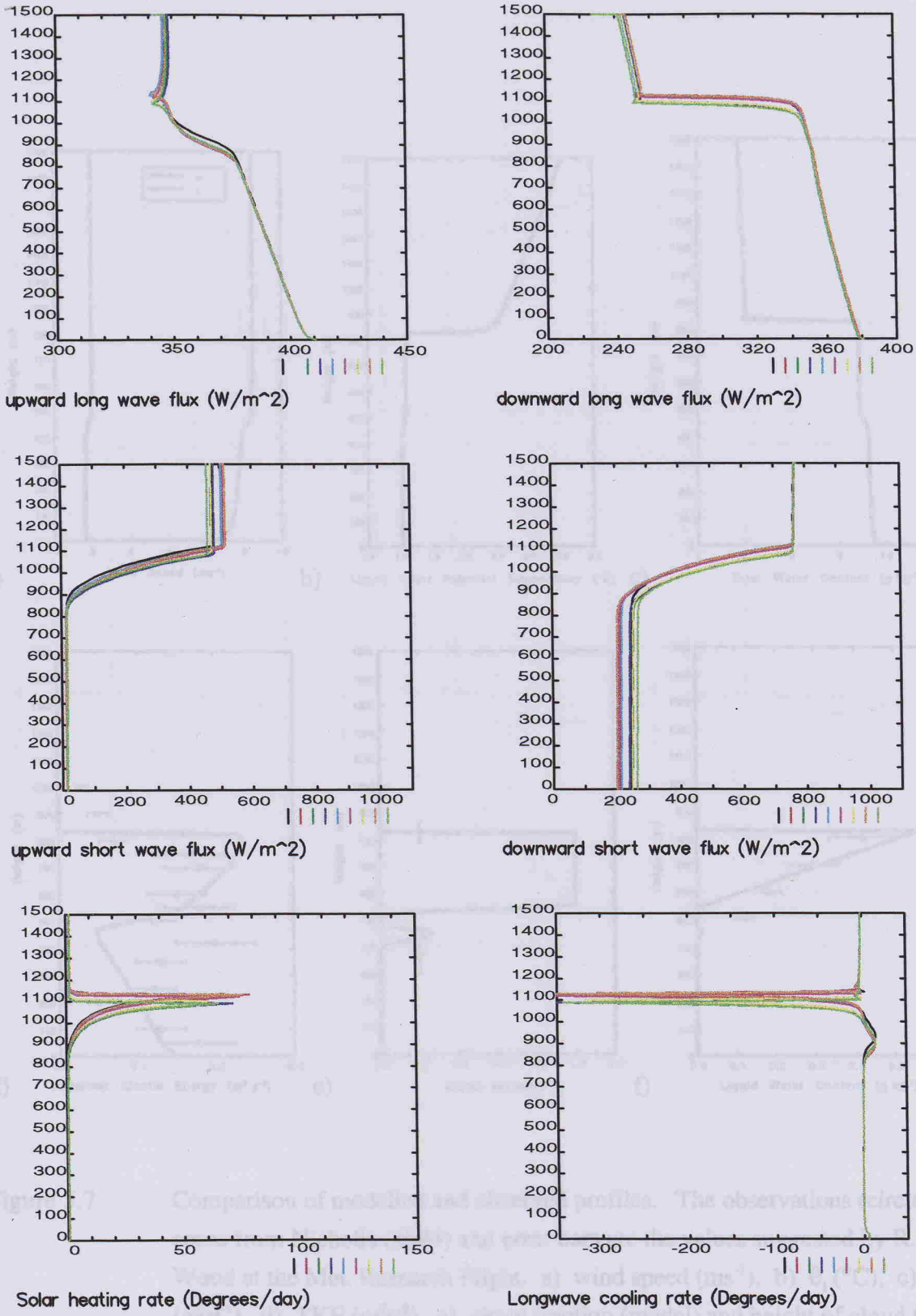

Figure 5.6c Model output showing effect of different initial conditions on the profiles. Black (standard), red (inversion height+20m), green (inversion height-20m), blue (θ_l+0.2°C), light blue (θ_l-0.2°C), pink (wind speed+10%), yellow (wind speed-10%), orange (q_t + 0.2 gkg^{-1}), bluegreen (q_t - 0.2 gkg^{-1}).

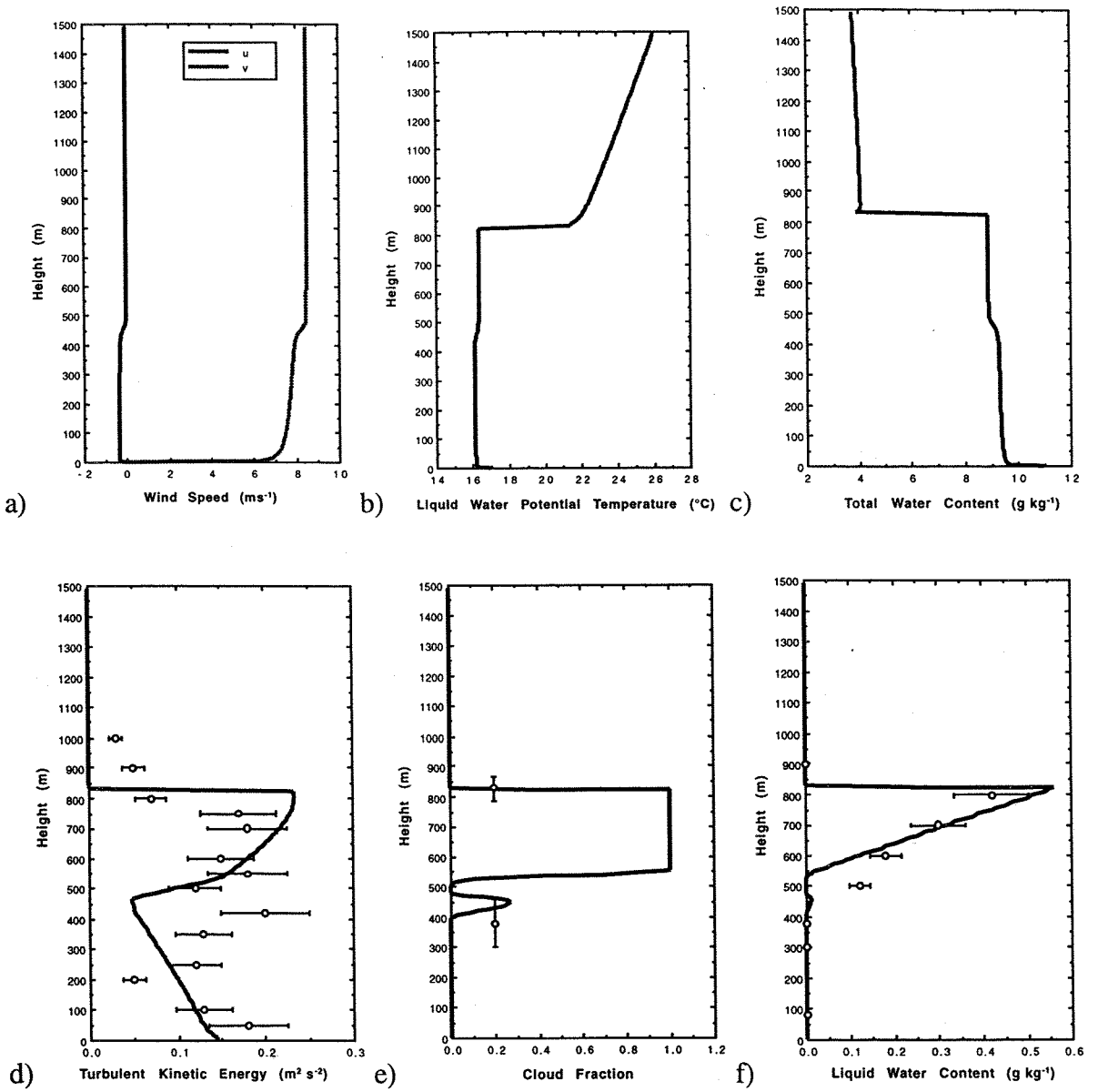

Figure 5.7 Comparison of modelled and observed profiles. The observations (circles) come from Nicholls (1984) and error bars are the values suggested by R. Wood at the Met. Research Flight. a) wind speed (ms^{-1}), b) θ_l (°C), c) q_t (gkg^{-1}), d) TKE (m^2s^{-2}), e) cloud fraction (model) and height of cloud top and cloud base (observations), f) liquid water content (gkg^{-1}).

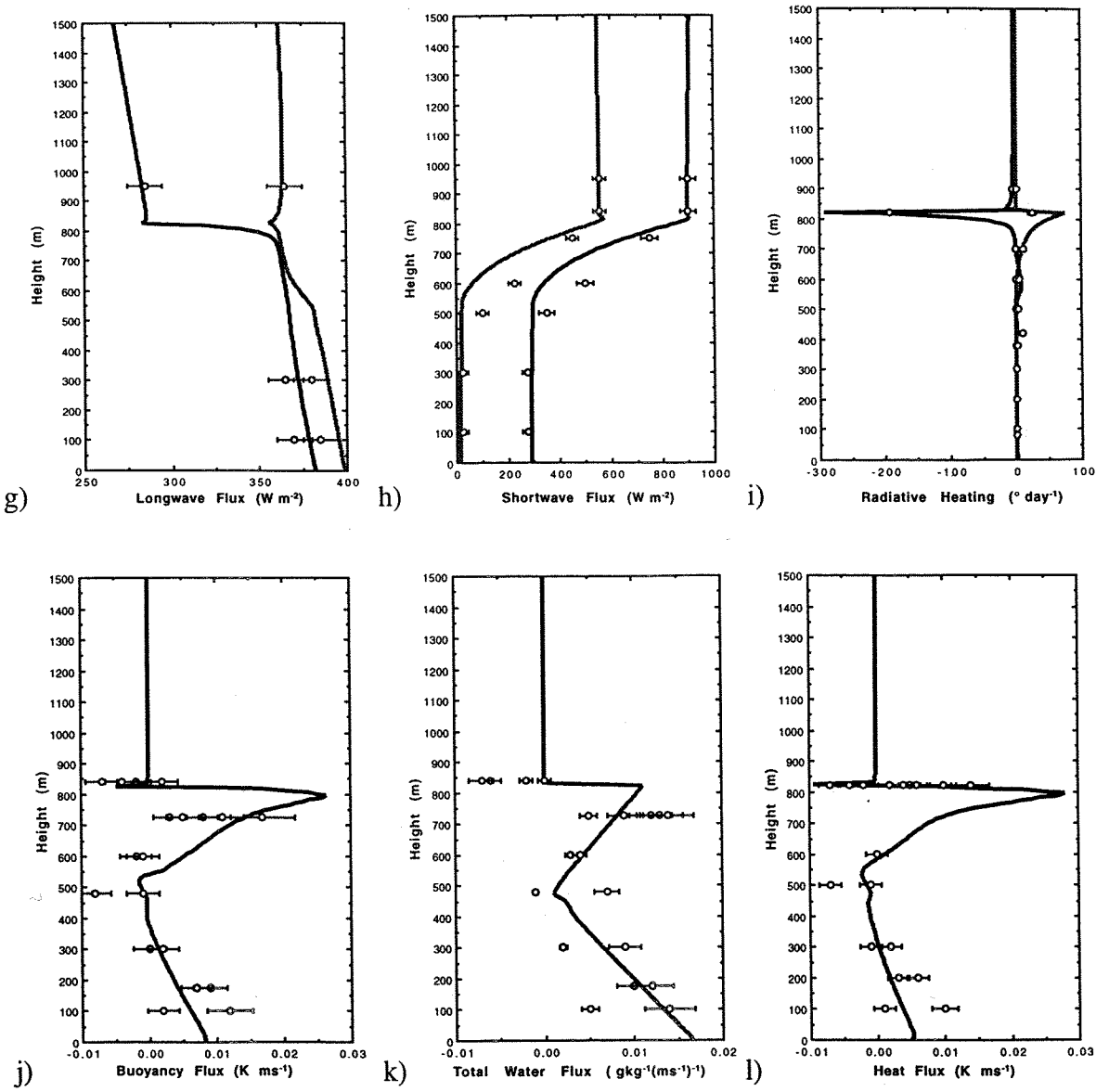

Figure 5.7 cont. g) longwave flux (Wm^{-2}), h) shortwave flux (Wm^{-2}), i) radiative heating rate ($°C\ day^{-1}$), j) buoyancy flux (Kms^{-1}), k) q_t flux (ms^{-1}), l) θ_l flux (Kms^{-1}).

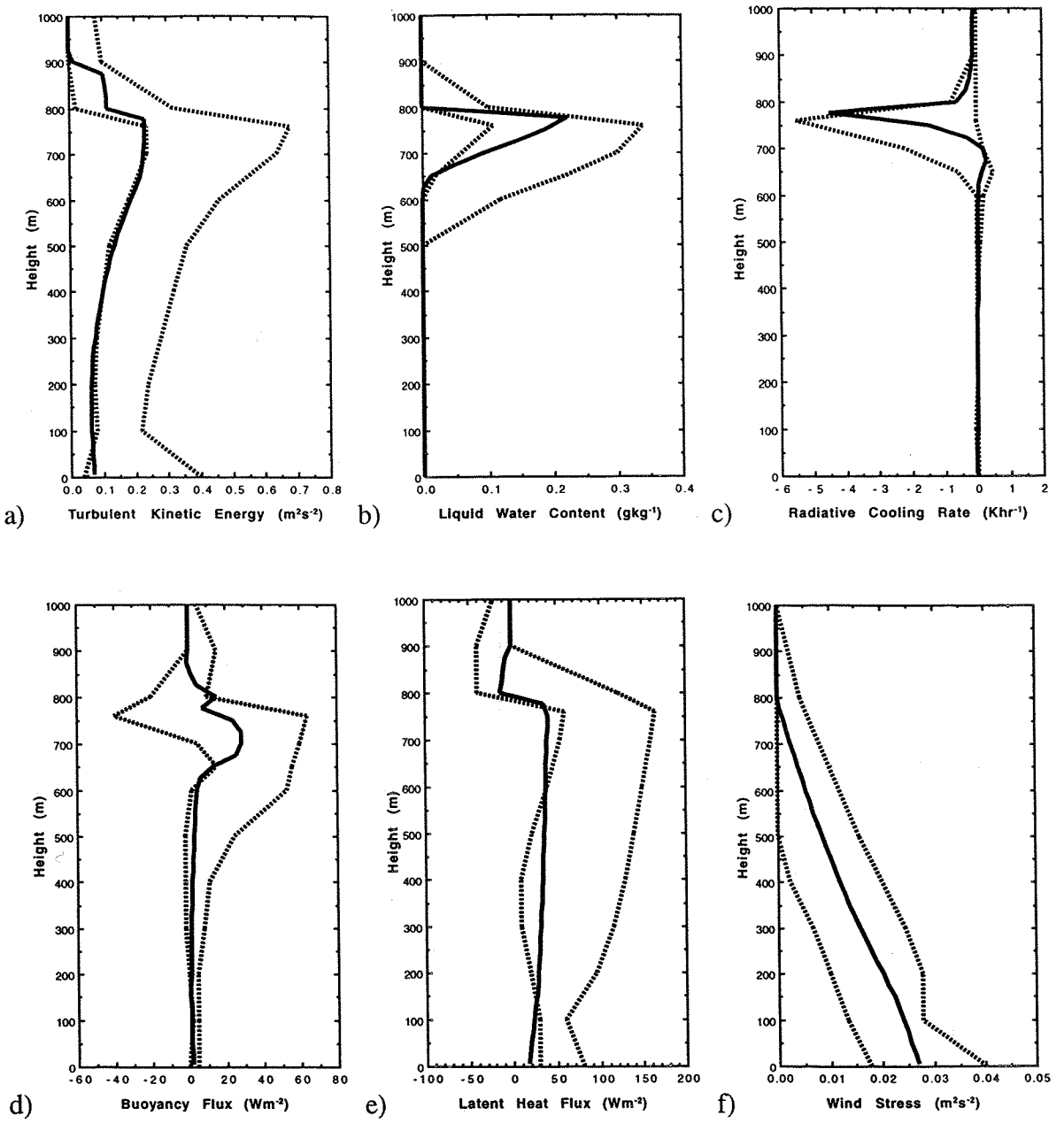

Figure 5.8 Comparison of modelled profiles with output of Large Eddy Simulations (Bechtold et al. 1996, Moeng et al. 1996). Solid line is the model output and the dashed lines represent the upper and lower limits of the output of LES of the same data. a) TKE (m^2s^{-2}), b) liquid water content (gkg^{-1}), c) radiative cooling rate ($K\ hr^{-1}$), d) buoyancy flux (Wm^{-2}), e) latent heat flux (Wm^{-2}), f) wind stress (m^2s^{-2}).

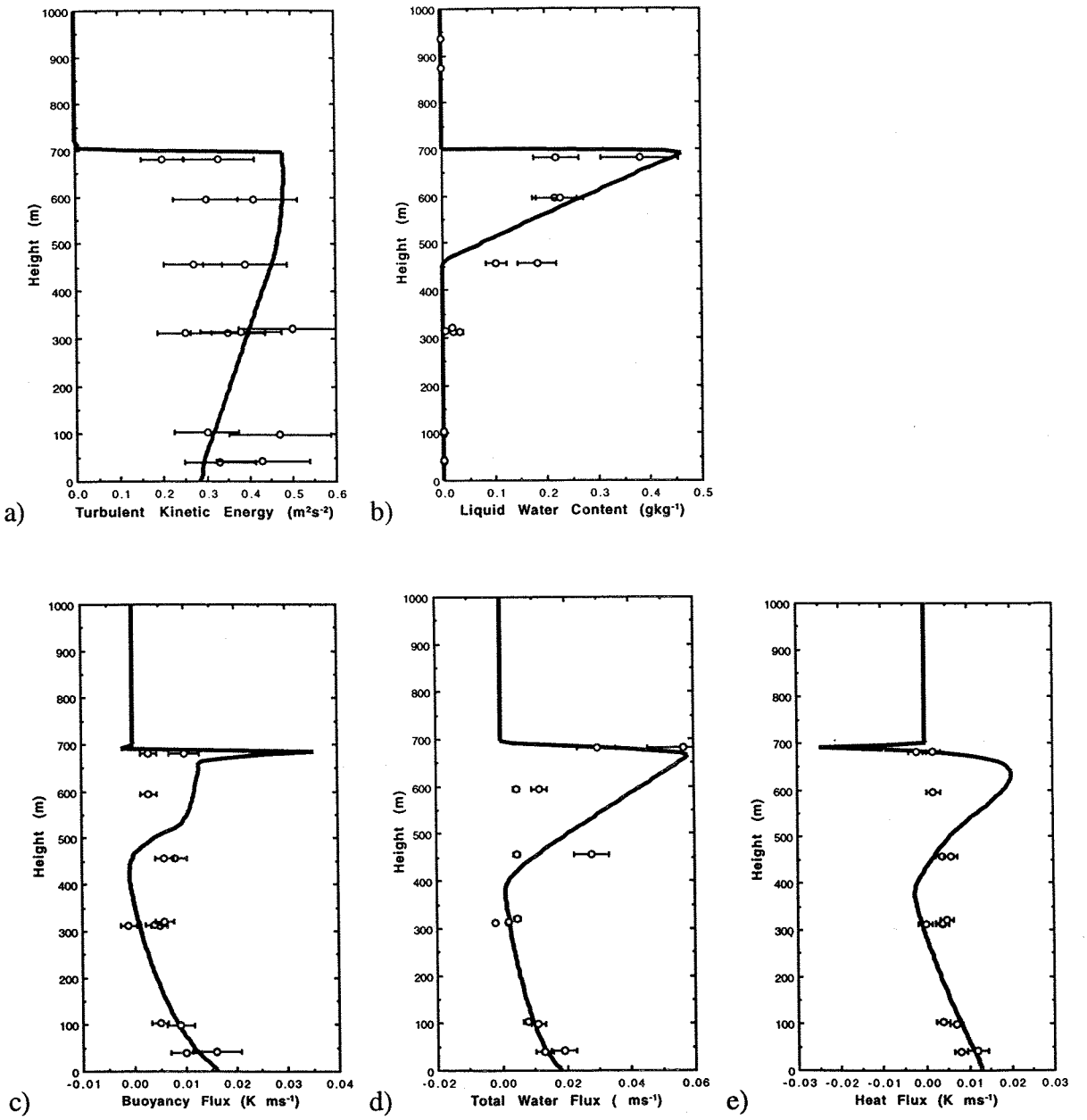

Figure 5.9 Comparison of modelled profiles with aircraft data for the 3rd flight of the ASTEX First Lagrangian Experiment. Solid line is the model output and open circles the aircraft measurements. Error bars are given in Table 5.2. a) turbulent kinetic energy (m^2s^{-2}), b) liquid water content (gkg^{-1}), c) buoyancy flux ($K\ ms^{-1}$), d) q_t flux (ms^{-1}), e) θ_l flux ($K\ ms^{-1}$).

6. THE STABILITY OF STRATOCUMULUS LAYERS AND THE TRANSITION TO CUMULUS

6.1 Introduction

This chapter will firstly consider the environmental conditions under which stratocumulus are unstable or the stratocumulus to cumulus transition occurs. Data from the North Atlantic and the North Pacific in both January and July will be used to determine the environmental conditions (Section 6.2) which are then used to simulate the evolution of a stratocumulus boundary layer as it advects towards the tradewind region (Section 6.3.1). The evolution of the boundary layer from stratocumulus to a cumulus under stratocumulus boundary layer is described (Section 6.3.2). Tracers are used to quantify the relative importance of entrainment and turbulence originating at the sea surface (Section 6.3.3). The simulation does not proceed to a cumulus only boundary layer; a possible reason for this is discussed in Section 6.3.4. Section 6.4 compares the simulation to observations, mostly from ASTEX, and to other model studies from the literature, particularly those of Krueger et al. (1995a,b) and Wyant et al. (1997).

6.2 Environmental Conditions

Figure 6.1a shows the monthly mean surface conditions over the North Pacific in January from 1980 to 1993 from the SOC Climatology (Josey et al. 1999). Figure 6.1b shows the cloud cover from the SOC Climatology and the proportions of reports with clear sky, cumulus, stratocumulus and stratus calculated from COADS reports as described in Section 2.3.1. In addition upper air data from the NCEP reanalysis project (Kalnay et al. 1996) are shown: the relative humidity and vertical motion at 700 mb and the potential temperature gradient between 700 and 500 mb. Figures 6.2 to 6.4 show the same information for July in the North Pacific and for January and July in the North Atlantic respectively. It should be noted that the data density varies across the regions shown in these figures. In the main shipping lanes there is good data coverage (typically in Northern Hemisphere midlatitudes) but the sampling is poor in equatorial regions, particularly below 20°N in the Pacific. The quality of the data will depend on the data density. In particular the data in the southern North Pacific are noisy (Figures 6.1 and 6.2).

The data in Figures 6.1 to 6.4 will be used to identify the mean conditions that give rise to stratocumulus or to a stratocumulus to cumulus transition. From these conditions we can see several features common to each stratocumulus region. We will in this section consider the subtropical stratocumulus region found in the eastern side of each basin below

about 35°N. Each of these regions is dominated in the monthly mean by high pressure which in January is centred close to the eastern coast at about 30°N in each basin (Figures 6.1a and 6.3a). In July the high pressure region is broader and is positioned further northwards and offshore (Figures 6.2a and 6.4a). In all but the North Atlantic in January the region of peak subtropical stratocumulus occurrence is to the south east of the high pressure region (Figures 6.1b, 6.2b. 6.4b). In the North Atlantic (Figure 6.3b) there is a peak of occurrence in the centre of the high pressure region and the occurrence off the coast of Morocco is much lower than in the summer and positioned to the south west of the centre of the high pressure. We will firstly compare the three most distinct regions of subtropical stratocumulus (North Pacific in both January and July and the North Atlantic in July) and contrast this with the much less persistent region of stratocumulus off the coast of Morocco in January. Table 6.1 summarises conditions associated with the occurrence of subtropical stratocumulus for the four cases considered. Conditions for three days upstream, at the peak occurrence of the stratocumulus, and five days downstream are considered using trajectories derived from the monthly mean wind field. Although this monthly averaged wind field may never exist, steady conditions associated with the subtropical high pressure and trade wind regions (the trade wind circulation is present 80 - 90 % of the time, Riehl 1979) means that the monthly mean trajectory should represent typical conditions associated with an air mass.

In January, monthly mean conditions in the North Pacific (Figure 6.1a) are characterised by a relatively small Pacific high pressure region with a centre positioned close to the California coast (30°N, 130°W) and elongated to the west. The region of peak stratocumulus occurrence occurs to the south east of the centre of the high. In July (Figure 6.2a) the high pressure region is broader and centred at about 35°N, 150°W. The pressure field in the North Atlantic is similar; in January (Figure 6.3a) the Azores high is narrow and centred around 35°N, 20°W, in July (Figure 6.4a) it is broader and centred at 35°N, 30°W. It seems likely that the positioning of the high pressure region near the coast in winter leads to the low stratocumulus occurrences in the subtropical North Atlantic in winter. The main difference among the properties quoted in Table 6.1 between the North Atlantic in January and the other three regions of more persistent subtropical stratocumulus is the low upstream relative humidity, less than 75% whilst the other regions are between 75 to 90%. The geometry of the coastline and the positioning of the high pressure region mean that some of the air reaching the stratocumulus maximum will have come from either North Africa or Southern Europe. The occurrence of clear skies (Figure 6.3b) suggests dry air flowing westwards off the African continent and then forming shallow cumulus clouds further out to sea. This complicates the more steady progression from stratocumulus to cumulus seen in the other three cases as the air moves around the subtropical high. Looking separately at the

cloud progression for winds coming off Africa and for winds that have travelled exclusively over the ocean might help to simplify the picture although this has not been done here.

The upstream conditions presented in Table 6.1 can be used to define typical conditions associated with the stratocumulus to cumulus transition. In the monthly mean, air reaching the region of peak stratocumulus occurrence has experienced an SST gradient of between 1.6 and 2.5 °C day^{-1}, a wind speed between 6.5 and 9.0 ms^{-1} and a near surface relative humidity between 76 and 88%. Sea-air temperatures are likely to be between 0.2 and 1.0°C although further upstream conditions are stable in the July North Pacific case. Upper air data taken from the NCEP reanalysis suggest that upstream the subsidence rate is between -0.002 and -0.008 ms^{-1}, the relative humidity at 700 mb is between 25 and 45% and the potential temperature gradient ranges from 0.0045 to 0.006 Km^{-1}. Where the subtropical stratocumulus are most persistent the SST is about 19°C in the North Pacific and 24°C in the North Atlantic. Downstream, wind speeds and sea-air temperature differences are more variable, but most of the other variables show consistent changes. The SST continues to rise, but at a slower rate; the near surface relative humidity is between 75 and 84% ; and the subsidence rate decreases. The relative humidity at 700 mb increases as does the potential temperature gradient between 700 and 500 mb. The datasets shown do not contain inversion height or the temperature and humidity jumps across the inversion which will be taken from the literature. The data shown in Figures 6.1 to 6.4 will guide the choice of external forcing in the simulation of the stratocumulus to cumulus transition described in the following section.

6.3 Model Simulation of the Transition

6.3.1 Model Initialisation and Environmental Conditions

The model described in Chapter 4 and tested in Chapter 5 will now be used to examine the stability of stratocumulus layers and simulate the stratocumulus to cumulus transition. The simulation is initialised with a well-mixed boundary layer with 80% near surface relative humidity and θ_l of 10.5 °C. The initial sea-air temperature difference is 1.3°C and the wind speed is 7.8 ms^{-1} (both as in Wyant et al. 1997) from northeast to southwest and the model column is assumed to translate with this speed. The inversion height is set at 600 metres (again following Wyant et al. 1997) and θ_l increases by 9°C and the q_t decreases by 3.5 gkg^{-1} across the inversion. q_t decreases above the inversion at a rate of 0.5 $gkg^{-1}km^{-1}$. There is no wind shear across the inversion. The θ_l gradient above the inversion is set to 0.006 °Cm^{-1}. The radiation is calculated for the position 50°N, 30°W and for mid June, the simulation starts on Julian day 164 (June 13th). To isolate the effects of

diurnal decoupling from the effects of deepening decoupling, daytime diurnally averaged values of solar radiation are used. Using the average of only daytime values gives the best agreement between simulations with and without the daily solar cycle (Hanson and Gruber 1982). The effect of the diurnal cycle on simulations is discussed in Chapter 7. The SST gradient was set to 1.5 $°Cday^{-1}$. The profile of vertical velocity is the same as that used by Wyant et al. (1997): a constant divergence of $3x10^{-6}s^{-1}$ is set in the boundary layer and the vertical velocity calculated by integrating this divergence from the surface. The vertical velocity above the inversion is set to the value at the inversion. Thus the vertical velocity at the inversion and above increases at the same rate as the boundary layer growth in height. This was found necessary to suppress the boundary layer growth in the latter part of the simulation. The effects of vertical velocity on the simulation are discussed in Chapter 7. The θ_l and q_t profiles above the inversion are relaxed to their original profiles with a timescale of 8 hours and 3 hours respectively. This in effect holds q_t close to its original value above the rising inversion height but allows θ_l to warm with time. Some relaxation is required, particularly in the latter part of the simulation since the large vertical velocities imposed would lead to very strong advective warming in this period. Although we do not expect the combination of radiative cooling, advective warming and the imposed relaxation to correctly predict the changes of temperature above the inversion (which are likely in the real world to be affected by differential advection) we note that the above inversion temperature is likely to increase along the trajectory (e.g. Albrecht et al. 1995b). Allowing an 8 hour timescale for the temperature relaxation allows some warming above the inversion, as observed. The evolution of the clouds is rapid in the cumulus under stratocumulus regime and the radiation needs recalculating frequently. In the stratocumulus regime rates of change are much smaller and the radiation can be recalculated less often. The model timestep is 5 seconds, the radiation scheme is run every 5 minutes for the first 6 days and thereafter every 30 seconds. The output shown is averaged over 10 minutes. The grid spacing is 10 metres throughout the 5 km domain. The simulation is run for 12 days.

6.3.2 The Simulated Boundary Layer Evolution

Figure 6.5 shows the simulated cloud fraction after 4 days (Julian day 168, Figure 6.5a) when the boundary layer is still solid stratocumulus, after 6 days (Julian day 170, Figure 6.5b) when the base of the stratocumulus has started to become ragged, after 7 days (Julian day 171, Figure 6.5c) when small cumulus are seen rising below a solid stratocumulus layer and after 11 days (Julian day 175, Figure 6.5d) when the cumulus cloud layer is much deeper than the stratocumulus layer at the boundary layer top. Note that for the first two days, 12 hours of simulation are shown, and for the last two days 6 hours of simulation. We shall refer to these particular days simulations as: stratocumulus (the 4th

day of simulation, Julian day 168), ragged stratocumulus (the 6th day of simulation, Julian day 170), shallow cumulus under stratocumulus (the 7th day of simulation, Julian day 171) and deeper cumulus under stratocumulus (the 11th day of simulation, Julian day 175). Figure 6.6 shows the TKE for the same periods as Figure 6.5.

In the stratocumulus case the boundary layer depth has increased over four days from the initial 600 metres to about 1000 metres and the cloud layer is about 400 metres deep (Figure 6.5a). Two days later the boundary layer depth has increased to about 1500 metres and the cloud layer has deepened (Figure 6.5b). The base of the stratocumulus is now more ragged and the cloud fraction decreases more gradually at the cloud base. Small undulations can now be seen in the cloud base with a period of about an hour. Just at the end of the twelve hour period presented, the first of the cumulus clouds appears below the stratocumulus layer. One day later the simulation predicts shallow cumulus under stratocumulus; the period between the appearance of each cumulus cloud is about an hour (Figure 6.5c, the plot now only shows six hours of evolution rather than twelve) and each cumulus cloud typically lasts for about fifteen minutes. The thickness of the solid stratocumulus at the boundary layer top is similar to that in the ragged stratocumulus case but the cloud thickness increases after each cumulus cloud injects water into the solid cloud layer and subsequently decreases. The cumulus clouds typically form at about 900 metres height, about 400 metres below the base of the solid cloud layer, which is about 400 metres thick. Four days later the boundary layer is just over 2500 metres deep and the solid stratocumulus layer has thinned to between 200 and 350 metres thick (Figure 6.5d). Variability is large in this part of the simulation. The size of the cumulus clouds is more variable and the initial height of formation varies by about 250 metres. The thickening of the solid cloud layer as the cumulus clouds detrain more liquid water into the cloud is more pronounced. Although the upper cloud deck has not broken, we can see that the cumulus clouds beneath dominate the boundary layer. Running the simulation for longer does not lead to the solid stratocumulus layer breaking up. The simulation continues to become more variable but the cloud cover remains full.

Looking now at the accompanying TKE (Figure 6.6) we again see that the profiles increase in variability with time. Some variability can be seen in the stratocumulus case (Figure 6.6a) with a decrease in TKE throughout the cloud layer and part of the subcloud layer following each entrainment event (where the boundary layer grows in height by one grid level). The period of these variations is a little over an hour. The variability increases and remains periodic in the ragged stratocumulus case (Figure 6.6b), the incloud TKE has increased and each entrainment event is clearly seen in the TKE profile. The TKE in the subcloud layer has decreased as the boundary layer decouples. In the shallow cumulus

under stratocumulus case (Figure 6.6c), TKE is even more variable, with stronger peaks in TKE preceding entrainment. The TKE below the solid cloud layer now becomes more complex. Entrainment is driven by incloud processes as before, but the rising of individual cumulus clouds into the solid cloud layer can also cause boundary layer deepening. In this stage of the simulation small amounts of TKE can be seen above the boundary layer. This is thought to be due to the breakdown of the Rotta (1951) energy redistribution assumption in the highly convective conditions where buoyancy is important (Moeng and Arakawa 1980). The effects also include a spurious negative flux of q_t and θ_l just above the inversion. This leads to a well mixed temperature region and a slight decrease in total water content in the region just above the inversion. Moeng and Arakawa (1980) remove this effect by arbitrarily setting the fluxes to zero above the inversion. This has not been done in the present study although the TKE has been relaxed to zero above the inversion to ensure that any mixing above the inversion decays rapidly. Similar well-mixed temperature profiles and humidity minima are seen above the inversion in the simulation of Krueger et al. (1995a). Figure 6.6d shows the TKE for the deeper cumulus under stratocumulus case.

Figure 6.7 shows 12 hours of boundary layer evolution of θ_l (Figure 6.7a), q_t (Figure 6.7b), radiative heating (Figure 6.7c) and cooling (Figure 6.7d), liquid water content (Figure 6.7e) and the fluxes of q_t (Figure 6.7f), θ_l (Figure 6.7g) and buoyancy (Figure 6.7h) for the stratocumulus case. The boundary layer is warming at all levels, keeping roughly in step with the SST increase of 1.5 °C day^{-1}. Just below the inversion θ_l increases slightly more rapidly than in the rest of the boundary layer due to the entrainment of potentially warm air from above the inversion. During this twelve hour period the boundary layer depth grows by about 100 metres, from just over 1000 metres to about 1100 metres in distinct entrainment steps. Each step increase in the inversion height is accompanied by a noticeable decrease in q_t just below the inversion that modulates the steady increase in q_t throughout the boundary layer. The cloud thickness remains constant at about 400 metres. The radiative cooling and solar heating profiles remain uniform throughout this part of the simulation with the peak of the daily average longwave cooling at the cloud top about 1.5 °C h^{-1} and the warming at the cloud base just under 0.5 °C h^{-1} (red line, Figure 6.11). The daily average peak shortwave heating is also about 0.5 °Ch^{-1}. Peak liquid water content is about 0.6 gkg^{-1}. The flux of q_t is about 0.035 ms^{-1} with slight maxima accompanying each entrainment event. Just after entrainment the surface buoyancy flux increases in response to the drying of the boundary layer. This plot clearly shows the slightly negative flux values above the inversion that are attributed to the same breakdown in assumptions that causes the spurious TKE above the inversion. These erroneous values remain much smaller than the boundary layer fluxes throughout the simulation and do not seem to impact on the results. The θ_l flux falls to zero just below the cloud base but the buoyancy flux remains positive throughout the boundary

layer. Each entrainment event reduces the θ_l flux and promotes the minima in this flux below the cloud layer. This flux minimum becomes more pronounced during the 12 hours and near the end of the period the flux remains negative below the cloud base at all times.

Two days later on the 6th day of simulation (Julian day 170, Figure 6.8) the θ_l and q_t profiles have started to become stratified below the cloud base. Daily average profiles are shown in Figure 6.11, the green profiles represent this particular day. The boundary layer is now moistening near the surface and drying out within the cloud. The peak liquid water content is still about 0.6 gkg^{-1}. Although the cloud layer is starting to become decoupled from the subcloud layer (see the negative buoyancy flux below the cloud base) the entrainment drying still acts to promote an increased surface water flux. The heat flux is now negative over nearly 1000 metres depth. Just at the end of the 12 hour period shown, the first cumulus cloud forms. The shallow cumulus under stratocumulus regime will be discussed later. Figure 6.11 shows that the radiative heating and cooling profiles are similar in magnitude during this period to those from the stratocumulus case.

One day later in the simulation (Julian day 171, Figure 6.9) the evolution is strongly variable due to the effect of individual cumulus clouds. Figure 6.9 shows 6 hours of evolution (half that of the previous figures). The stratification in θ_l is now even stronger (Figure 6.9a, see also the dark blue lines in Figure 6.11). The formation of each cumulus cloud occurs at the top of the surface mixed layer where a small humidity inversion strengthens as the surface mixed layer moistens in this strongly decoupled boundary layer. Once a cloud has formed and liquid water is present, radiative processes become important in the subcloud region (Figure 6.11). The feedback between the radiative processes and the liquid water content make the profiles of these quantities, and also the heat and buoyancy fluxes, highly variable and they look noisy[8]. It should be noted that a bulk radiation scheme would be unlikely to perform well under these conditions. The cloud, once formed, grows both upwards (as the subcloud layer is conditionally unstable) and downwards (as the surface layer moistens) until it is buoyant enough to rise and detrain its moisture into the stratocumulus layer above. This sometimes happens in two phases with the upper and lower portions of the cloud rising successively. The cloud draws water from the surface layer as it rises and the cloud layer is both moistened and cooled by the cumulus cloud as it rises into

---

[8] Some of the contour plots look very step-like. This is because of the combination of horizontal and vertical resolution of the data. In the vertical the resolution is 10 metres and the cumulus cloud is well resolved. In contrast the ten-minute averaging required to make the output data of manageable size has not fully captured the details of the evolution. It should be noted however that 120 timesteps and 20 runs of the radiation code are performed in each 10 minute averaging period and the evolution should be well defined within the ten minute period.

the main cloud layer. Each cumulus cloud warms and dries the surface layer. The TKE generated by the rising cumulus can lead to entrainment, four of the six cumulus clouds in this part of the simulation directly cause an increase in boundary layer height. The stratocumulus cloud layer is no longer drying out, the total water content is being maintained at an approximately constant level by the input of water from below.

After another four days (the 11th day of simulation, Julian day 175, Figure 6.10) the characteristics are similar to the shallow cumulus under stratocumulus case just described, but now the cumulus layer is much deeper. The increase in variability continues.

Figure 6.11 shows examples of daily averaged profiles from the simulation. The growth in the boundary layer and increasing stratification in both θ_l and q_t is clear. The cloud cover remains total throughout the simulation but the upper solid stratocumulus layer thins and cloud cover in the region below the stratocumulus increases with time. Once the cumulus under stratocumulus structure has developed (green line) the average height of the base of the cumulus clouds remains fairly constant leading to a large increase in the depth of the cumulus layer as the boundary layer height grows. The peak liquid water content decreases with time but the liquid water in the cumulus layer becomes almost as large as the stratocumulus cloud liquid water content by the end of the simulation. The integrated liquid water content in the cumulus under stratocumulus boundary layer is much greater than that in the stratocumulus boundary layer. Despite the reduction in cloud-top liquid water content the decrease in temperature of the cloud top means that the longwave cooling remains similar throughout the simulation, as does the shortwave heating.

Figure 6.12 shows timeseries of variables taken from different levels from the deeper cumulus under stratocumulus part of the simulation (Julian day 175). The levels represent the surface, subcloud (sub-stratocumulus layer but within the cumulus layer), cloud base and cloud top. In this deeper cumulus under stratocumulus part of the simulation the growth in the inversion height and cloud top height is strongly controlled by entrainment generated by the cumulus clouds rising into the stratocumulus cloud layer (Figure 6.12a). All levels from the subcloud layer upward increase in q_t, typically by 0.5-1.0 gkg^{-1}, with the dissipation of each cumulus cloud (Figure 6.12b). The surface layer dries by a smaller amount. Peaks in the cloud top liquid water content of about 0.2 to 0.4 gkg^{-1} follow each sharp spike in the cumulus layer liquid water content (Figure 6.12c) which are of similar size to the total water peaks in this region. The cloud base liquid water content varies little, reflecting the change in cloud base height with each injection of cumulus liquid water. The boundary layer is still warming under the influence of the increasing SST and increasing entrainment by 1.8 °C during the day, suggesting that entrainment has warmed the boundary

layer by about 0.3 °C (Figure 6.12d). The dissipation of each cumulus cloud leads to a cooling of about 0.2 °C in the upper part of the boundary layer as cooler surface air is mixed upwards. The surface layer correspondingly warms. Peaks in TKE up to 0.8 m^2s^{-2} due to cumulus activity occur at all levels except the surface (Figure 6.12e). The increase in cloud top longwave cooling with each cumulus detrainment is clear and the subcloud longwave cooling also shows the effects of individual cumulus clouds (Figure 6.12f). The cloud base warming is increased by the increase in liquid water but the effect is smoothed by the moving height of the cloud base through the day. The peaks in solar heating become progressively smoother with height (Figure 6.12g). The fluxes of q_t, θ_l and buoyancy are consistent with the changes in θ_l and q_t generated by the cumulus clouds (Figures 6.12h-j).

Later in the simulation, a progression to broken cloud cover would be expected. This did not happen, the cloud at the top of the boundary layer remains complete. The model does not simulate the final part of the transition to cumulus clouds but remains in a cumulus under stratocumulus regime. This is possibly due to the way that the clouds are parameterised (Section 6.3.4) or to the lack of precipitation in the model.

6.3.3 Using Tracers to Understand the Modelled Boundary Layer Evolution

In order to understand and quantify how the processes in the boundary layer evolve with time, tracers have been added to the simulation. We have used a surface layer tracer to indicate how properties from the surface layer are mixed throughout the boundary layer. The tracer is re-initialised every day to show how the mixing evolves. On initialisation the tracer has value one in the lowest 10% of the boundary layer and zero elsewhere. The value of the tracer is held at one at the bottom boundary allowing a flux of tracer into the boundary layer. This tracer is therefore non-conservative, but will track the influence of surface layer processes at higher levels in the boundary layer. With this tracer we can monitor the degree of homogeneity of the boundary layer and examine how the surface layer properties are transferred into the cloud layer. The second tracer is a free atmosphere tracer and shows the amount of entrainment of above inversion air into the boundary layer. On initialisation this tracer has value one above the inversion height and zero below. This tracer is also not conservative due the effects of vertical advection. The relative importance of mixing from the surface and from above the inversion can therefore be determined as a function of time using the tracers. Each tracer is transported using the same form of predictive equation as for the heat transport (equation 4.6) but source terms are set to zero. Both tracers are reinitialised at the start of each day.

Figure 6.13 shows the evolution of the surface tracer for the first 6 hours of the same days as presented in Figures 6.5 to 6.10. In the stratocumulus case (Figure 6.13a) the surface tracer does not form sharp gradients in the vertical although the continued input in tracer concentration at the surface during the day ensures the tracer does not become fully mixed throughout the boundary layer. The peak tracer concentration at the inversion at the end of 6 hours simulation is 0.17. In the ragged stratocumulus case (Figure 6.13c) the decoupling has started and a vertical tracer gradient is set up at cloud base with less surface tracer reaching the cloud layer. The surface tracer reaching the cloud layer is well mixed within the cloud layer. The tracer concentration at the inversion after 6 hours simulation is less than 0.12. In the shallow cumulus under stratocumulus case (Figure 6.13e) the effect of the individual cumulus clouds on the tracer concentration is marked. The tracer concentration in the cloud increases in steps and the tracer concentration reaches slightly less than 0.1 after 6 hours. A sharp vertical gradient in the surface tracer concentration is seen at the top of the surface mixed layer at about 800 metres height. The deeper cumulus under stratocumulus case (Figure 6.13g) shows less than half the surface tracer reaching the stratocumulus cloud layer than in the shallow cumulus under stratocumulus case and the vertical gradients are again stronger. This is also demonstrated in Figure 6.14 which shows tracer concentrations for these four days at levels defined using the same criteria as used in Figure 6.12.

Figure 6.13 also shows the distribution of entrainment tracer for 6 hours of each of these four selected days. In the stratocumulus case (Figure 6.13b) there is an approximately uniform gradient of entrainment tracer distribution throughout the boundary layer, only later in the ragged stratocumulus case (Figure 6.13d) is the subsequent mixing of cloud layer air into the subcloud layer inhibited, causing a gradient in entrainment tracer near the cloud base. Once the cumulus activity starts, the mixing of entrainment tracer to the surface is reduced and occurs intermittently (Figures 6.13 f and h). Figure 6.15 shows timeseries similar to those in Figure 6.14 but for the entrainment tracer within the boundary layer. The amount of entrainment tracer reaching the surface layer per day decreases throughout the simulation, by 40% between the stratocumulus and the deeper cumulus under stratocumulus cases. The entrainment tracer concentration below the inversion increases through the simulation. Peaks in the concentration in the cumulus under stratocumulus part of the simulation indicate entrainment events driven by cumulus rising into the stratocumulus layer. The boundary layer growth is approximately constant with time in this latter period and the vertical velocity at the inversion height is increasing. The entrainment rate must therefore also be increasing. The increase in entrainment tracer concentration below the inversion therefore results from an increase in entrainment and not just a reduction of mixing to lower levels.

6.3.4 The Effect of the Cloud Parameterisation on the Simulation

The failure of the simulated stratocumulus layer to break up under external forcing which would be expected to give rise to a stratocumulus to cumulus transition needs to be explained. One possible reason for this is the method of cloud parameterisation used, this will be discussed in this section. Another possible reason is the omission of precipitation, this is discussed in Section 7.2.1.

The cloud and liquid water parameterisations of Mellor (1977) and Sommeria and Deardorff (1977) are discussed by Bechtold et al. (1995), Cuijpers and Bechtold (1995) and Bechtold and Siebesma (1998). Bechtold et al. (1995) suggest that both stratocumulus and deep convective cumulus clouds can be modelled with the same cloud model. The Gaussian distribution represents variability of q_t and θ_l within stratocumulus clouds, but an exponential distribution is more appropriate for the skewed distribution within cumulus clouds. Bechtold et al. (1995) interpolate between these two distributions using the normalised saturation deficit (Section 4.5.1) to determine the type of distribution. In the present simulation, the cumulus clouds beneath the stratocumulus layer are well simulated, it is in the later, more convective stages that a specific cumulus parameterisation would be required. Bechtold et al. (1995) introduce their cumulus type distribution only where the grid level is unsaturated. In the present simulation the stratocumulus layer remains saturated throughout. An explicit cumulus parameterisation will therefore not help to break up the solid stratocumulus deck in the present study.

Cuijpers and Bechtold (1995) used LES to test a cloud parameterisation similar to that of Bechtold et al. (1995) and find that their parameterisation of σ_s (using an expression similar to equation 4.51) works well in predicting the cloud amount and liquid water content. σ_s is parameterised both by Bechtold et al. (1995) and in the present study as proportional to the gradients of θ_l and q_t (equation 4.51). Where there are strong gradients the predicted σ_s is large, but in well mixed regions it is close to zero. In regions of strong gradients the cloud parameterisation can predict partial cloud fraction over a wide range of under and oversaturated conditions. In well mixed regions however the parameterisation is in effect switched off and the predicted cloud cover is 1 in saturated conditions or 0 in unsaturated conditions. This causes a problem predicting the breakup of a stratocumulus layer. Near the stratocumulus cloud top, longwave cooling is strong which promotes mixing at the cloud top. The region below the inversion is therefore always well mixed and the cloud parameterisation cannot predict broken cloud. If the air near the top of the boundary layer is in the mean saturated, the cloud cover will always be full. The cloud fraction is used in the equation to predict liquid water content (equation 4.47) and therefore if σ_s is underestimated

in these conditions the liquid water will be overestimated, leading to stronger longwave cooling and more mixing. There is variability with time in liquid water content, q_t and θ_l near the cloud top (Figures 6.12b-d). It seems unlikely therefore that the true value of σ_s should be near zero in this region, despite the cloud top profiles being, in the mean, well mixed.

Cuijpers and Bechtold (1995) simulate four different boundary layers initialised with between 8% and 98% cloud cover and with mean profiles from experiments. Their cases with low cloud cover are initialised with strong gradients in both liquid water potential temperature and total water content within the cloud layer, their cases from ASTEX and FIRE have more nearly well mixed profiles. The types of profiles used by Cuijpers and Bechtold (1995) would mean that the parameterisation could predict broken cloud since in-cloud gradients of temperature and humidity were imposed on initialisation. However, in the present simulation of the stratocumulus to cumulus transition, the boundary layer in the stratocumulus regime is well mixed under a sharp inversion. As the transition progresses, the profiles of liquid water potential temperature and total water content become stratified, except in the surface mixed layer and near the cloud top (where the presence of liquid water generates mixing through longwave cooling). This well mixed layer at the cloud top means that the cloud parameterisation cannot predict a fractional cloudiness at the cloud top and thus unbroken stratocumulus is predicted. In these conditions the cloud cover will remain total until the cloud layer dries enough to become unsaturated throughout. The stratocumulus layer will then disappear. It is possible that the prediction of near zero incloud variance in the well mixed region near the cloud top leads to the failure of the cloud layer to break up, although including precipitation in the simulation would help. An attempt was made to use the model variability of the incloud parameters to estimate σ_s but this degraded the representation of the cumulus clouds below the main stratocumulus layer.

6.4 Comparison with Observations and with Models

6.4.1 The Evolution of Near Surface Variables

The simulation described in Section 6.3 lasts for 12 days, much longer than other simulations with one-dimensional models from the literature. For simulations of this length we can gain an integrated measure of the model performance by comparing the evolution of near surface variables with those typically observed (Section 6.2). A climatologically realistic SST gradient has been imposed which drives the growth of the boundary layer. The wind speed has also been imposed. The response of the model boundary layer to this forcing can be compared to the observations presented in Section 6.2 and the upstream and

downstream conditions from the monthly mean trajectories presented in Table 6.1. It should be noted that the observations from ship data become sparse below about 20°N, particularly in the North Pacific. The observed values in the later part of the transition region will therefore be noisy and perhaps not particularly reliable (Kent et al. 1999a,b).

The initial sea-air temperature difference was 1.3 °C, for the first two days the temperature difference rises, reaching a maximum of over 1.8 °C then reduces gradually for the remainder of the simulation. At the end of the simulation the sea is 0.4 °C warmer than the air. The observations do not show a clear trend in sea-air temperature difference but the simulated values are within the range observed in the regions shown in Figures 6.1a-6.4a. The near surface relative humidity reaches a maximum of 90% after one days simulation and decreases steadily thereafter. By the end of the simulation the relative humidity is slightly over 50%, much less than the minimum of 75% suggested by the observations. The surface sensible heat flux in the simulation follows the trend of the sea-air temperature difference. The values are small, the peak value is 16 Wm^{-2} and the final value is less than 3 Wm^{-2}. The observations suggest that the surface sensible heat flux should be between about 0-10 Wm^{-2}, again there is no clear trend in the four regions with time. The observations do show an increasing latent heat flux along the transition, the peak value is about 150 Wm^{-2}. This value of surface latent heat flux is predicted in the simulation after 6 days, the latent heat flux continues to rise throughout the simulation, reaching 300 Wm^{-2} by the end of 12 days. Thus the drying of the simulated surface layer is more than that expected from the observations, even though the stratocumulus cloud layer does not dissipate throughout the simulation. Thus it seems that the cumulus clouds in the simulation are too efficient at recoupling the surface and cloud layers and the vertical humidity gradient may not be as large as in the real boundary layer. This may be caused by the presence of the cumulus-coupled regime after the transition to scattered cumulus would have been expected.

6.4.2 The Stratocumulus-topped Boundary Layer (up to day 5)

The model simulation of the stratocumulus-topped boundary layer was tested in Section 5.3. The boundary layer is well mixed (Nicholls and Leighton 1986) and the inversion is sharp, typically 10 - 20 metres (1-2 grid levels in thickness). Measurements of the inversion structure and thickness are difficult to make as radiosondes do not have adequate resolution. Tethered balloon measurements of the inversion above a stratocumulus-topped boundary layer over land (Roach et al. 1982) suggest that the inversion above stratocumulus is indeed as sharp as in the simulation. The surface relative humidity in the stratocumulus regime is 80-90%, typical of observed values in marine stratocumulus regions (Figures 6.1 to 6.4). The TKE in this region is larger in the cloud layer than near the

surface but no minimum in TKE is observed, suggesting that the boundary layer is well mixed throughout (Figure 6.6). Similar structure was noted by Albrecht et al. (1985) in solid stratocumulus off the coast of California. The liquid water potential temperature flux becomes slightly negative below the cloud base following each entrainment event, suggesting that the boundary layer will not remain well mixed for much longer (Figure 6.7) but the buoyancy flux remains positive throughout the boundary layer. Stratocumulus-topped boundary layers with weak and intermittent decoupling are common over the oceans (Businger and Shaw 1984, Nicholls and Leighton 1986). The boundary layer depth which grows from 600 metres to over 1000 metres in this period is typical of those found in stratocumulus regions off the coast of California (Neiburger et al. 1961) and in the subtropical Atlantic (Riehl 1979). The inversion strength is maintained near the often observed value of 9 °C (Kuo and Schubert 1988) reducing slightly through the stratocumulus period. Initially the total water content drops by 3.5 gkg^{-1} over the inversion, this increases to about 7 gkg^{-1}, again in line with observations (Kuo and Schubert 1998).

6.4.3 The Cumulus-Coupled Boundary Layer (days 6 to 12)

Studies of cumulus rising into stratocumulus are largely limited to ASTEX (Albrecht et al. 1995a, Martin et al. 1995, Wang and Lenschow 1995, deRoode and Duynkerke 1996;1997, Martin et al. 1997) although these conditions were also common during JASIN 1978. The simulations of Krueger et al. (1995a,b) and Wyant et al. (1997) described in Section 3.5 model this regime.

Bretherton and Pincus (1995) describe mean conditions from the two ASTEX Lagrangian experiments. In the first Lagrangian experiment the boundary layer evolved from shallow stratocumulus to cumulus under stratocumulus in 36 hours in response to a rapidly increasing SST. The temperature difference across the inversion was 2-4 °C and initially there was no humidity decrease across the inversion. As the boundary layer grew in height from about 1 km to 2 km the humidity inversion increased. In the second Lagrangian experiment little change in structure was observed throughout the 36 hours. Cumulus under stratocumulus was observed throughout this period. The temperature increase across the inversion was 6-8 °C and the humidity difference between the surface layer and the cloud layer was 2-3 gkg^{-1}. The humidity above the inversion was highly variable. During both Lagrangian experiments the sensible heat fluxes were small, less than 10 Wm^{-2}, and the latent heat fluxes were 100 - 150 Wm^{-2}, increasing with time (Bretherton et al. 1995). The simulation agrees fairly well with the observations from the second Lagrangian experiment. Figures 6.9 and 6.10 show the total water content difference between the surface layer and the cloud layer rise from about 1.5 gkg^{-1} to about 3 gkg^{-1}. The temperature increase across

the inversion in the simulation is 7 °C in this part of the simulation, in agreement both with the value from the ASTEX second Lagrangian experiment and with Kuo and Schubert (1988). The humidity decrease across the inversion of about 6 gkg^{-1} is also reasonable (Kuo and Schubert 1988). There is a difference of about 6 gkg^{-1} in total water content between the surface layer and the cloud layer (Figure 6.11). The sensible and latent heat fluxes are comparable with the observations at the beginning of the cumulus-coupled part of the simulation, but as noted in Section 6.4.1 the latent heat fluxes rise to much greater values by the end of the simulation.

Albrecht et al. (1995a) suggest that decoupling in response to the growing boundary depth forced by the increasing SST is the mechanism for the transition from stratocumulus to cumulus. The simulation shows that the boundary layer starts to become decoupled when it is about 1500 metres deep. The boundary layer grows steadily deeper with the surface layer remaining about 750 to 1000 metres deep. As the boundary layer height grows the region of negative buoyancy flux above the surface layer also becomes deeper, promoting the decoupling. The transition layer between the surface and the cloud layers is conditionally unstable, the buoyancy effect of moisture is required to couple the surface and cloud layers, the role of the cumulus. This cumulus-coupled boundary layer was often observed in ASTEX and the cloud reporting code for cumulus under stratocumulus is the most commonly observed in the ASTEX region. Cumulus-coupled boundary layers were also predicted in the simulations of Krueger et al. (1995a,b) and Wyant et al. (1997) although they do not present the details of individual cumulus interactions with the cloud layer as in the present study. In addition this study shows that cumulus convection under a stratocumulus layer can be successfully modelled without explicitly resolving individual updrafts and downdrafts.

Albrecht et al. (1995a) present a time section of water vapour with a schematic of the observed cloudiness superimposed, from the first ASTEX Lagrangian experiment. Approximately 4 cumulus clouds are observed per day, many less than in the present simulation. The time section has been generated from aircraft profiles and it is possible that any smaller cumulus are missed by the aircraft sampling (as the sampling by the aircraft is not Lagrangian). The water vapour profiles do however show that the clouds usually act to dry the surface layer as in the simulation.

Martin et al. (1995) present aircraft measurements taken in a cumulus under stratocumulus boundary layer during ASTEX both within the stratocumulus layer and within the cumulus layer. Fluctuations in total water content associated with the cumulus clouds are about 2 gkg^{-1}. On day 11 of the simulation (Figure 6.12b) the total water fluctuations are about 1 gkg^{-1} peak to peak. Fluctuations in total water content in the stratocumulus

associated with cumulus penetration of the stratocumulus layer are typically 0.5 gkg^{-1} peak to peak, similar to those simulated. Observed liquid water fluctuations in the stratocumulus layer associated with the cumulus clouds are about 0.2 gkg^{-1} peak to peak, again similar to the simulated cloud top variations in liquid water content (Figure 6.12c).

Miller and Albrecht (1995) use 94 GHz radar to map stratocumulus interaction with cumulus during ASTEX. They show three one-hour periods of backscatter intensity from a day when cumulus under stratocumulus and a decoupled stratocumulus-topped boundary layer was observed. During the nighttime, cumulus convection is not present and circulation cells with period of 1 hour are observed in the stratocumulus-topped boundary layer. This timescale is similar to that seen in Figures 6.7 and 6.8 in the stratocumulus layer before the cumulus clouds appear. In the remaining two hours cumulus-stratocumulus interaction is seen, with two events occurring in each hour shown. The interaction periods when cumulus are present are between 10 and 30 minutes long, comparable to those shown in Figures 6.9 and 6.10.

Wang and Lenschow (1995) use conditional sampling of regions which are cumulus-coupled and those in which no cumulus are present beneath the stratocumulus to demonstrate the enhanced entrainment in cumulus-coupled regions. The impact of cumulus rising into stratocumulus on entrainment in the simulation is shown in Figures 6.9 and 6.10. The simulation also confirms the conclusions of Martin et al. (1995) that cumulus clouds will locally thicken the stratocumulus layer and increase liquid water content and optical paths, and that localised increases in q_t and equivalent potential temperature are observed when the cumulus penetrate the stratocumulus layer.

deRoode and Duynkerke (1997) examine the dynamics of the cumulus under stratocumulus and conclude that the turbulent transport of TKE is important in allowing the cumulus clouds to rise in the stratocumulus layer. This term is included in the present simulation but neglected in models of a lower order (Section 3.4.2). They also suggest that entrainment could be generated by the upward motions of the cumulus clouds, again as shown in the present study.

Aircraft measurements cannot fully sample a cumulus-stratocumulus interaction event such as is shown in the simulation. Flights at a constant level can sample many different small cumuli in the subcloud layer but a subsequent run at a different level is unlikely to sample the same cloud, which may well have dissipated in the intervening period. Thus the information provided by this simulation is different in character to that from aircraft sampling. Model data of this type could prove useful in interpreting aircraft data in the

highly variable cumulus under stratocumulus region. It is also noted that microphysical effects can be important in the interaction of cumulus and stratocumulus (e.g. Martin et al. 1997) and that drizzle is often observed during these conditions. These effects are not included in the simulations in the present study.

6.5 Summary and Discussion

The environmental conditions under which stratocumulus occurs or there is a transition to cumulus have been determined for January and July in both the North Atlantic and the North Pacific. Typical conditions have been used to initialise the model and for the external forcing. These conditions include: a wind speed of 7.8 ms^{-1}; a SST gradient of 1.5 °C day^{-1}; an inversion height of 600 metres; a decrease of 9°C in θ_l and an increase of 3.5 gkg^{-1} in q_t across the inversion; and a vertical gradient of θ_l of 0.006 °C m^{-1} above the inversion. The divergence used was $3x10^{-6}$ s^{-1} throughout. The use of a constant divergence in the simulation, although common in the literature (e.g. Krueger et al. 1995a,b and Wyant et al. 1997) leads to an unrealistic evolution of vertical velocity. This is however necessary for the simulation of the transition from stratocumulus to cumulus under stratocumulus. This is discussed in Chapter 7 where possible reasons for this requirement are given.

The simulation of the stratocumulus to cumulus transition is described in detail. The stratocumulus and cumulus under stratocumulus regimes are well simulated. The simulation shows cumulus clouds forming below the stratocumulus layer 6 days into the 12 day simulation and cumulus clouds of variable size, lifetime and base height forming approximately every hour thereafter. Whilst the variability in the simulated cumulus clouds is undoubtedly less than would be observed in reality a one-dimensional simulation would not be expected to reproduce large variability as spatial variability cannot be modelled. Later in the simulation, by day 11, the cumulus clouds are deeper and occur slightly less frequently on average. The liquid water in the stratocumulus layer remains fairly constant with the drying effect of entrainment approximately balanced by the input of water from the cumulus clouds. The model does not therefore simulate the shallow cumulus regime expected by the end of the simulation. This may be due to the lack of a precipitation parameterisation or to weaknesses in the Mellor-Yamada formulation for incloud variances.

The mechanism for the simulated transition from stratocumulus to cumulus under stratocumulus is that suggested by Albrecht et al. (1995a) whereby the boundary layer deepens under the increased surface forcing as the SST increases. Decoupling of the cloud and subcloud layers occurs when the surface forcing is no longer sufficient to keep the boundary layer well mixed, but the boundary layer height continues to grow through

entrainment generated by cloud processes such as longwave cooling. Eventually the surface layer moistens enough to allow small cumulus clouds to form at the top of the surface layer and the boundary layer becomes 'cumulus-coupled' (Krueger et al. 1995a). The cumulus clouds periodically inject moisture into the upper stratocumulus layer and can also promote entrainment of above inversion air into the boundary layer. The balance between the cumulus cloud moistening the cloud layer and drying the cloud layer by enhancing entrainment is seen in the simulation. The importance of CTEI cannot be determined in this one-dimensional simulation as the contribution of dense downdrafts to the turbulence and entrainment cannot be isolated from the contribution of buoyant updrafts. The model does include the processes required to represent CTEI. Krueger et al. (1995b) however show that in their simulation the relative importance of dense downdrafts originating near the cloud top decreases with time. This suggests that CTEI is not necessary to promote the transition. The simulated transition in the present study is not complete as the stratocumulus layer does not break up. This is attributed partly to the inability of the cloud parameterisation to predict broken cloud in well mixed conditions, such as those found just below an entraining cloud top, and partly to the lack of a drizzle parameterisation.

The next chapter will examine the effect of changing external forcing on the simulation of the stratocumulus to cumulus transition.

	North Pacific January	North Pacific July	North Atlantic January	North Atlantic July
upstream SST gradient	2.5 °C day^{-1}	1.7 °C day^{-1}	1.6 °C day^{-1}	1.7 °C day^{-1}
upstream wind speed	6.5 - 8.0 ms^{-1}	6.5 - 9.0 ms^{-1}	7.5 - 9 ms^{-1}	7.0 - 8.5 ms^{-1}
upstream relative humidity	78 - 84 %	84 - 88 %	73 - 75 %	76 - 80 %
upstream sea-air temperature difference	0.6 - 1.1 °C	-0.4 - 0.8 °C	0.6 - 1.0 °C	0.2 - 0.6 °C
upstream subsidence rate	-0.002 to - 0.004 ms^{-1}	-0.008 to - 0.004 ms^{-1}	-0.004 to - 0.003 ms^{-1}	-0.007 to - 0.004 ms^{-1}
upstream relative humidity at 700 mb	25 - 45 %	25 - 45 %	25 - 30 %	15% - 35 %
upstream θ gradient between 700 and 500 mb	0.005 Km^{-1}	0.005 - 0.006 Km^{-1}	0.005 - 0.006 Km^{-1}	0.0045 - 0.0055 Km^{-1}
SST	19 °C	19 °C	24.5 °C	24 °C
wind speed	6.5 ms-1	6.5 ms-1	8 ms-1	7.5 ms-1
relative humidity	78 %	84 %	75 %	80 %
sea-air temperature difference	1.0 °C	0.6 °C	1.0 °C	0.4 °C
subsidence rate	-0.004 ms^{-1}	-0.004 ms^{-1}	-0.003 ms^{-1}	-0.002 ms^{-1}
relative humidity at 700 mb	28 %	30 %	30 %	35 %
θ gradient between 700 and 500 mb	0.005 Km^{-1}	0.006 Km^{-1}	0.006 Km^{-1}	0.0055 Km^{-1}
downstream SST gradient	2.0 - 1.25 - 0.0 °C day^{-1}	2.2 - 1.7 - 1.0 °C day^{-1}	0.9 - 0.0 - ... °C day^{-1}	1.2 - 0.6 - 0.2 °C day^{-1}
downstream wind speed	6.5 - 8.0 ms^{-1}	6.0 - 7.5 ms^{-1}	7.5 - 9.7 ms^{-1}	7.5 - 5.0 ms^{-1}
downstream relative humidity	76 - 80 %	80 - 84 %	75 - 84 %	80 - 84 %
downstream sea-air temperature difference	0.8 - 1.0 °C	0.4 - 1.2 °C	1.0 - 0.4 °C	0.2 - 1.6 °C
downstream subsidence rate	-0.004 to - 0.002 ms^{-1}	-0.004 to 0.0 ms^{-1}	-0.003 to 0.002 ms1	-0.002 to 0.002 ms^{-1}
downstream relative humidity at 700 mb	28 - 38 %	30 - 45 %	30 - 50 %	35 - 50%
downstream θ gradient between 700 and 500 mb	0.005 - 0.0065 Km^{-1}	0.006 - 0.007 Km^{-1}	0.006 - 0.007 Km^{-1}	0.0055 - 0.007 Km^{-1}

Table 6.1: Upstream and downstream conditions for the region of peak occurrence of stratocumulus in the North Pacific and North Atlantic in January and July. Upstream conditions are for the previous three days, downstream conditions are for the following five days as calculated from the monthly mean wind field. Three downstream SST gradients are quoted and represent, the first two days, days three and four and day five respectively. In the North Atlantic in January the trajectory only lasts for three days before reaching land, only two SST gradients are thus shown.

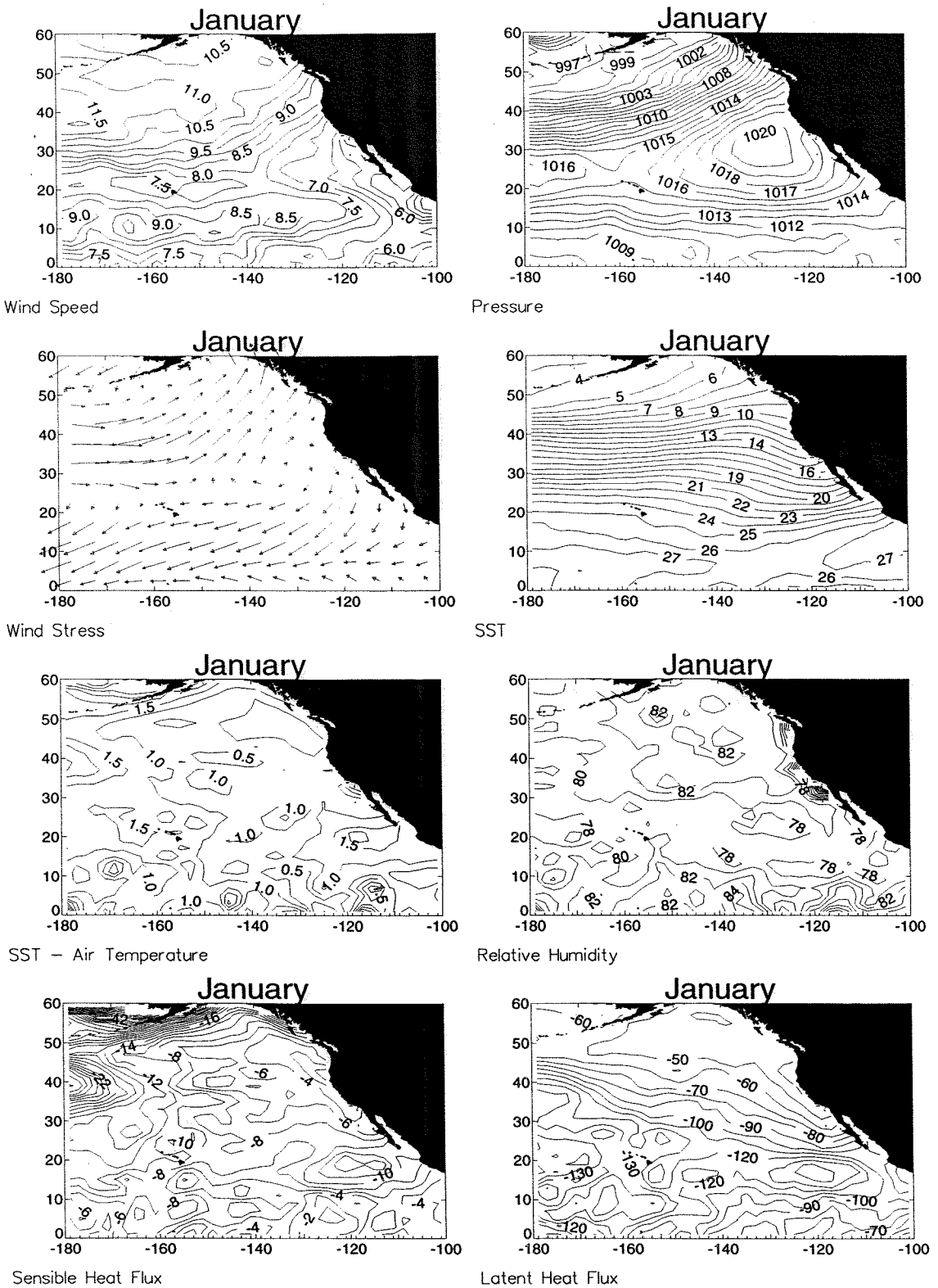

Figure 6.1a Monthly mean surface conditions for January in the North Pacific from the SOC Climatology.

top row: left: wind speed (ms^{-1}), right: pressure (mb)
second row: left: wind stress (Nm^{-2}), right: SST (°C)
third row: left: air-sea temperature difference (°C), right: relative humidity (%)
bottom row: left: sensible heat flux (Wm^{-2}), right: latent heat flux (Wm^{-2})

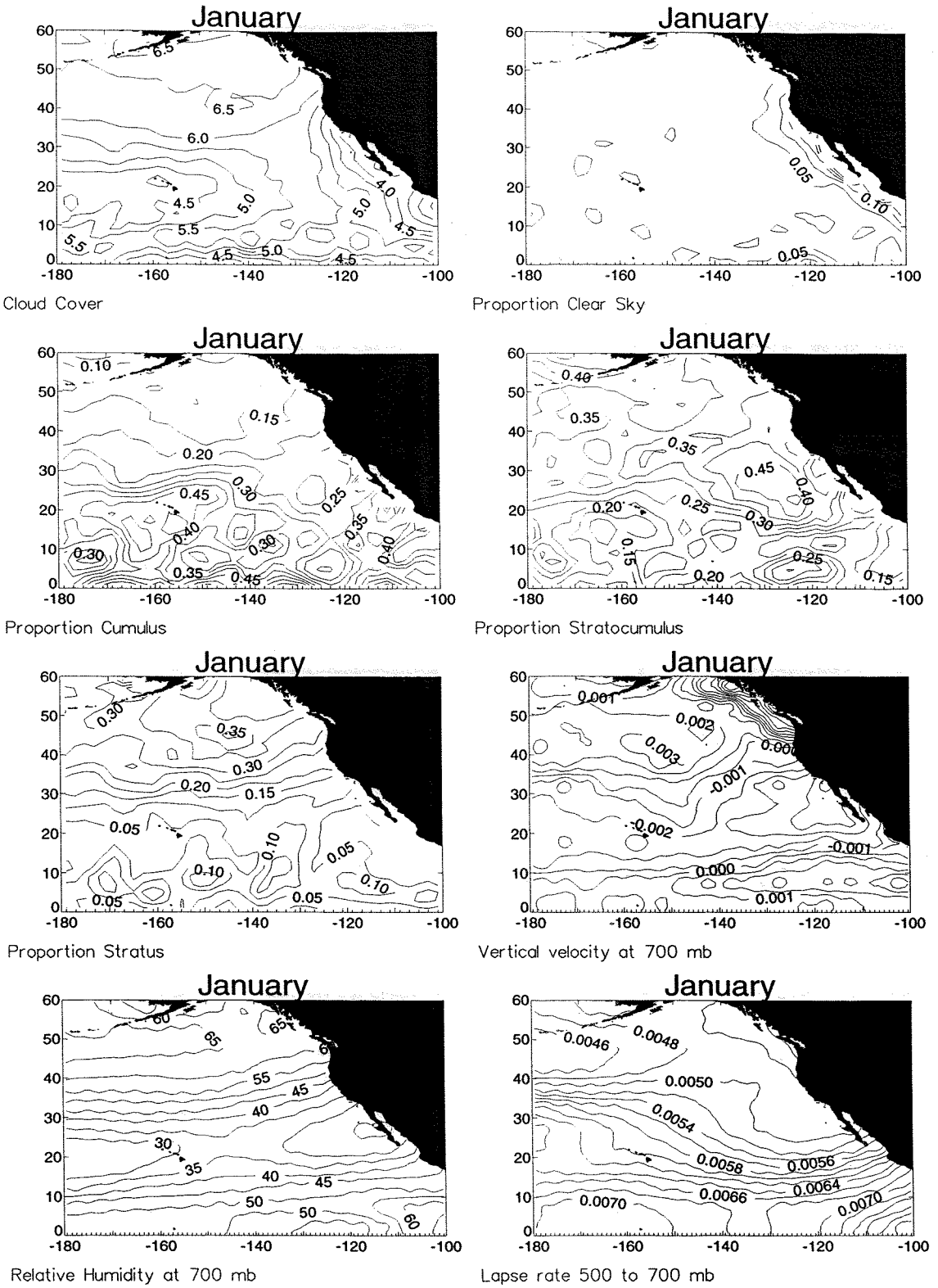

Figure 6.1b Monthly mean cloud (from COADS cloud reports) and upper air data (from the NCEP reanalysis) for January in the North Pacific.

top row: left: cloud cover (octas), right: proportion of clear sky
second row: left: proportion of cumulus, right: proportion of stratocumulus
third row: left: proportion of stratus, right: vertical velocity at 700 mb ($m\ s^{-1}$)
bottom row: left: relative humidity at 700 mb (%), right: lapse rate of θ between 500 and 700 mb (Km^{-1})

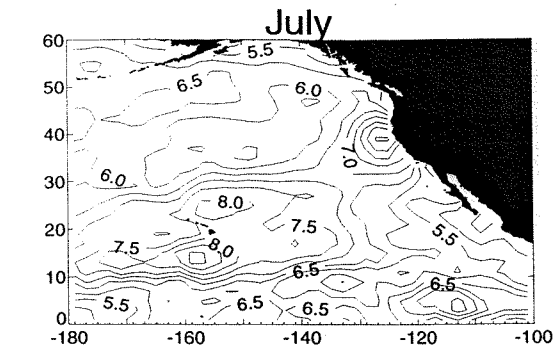

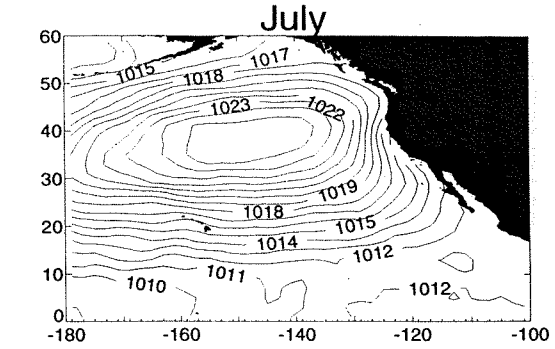

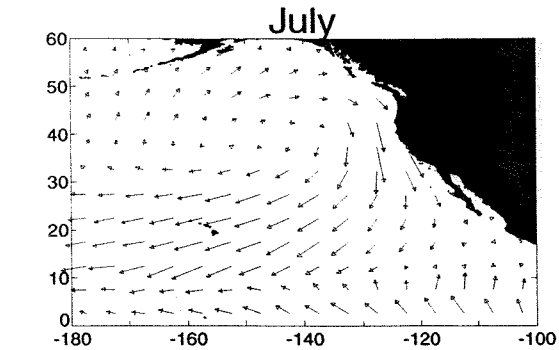

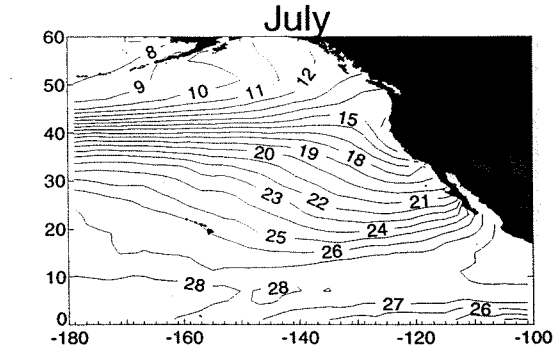

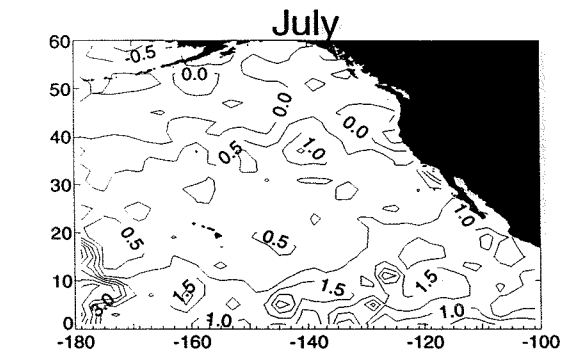

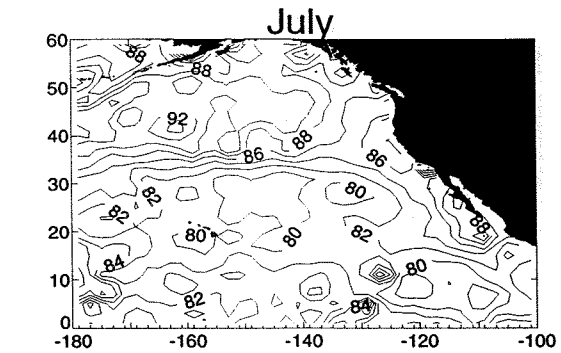

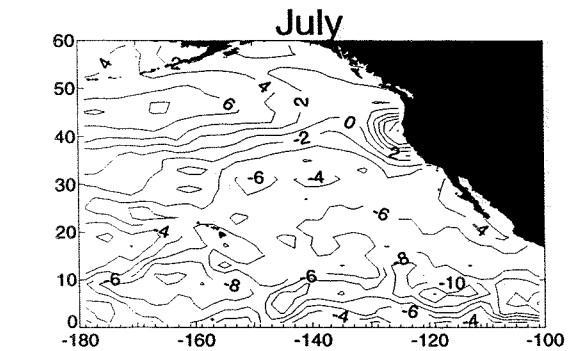

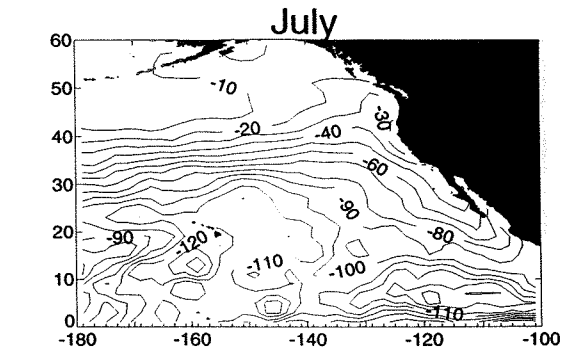

Figure 6.2a As Figure 6.1a but for July.

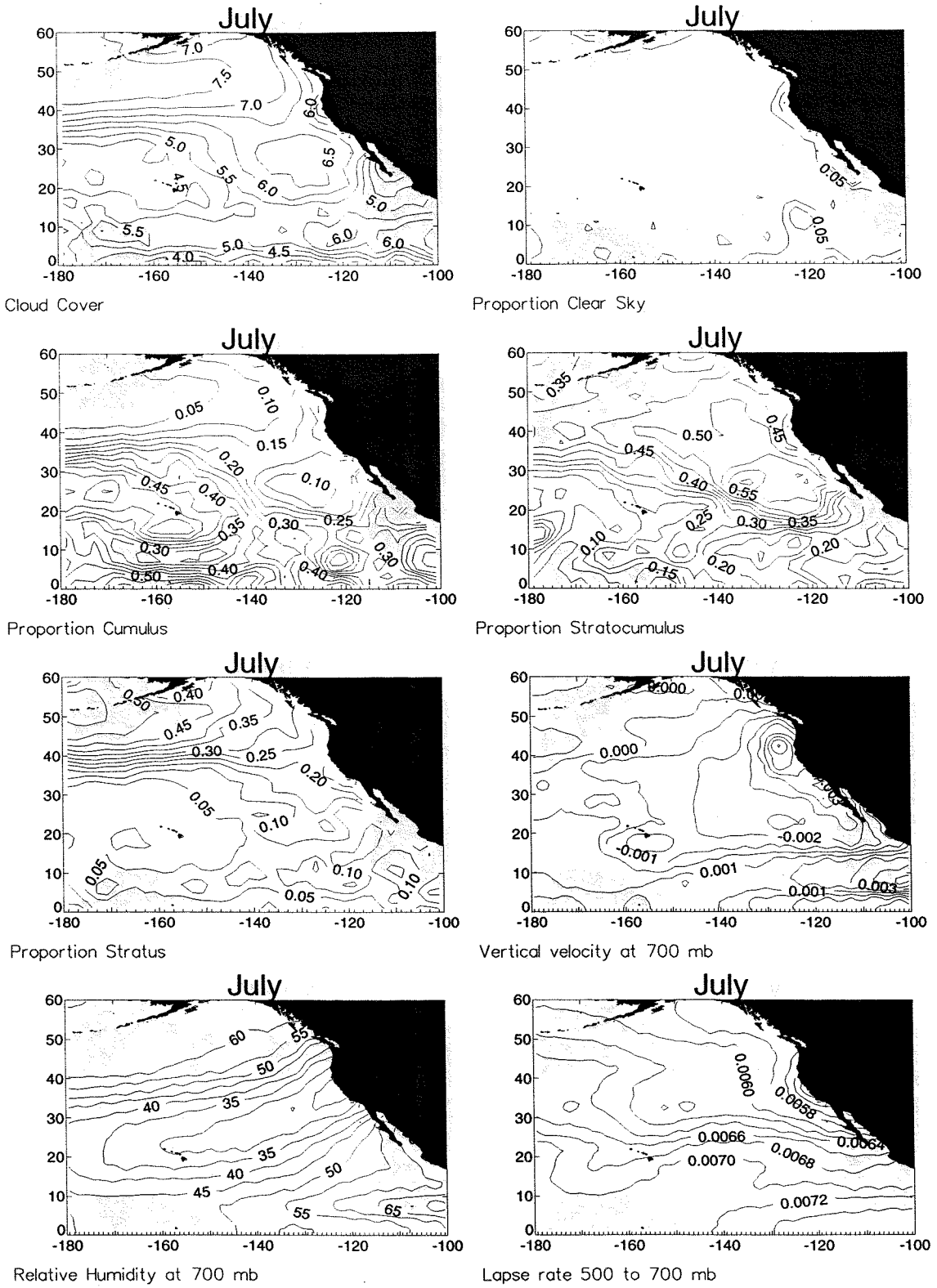

Figure 6.2b As Figure 6.1b but for July.

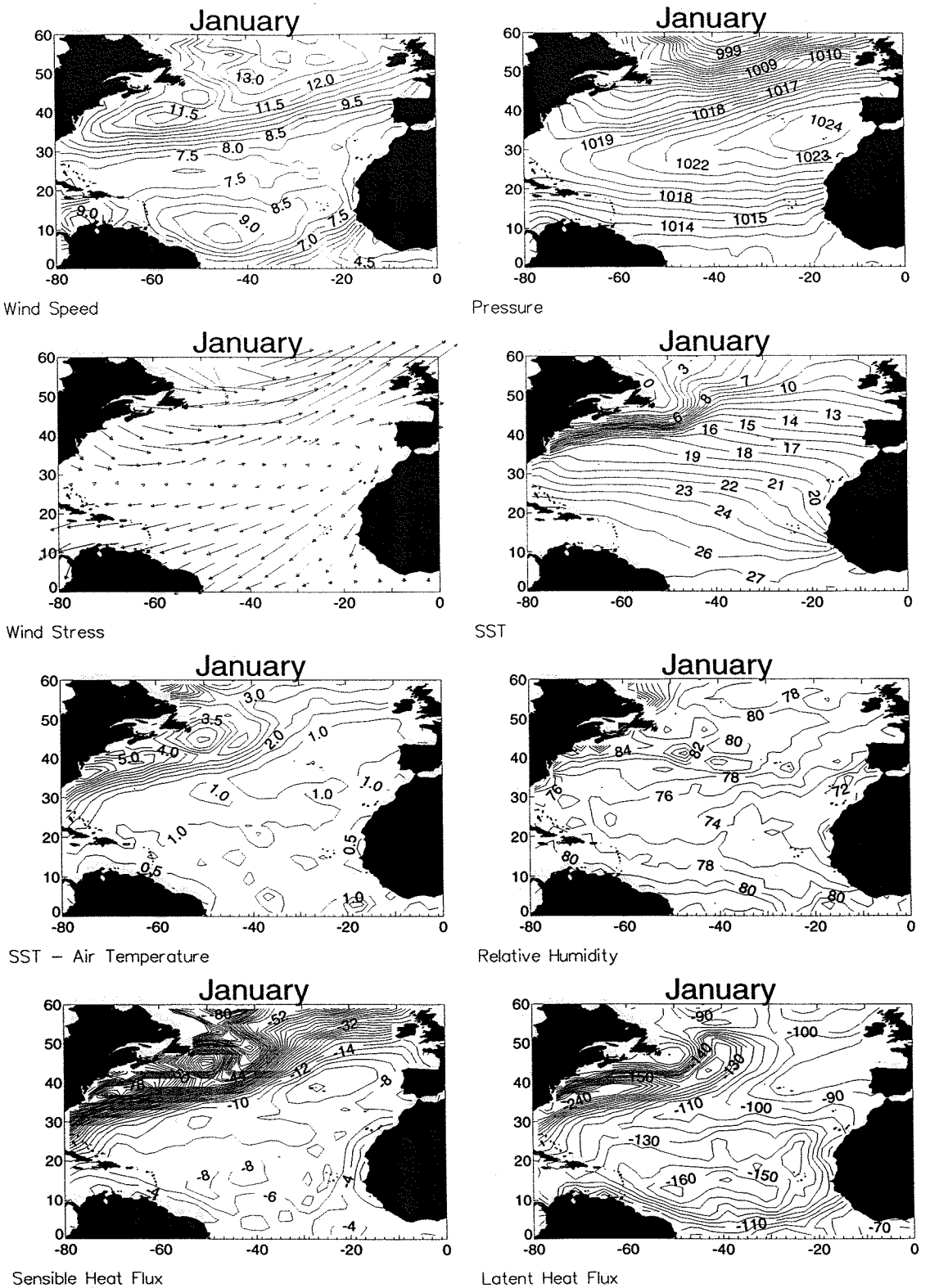

Figure 6.3a Monthly mean surface conditions for January in the North Atlantic from the SOC Climatology.

top row: left: wind speed (ms^{-1}), right: pressure (mb)
second row: left: wind stress (Nm^{-2}), right: SST (°C)
third row: left: air-sea temperature difference (°C), right: relative humidity (%)
bottom row: left: sensible heat flux (Wm^{-2}), right: latent heat flux (Wm^{-2}).

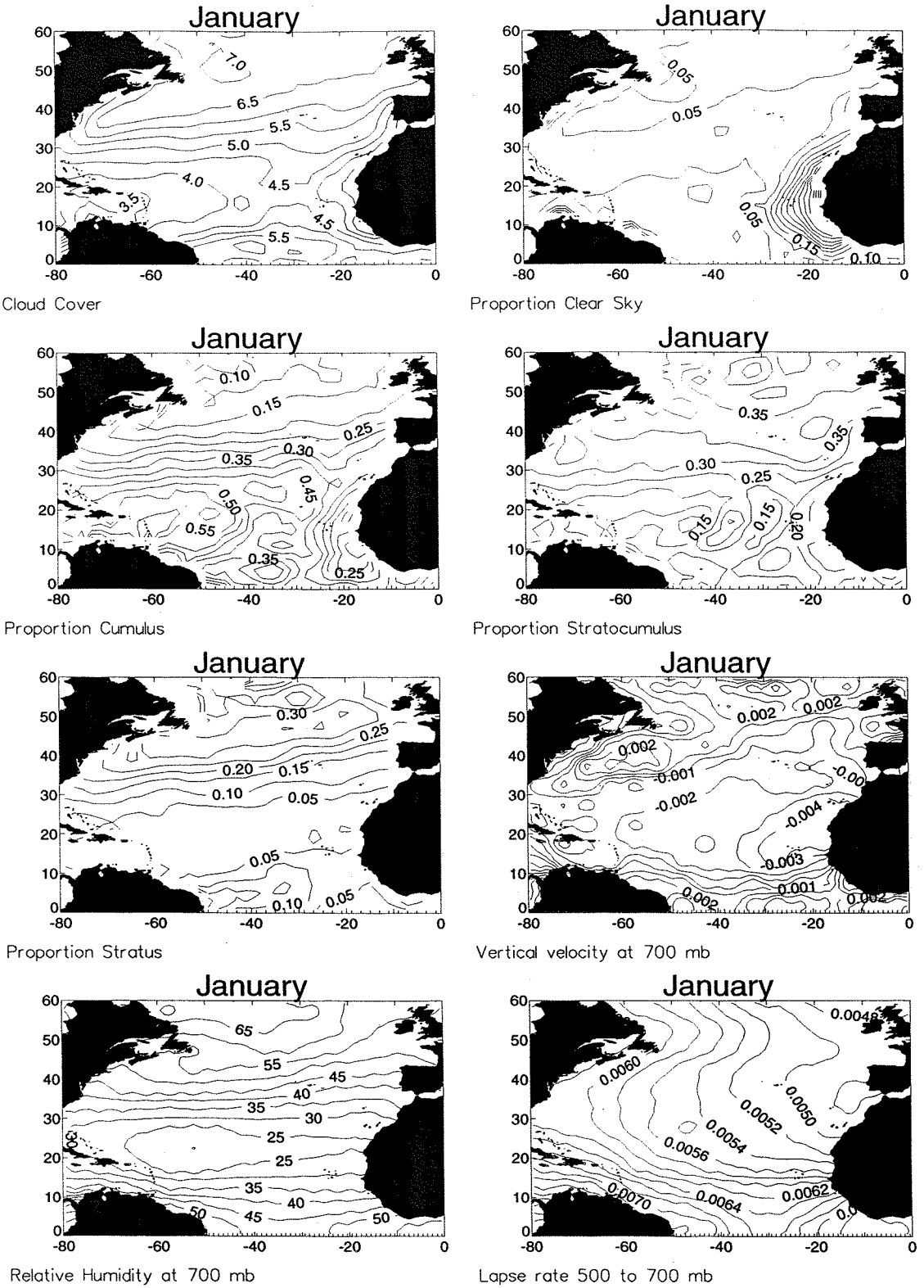

Figure 6.3b Monthly mean cloud (from COADS cloud reports) and upper air data (from the NCEP reanalysis) for January in the North Atlantic.

top row: left: cloud cover (octas), right: proportion of clear sky
second row: left: proportion of cumulus, right: proportion of stratocumulus
third row: left: proportion of stratus, right: vertical velocity at 700 mb ($m\ s^{-1}$)
bottom row: left: relative humidity at 700 mb (%), right: lapse rate of θ between 500 and 700 mb (Km^{-1}).

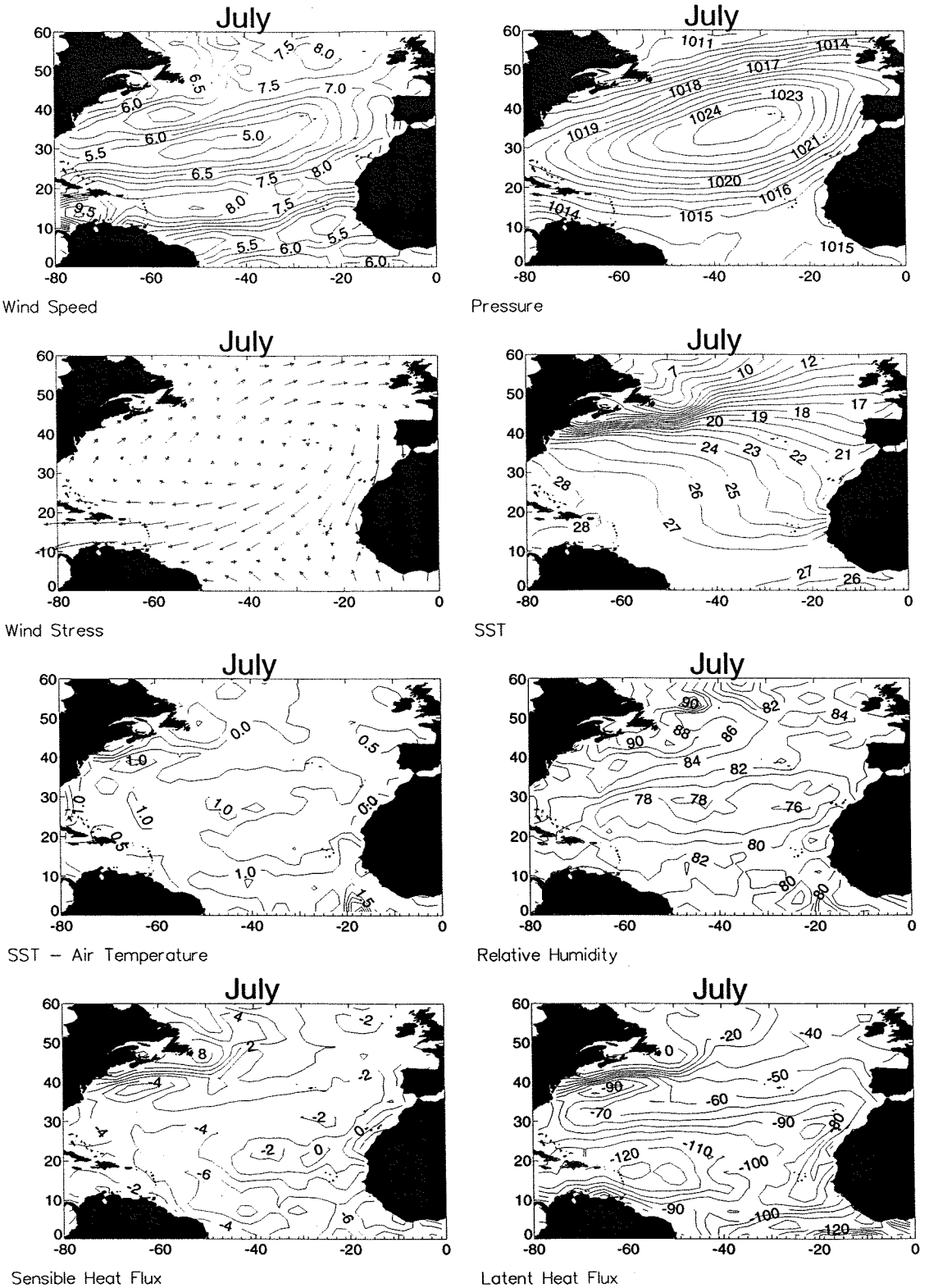

Figure 6.4a As Figure 6.3a but for July.

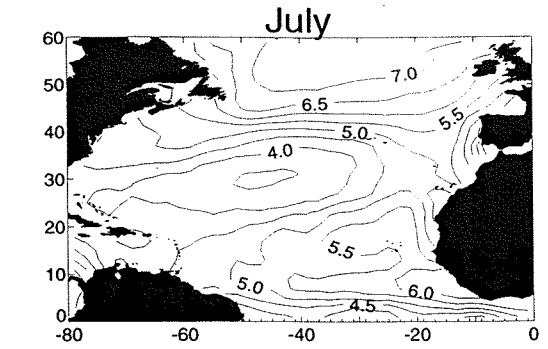

Cloud Cover

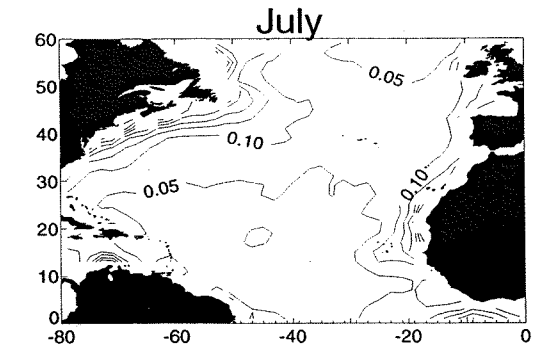

Proportion Clear Sky

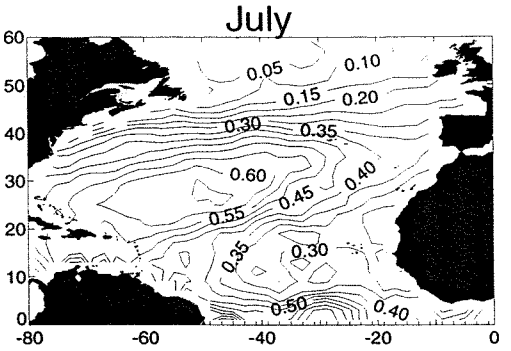

Proportion Cumulus

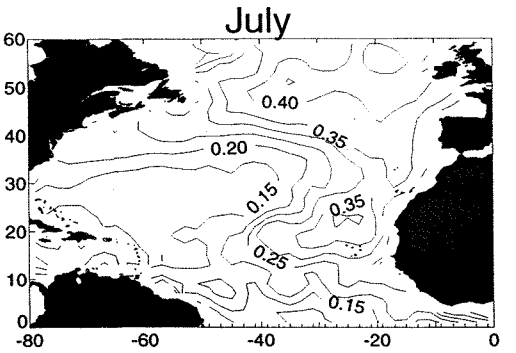

Proportion Stratocumulus

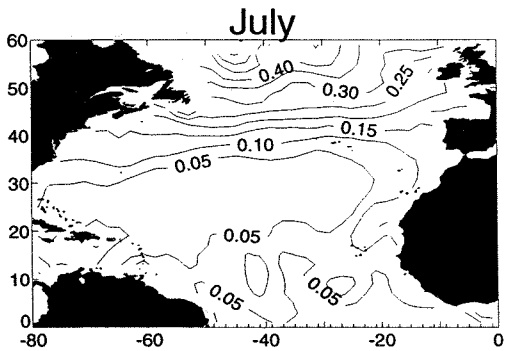

Proportion Stratus

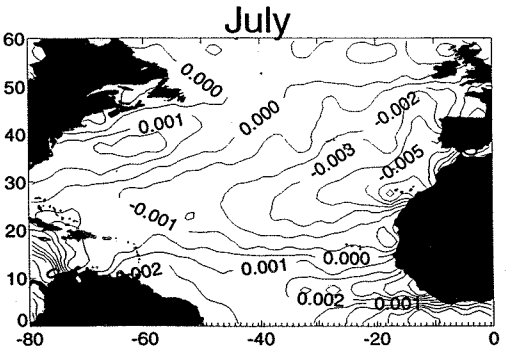

Vertical velocity at 700 mb

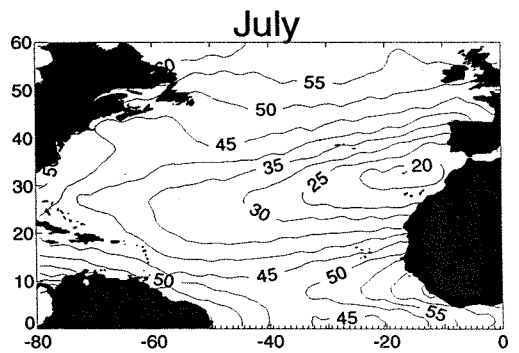

Relative Humidity at 700 mb

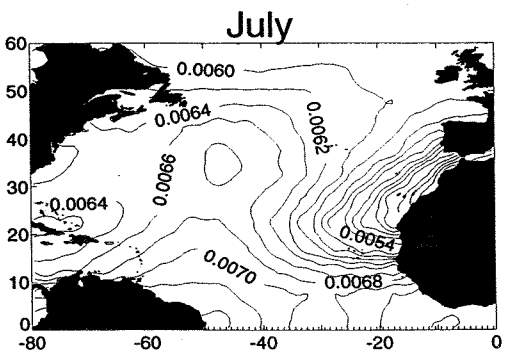

Lapse rate 500 to 700 mb

Figure 6.4b As Figure 6.3b but for July.

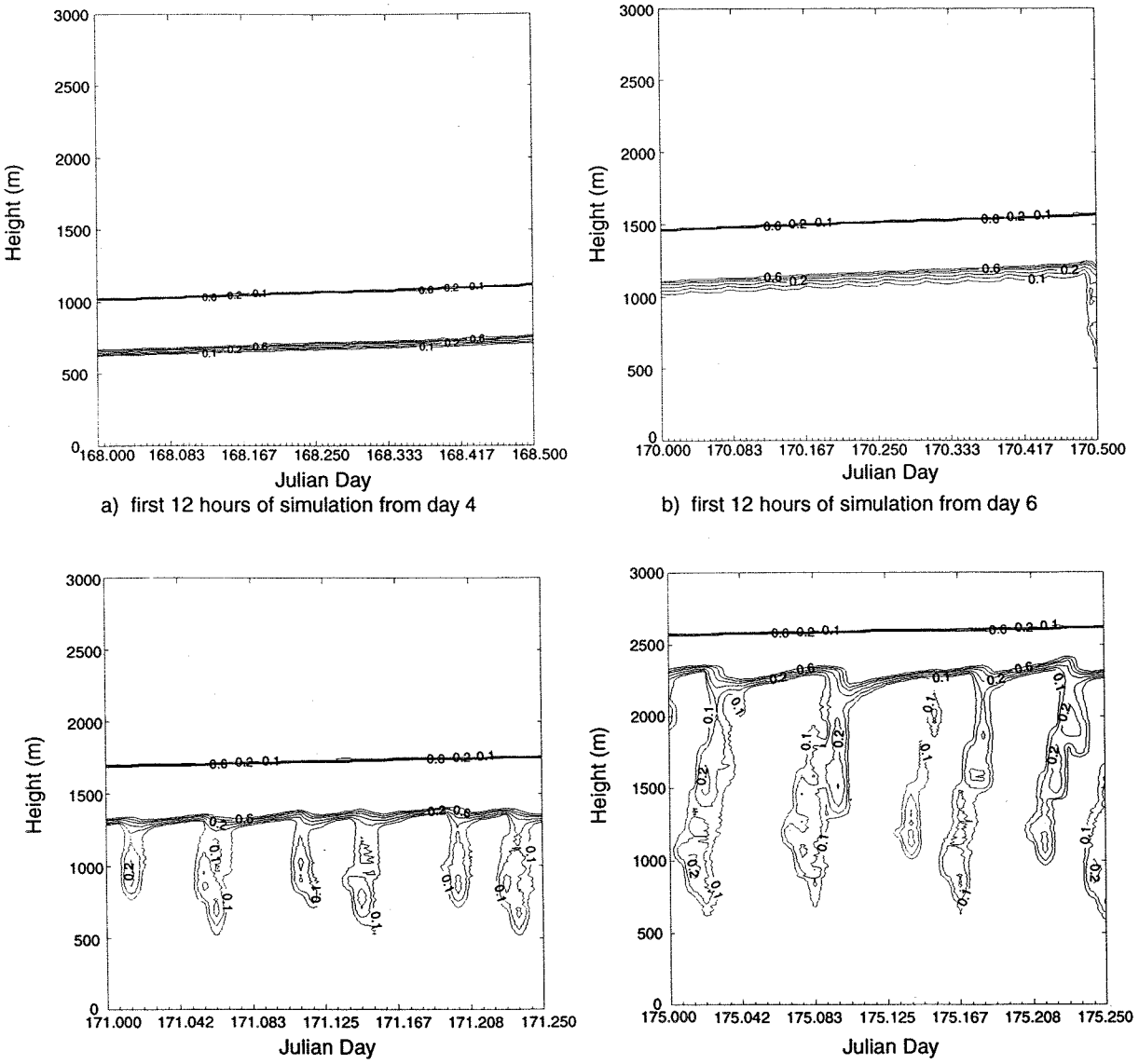

Figure 6.5 Contour plot of cloud fraction taken from the simulation described in Section 6.3. The start of the simulation is at day 164, in mid-June. Top panel shows 12 hours of evolution, the bottom panel 6 hours. a) day 4 of simulation, b) day 6, c) day 7, d) day 11.

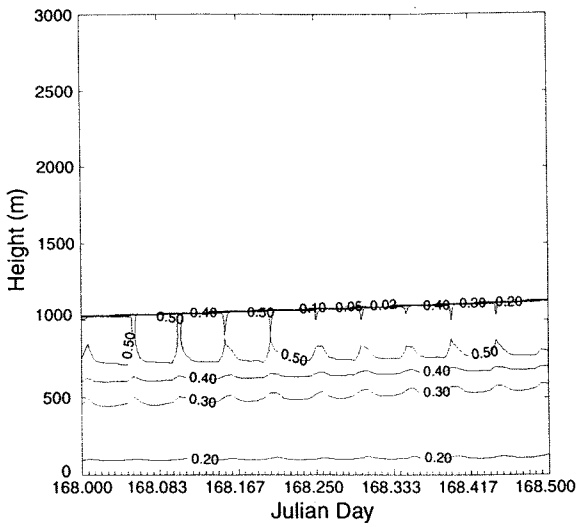

a) first 12 hours of simulation from day 4

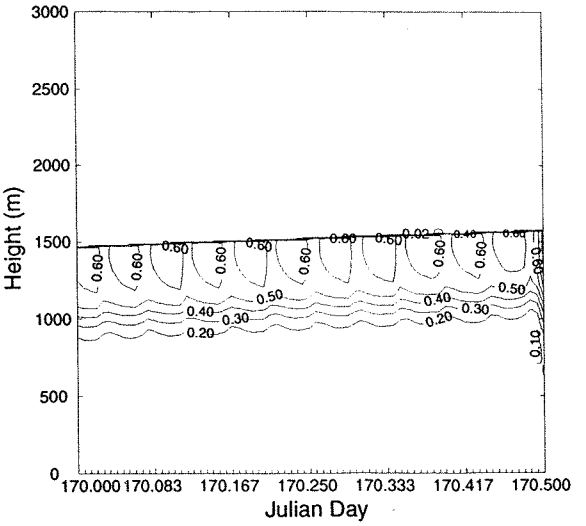

b) first 12 hours of simulation from day 6

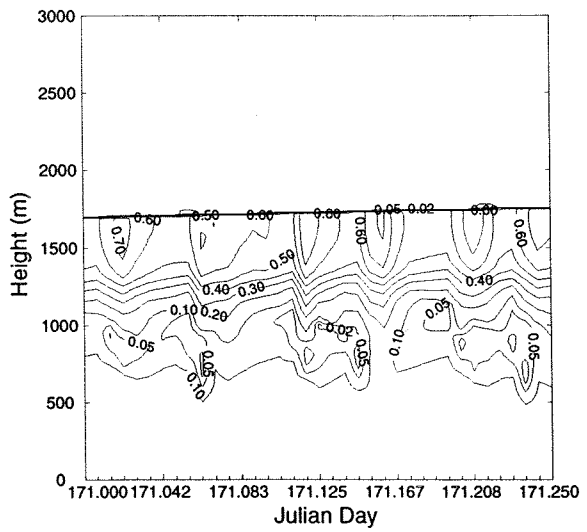

c) first 6 hours of simulation from day 7

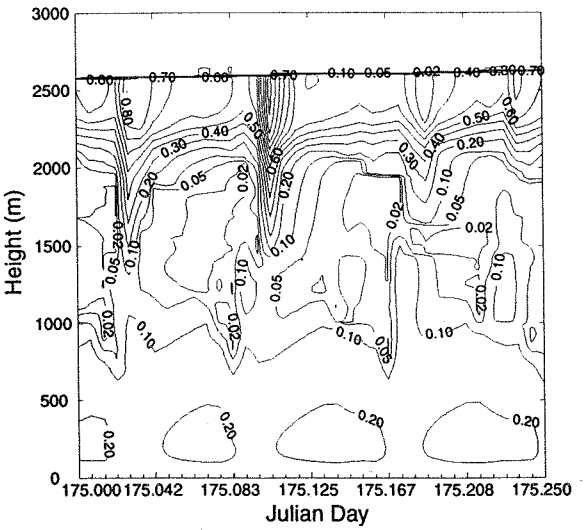

d) first 6 hours of simulation from day 11

Figure 6.6 As Figure 6.5 but for the TKE (m^2s^{-2})

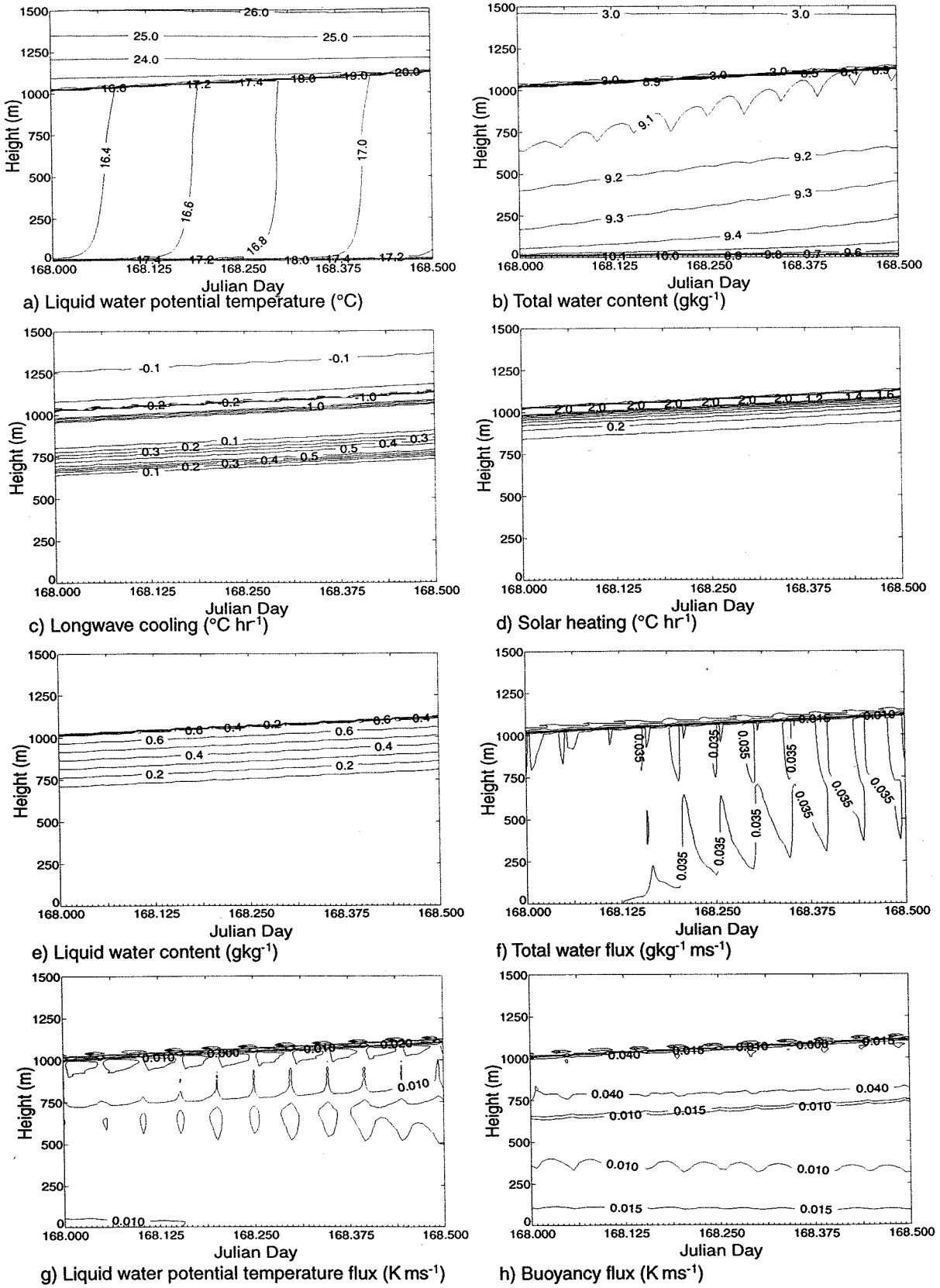

Figure 6.7 Twelve hours of boundary layer evolution from day 4 of the simulation. a) θ_l (°C), b) q_t (gkg^{-1}), c) longwave cooling (°C h^{-1}), d) shortwave heating (°C h^{-1}), e) liquid water content (gkg^{-1}), f) total water flux (ms^{-1}), g) θ_l flux (Kms^{-1}) h) buoyancy flux (Kms^{-1}).

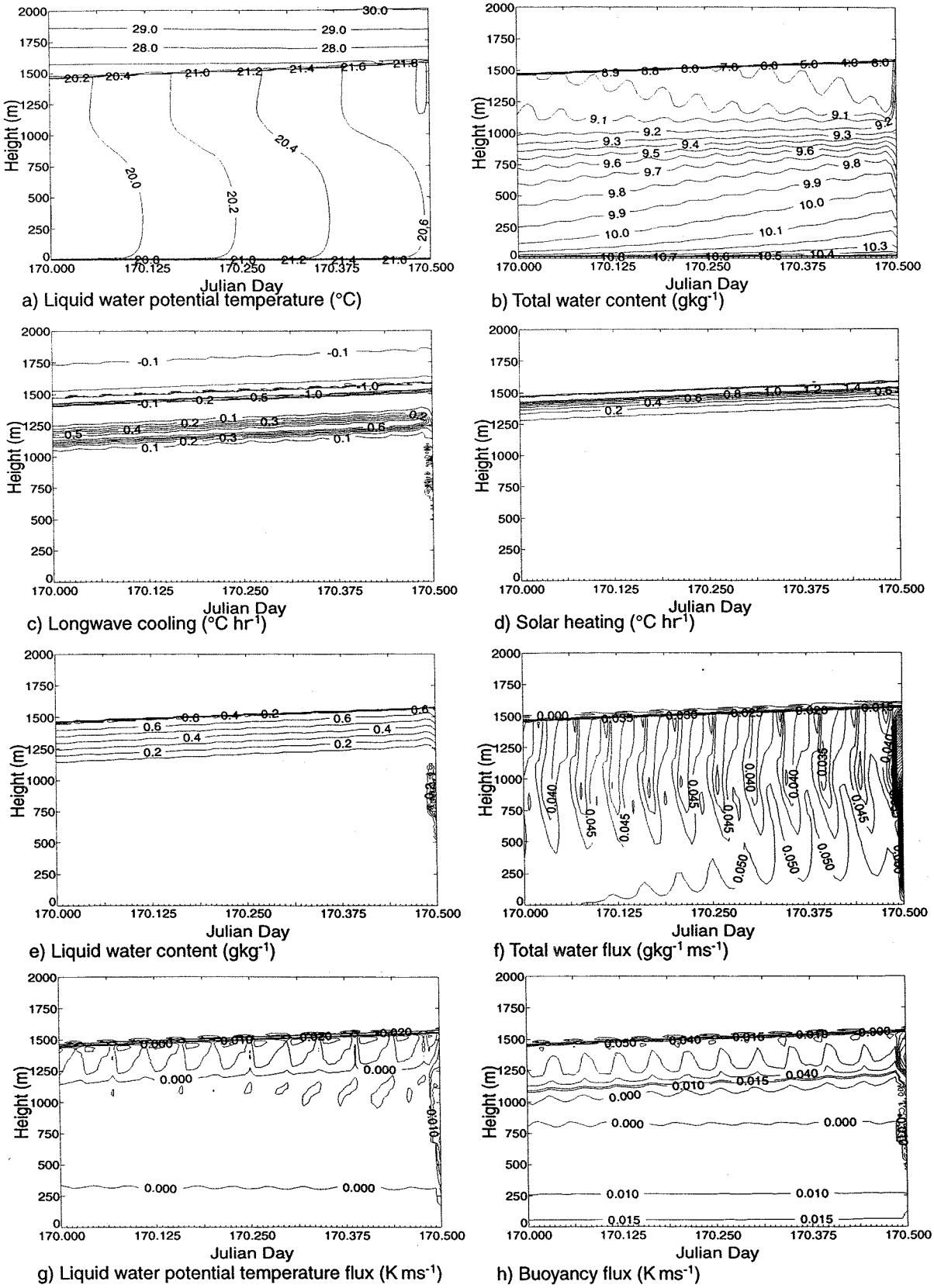

Figure 6.8 As Figure 6.7 but for day 6 of the simulation. Note the change in vertical scale.

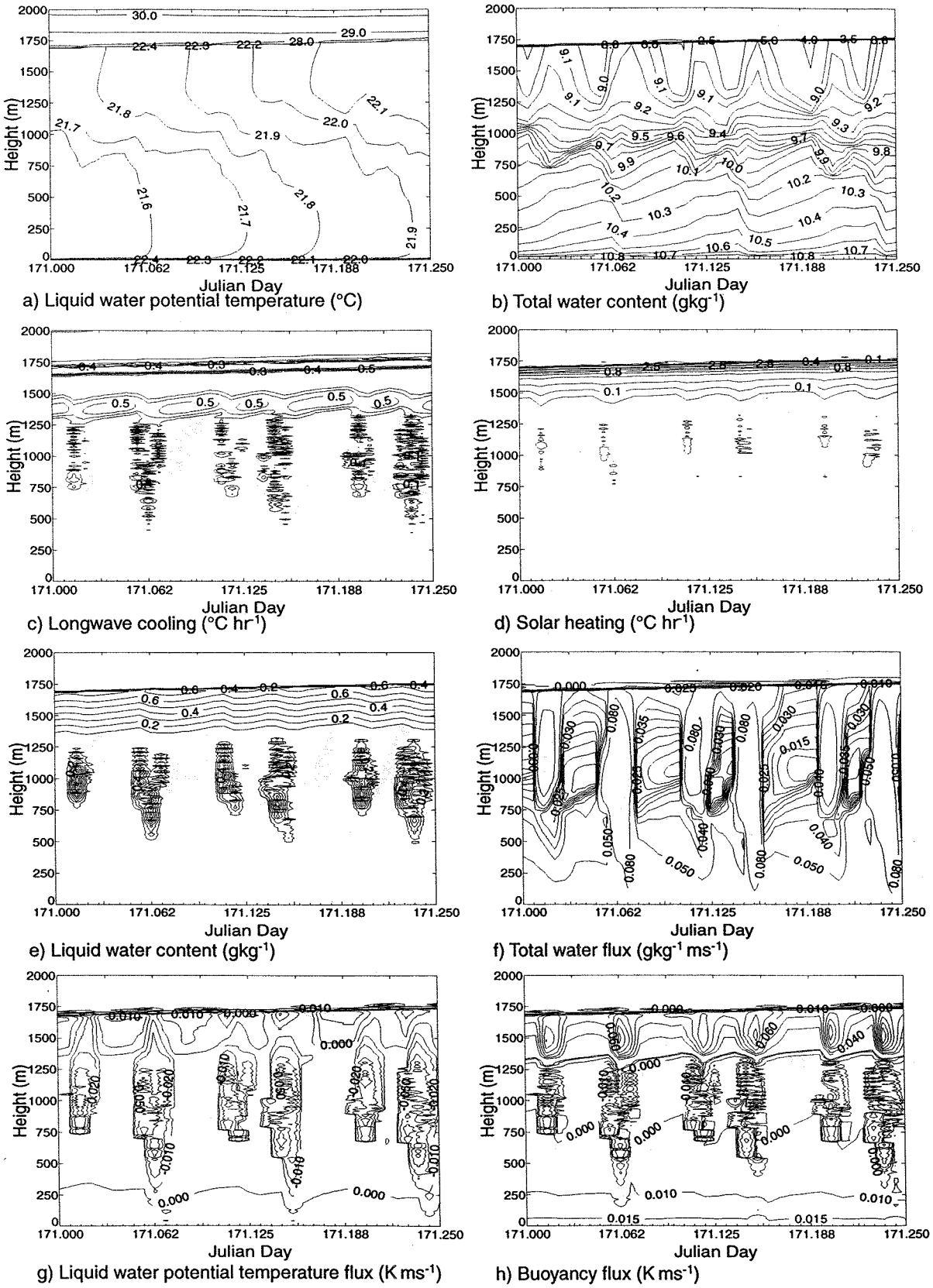

Figure 6.9 As Figure 6.7 but for the first six hours from day 7 of the simulation.

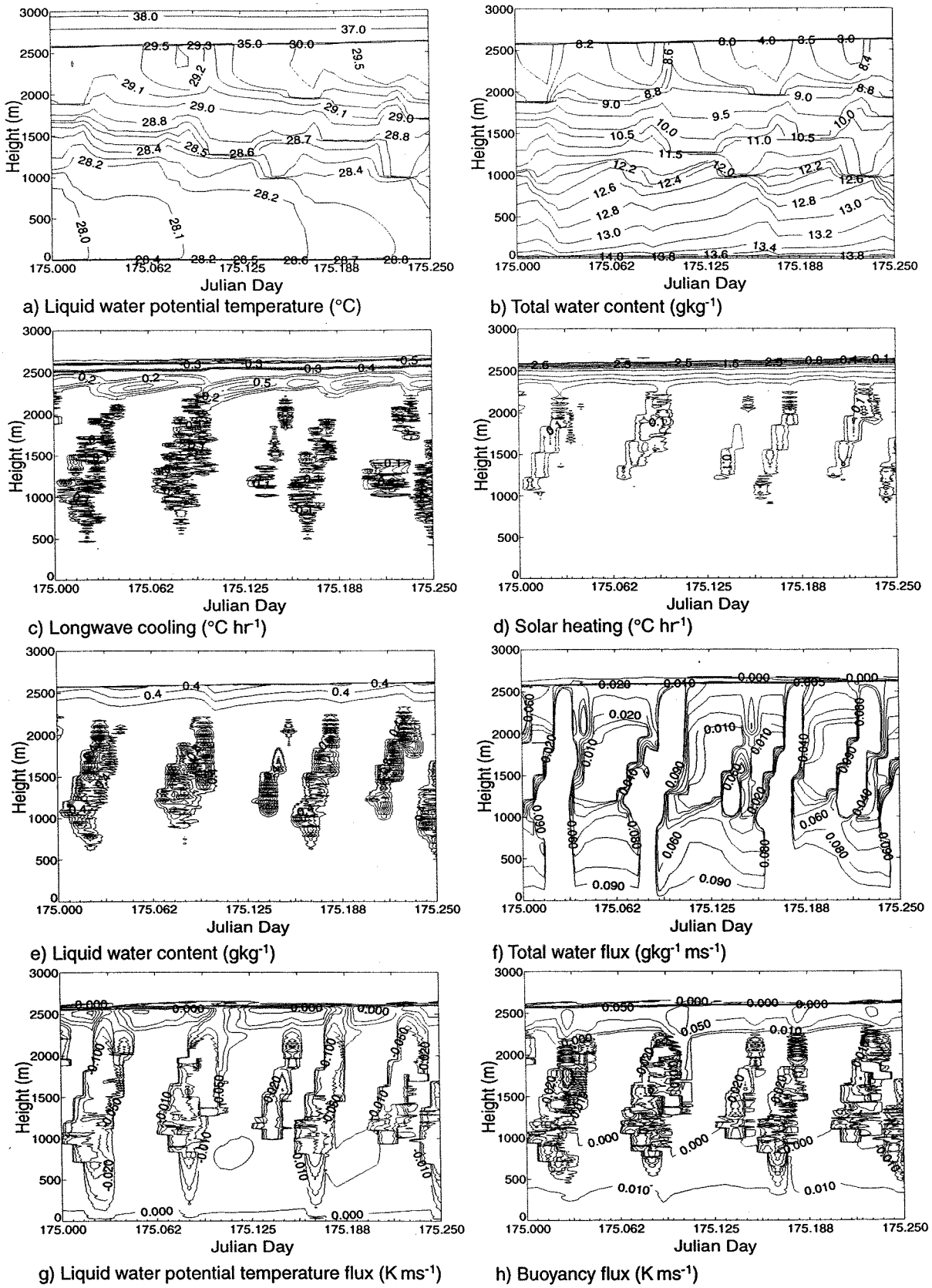

Figure 6.10 As Figure 6.7 but for the first 6 hours from day 11 of the simulation. Note the change of vertical scale.

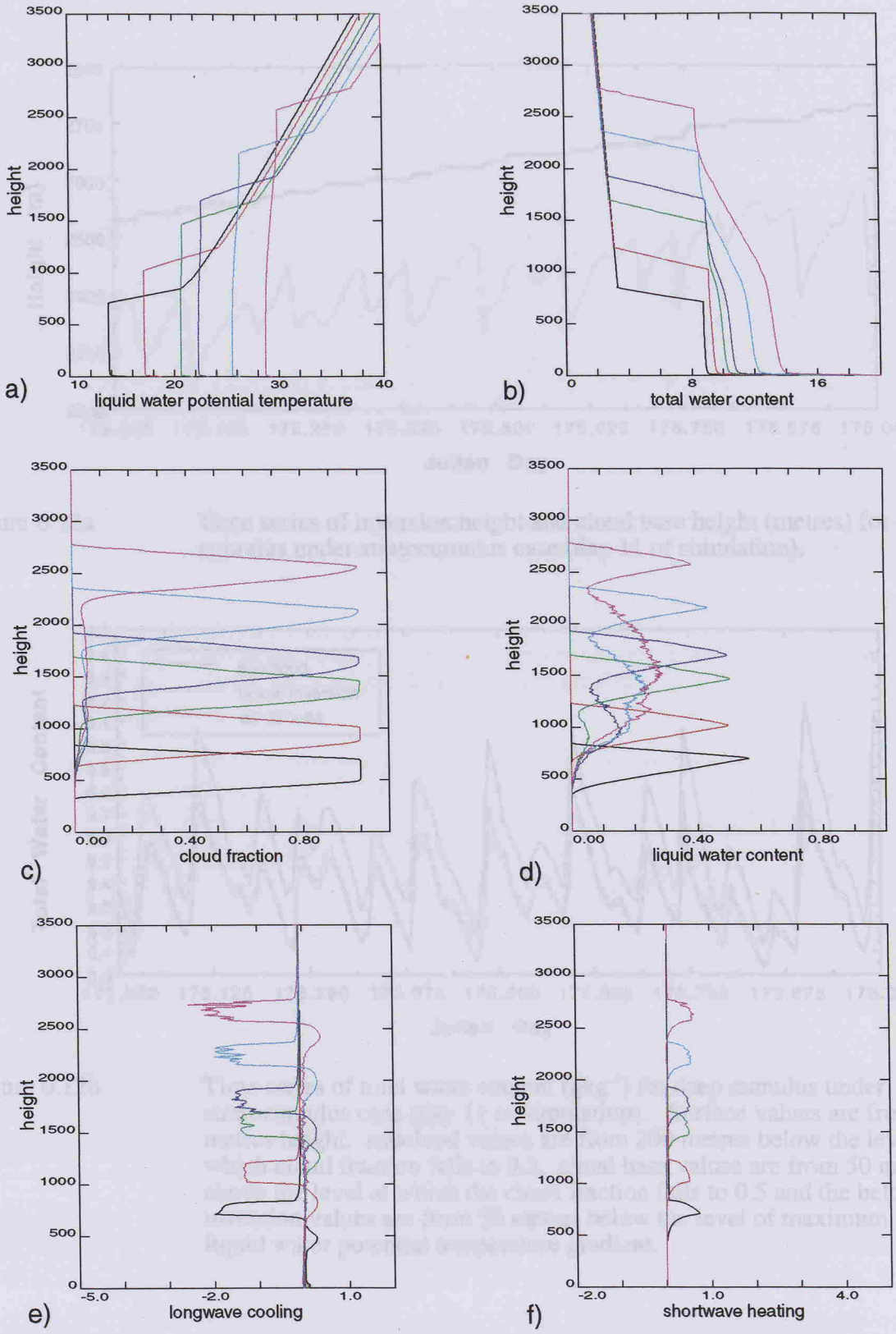

Figure 6.11 Daily average profiles from the simulation. Black day 2, red day 4, green day 6, dark blue day 7, light blue day 9, pink day 11.
a) θ_l (°C), b) q_t (gkg^{-1}), c) cloud fraction, d) liquid water content (gkg^{-1}), e) longwave cooling (°C h^{-1}), f) shortwave heating (°C h^{-1}).

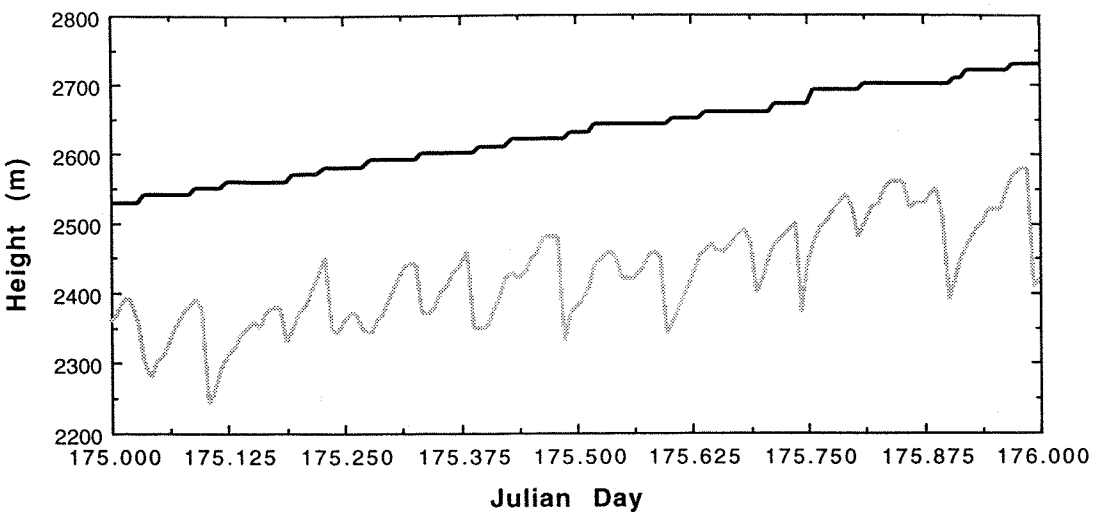

Figure 6.12a Time series of inversion height and cloud base height (metres) for deep cumulus under stratocumulus case (day 11 of simulation).

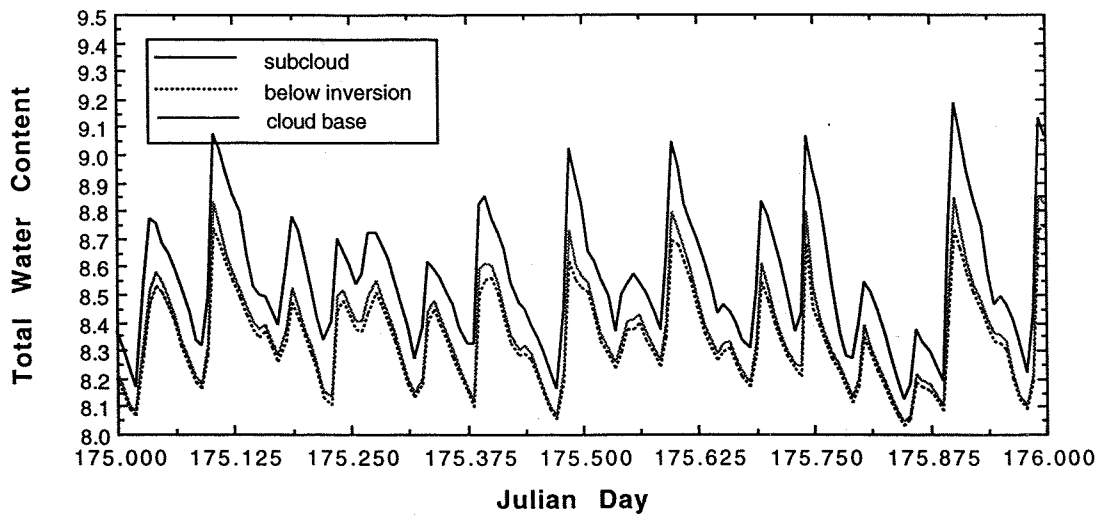

Figure 6.12b Time series of total water content (gkg^{-1}) for deep cumulus under stratocumulus case (day 11 of simulation). Surface values are from 20 metres height, subcloud values are from 200 metres below the level at which cloud fraction falls to 0.5, cloud base values are from 50 metres above the level at which the cloud fraction falls to 0.5 and the below inversion values are from 30 metres below the level of maximum liquid water potential temperature gradient.

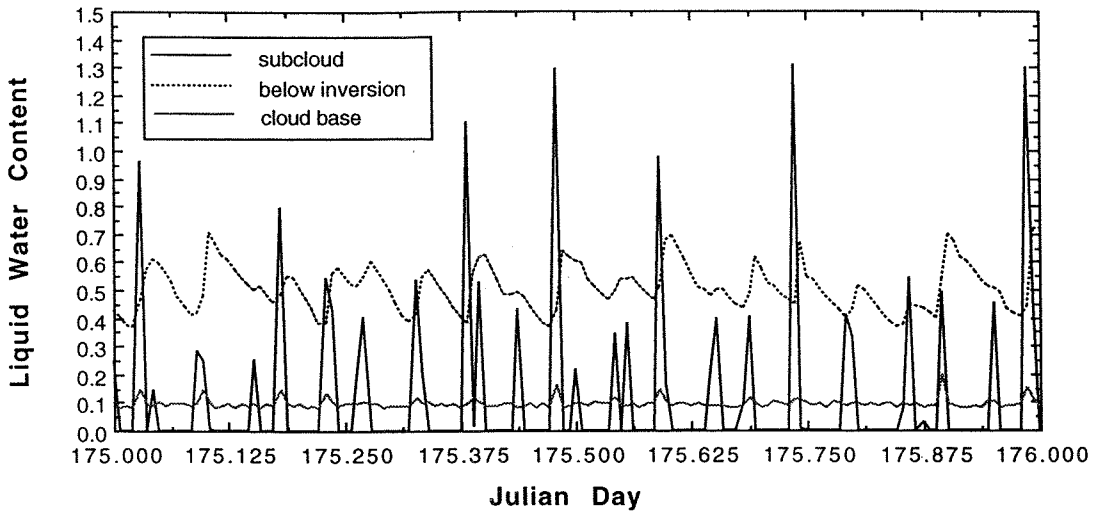

Figure 6.12c Time series of liquid water content (gkg^{-1}) for deep cumulus under stratocumulus case (day 11 of simulation). Surface values are from 20 metres height, subcloud values are from 200 metres below the level at which cloud fraction falls to 0.5, cloud base values are from 50 metres above the level at which the cloud fraction falls to 0.5 and the below inversion values are from 30 metres below the level of maximum liquid water potential temperature gradient.

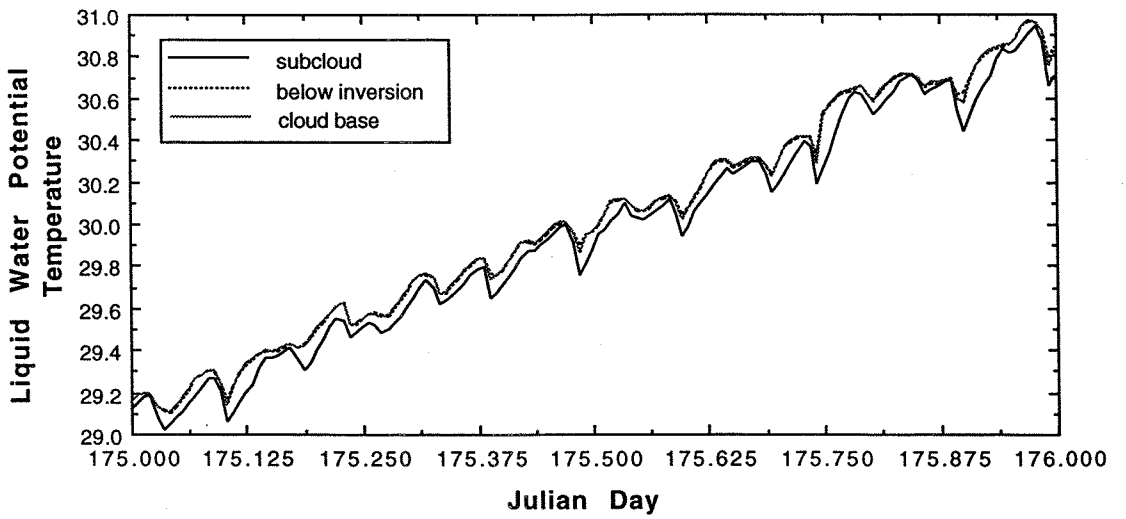

Figure 6.12d As Figure 6.12c but for liquid water potential temperature (°C).

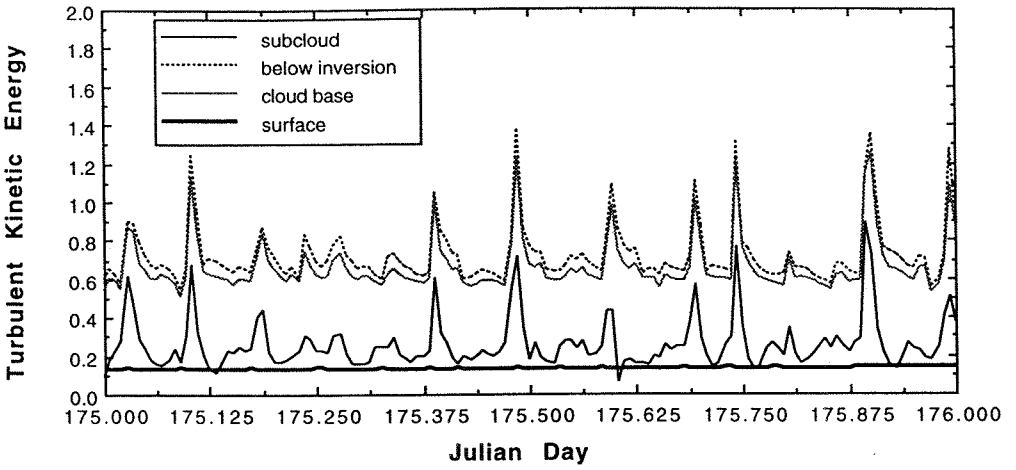

Figure 6.12e As Figure 6.12c but for turbulent kinetic energy (m^2s^{-2}).

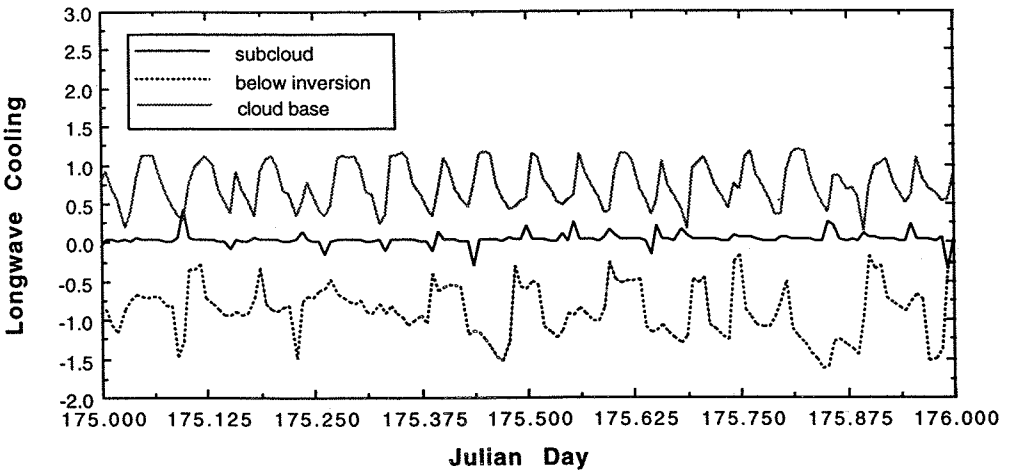

Figure 6.12f As Figure 6.12c but for longwave cooling (°C h^{-1}).

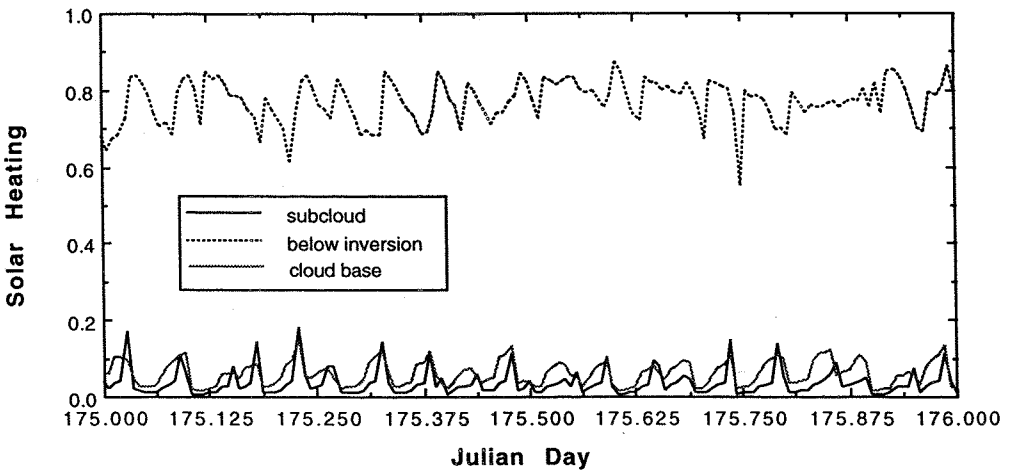

Figure 6.12g As Figure 6.12c but for shortwave heating (°C h^{-1}).

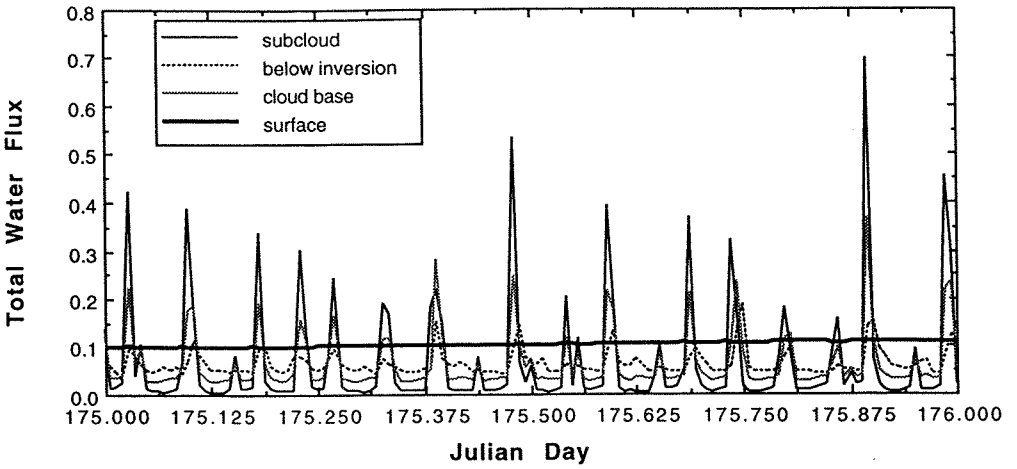

Figure 6.12h As Figure 6.12c but for q_t flux (ms^{-1}).

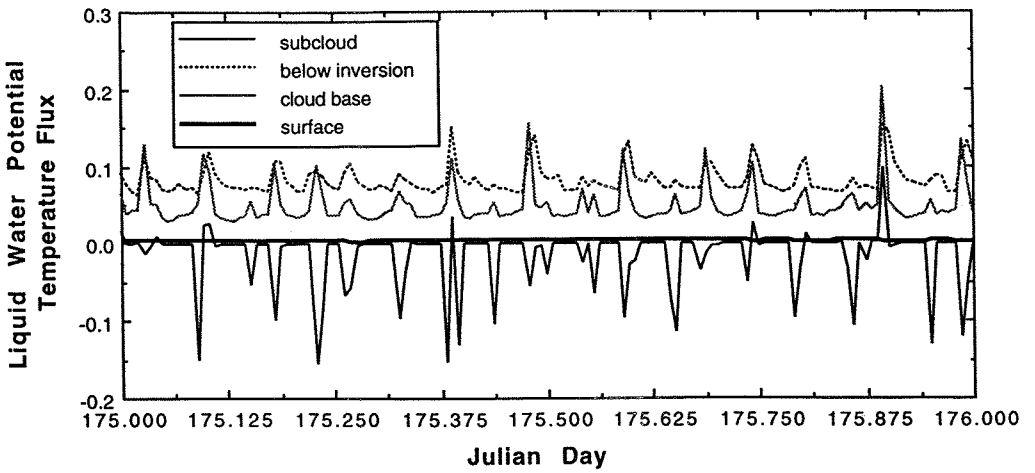

Figure 6.12i As Figure 6.12c but for θ_l flux (Kms^{-1}).

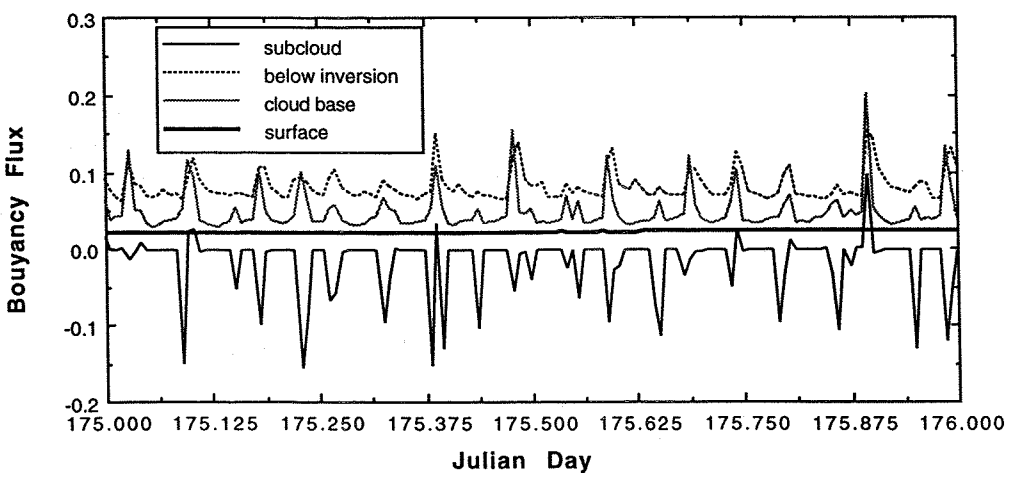

Figure 6.12j As Figure 6.12c but for buoyancy flux (Kms^{-1}).

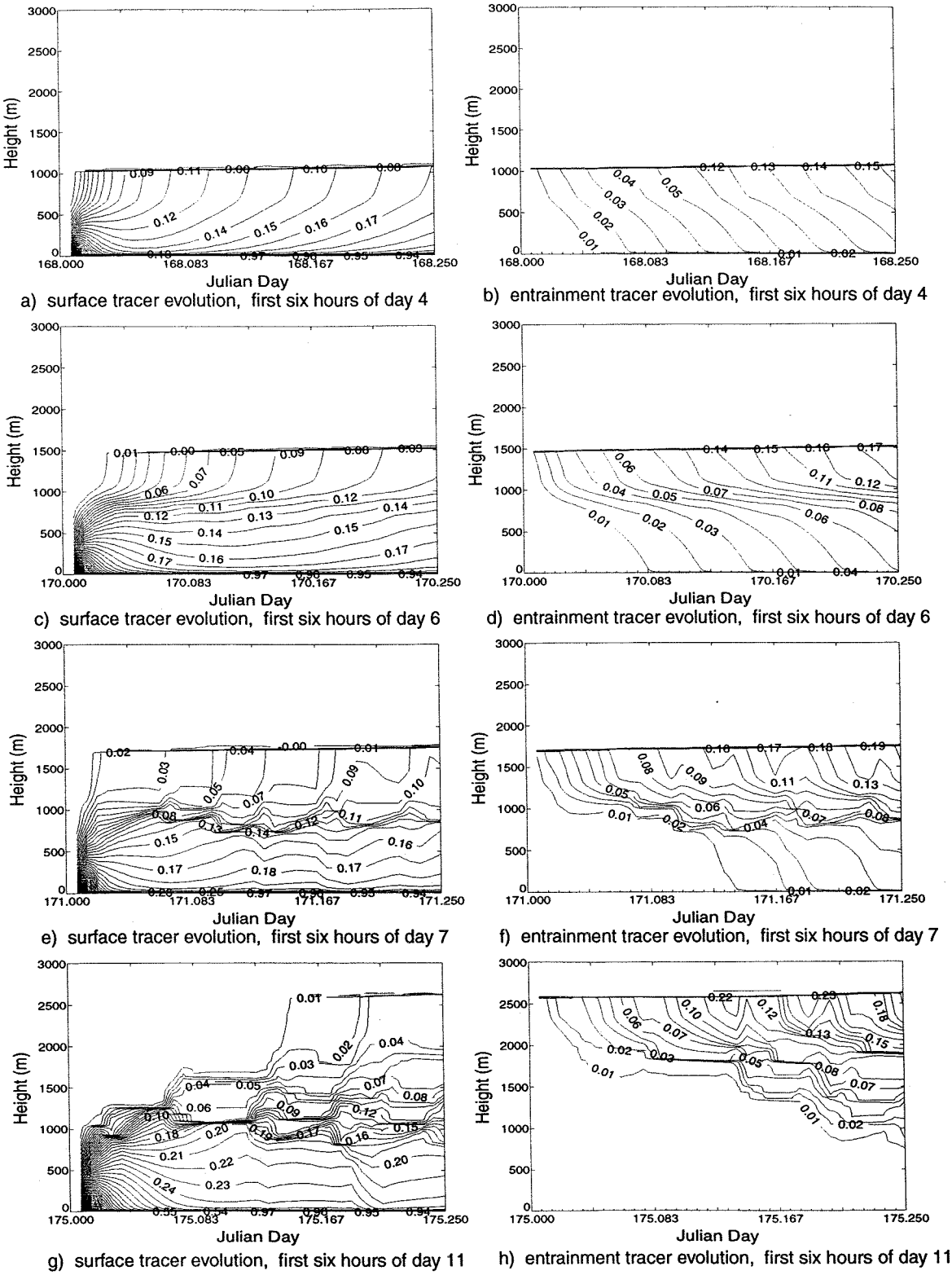

Figure 6.13 Evolution of tracer distribution within simulation. The surface tracer fills lower 10% of boundary layer at the start of each day and the entrainment tracer fills the free atmosphere at the start of each day. Both tracers are zero elsewhere on re-initialisation each day.
a) surface tracer, day 4, b) entrainment tracer, day 4,
c) surface tracer, day 6, d) entrainment tracer, day 6,
e) surface tracer, day 7, f) entrainment tracer, day 7,
g) surface tracer, day 11, h) entrainment tracer, day 11.

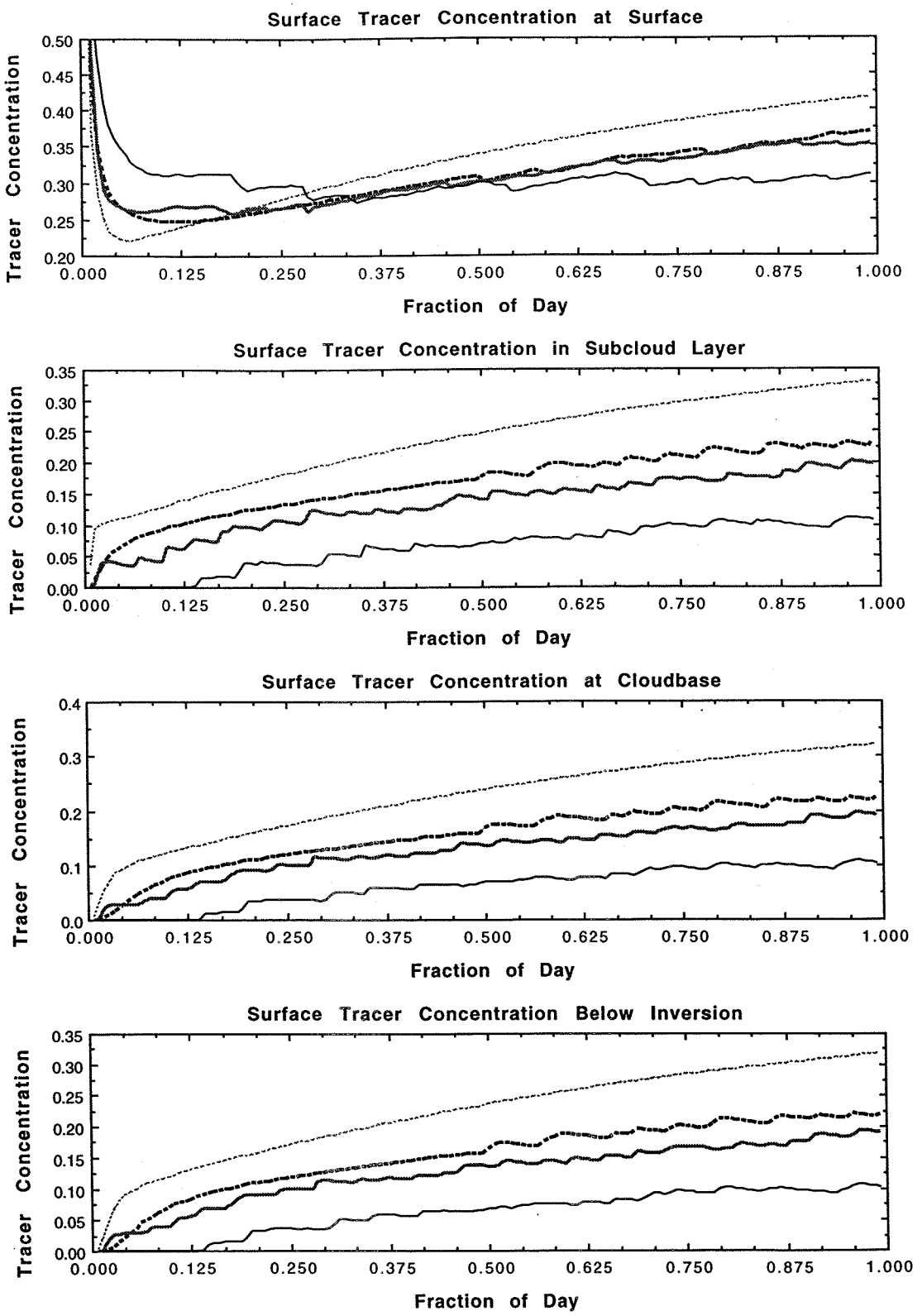

Figure 6.14 Evolution of surface tracer concentration at different levels in the simulation. Light dotted line: day 4 of simulation, dashed line: day 6, light solid line: day 7, solid line: day 11.

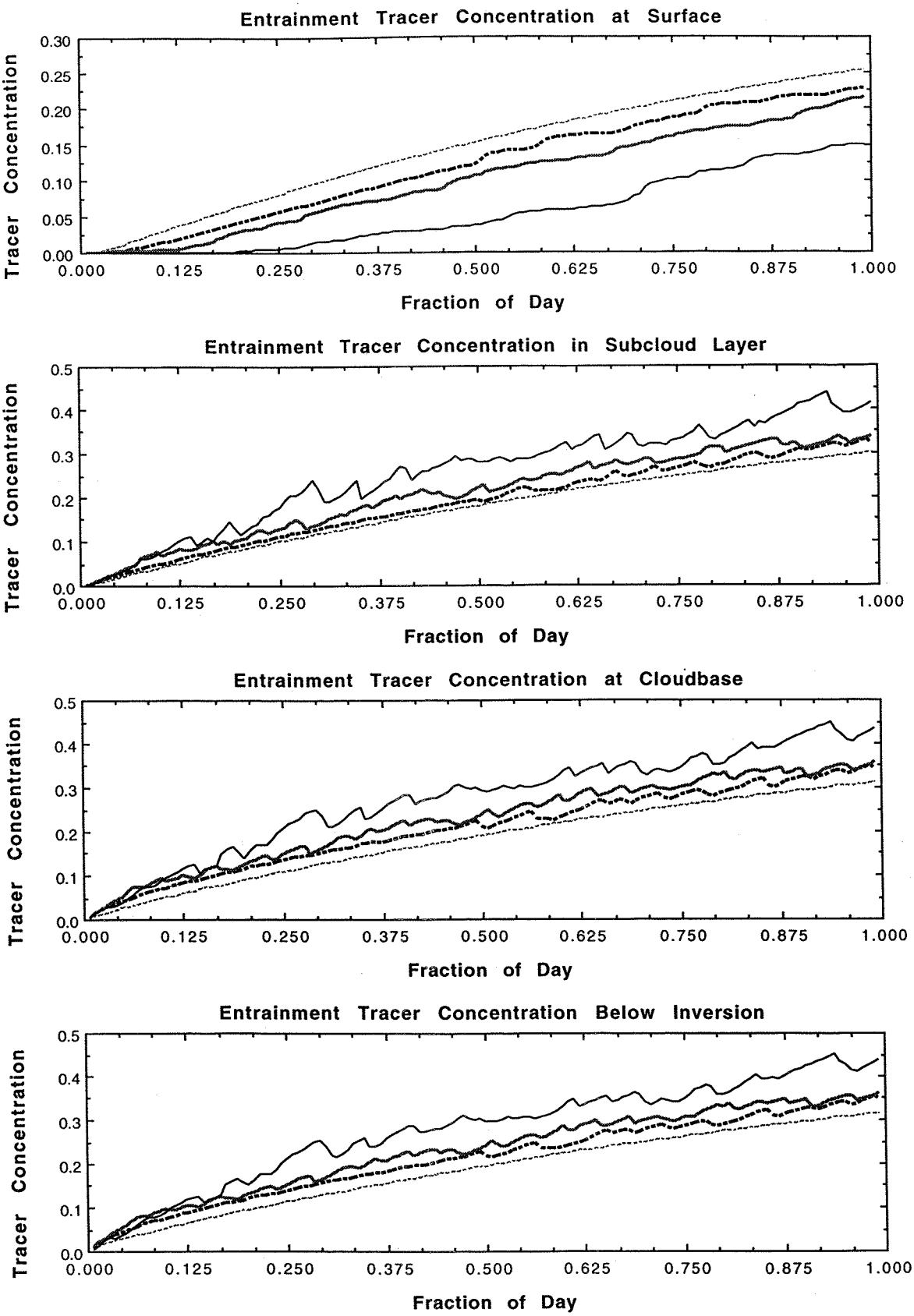

Figure 6.15 Evolution of entrainment tracer concentration at different levels in the simulation. Light dotted line: day 4 of simulation, dashed line: day 6, light solid line: day 7, solid line: day 11.

7. IMPACT OF VARYING EXTERNAL FORCING

7.1 Introduction

This chapter will build on the results of Chapter 6 by investigating the external factors that affect the simulated transition from stratocumulus to cumulus under stratocumulus. The computational efficiency of the present model allows investigation of the effects of a range of external forcing on the long-term evolution of the boundary layer in a way only possible in the past with mixed layer models. Typically two-dimensional model studies of the stratocumulus to cumulus transition present only two or three different simulations. In the present study the impact of varying vertical velocity has been investigated and possible shortcomings in the model highlighted (Section 7.2). The effects of above inversion temperature and humidity structure on the simulated boundary layer evolution are presented (Section 7.3). A possible feedback between CTEI and boundary layer dynamics in the decoupled boundary layer is discussed. Further simulations show the effects of changing wind speed and SST gradients on the model boundary layer evolution (Section 7.4) and also the effects of solar radiative forcing and the diurnal cycle (Section 7.5). Comparisons with other model and climatological studies are made in Section 7.6. The results are summarised in Section 7.7.

7.2 Varying Vertical Velocity

7.2.1 The Observed Variation of Vertical Velocity through the Transition Region

Section 6.2 showed from climatological NCEP data that the vertical velocity should be strong at the start of the simulation in the high pressure regions associated with large stratocumulus amounts, but decrease towards the trade wind region. This is also intuitively reasonable. However the simulation described in Section 6.3 uses a constant divergence for the entire simulation. The vertical velocity is then found by integrating the divergence from the surface to the inversion height. The vertical velocity is held constant at its value at the inversion height at all levels above the inversion.

Most of the model simulations from the literature are run with a similar constant divergence. In all the simulations the vertical velocity at the inversion increases through the simulation as the inversion height grows. This is not what is expected from either the NCEP climatology or from the climatological pressure distributions. Albrecht (1984) and Wang (1993) decrease the divergence through their simulations, but not sufficiently to actually decrease the vertical velocity at the inversion height. If the inversion height grows from 500

metres to 2500 metres (as in the Wyant et al. 1997 simulation) the magnitude of the vertical velocity at the inversion increases from -0.0015 ms^{-1} to -0.0075 ms^{-1} for a constant divergence of $3x10^{-6}$ s^{-1}. Table 6.1 suggests that the initial vertical velocity is too low for the stratocumulus region and that the final vertical velocity should be small.

If we consider a boundary layer with no turbulence, the effect of the downwards vertical motion is to bring dry, potentially warm air down from above. The inversion will decrease in height at a rate equal to the vertical velocity. This can be thought of as a horizontal outflow of boundary layer air from the column, which is replaced by air from above. In reality subsidence will also act to warm and dry the free atmosphere above the inversion, but in the present study this effect is reduced by the relaxation of the profiles which has been applied above the inversion. This is also done by Krueger et al. (1995a,b) and Wyant et al. (1997). If the large vertical velocities used in these and the present studies were allowed to warm the air above the inversion, the resulting profiles would become unphysical. In a cloud-topped boundary layer the decrease in inversion height is opposed by the turbulent entrainment of air into the boundary layer from above. Entrainment is an inversion process and the entrained air will act to stabilise the top of the cloud layer (unless the conditions exist for CTEI). Thus entrainment tends to stratify the boundary layer (although this stratification is usually reduced or removed by turbulence within the cloud) whereas a uniform subsidence tends to retain the original boundary layer structure.

Figure 7.1 shows the liquid water content for days 4, 6, 7 and 11 from a simulation performed with a constant vertical velocity ($w = -0.003$ ms^{-1}) at and above the inversion, decreasing linearly to zero at the sea surface. This vertical velocity profile is the same as that used in the standard simulation when the inversion height is 1000 metres. For lower inversion heights the vertical velocity is stronger than in the standard simulation, for higher inversions it is weaker. The boundary layer growth is at first inhibited by the strong vertical velocity (Figure 7.1a) and initially the boundary layer contains less liquid water. By the time the first cumulus clouds form however, the liquid water is larger compared to the standard simulation and the boundary layer is deepening faster (Figure 7.1b). The liquid water content continues to increase and the boundary layer entrains and deepens faster as the vertical velocity reduces relative to the constant divergence case (Figures 7.1 c,d). The result after 12 days of simulation is a boundary layer 4.4 km deep (compared to 2.8 km in the constant divergence case) with a cloud 1.8 km deep (compared with about 250 metres) and a peak liquid water content of 3.6 gkg^{-1} (compared with 0.6 gkg^{-1}). So rather than the expected drying out and breaking up of the stratocumulus, this simulation predicts moistening and thickening.

Only when the divergence is held constant (and the downwards vertical velocity at the inversion increases with time) is the expected evolution of the boundary layer observed in the simulation. The effect of the increasing vertical velocity at the inversion height on simulations of stratocumulus to cumulus transition is not discussed in the other model studies. It is therefore not clear whether these other models would also predict a thickening and moistening of the stratocumulus layer if climatological vertical velocities were imposed. The mixed layer model of Wang (1993) does however show a tendency to form increasingly thick cloud layers and very deep boundary layers when the divergence is decreased through the simulation.

The reason for the requirement for stronger than expected vertical velocity is not clear. Schubert et al. (1995) note that the increase in height of the trade inversion in the North Atlantic, North Pacific and the Caribbean as the air flows towards the tropics is less than expected from local considerations alone. They suggest that the inversion height in the trade wind region is dynamically constrained to be more horizontally uniform than suggested by local thermodynamics. Rapid spatial variations in the trade inversion height are dynamically smoothed. Any such effect could not be included in a one-dimensional model, or by the small domain two-dimensional models of Krueger et al. (1995a,b) and Wyant et al. (1997), all of which simulate boundary layer evolution in a Lagrangian mode. Another possibility is that the problem lies with the lack of a drizzle parameterisation. Without precipitation the only method the boundary layer has of losing moisture is by horizontal advection of moist boundary layer out of the air column, driven by a downwards vertical velocity. In the absence of strong, drying, subsidence as the boundary layer deepens, the liquid water content in the cloud increases and strong longwave cooling leads to further entrainment. This could cause the rate of boundary layer growth to increase with time. Another possibility is that the effects of wind shear above the inversion might be important in some cases but this has not been investigated in the present study.

7.2.2 Effect of Different Divergence Rates on the Simulation

Figure 7.2 shows the liquid water content for the eighth day of simulation for different assumptions with regard to the divergence. The standard simulation (as described in Chapter 6) is shown in Figure 7.2a and the simulation with a constant vertical velocity (as in Figure 7.1) in Figure 7.2b. Also shown is the liquid water content for simulations with smaller and larger divergences than in the standard simulation, all other parameters remain the same (Figures 7.2c,d). Table 7.1 summarises some boundary layer characteristics for these simulations, and others described in the remainder of the chapter.

Decreasing the vertical velocity (by decreasing the imposed divergence rate by 20%, Figure 7.2c) results in a deeper boundary layer compared to the standard simulation (Figure 7.2a), as expected. This deeper boundary layer is on average warmer, drier and more decoupled than that in the standard simulation (Table 7.1). The liquid water content at the cloud top is greater, which leads to larger longwave cooling and hence in-cloud TKE shown in Figure 7.3 (compare Figures 7.3a and 7.3c). The background in-cloud TKE and the peaks generated by the buoyancy input from each individual cumulus cloud are all greater for this case. The cumulus clouds below the stratocumulus layer form nearly a day earlier in the simulation with decreased vertical velocity than in the standard simulation. The stability of the strong gradient region near the cumulus cloud base is much stronger when the divergence is weaker due to increased entrainment.

The converse is true for an increased subsidence rate (an increase in the divergence by 20%, Figures 7.2d and 7.3d). Increasing the downwards vertical velocity acts to introduce more dry and warm air into the boundary layer (the profiles above the inversion are relaxed to their original values). This is accompanied by increased surface fluxes as the shallower boundary layer is more nearly well mixed with the surface layer cooler and drier than in the decreased subsidence case. This is because an increase in subsidence leads to a shallower boundary layer with a thinner cloud layer and lower in-cloud liquid water. The cumulus clouds below the stratocumulus layer form nearly a day later than in the standard simulation. The whole boundary layer is cooler as the thin cloud layer loses a similar amount of heat due to long wave cooling compared to the standard case. The θ_l and q_t contrasts between the surface and the stratocumulus layer are reduced in the increased subsidence case and so the impact of each cumulus cloud on the stratocumulus layer is reduced (compare 7.3a and d). The TKE in the cloud in the increased subsidence case is lower than any of the other simulations (Figure 7.3d). TKE in the surface layer is however slightly larger and the minimum in TKE below the cloud base less well defined than the other cases.

7.3 Varying Inversion Jumps and Above Inversion Profiles

7.3.1 Lower Tropospheric Stability

The effect of temperature structure above the inversion has often been described using the concept of lower tropospheric stability (LTS). LTS can be defined as the potential temperature difference between 700 mb and the sea surface ($\theta_{700mb} - \theta_0$). Klein and Hartmann (1993) used data from surface based cloud climatologies to show a relationship between LTS and the areal cloud coverage on seasonal timescales. They suggested an

increase in LTS of 1K should lead to an increase in cloud coverage of 6%. LTS depends on the inversion height, the inversion temperature strength, the potential temperature gradient above the inversion and the surface temperature and pressure. Reducing the potential temperature lapse rate above the boundary layer, increasing the boundary layer height, reducing the inversion strength or reducing the surface pressure should all reduce the LTS and therefore lead to lower cloud cover. LTS is a convenient quantity to consider, particularly in models with coarse vertical resolution where information may only be available at a few levels. It is not however easy to separate cause and effect when looking only at this single quantity.

Section 2.3.1 showed that stratocumulus are associated with high pressure regions and shallow boundary layers whilst cumulus are more frequently found in deeper boundary layers away from high pressure regions. A strong relationship between boundary layer depth and cloud cover would therefore be expected just from regional considerations. In regions where there is a climatological transition from stratocumulus to cumulus, there will be a strong correlation between the depth of the boundary layer, cloud type, and hence cloud fraction, as synoptic conditions cause a more, or less, rapid transition than in the climatological mean. It is not clear whether the LTS/cloud amount relationship is giving any more information than the climatological relationship between cloud type and boundary layer depth. The dependence on surface pressure includes the effect of the strong subsidence expected in high pressure regions on the boundary layer depth, as do the stability of the pressure gradient above the inversion and the inversion strength. The usefulness of LTS may simply lie in its relationship to boundary layer depth, a quantity that may be less precisely defined in large scale atmospheric models than the temperature at 700 mb height.

7.3.2 Effect of Varying Temperature Structure above the Inversion

Simulations with varying inversion jumps in both θ_l and q_t, with varying θ_l vertical gradient above the inversion and with varying θ_l relaxation have been performed. Figure 7.4 shows the liquid water content during the eighth day of simulations with different above inversion characteristics. These are: inversion θ_l jumps of 13 °C and 5 °C (rather than the standard 9 °C), an inversion q_t jump of 7 gkg^{-1} (rather than the standard 3.5 gkg^{-1}, this simulation is discussed in the following section), vertical θ_l gradients above the inversion of 0.003 $°Cm^{-1}$ and 0.007 $°Cm^{-1}$ (rather than the standard 0.006 $°Cm^{-1}$) and relaxation timescales for the above inversion θ_l of 3 hours and 24 hours (rather than the standard 8 hours). Figure 7.4 shows that changing processes in the free atmosphere can significantly affect the boundary layer depth, the cloud thickness and peak liquid water content, and the degree of decoupling and cumulus-coupling between the surface and stratocumulus cloud layers.

As expected, decreasing the θ_l inversion (Figure 7.4d), decreasing the θ_l gradient above the inversion (Figure 7.4e) and increasing the amount of temperature relaxation (equivalent to cooling the free atmosphere and reducing the temperature inversion, Figure 7.4h) all lead to deeper boundary and cloud layers (Table 7.1) than in the standard simulation (Figure 7.4a).

Most of the simulations shown in Figure 7.4 (the exception is Figure 7.4b the reduced above inversion q_t case) show characteristics that can be understood in terms of the stability of the lower troposphere. When the potential temperature of the atmosphere above the inversion is warmer, more potential energy is required to entrain above inversion air into the boundary layer, thus more TKE is required to increase the boundary layer depth. As the entrained air is warmer, the region near the cloud top is stabilised, reducing the TKE near the cloud top (although it must be remembered that destabilising processes such as longwave cooling and the evaporation of cloud droplets are still occurring). Figure 7.5 shows daily average profiles of θ_l, q_t, liquid water content and q_t flux from the same day of the same simulations shown in Figure 7.4. The simulation with the lowest potential temperature gradient above the inversion shows the deepest boundary layer, the simulation with the large initial θ_l inversion jump the shallowest. The depth of the boundary layer for all cases where the changes are made to the temperature structure (i.e. varying in θ_l inversion strength, varying the θ_l gradient above the inversion and varying the temperature relaxation conditions above the inversion) is well predicted by the LTS. The boundary layer depth is however better correlated to the mean boundary layer θ_l and q_t than to the LTS. Faster boundary layer growth leads to a more nearly well mixed boundary layer for a given boundary layer depth.

7.3.3 Effect of Varying Humidity Structure above the Inversion

Figure 7.5 clearly shows the anomalous behaviour of the simulation with low humidity above the inversion (the q_t inversion jump was increased from 3.5 gkg^{-1} in the standard simulation to 7 gkg^{-1}). The peak liquid water content for this cumulus under stratocumulus stage of the simulation is the highest among the simulations with changed above inversion characteristics, the boundary layer is coolest and the total water flux greatest at all levels. The boundary layer is also less stratified, both in θ_l and in q_t. This is emphasised in Figure 7.6, which shows θ_l, q_t, liquid water content and TKE for two simulations with similar boundary layer heights. The simulation with low humidity above the inversion (blue line in Figure 7.5, hereafter $\Delta q+$) and the simulation with increased temperature relaxation above the inversion (orange line in Figure 7.5) show very different characteristics. The reduced humidity above the inversion has resulted in a colder drier boundary layer than in the comparison case (Figures 7.6a,b). The boundary layer is however

more nearly well mixed in the Δq+ case and the result is a similar q_t at the cloud top in the two simulations (0.2 gkg^{-1} different, Figures 7.6c,d). As the boundary layer in the Δq+ case is cooler, this gives rise to the large stratocumulus layer liquid water content. The reduced stratification of the boundary layer in the Δq+ case means that the boundary layer is more coupled than in the other cases (although similar to the case with the large initial temperature inversion, which has a much shallower boundary layer than the Δq+ case). The first cumulus cloud forms a day later in the Δq+ case (Table 7.1). The cumulus clouds in the Δq+ case are therefore smaller than the comparison case (Figures 7.6e,f). The coupling between the surface and stratocumulus layers in the Δq+ case results in a drier surface layer which in turn leads to an increased total water flux (Figure 7.5). This tends to reinforce the tendency to form a more coupled boundary layer and partially offsets the extra drying of the cloud layer due entrainment of very dry air from above the inversion. The TKE (Figures 7.6g,h) generated by the rise of each cumulus cloud into the stratocumulus layer is greater in the Δq+ case.

7.3.4 Boundary Layer Dynamics and CTEI

The simulations shown in Figure 7.6 are both unstable to CTEI according to Deardorff (1980) and both stable according to MacVean and Mason (1990). The Δq+ case is the more unstable of the two. CTEI cannot be considered just in terms of the temperature and humidity contrasts between cloud and above inversion air (Sections 2.2.3, 2.3.3 and 3.2.3). Lewellen and Lewellen (1998) realised that it was necessary to consider the contribution of eddies on all scales up to the boundary layer scale. They studied entrainment in well mixed boundary layers in quasi-steady state under strongly stable inversions using LES. They argued that in well mixed conditions the small-scale eddies near the inversion (as studied by MacVean and Mason 1990) are controlled by the boundary layer-scale eddies. There is still little consensus about the conditions that are both necessary and sufficient for CTEI to occur and to break up a cloud layer. This study suggests that in boundary layers that are not well mixed that the boundary layer structure and the degree of decoupling may need to be known to predict the effect of CTEI on the cloud.

The present study suggests the following possible interaction between CTEI and the structure of the deep decoupled or cumulus-coupled boundary layer:

a) Entrainment of air much drier but only slightly potentially warmer than the cloud top air initially strongly dries and weakly warms the cloud top region.

b) Evaporation of cloudy air droplets that have mixed into the entrained parcel cause the parcel to be strongly cooled and if dense enough the entrained parcel can sink through the cloud.

c) The negative buoyancy that can be generated under these circumstances can act to recouple the cloud and surface layers. The resulting mixing acts to moisten and cool the cloud layer and to warm and dry the surface layer. The cloud liquid water is thus replenished by the injection of moisture from the surface. Further feedback includes the increase in longwave cooling due to increased liquid water (and during the day an increase in shortwave heating) and the increased latent heat flux driven by the drying of the boundary layer by mixing. In the simulation shown the whole boundary layer is cooled by increased longwave cooling. Surface heat and buoyancy fluxes are also increased, promoting the tendency to form a coupled boundary layer.

d) In a recoupled boundary layer the cloud top will be moister and colder than in a decoupled boundary layer. The inversion jump in both q_t and θ_l will thus increase, the former acting to increase the tendency for CTEI, the latter to reduce it. Both however act to sustain the cloud liquid water.

Whilst the feedback mechanisms have not been quantified in the present study, the role of dense downdrafts originating near the cloud top in maintaining coupling in deeper boundary layers suggests boundary layer, and not just inversion, structure needs to be taken into account when considering the criteria for breakup of cloud layers. It was suggested in Section 2.3.3 that input of moisture from the surface layer might prevent the marine stratocumulus layer from drying out. The recoupling of surface and cloud layers driven by dense downdrafts shown in the model may provide a mechanism for the observed persistence of marine stratocumulus under conditions where they might, from consideration of cloud top processes alone, seem vulnerable to rapid dissipation. Figure 7.5 clearly shows that the $\Delta q+$ boundary layer is on average drier than all the other cases so maintenance of the cloud would eventually not be possible as the surface layer becomes too dry to maintain the stratocumulus. The model shows however that dry air above the boundary layer results in a boundary layer that remains fully coupled for longer.

7.4 Varying SST Gradient and Wind Speed

Figure 7.7 shows the effect of varying the SST gradient and wind speed on the simulation both separately and together. Simulations are performed with SST gradients of 2 °C day^{-1} (Figure 7.7a), 1 °C day^{-1} (Figure 7.7b, the standard simulation has a SST gradient of

1.5 °C day^{-1}), with wind speeds increased (Figure 7.7c) and decreased by 50% (Figure 7.7d) from the standard 7.8 ms^{-1}, and with SST gradients and wind speeds both increased Figure 7.7e) and decreased by 20% (Figure 7.7f). The liquid water content is shown for 12 hours from the eighth day of simulation for these 6 cases with varying SST gradients and wind speeds.

Increasing the SST gradient (Figure 7.7a) initially acts to warm and moisten the boundary layer with the result that the cloud layer has approximately the same thickness and liquid water content as the standard simulation. The surface fluxes are larger in the increased SST gradient case. By the third day of the simulation the boundary layer is about 200 metres deeper, the additional entrainment being driven primarily driven by the increase of surface water flux. By this stage the boundary layer is 1.8°C warmer than the standard case (the SST is 2.0 °C warmer) and 0.3 gkg^{-1} moister. Again the cloud is of similar thickness to the standard case and the maximum liquid water content is about 0.6 gkg^{-1} in both cases. The TKE at the cloud top is slightly greater in the case with the larger SST gradient. Entrainment events occur more frequently, as expected from the increased boundary layer depth. On the third day of the simulation the heat flux below the cloud base becomes negative but in the standard simulation remains positive. Both simulations show the drying effect of entrainment on the surface layer at this stage, with peaks in the surface total water flux following each entrainment event. By the start of the sixth day of simulation the higher SST gradient case is much more stratified in both θ_l and q_t. Cumulus clouds first formed on the fifth day, a day earlier than in the standard case (Table 7.1). The cumulus clouds on day six of the simulation are increasing the stratocumulus liquid water content faster than the entrainment can decrease it. The boundary layer is more than 400 metres deeper than in the standard case, which has a boundary layer depth of about 1500 metres. By day eight the cumulus clouds are still acting to moisten the stratocumulus layer in the increased SST gradient case but the liquid water remains approximately constant in the standard case at this stage. The increased water input to the stratocumulus is due to the larger surface total water flux in the increased gradient case. Both the standard and the increased SST gradient case are decoupled but the decoupling is greater in the latter case.

The simulation with a decreased SST gradient (Figure 7.7b) shows the opposite features. The boundary layer is cooler and drier than the standard case. The cumulus clouds form late on in the simulation, on day eight (Table 7.1). The cumulus occur infrequently and those that do form act to input small amounts of liquid water into the cloud. This is enough to maintain the cloud because the entrainment rate is also small. The simulation with an increased wind speed (Figure 7.7c), like the increased SST gradient case, shows boundary layer warming and moistening due to increased surface fluxes. The TKE is

higher in this case throughout the boundary layer. Initially the cloud thickens and the liquid water content increases but the boundary layer growth is similar to the standard case. By the end of the third day the boundary layer is slightly deeper in the increased wind speed case. At this stage in the simulation the cumulus clouds are smaller than in the increased SST gradient case and input less water into the stratocumulus layer. Figure 7.7 e (f) shows the combined effect of increasing (decreasing) both the wind speed and SST gradient together. The results of these simulations are summarised in Table 7.1 and have predictable characteristics compared to the simulations where wind speed and SST are increased or decreased separately.

Figure 7.8 shows data from the same simulations but now plotted as a function of SST, between 21 and 23 °C. Although SST has been shown to be a good predictor of cloud amount (Hanson 1991, Norris and Leovy 1994) Figure 7.8 shows that the boundary layer history is important in predicting the simulated cloud thickness. The evolution in all cases can be understood in terms of the boundary layer depth and the degree of decoupling. Increasing the SST gradient deepens the boundary layer faster than in the standard simulation and the boundary layer tends to become more decoupled with time. Increasing the wind speed also deepens the boundary layer but increases the surface fluxes allowing the boundary layer to remain coupled for longer and then delaying the onset of the cumulus-coupled boundary layer. In the decoupled regime the simulated liquid water content at the top of the stratocumulus decreases with time whereas in the cumulus-coupled regime the simulated liquid water content remains fairly constant.

These simulations suggest that evolution of the boundary layer under conditions of varying SST gradients and wind speeds can be viewed in terms of the ability of the surface forcing to firstly promote boundary layer growth which leads to decoupling of the boundary layer (when entrainment driven by cloud processes becomes responsible for the boundary layer growth) and secondly to promote cumulus coupling which supplies water to the decoupled cloud layer (and can also drive entrainment). Thus it is only in the decoupled regime that boundary layer growth is not influenced by the surface fluxes, particularly the surface water flux.

7.5 Varying Solar Radiative Forcing and the Diurnal Cycle

This study has used diurnally averaged solar radiation in order that the boundary layer evolution can be more easily understood without the complication of diurnal variability, one of the advantages of models over reality. This study will not investigate the effect of diurnal forcing on the boundary layer but will here demonstrate that the daily average evolution is

similar if the diurnal cycle is included in the simulation. Figure 7.9 shows the effect of varying solar forcing on the liquid water content of the simulation. Including the diurnal cycle in the simulation (Figure 7.9b) leads to a clear difference between night and daytime conditions. During the night the liquid water content in the stratocumulus layer is large, more than 1 gkg^{-1}. During the day the stratocumulus layer is eroded completely. The boundary layer is diurnally decoupled, although later in the simulation the boundary layer is cumulus-coupled throughout the day. Daily mean values are however similar to the standard case with no diurnal cycle (Table 7.1) and remain so throughout the simulation. Figure 7.9 shows the stratocumulus layer reforming after strong mixing between the surface and cloud layers by cumulus clouds and can be considered to result from the spreading out of cumulus. The stratocumulus layer always reforms at night and is thicker than the stratocumulus layer in the simulation with diurnally averaged radiation. A strong diurnal signal is expected, but the simulations confirm the results of model studies (e.g. Krueger et al 1995a, Wyant et al. 1997) which suggest that diurnal forcing does not strongly affect the overall evolution of the boundary layer in the transition from stratocumulus to deep cumulus under stratocumulus boundary layers.

The effect of increasing and decreasing the diurnally averaged solar radiation on the simulated liquid water is also shown in Figure 7.9 and Table 7.1. Reducing the diurnally averaged solar radiation (daily mean solar zenith angle of 0.4 rather than the standard 0.5, Figure 7.9d) increases the amount of turbulence near the cloud top as there is less shortwave heating to offset the longwave cooling. The boundary layer therefore grows faster than in the standard case and is more decoupled. The boundary layer is cooler, despite entraining more warm air from above the inversion and the mean q_t is lower. The reverse is true for the case with increased solar radiation (daily mean solar zenith angle of 0.6, Figure 7.9c). These simulations indirectly show the effect of the longwave cooling in coupling the boundary layer by offsetting this cooling by varying amounts. The change in cloud top radiative forcing due to this change in solar radiation is enough to reverse the expected increase in decoupling with increasing inversion height (Table 7.1). The case with weak solar radiation has a much higher liquid water content in the cloud as the conditions are cooler and the cloud and subcloud layers are more coupled in this simulation than in the standard simulation.

7.6 Comparison with Other Studies

7.6.1 Cloud Climatological Studies

As relatively few measurements have been made in the midlatitude transition region the model predicted effects of varying external forcing cannot be validated from the results of experimental campaigns. It is therefore necessary to appeal to climatological studies using combinations of merchant and ocean weather ship cloud observations, radiosonde measurement from OWS (particularly OWS N which operated at 30°N 140°W between 1949 and 1974), ERBE (Earth Radiation Budget Experiment) radiation data and reanalysis model output. These studies are hampered by problems with the observations used such as: coarse 50 mb resolution of most of the archived OWS radiosonde data and solar heating of the humidity sensor for part of the period (Klein et al. 1995, Klein 1997, Norris 1998), the difficulty of observing clouds on dark nights and the use of the combined stratiform cloud type (observations of stratocumulus, cumulus under stratocumulus, stratus and fog are all combined, Klein and Hartman 1993, Weaver and Ramanathan 1997).

The present study suggests that the divergence has an important effect on the boundary layer structure, drying the boundary layer and suppressing its growth. In contrast Klein and Hartmann (1993) found no relationship between the seasonal cycle of stratiform cloud amount and the divergence or the strength of the subtropical high. Although the timescales studied here and by Klein and Hartmann (1993) are very different, Klein (1997) found the same relationships between low cloud amount and meteorological variables on monthly mean and synoptic timescales. Strong relationships are found by Klein and Hartmann (1993), Klein (1997), Klein et al. (1995) and Norris (1998) between low cloud amounts and LTS. The simulations presented in this study all retain an unbroken stratocumulus layer so comparisons with cloud fraction are not possible. The simulations do show however that for LTS between 8 and 17°C that the total column liquid water content decreases by 7% per 1°C decrease in LTS. Klein and Hartmann (1993) predict a 6% decrease in areal cloud fraction in stratocumulus regions per 1°C decrease in LTS. Thus the simulations show a similar tendency to the observations in this respect. Figure 7.5 also shows that the deepest boundary layers tend to be the most stratified. This is consistent with the findings of Norris (1998) and Albrecht et al. (1995b). Norris (1998) also notes that in soundings taken in cumulus under stratocumulus conditions during ASTEX the region of strongest gradient in both potential temperature and q_t is in a single jump near the middle of the boundary layer. This study shows strongly stratified regions near the base of the cumulus clouds, consistent with these observations from ASTEX. The OWS soundings are at too coarse a resolution to show this. Klein et al. (1995) use summer data from OWS N

and COADS to study the factors which affect cloudiness at OWS N. They conclude that high cloud cover can exist long after the boundary layer has ceased to be well mixed, as shown in the present study. High cloud amounts are correlated with warm dry air above the inversion. Warm dry air above the inversion is associated with increased subsidence and so this is not unexpected. However this relationship with dry air above the inversion is also what is predicted by the model in the present study due to the enhanced recoupling of the decoupled boundary layer under conditions of CTEI. The two effects cannot be separated from the data presented by Klein et al. (1995). Existing theories of CTEI suggest the effects of warm air and dry air above the inversion should have opposing effects on the cloud amount.

7.6.2 Model Studies

The two-dimensional modelling studies of Krueger et al. (1995a,b) and Wyant et al. (1997) were too computationally intensive to perform many simulations with differing external conditions. The results of the mixed layer model studies of Albrecht (1984) and Wang (1993) have been shown by Bretherton (1993) to strongly depend on assumptions made about dependencies that are poorly known (see Section 3.3.4). Reliable model data of the effect of varying external forcing on long simulations of stratocumulus-topped boundary layer evolution are therefore not available. However, from the results presented in the previous sections some inference about the possible effects of the choice of external forcing made by Krueger et al. (1995a,b) and Wyant et al. (1997) can be made.

The present study suggests that LTS is a good predictor of model boundary layer growth and that deeper boundary layers tend to be more decoupled. Observations of cloudy boundary layers suggest that deeper boundary layers are likely to contain cumulus clouds and have lower cloud cover. The simulations from the literature are therefore likely to be affected by the choice of inversion and above inversion structure. Krueger et al. (1995a,b) used a potential temperature gradient above the inversion of 0.0064 $°Cm^{-1}$, Wyant et al. (1997) used 0.0034 $°Cm^{-1}$. Table 6.1 suggests the potential temperature gradient above the inversion typically varies between 0.005 and 0.007 $°Cm^{-1}$. The initial θ_l jump across the inversion in the simulation of Krueger et al. (1995a,b) was 14°C and Wyant et al. (1997) used 12.6°C, both greater than the typical value of 9°C suggested by the observations presented by Kuo and Schubert (1988). Both Krueger et al. (1995a,b) and Wyant et al. (1997) effectively hold the potential temperature above the inversion constant throughout the simulation. This means that as the boundary layer grows the depth the difference between the potential temperature at 700mb and the SST must decrease (and hence the LTS). The composite profiles of Albrecht et al. (1995b) however suggest that the above inversion

temperature is usually higher in cumulus rather than stratocumulus conditions. Thus the reduction in LTS through the transition is probably over estimated in these models. The air entrained into the boundary layer will be cooler in these simulations compared to a simulation in which the subsidence is allowed to warm the free atmosphere (although it is noted that the large subsidence rates used in all the simulations would lead to unrealistically large heating above the inversion). Results from the present study suggest that these choices of above inversion structure will have affected these simulations from the literature in the following way. The large initial θ_l jumps across the inversion would be expected to suppress the boundary layer growth at first, particularly for the Krueger et al. (1995a,b) simulation. This is not however observed. In the present study increasing the initial θ_l jump across the inversion to 13 °C (rather than the more commonly observed 9°C) resulted in a boundary layer 1.5 km deep, 25 % shallower than the standard case. After eight days simulation the boundary layer was 0.4 °C cooler and 1.3 gkg^{-1} moister. This shallow boundary layer is well mixed and remains coupled for longer with the first cumulus cloud appearing two and a half days later than in the standard simulation. Figure 7.10a shows the evolution of the inversion height for four simulations from Section 7.2.2. These are the standard simulation, the simulation with an initial θ_l jump of 13 °C (rather than 9°C), the simulation with a potential temperature gradient above the inversion of 0.0035 $°Cm^{-1}$ (rather than 0.006 $°Cm^{-1}$) and the simulation with a temperature relaxation timescale of 3 hours (rather than the standard 8 hours). In the simulation with the large initial temperature jump across the inversion the growth of the boundary layer is initially small but in the latter part of the simulation the growth rate is similar to the standard simulation. Figure 7.10b shows the humidity difference between the surface layer and just below the inversion for these four simulations. This gives a good indication of the degree of decoupling of the boundary layer. The simulation with the strong initial temperature inversion remains more coupled than the other simulations but Figure 7.10c which plots the same data as a function of boundary layer depth shows that for a particular boundary layer depth this simulation is slightly more decoupled than the others. These simulations show that a low θ_l vertical gradient above the inversion will lead to a deeper boundary layer (40% deeper than the standard case after eight days) which continues to grow faster throughout the simulation. The boundary layer at a particular time in this simulation is the most decoupled (Figure 7.10b), but for a given depth actually more well mixed (Figure 7.10c). The importance of the increased θ_l relaxation above the inversion increases with time (Figure 7.10a) and after about 5 days simulation the boundary layer depth is increasing faster than the standard simulation as the θ_l inversion strength decreases with time relative to the standard simulation. Neither of the two-dimensional simulations show a suppressed initial boundary layer growth due to the very stable inversion structure. The boundary layer growth the in Wyant et al. (1997) simulation is similar to the standard simulation in the present study but the growth rate is very nearly constant

throughout. The conditions imposed by Wyant et al. (1997) might be expected to show little growth for the first few days then an increasing rate of growth as the effects of the low potential temperature gradient and strong temperature relaxation become important as the boundary layer grows. The growth rate in the Krueger et al. (1995a,b) simulation is also fairly constant, despite an even larger initial temperature inversion strength. This may be partly due to the higher initial SST used in this study and the slightly larger SST gradient of 1.8 °Cday^{-1}. The model in the present study shows reduced growth when the temperature inversion is strong. The growth remains small until the temperature inversion has been eroded by warming of the boundary layer to values close to those commonly observed (Kuo and Schubert 1988). This model behaviour seems reasonable but at variance with the two-dimensional model results.

7.7 Summary and Discussion

The deepening and decoupling of stratocumulus-topped boundary layers has been investigated under varying conditions. This has only been possible in the past with mixed layer models, here we have performed a wide range of simulations of up to twelve days duration. Simulations are all run with increasing SST in order that the boundary layer deepens with time. As in the simulation described in Section 6.3 the diurnal cycle has been excluded to concentrate on longer timescale evolution. Strong subsidence is required to constrain the rapid growth of the inversion height in the latter part of the simulation, decreasing the vertical velocity results in deeper, more decoupled boundary layers with thicker cloud layers containing more liquid water. The converse is true for simulations with increased vertical velocity. The structure above the boundary layer impacts on the properties and structure of the boundary layer. Most of the effects can be understood in terms of the stability of the lower troposphere defined in terms of the potential temperature difference between 700 mb and the SST. More stable conditions lead to shallower, cooler and moister boundary layers. These shallower boundary layers are more well mixed than the deeper boundary layers predicted when the conditions are less stable and take longer to reach the decoupled and cumulus-coupled stage of development. Faster boundary layer growth results in a boundary layer that is more coupled than a boundary layer of comparable depth that has grown more slowly.

The simulated effect of dry air above the inversion on the structure of the decoupled boundary layer suggests a mechanism for the maintenance of stratocumulus under conditions where CTEI might be expected to be important. Many criteria have been suggested for the onset of the instability, which has the potential to cause rapid entrainment of dry air and thus dissipate the cloud. The criteria have become more stringent with time as the evidence for

stratocumulus layers persisting under conditions thought to be unstable has grown. If, as in the present study, the instability acts to recouple the decoupled boundary layer and mix water from the surface layer into the cloud, then CTEI may act to maintain the cloud, at least initially. The mean boundary layer is drier when the air above the inversion is drier, as expected, but q_t near the inversion can be greater due to greater mixing between the cloud and subcloud layer. It seems likely therefore that CTEI might act to delay decoupling in deep boundary layers and delay the breakup of the cloud layer until the whole boundary layer has dried sufficiently.

Varying the wind speed and SST gradient affects the surface forcing, which in turn controls the boundary layer growth, the tendency to decouple and the rate of warming and moistening of the boundary layer. Increased surface fluxes initially promote boundary layer growth. As the boundary layer increases in depth, the tendency for the surface and cloud layers to decouple also increases but this is then opposed by the increased surface total water flux which promotes cumulus coupling in the later stages of the simulation. Whilst in general increased wind speeds or SST gradients lead to deeper boundary layers, the degree of decoupling, and hence the cloud liquid water, is dependent on the details of the surface forcing. For example, in the increased SST gradient simulation performed, the peak cloud liquid water is increasing with time in the later part of the simulation as the strong total water flux is forcing strong cumulus coupling of the surface and stratocumulus layers. The remainder of the simulations show nearly constant peak liquid water content in the cumulus coupled stage of the simulation as the surface water fluxes are weaker and are offset by the drying effects of entrainment. In the lowest wind speed case the surface forcing is not strong enough to form a well mixed boundary layer at any stage of the simulation. The boundary layer remains decoupled for the whole simulation and the cumulus clouds which do form are very intermittent.

This study has focussed on boundary layer evolution over periods of several days using averaged solar forcing to more clearly show the longer time scale evolution. Diurnal variability and decoupling has been extensively observed (e.g. Nicholls 1984, Betts et al. 1995, Miller et al. 1998) and modelled (e.g. Bougeault 1985, Duynkerke and Hignett 1993). Simulated daily averaged boundary layer evolution is however similar with and without the diurnal cycle. The diurnal cycle does strongly modulate the boundary layer growth, cloud thickness, liquid water content and the degree of boundary layer decoupling and this should be remembered when comparing these model results with observations. The effect of increasing the solar forcing (with no diurnal cycle) is a shallower, more decoupled boundary layer than in the standard case. The warming due to increased solar absorption is offset by a reduction in entrainment warming and the simulations are of comparable mean θ_l and q_t.

The very decoupled boundary layer structure however means that the cloud layer is both warmer and drier than the standard case and the liquid water content is much reduced. The reverse is true when the solar forcing is reduced. The boundary layer grows faster as the entrainment is greater and the liquid water content in the relatively well mixed boundary layer is significantly larger than in the standard case.

Simulation	boundary layer depth (km)	mean boundary layer θ_l (°C)	mean boundary layer q_t (gkg^{-1})	LTS (°C)	Δq_t surface - cloud top (gkg^{-1})	peak liquid water (gkg^{-1})	first cumulus cloud (day, SST °C)
Standard	1.99	24.2	10.1	12.3	3.7	0.60	6.5 (20.7)
w = -0.003 ms^{-1}	2.46	24.0	10.2	10.6	4.1	1.47	6.8 (20.9)
Divergence + 20%	1.81	24.0	10.2	13.1	3.1	0.45	7.4 (22.1)
Divergence - 20%	2.21	24.4	10.0	12.2	4.1	0.91	5.9 (19.8)
$\Delta q_t = 7\ gkg^{-1}$	2.18	23.5	8.9	12.8	3.2	0.78	7.9 (22.3)
$\Delta\theta_l = 5$ °C	2.39	24.4	9.2	9.7	5.0	0.63	4.3 (17.3)
$\Delta\theta_l = 13$ °C	1.54	23.8	11.4	15.1	2.3	0.55	9.0 (24.6)
$\left.\frac{\partial\theta_l}{\partial z}\right\|_{\text{above inv.}} = 3.5\,°C\,km^{-1}$	2.78	24.5	8.3	6.3	5.9	0.64	5.0 (18.4)
$\left.\frac{\partial\theta_l}{\partial z}\right\|_{\text{above inv.}} = 7\,°C\,km^{-1}$	1.79	24.1	10.7	12.7	3.0	0.61	7.0 (21.5)
relaxation time scale = 24 hours	1.76	24.1	10.8	14.4	2.9	0.61	7.3 (22.0)
relaxation time scale = 3 hours	2.18	24.3	9.6	11.1	4.2	0.62	6.2 (20.2)
increased SST gradient	2.55	28.2	10.8	9.1	5.8	0.75	5.6 (21.7)
decreased SST gradient	1.47	20.0	9.5	15.7	1.9	0.61	8.1 (19.5)
wind speed + 50%	2.13	24.9	10.6	12.5	4.5	0.76	6.1 (20.5)
wind speed - 50%	1.59	22.0	9.4	11.5	3.8	0.30	9.5 (24.1)
inc. SST gradient and wind speed	2.41	27.1	10.8	10.6	5.3	0.75	5.6 (21.1)
dec. SST gradient and wind speed	1.59	21.3	9.5	14.1	2.3	0.52	8.0 (20.7)
increased solar forcing	1.81	24.4	10.3	12.4	3.8	0.38	6.5 (21.0)
reduced solar forcing	2.12	24.0	9.9	12.2	3.5	0.90	6.9 (21.2)
diurnal cycle	2.09	24.1	9.8	12.0	3.6	0.69	2.7 (14.3)

Table 7.1: Mean boundary layer depth (km), mean boundary layer θ_l (°C), mean boundary layer q_t (gkg^{-1}), Lower Tropospheric Stability, LTS, (°C), Δq_t (surface - cloud top, gkg^{-1}), liquid water content below inversion (gkg^{-1}), day of simulation and SST when first cumulus clouds appear (day, SST °C). Mean values quoted are for the eighth day of simulation (Julian day 172).

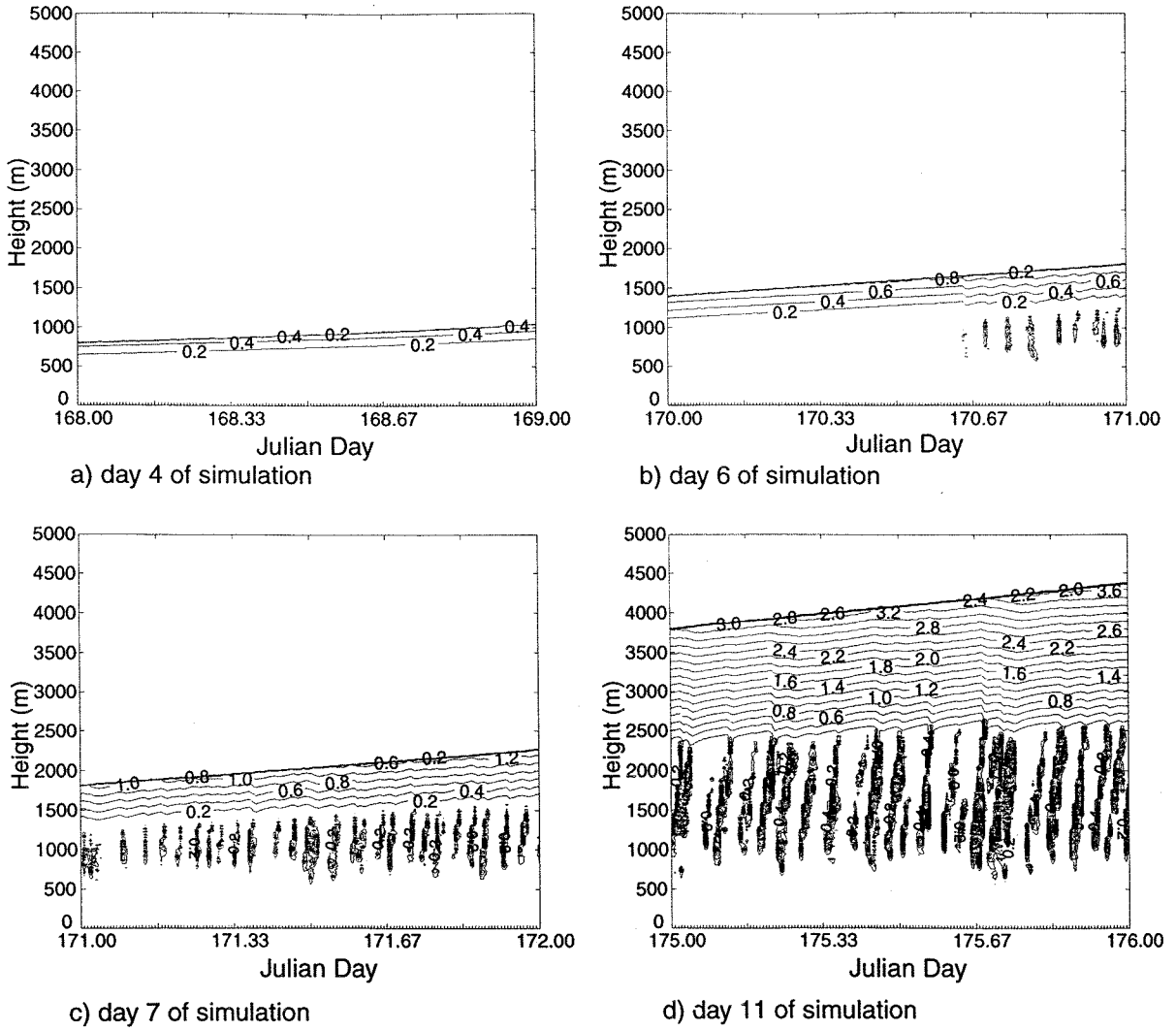

Figure 7.1 Liquid water content (gkg^{-1}) for four days from a simulation with constant vertical velocity at the inversion height. The start of the simulation is at day 164. Each panel shows 24 hours of evolution. a) day 4 of simulation, b) day 6, c) day 7, d) day 11.

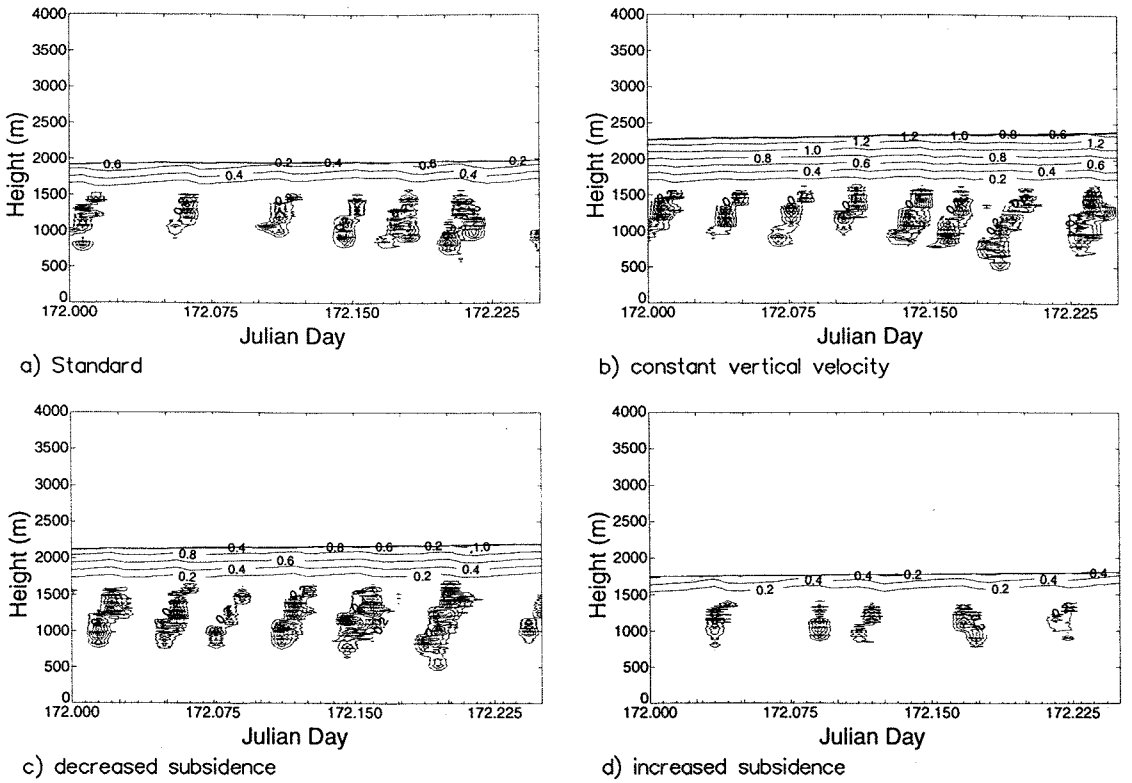

Figure 7.2 The effect of vertical velocity on the simulations. Liquid water content from the first six hours of day eight of the simulation for a) the standard simulation (as described in Chapter 6), b) with constant vertical velocity (the simulation plotted in Figure 7.1), c) with a decreased subsidence rate and d) with an increased subsidence rate. See text for more details.

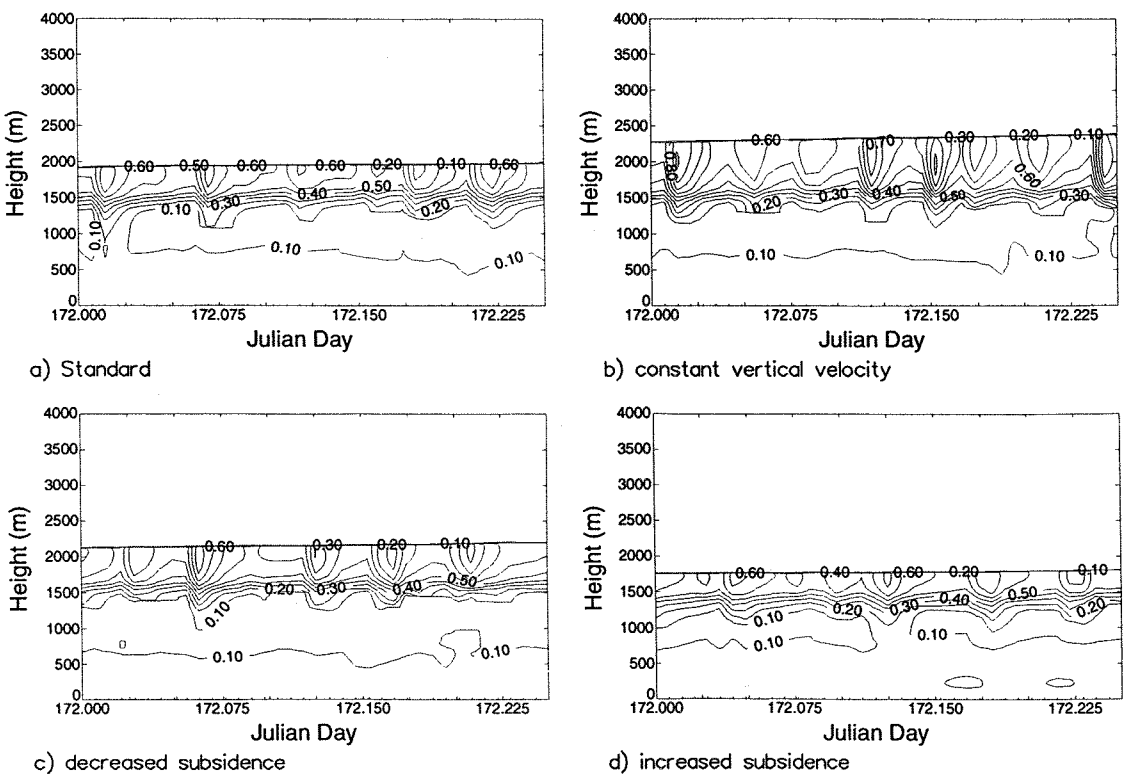

Figure 7.3 As Figure 7.2 but for TKE.

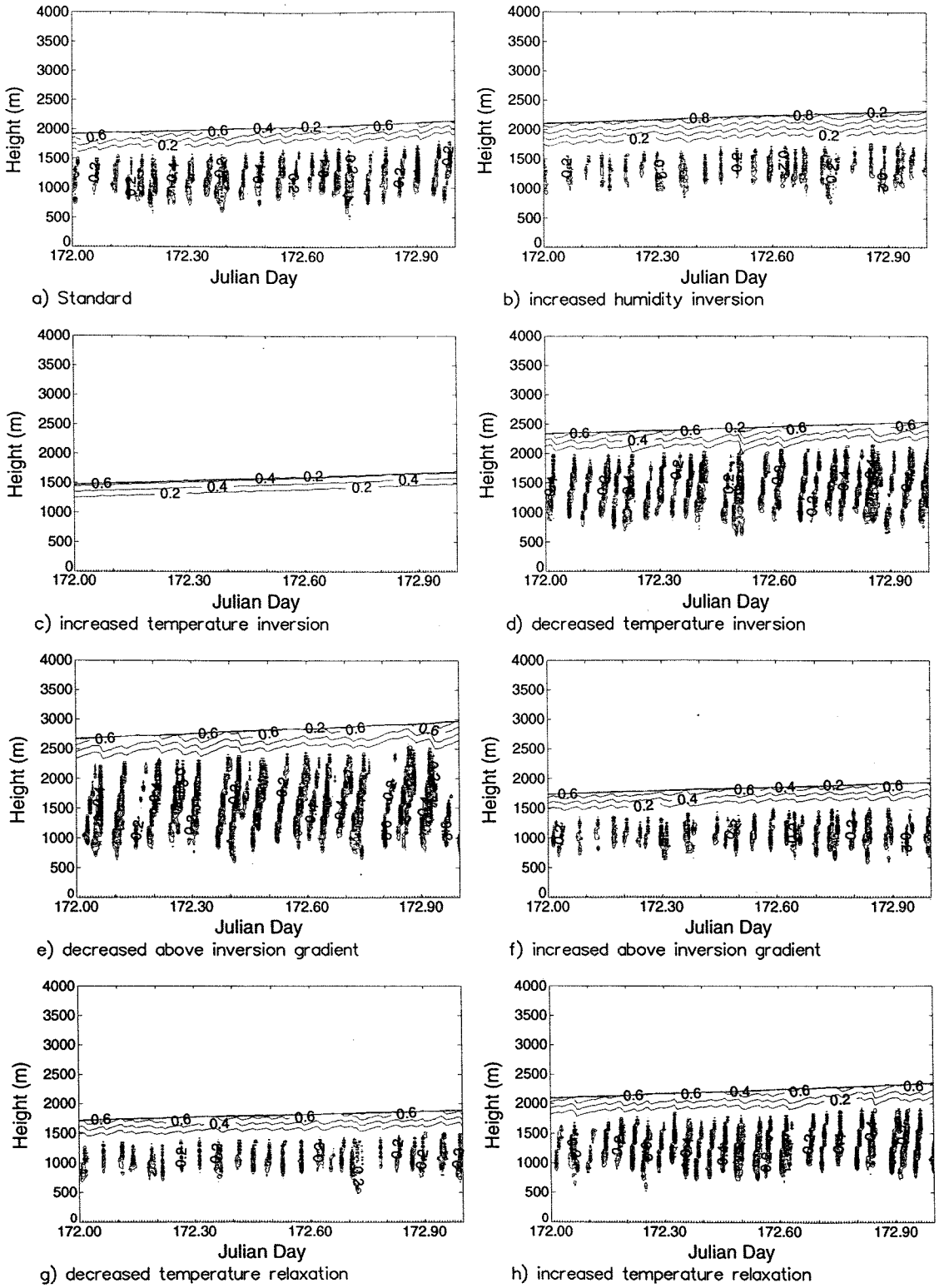

Figure 7.4 The effect of inversion and above inversion structure on the simulations. Plotted is liquid water content (gkg^{-1}) from day eight for different simulations:
a) standard simulation, b) increased q_t jump across inversion, c) increased θ_l jump across inversion, d) decreased θ_l jump across inversion, e) decreased θ_l gradient above inversion, f) increased θ_l gradient above inversion, g) decreased θ_l relaxation above inversion and h) increased θ_l relaxation above inversion. See text for further details.

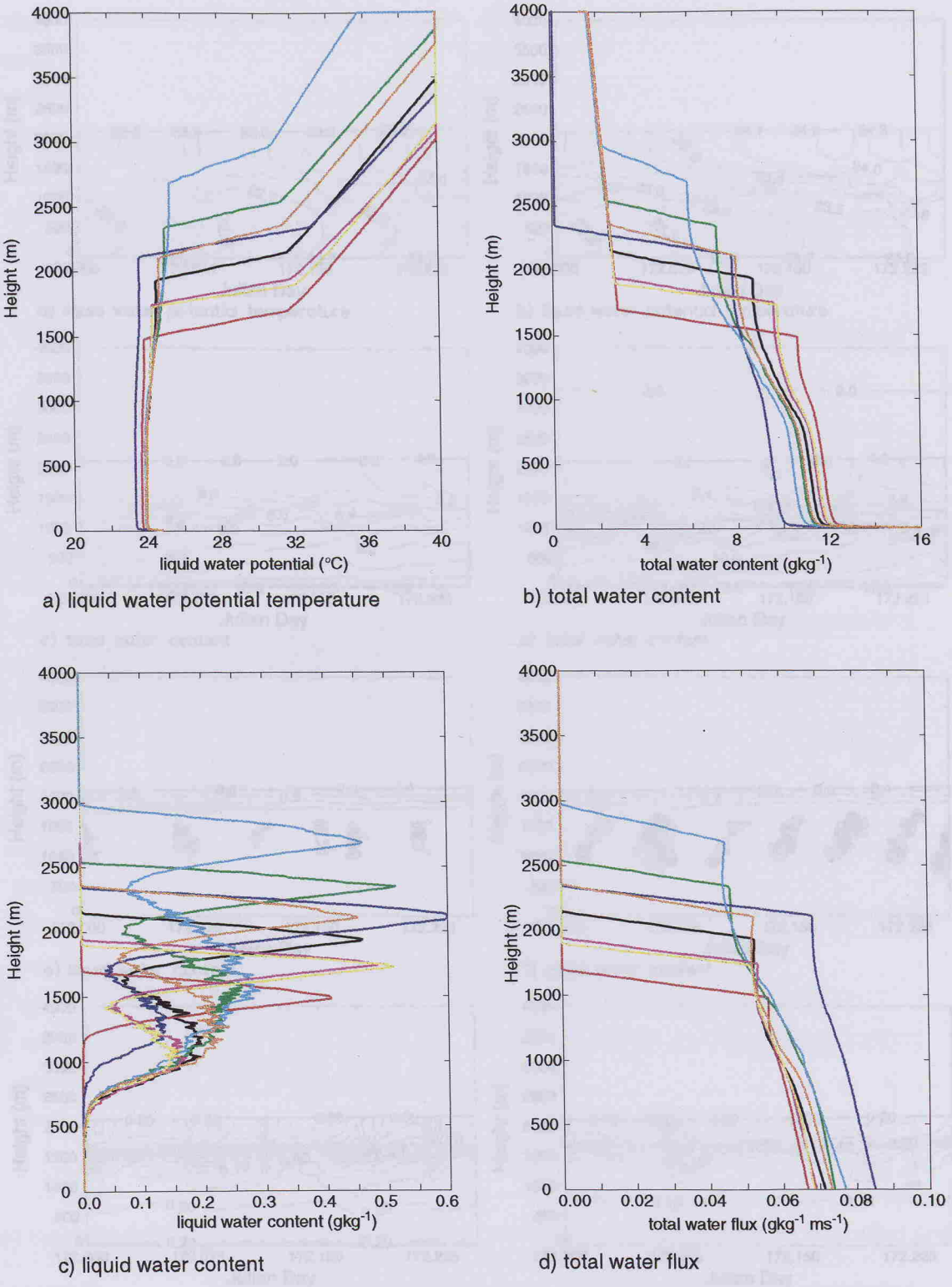

Figure 7.5 Daily average profiles for day 8 from the simulations shown in Figure 7.4. a) θ_l (°C), b) q_t (gkg^{-1}), c) liquid water content (gkg^{-1}), d) q_t flux (ms^{-1}).
Black (standard simulation), red (increased θ_l jump across inversion), green (decreased θ_l jump across inversion), blue (increased q_t jump across inversion), light blue (decreased θ_l gradient above inversion), pink (increased θ_l gradient above inversion), yellow (decreased θ_l relaxation above inversion) and orange (increased θ_l relaxation above inversion).

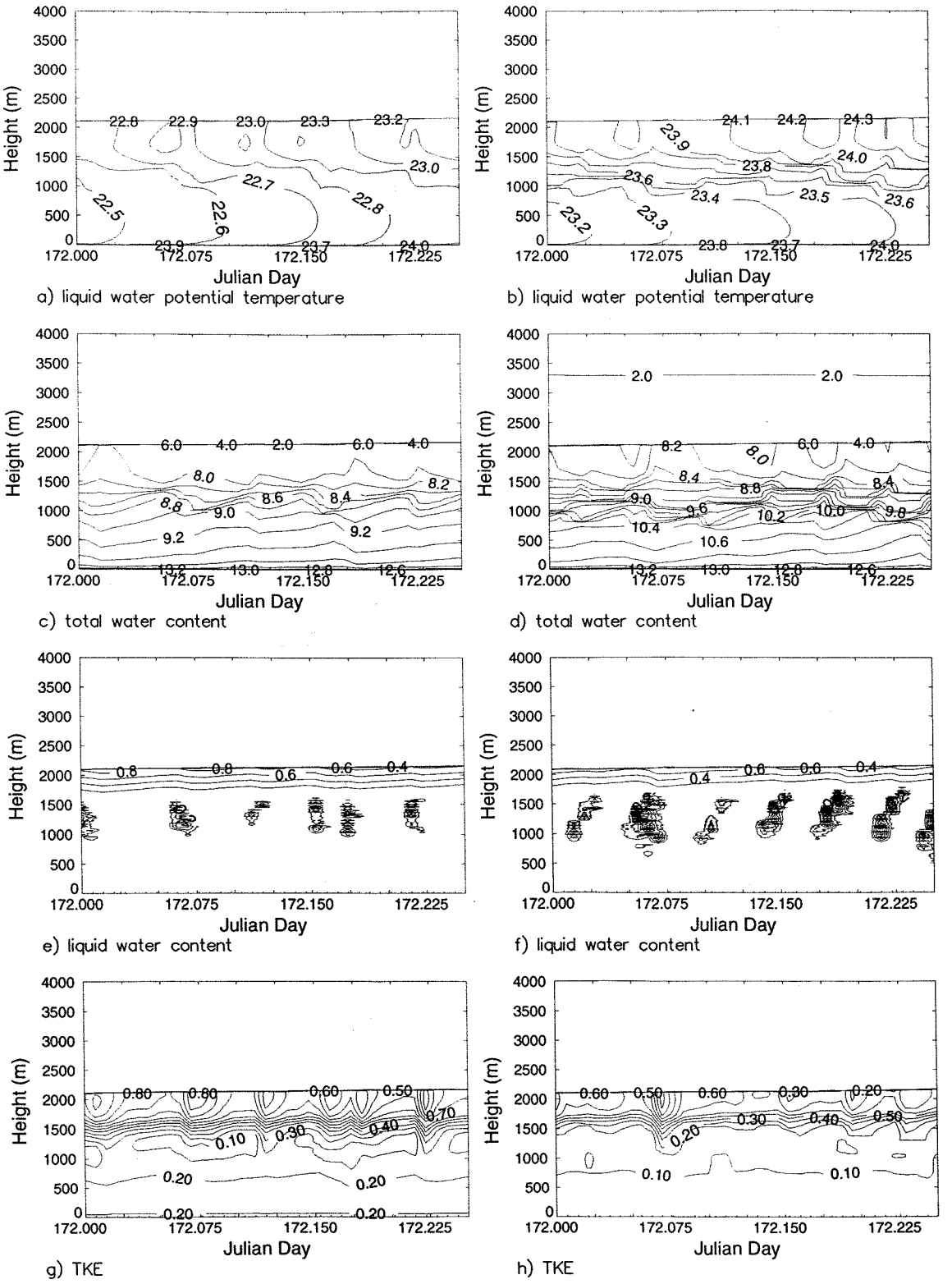

Figure 7.6 Comparison of simulations with similar boundary layer heights but with different above inversion structure. Plots show six hours of evolution from day eight of the simulation. Left: decreased humidity above inversion, Right: weak temperature relaxation above the boundary layer (equivalent to increased temperature above the inversion). a,b) θ_l, (°C), c,d) q_t (gkg^{-1}), e,f) liquid water content (gkg^{-1}), g,h) TKE (m^2s^{-2}).

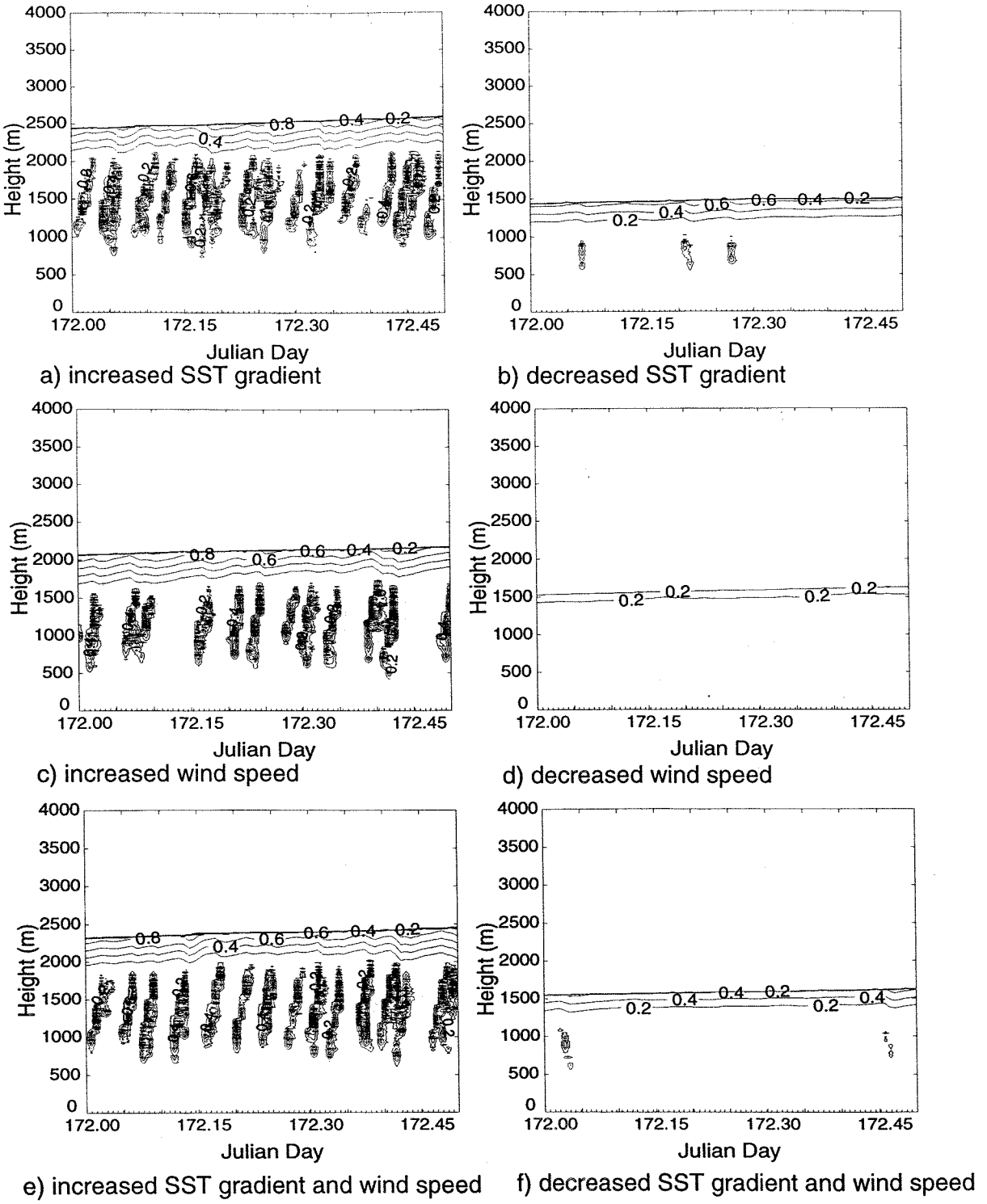

Figure 7.7 Effect of varying SST gradient and wind speed on the simulation. Plots show liquid water content evolution (gkg^{-1}) for 12 hours from day eight of simulation. a) SST gradient = 2 °C day^{-1}, b) SST gradient = 1 °C day^{-1}, c) wind speed = 11.7 ms^{-1}, d) wind speed = 3.9 ms^{-1}, e) SST gradient = 1.8 °C day^{-1} and wind speed = 9.4 ms^{-1} and f) SST gradient = 1.2 °C day^{-1} and wind speed = 6.2 ms^{-1}.

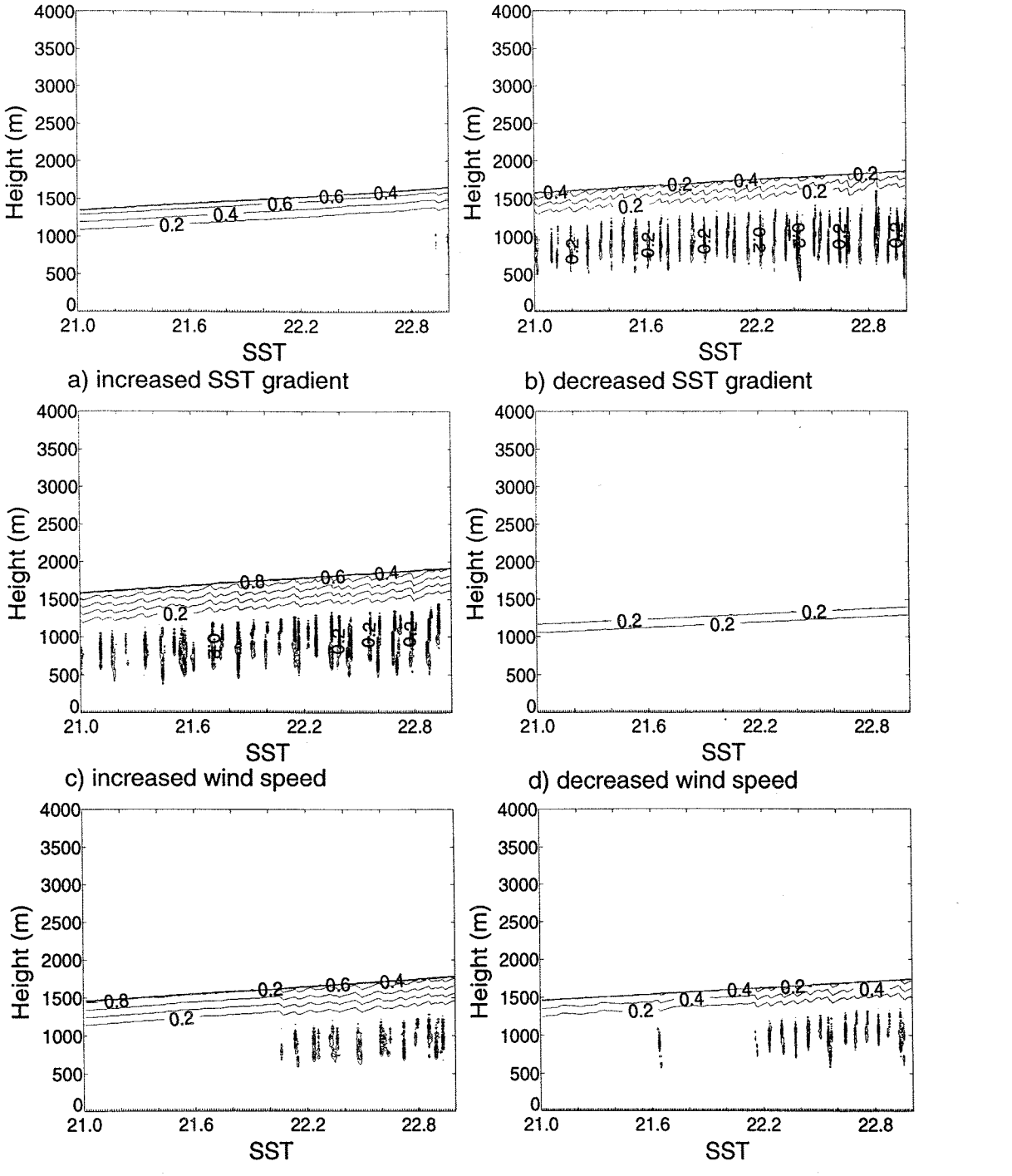

Figure 7.8 Liquid water content (gkg^{-1}) from the same simulations shown in Figure 7.7 but plotted against SST for SSTs between 21 and 23 °C.

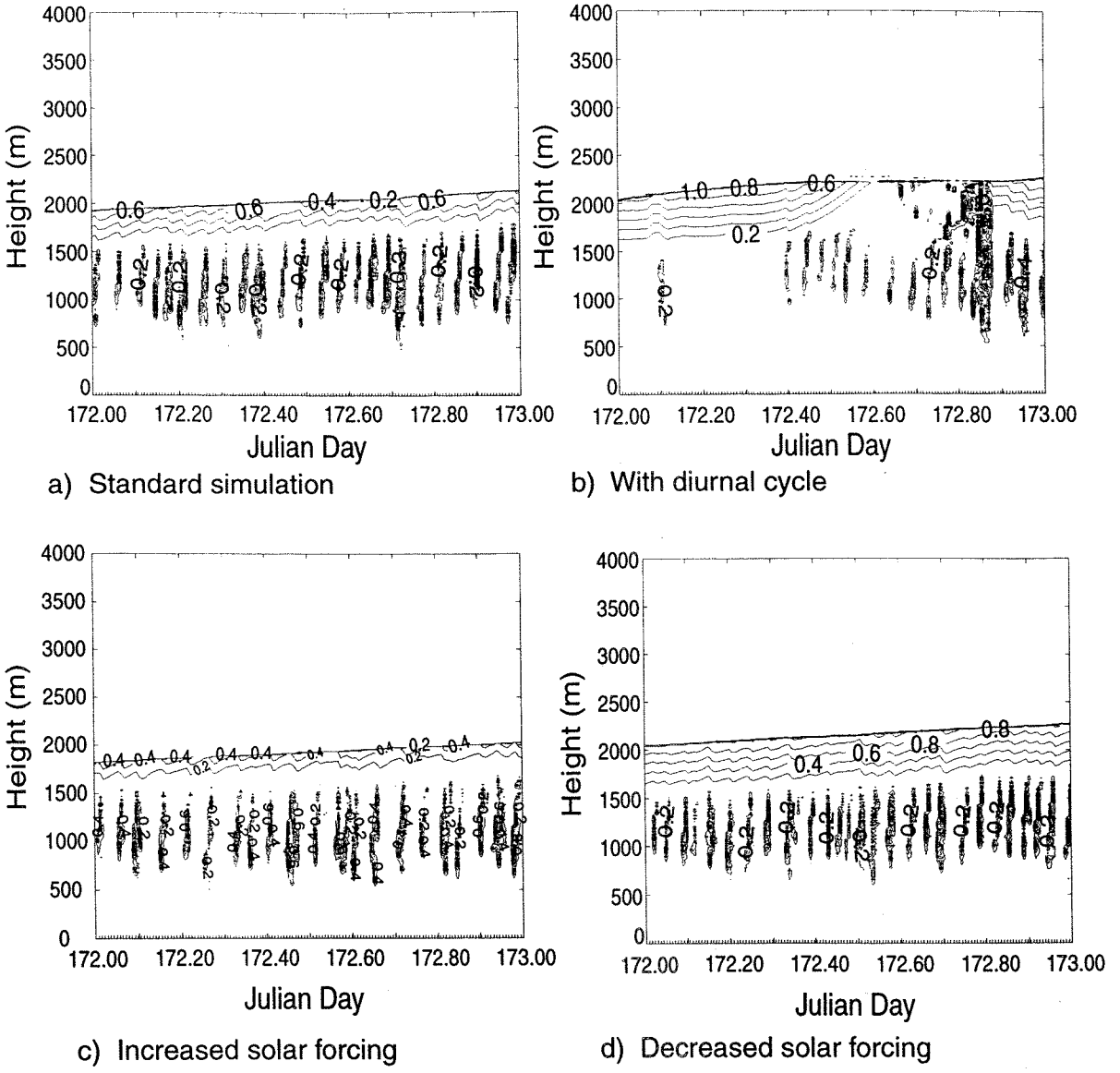

Figure 7.9 Liquid water content (gkg^{-1}) from simulations with different solar forcing, eighth day of simulation.

a) standard simulation,

b) standard simulation but including diurnal cycle,

c) as standard simulation but with increased solar forcing (mean solar zenith angle = 0.6),

d) as standard simulation but with decreased solar forcing (mean solar zenith angle = 0.4).

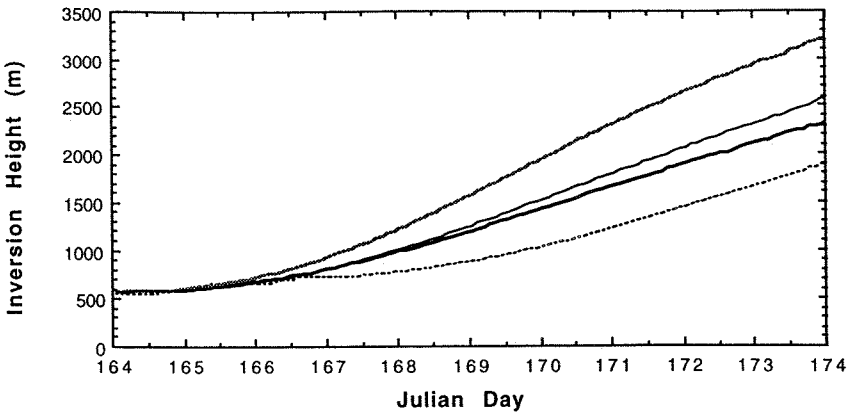

Figure 7.10a Boundary layer growth through the simulations. Thick line: standard simulation, dotted line: $\Delta_i\theta_l$ = 13 °C (standard = 9°C), grey line: potential temperature gradient above inversion 0.0035 °Cm^{-1} (standard = 0.006 °Cm^{-1}) and thin line: relaxation timescale = 3 hours (standard = 8 hours).

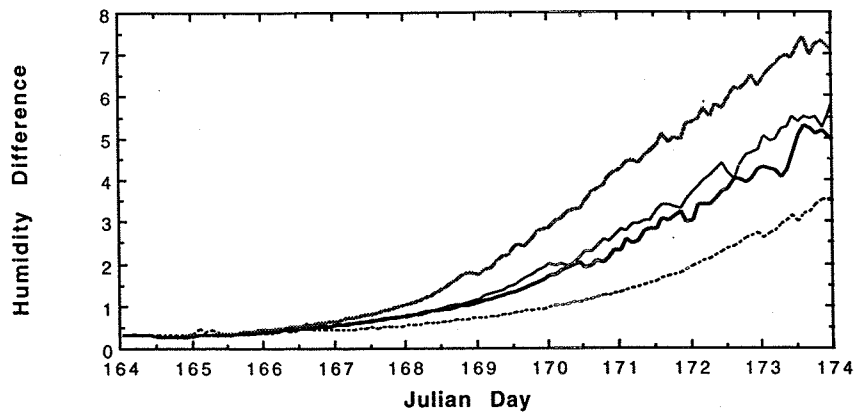

Figure 7.10b As Figure 7.10a but for humidity difference between surface layer and just below the inversion (gkg^{-1}).

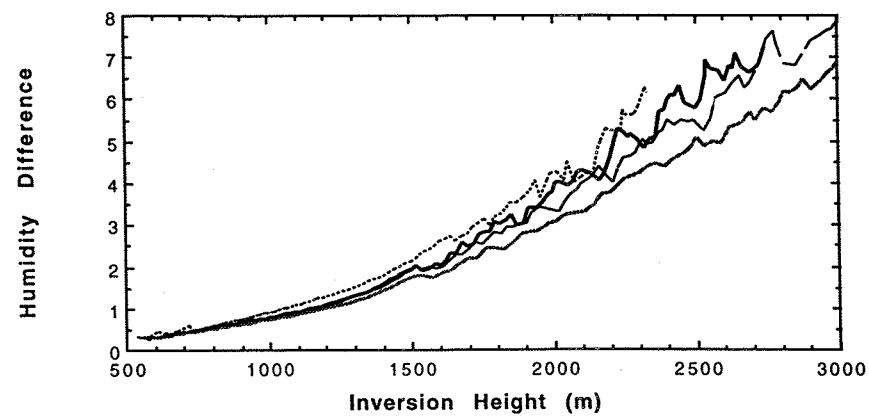

Figure 7.10c As Figure 7.10b but plotted against inversion height.

8. SUMMARY AND CONCLUSIONS

8.1 Model Development and Capabilities

The first part of this study comprised the development of an existing one-dimensional Mellor-Yamada type numerical model. Models of this type had been used in the past to simulate marine atmospheric boundary layers containing both stratocumulus and cumulus clouds. The Mellor-Yamada type model has a long history. First developments were by Mellor (1973) and Mellor and Yamada (1974) formalised a hierarchy of models with varying levels of turbulence closure. Only the model formulations with turbulence closure parameterising the second or third moments of boundary layer properties are practical and the most common type of model uses an intermediate complexity whereby the TKE is explicitly modelled and other second order terms parameterised. This is the approach taken in the present study.

It became clear that the parameterisation of radiation was crude, parts of the scheme dated back more than forty years. A sophisticated radiation scheme (Fu 1991) was therefore obtained and implemented. In common with some other models from the literature (see e.g. Bechtold et al. 1996 or Wyant et al. 1997) the surface forcing was poorly implemented in the model. This was remedied by imposing an eddy mixing coefficient consistent with the surface flux and the gradient of the mean profiles at the lowest flux level (fluxes and mixing coefficients are calculated at levels half way between those on which the mean profiles are defined). Not only did this approach remove the discontinuities in the fluxes of θ_l, q_t and buoyancy originally present between the sea surface (where surface layer theory is used to calculate the fluxes) and the model lower atmosphere (where the fluxes derive from eddy mixing coefficients) but the flux profiles became more physically realistic throughout the boundary layer. For historical reasons the model had a complex numerical scheme which had become redundant. Smoothing terms were required to make this scheme stable. An implicit numerical scheme was therefore implemented which was stable across a greater range of conditions and model gridsizes and timesteps. The changes made to the model during this study were shown to be important for the simulation of boundary layer structure and the model code predicted the mean profiles and fluxes for conditions from a range of boundary layer experiments from the literature. The model used in the present study is numerically stable and can be used for long simulations without problems.

One-dimensional modelling is a powerful tool for understanding the development of the boundary layer, but there are limitations on its applicability that must be remembered. Conditions must be close to homogeneous in the cross-wind direction. The model air

column can be assumed to represent the Lagrangian development of the boundary layer under these conditions. Although the model can parameterise the effects of wind shear on turbulence there are obvious conceptual problems if different parts of the air column are moving at different speeds. The model cannot explicitly resolve boundary layer circulations. Effects such as boundary layer organisation on the mesoscale are obviously beyond the scope of this type of model study. The model implementation has required several assumptions. Evolution of the mean profiles of θ_l, q_t, the components of wind speed and TKE depends on vertical advection, vertical mixing (which is parameterised using eddy mixing coefficients) and source terms (radiative heating, coriolis forcing or the buoyancy and shear generation of TKE). Storage, advection, turbulent diffusion, Coriolis, pressure diffusion and molecular diffusion contributions to the second-order moments have been neglected. The pressure-strain correlation is assumed to act to make the turbulence more isotropic (Rotta 1951). The dissipation terms follow Kolmogorov (1942). The model has no microphysical parameterisation and so physical processes have no feedback on cloud microphysical properties and vice versa. The cloud parameterisation contains the assumption that the distribution of θ_l and q_t within each model level is bi-normal.

8.2 Simulating the Evolution of the Stratocumulus-topped Boundary Layer

8.2.1 The Value of One-dimensional Modelling

The model developed during this study enables for the first time long simulations of conditions in the marine atmosphere to be performed with modest computational expense. Presently LES studies of the stratocumulus-topped boundary layer are limited to simulations of several hours duration due to the wide range of spatial scales that are involved from processes near a sharp inversion (with scale of order metres) to boundary layer circulations (with scale of order kilometres). It is presently necessary to reduce the computational intensity of LES models in order to simulate stratocumulus boundary layers. The different approximations made lead to a wide range of predictions from different models even under standard conditions (Bechtold et al. 1996, Moeng et al. 1996). Longer simulations are possible with two-dimensional, cloud resolving models (Krueger et al. 1995a,b and Wyant et al. 1997) but with coarser resolution than in the current study. Repeat simulations using varying external conditions have only been performed with mixed layer models (Albrecht 1984, Wang 1993, Bretherton 1993 and Bretherton and Wyant 1997). The results of such models have been shown to be strongly dependent on assumptions made about the parameterisation of cumulus lateral entrainment and mass flux, the correct representation of which is poorly known. The one-dimensional model developed in this study does not predetermine the structure of the boundary layer as is necessary with a mixed layer model.

The model cannot however explicitly represent updrafts, downdrafts or strongly skewed conditions as is possible with the two-dimensional cloud resolving models. The model developed in the present study represents a useful resource for the investigation of the evolution of stratocumulus-topped boundary layers over periods of several days.

8.2.2 Long Simulations of Stratocumulus-topped Boundary Layer Evolution

Running simulations over long periods requires careful thought about the external forcing applied. The easiest method of simulation is to run the model in a Lagrangian mode, for example imposing a varying SST or varying the wind speed or vertical velocity to mimic the expected evolution of the real boundary conditions. This approach has been followed in this study to investigate the evolution of stratocumulus-topped boundary layers in response to the increasing SST that would be encountered as a column of air moves from subtropical high pressure regions to trade wind regions. The simulations are run for 12 days and show the observed progression from a well mixed stratocumulus-topped boundary layer to a decoupled boundary layer. The boundary layer then recouples intermittently as cumulus clouds form at the top of the surface layer. There is a stable layer below the stratocumulus cloud base. The cumulus clouds moisten and cool the stratocumulus layer, maintaining the cloud. In the later part of the simulation the cumulus clouds are seen to directly drive entrainment, a process that acts to dissipate the cloud. In the simulation these opposing effects of the cumulus clouds approximately balance and hence the final part of the transition to a boundary layer containing only scattered cumulus does not occur. Possibly this transition depends on processes such as precipitation which are not presently included in the model (see the following section). Nevertheless processes within the deep decoupled boundary layer are well represented in the model.

8.2.3 Model Deficiencies and Future Model Development

In a one-dimensional model of the atmosphere the horizontal divergence cannot be calculated from the continuity equation and therefore an assumed profile of vertical velocity is imposed. This study follows others (e.g. Wyant et al. 1997, Krueger et al. 1995a,b) in assuming a constant divergence throughout the simulation and calculating the vertical velocity by integrating the divergence from the surface upwards. Such an approach leads to large vertical velocities at high levels in the atmosphere and if allowed to advect properties can quickly lead to unrealistic profiles above the boundary layer. This is countered by relaxing the profiles of θ_l and q_t above the inversion to their original values, following Wyant et al. (1997). An alternative method is to neglect vertical advection higher in the atmosphere (Krueger et al. 1995a,b). Strong vertical velocities are required to constrain the

boundary layer growth in the simulations with increasing SST. If the divergence is decreased with time (as observed between the subtropics and the tradewind region) the boundary layer evolves to form a thick, stratocumulus layer at the top of a boundary layer which deepens increasingly faster with time. Schubert et al. (1995) have suggested that the inversion height in the region studied is determined not only by local conditions but also by those upstream. Such effects could not be included in a one-dimensional model. Another possible reason is the lack of precipitation in the model.

The model, like others from the literature (e.g. Moeng and Arakawa 1980, Krueger et al. 1995a), suffers from numerical errors above the inversion, particularly when there is strong subsidence. This is thought to be due to the breakdown of the Rotta (1951) energy redistribution hypothesis (equation 4.13) in highly convective regions near sharp discontinuities (i.e. near the inversion, Moeng and Arakawa 1980). This acts to intermittently produce a region well mixed in θ_l and with a decreased q_t above the inversion. There is some TKE, a negative flux of q_t and a positive flux of θ_l in this region which is expected to support negligible turbulence. This acts to slightly increase the inversion strength in both θ_l and q_t and is therefore likely to make entrainment and boundary layer growth more difficult. The effects however are small for the simulations presented.

The simulation of boundary layers in which the cloud fraction and liquid water content are expected to decrease with time has highlighted a deficiency in the cloud parameterisation used in the model, that of Mellor (1977). It has been shown that the parameterisation, which relates boundary layer cloudiness to a parameterised variability within the cloud, can only predict partial cloudiness in stratified conditions. In well mixed conditions, such as those found just below the cloud top as a result of longwave cooling, the parameterisation can only predict total cloud cover or clear sky. In the present study the region near the cloud top remains saturated and therefore a stratocumulus layer with full cloud cover is predicted throughout the simulation. The cloud cover estimate is used in the calculation of the liquid water content, the full cloud cover therefore results in a larger liquid water content which in turn leads to strong longwave cooling and mixing near the top of the cloud.

The model formulation does not contain a drizzle parameterisation or any feedback between microphysical properties and boundary layer physical processes. Models containing microphysical parameterisations (e.g. Ackerman et al. 1995, Wyant et al. 1997) have lower order turbulence closure than the present model. There is however no reason why a microphysical parameterisation might not be included in the model in the future. Martin et al. (1995, 1997) present observations from ASTEX that demonstrate cumulus-

stratocumulus interaction can affect the microphysical properties of the stratocumulus clouds. Stratocumulus and cumulus under stratocumulus boundary layers are often associated with drizzle (Nicholls 1984, Bretherton et al. 1995). Drizzle that reaches the sea surface without evaporating acts to dry the boundary layer. Drizzle that evaporates acts to cool the subcloud layer and can therefore stabilise the boundary layer and promote decoupling. Whilst the inclusion of such effects would be likely to improve the simulations presented in this study, another set of complex interactions would be introduced to an already complex situation. In addition a further set of approximations and assumptions would be required and many extra variables and parameters would need to be defined. It seems justified therefore to consider cloud microphysical processes to be beyond the scope of the present study.

8.3 Processes in the Decoupled Boundary Layer

8.3.1 Physical Processes and Boundary Layer Evolution

Whilst one-dimensional modelling has been used in the past to simulate cloudy boundary layers, the evolution of the stratocumulus-topped boundary layer has not been modelled over longer periods in this way. The twelve day simulation, which uses diurnally averaged radiation, shows the evolution from a well mixed stratocumulus-topped boundary layer, to a decoupled boundary layer and then a cumulus-coupled boundary layer. The boundary layer deepens throughout the simulation and the deepening-decoupling model of Albrecht et al. (1995a) and Wyant et al. (1997) explains the boundary layer evolution well. The final breakup of the solid stratocumulus is not simulated, perhaps because the lack of a drizzle parameterisation or deficiencies in the cloud parameterisation used.

In the well mixed stratocumulus topped boundary layer conditions are fairly uniform. Variability is associated with individual entrainment events (when the boundary layer grows in depth by the model grid spacing) when the boundary layer is warmed and dried. As the boundary layer deepens the surface and cloud turbulence are not strong enough to keep the entire boundary layer mixed. The surface layer then becomes relatively cool and moist (due to a combination of strong latent and weak sensible heat fluxes and the isolation of the surface layer from the warming and drying effects of entrainment) and the cloud layer warm and dry (due to entrainment). The region between the surface and cloud layers becomes conditionally unstable and the small cumulus clouds that form at the top of the surface layer as the surface layer relative humidity builds up are able to rise into the stratocumulus layer. The variability of the boundary layer increases dramatically once the first cumulus clouds form. The one-dimensional nature of the model clearly shows the effect of individual cumulus clouds on the stratocumulus layer, firstly to maintain the cloud by increasing the

liquid water content and secondly to promote entrainment by the local increase in TKE. In the model these competing effects combine to give a fairly constant peak liquid water content in the stratocumulus layer.

Comparison of the model simulation with observations and with the output of other models suggests that the simulation results are reasonable.

8.3.2 The Impact of External Forcing on Boundary Layer Structure

As noted above the computational efficiency of the model allows many simulations to be run with different values for the external forcing. This study has examined the effects of varying vertical velocity, varying temperature and humidity conditions above the inversion, varying SST gradients and wind speed and varying solar forcing.

Increased (decreased) vertical velocity reduces (increases) the boundary layer growth as expected. The resulting average boundary layer θ_l and q_t remain similar however as the warming and drying due to increased subsidence in the increased vertical velocity case is similar to the warming and drying due to increased entrainment in the decreased vertical velocity case. The cloud is thus thicker in the deeper boundary layer.

The effect of varying θ_l conditions above the inversion is best explained in terms of the stability of the lower troposphere. Increasing the temperature above the inversion (e.g. a larger θ_l inversion or vertical gradient in the free atmosphere) makes entrainment of above inversion air into the boundary layer more difficult and the boundary layer growth is reduced under these conditions. The reverse is true for small θ_l inversions and gradients above the boundary layer. The relaxation of θ_l above the inversion necessary in these long simulations also affects the boundary layer growth in a predictable way.

Contrary to traditional pictures of the instability of cloud layers, when there is very dry air above the boundary layer, the model suggests that negatively buoyant downdrafts driven by buoyancy reversal may be important in maintaining coupling between surface and cloud layer in deep cloudy boundary layers. The enhanced coupling and mixing between the surface and cloud layers allows the cloud liquid water to be maintained, but at the expense of the surface layer humidity. The resulting cooler, drier surface layer causes an increased surface buoyancy flux which also helps to keep the boundary layer coupled. As on average the boundary layer is drier than when the air above the boundary layer contains more water, the maintenance of the cloud by water input from the surface will cease when the surface layer has dried to a sufficient extent.

Varying the SST gradient and wind speed changes the surface fluxes which have a complex role in boundary layer development. Initially increased surface fluxes result in faster boundary layer growth and hasten the onset of a decoupled boundary layer. In a decoupled boundary layer the cloud layer dries out due to entrainment of warm dry air into the cloud. The increased surface fluxes however promote cumulus coupling of the surface and cloud layers in the later stage of the boundary layer development. High surface water flux can result in the stratocumulus layer in the cumulus coupled boundary layer thickening. At low wind speeds the fluxes can be low enough that cumulus coupling is not observed in the simulation.

8.4 Conclusions

A one-dimensional model with second-order turbulence closure has been developed which is suitable for long simulations of atmospheric boundary layer evolution.

Reasonable climatological boundary conditions for the boundary layer evolution between the subtropics and the trade wind region in the North Atlantic have been determined from a combination of merchant ship and model data.

The model evolves under realistic forcing from well mixed to decoupled to cumulus-coupled as observed. The effect of individual cumulus clouds on the boundary layer structure and their role in mixing the boundary layer and driving entrainment examined. The model gives detailed Lagrangian information which is not available from traditional observing platforms such as aircraft or research ships.

The effect on boundary layer evolution of varying external forcing has been examined. The most interesting prediction of these simulations is that very dry air above the inversion, rather than causing the cloud to dissipate, can act to mix a decoupled boundary layer and export water from the surface layer into the cloud layer. Further investigation is however needed.

8.5 Future Work

The one-dimensional atmospheric boundary layer numerical model developed and described in this study now constitutes a useful tool for study of the both the well-mixed and decoupled marine boundary layer in regions where stratocumulus clouds are common. In particular the improvement in the model surface forcing should allow improved estimates of the effect of surface forcing on the structure and evolution of the boundary layer compared to

any model in which the fluxes in the interior of the model are not matched to those at the surface. In addition the model is now well documented which will simplify further model developments. Possible future model developments such as the inclusion of a drizzle parameterisation are detailed in Section 8.2.3.

Whilst the combination of fine vertical resolution, sophisticated radiation parameterisation, surface flux matching and relatively high order turbulence closure should allow better simulation of the boundary layer and cloud structure than an AGCM, the specification of parameters external to the boundary layer such as SST and above inversion structure are not well defined. Embedding the boundary layer model within an AGCM could combine the good definition of boundary layer structure with more realistic large scale parameters and produce more realistic simulations. Using either daily or 6-hourly archived reanalysis model output would allow an ensemble of model runs to be performed. For a chosen position and time, trajectories of an air column could be calculated for the reanalysis dataset and data extracted from the reanalysis data along the trajectory. The boundary layer model could then be run using the reanalysis data to initialise the boundary layer model and to provide the SST, wind speed and above inversion structure. The ensemble would be made up from model runs initialised with data from different reanalysis output times. Thus an estimate of the variability of the boundary layer structure could be determined, along with information about the important causes of that variability.

AGCMs are poor at simulating regions where stratocumulus clouds are important over the ocean, partly due to their coarse resolution (Bushell and Martin 1999). The region of stratocumulus off the coast of Peru is strongly affected by El Niño variability and additionally this region has not been well sampled by observational programs. The variability of the Peruvian stratocumulus region is not well understood. Using the high resolution boundary layer model in conjunction with large scale forcing and surface fluxes appropriate for the different phases of El Niño it would be possible to investigate the resulting variability in the stratocumulus clouds. Intercomparison of the boundary layer model fluxes and mean profiles with those predicted by an AGCM could give an indication of the important processes not captured by the AGCM and suggest how these processes might be included in future models.

Another subject for additional study would be the determination of the effects of dry upper air on clouds in deep decoupled and cumulus coupled boundary layers. Further model simulations are required to determine the range of conditions under which the effect could be important. An investigation of observed boundary layer structure, probably at OWS N (30°N, 140°W), from radiosonde data and cloud reports could be used to test the model

predictions. High resolution radiosonde data would be required to resolve the boundary layer stratification and only the more recent data from OWS have been archived to a suitable resolution.

The present study has shown that surface fluxes have an important impact on entrainment both when the atmospheric boundary layer is well-mixed and also in deeper boundary layers that are cumulus-coupled. The effects of entrainment on the boundary layer also feedback into the surface fluxes, for example the entrainment of warm dry air at the boundary layer top acts to reduce the sensible heat flux and to increase the latent heat flux at the surface. The surface latent heat flux is thus related to the amount of entrainment that has occurred. Both the latent heat flux and the boundary layer height are therefore related to the history of the boundary layer. The nature of these individual relationships with boundary layer history could be studied using the boundary layer model in Lagrangian simulations and the possibility of a relationship between the surface latent heat flux and the inversion or cloud top height could be investigated.

APPENDIX 1: NOTATION

An overbar denotes an average

A dash denotes a fluctuating component

subscripts i,j,k indicate summation notation (see e.g. Stull, 1988)

subscript 0 denotes the surface

A_1	mixing length constant, $l_1 = A_1\ell = 0.92\ell$	
A_2	mixing length constant, $l_2 = A_2\ell = 0.74\ell$	
AA_k	element of tri-diagonal matrix	
a	defined by equation 4.52	
B_1	mixing length constant, $\Lambda_1 = B_1\ell = 16.6\ell$	
B_2	mixing length constant, $\Lambda_2 = B_2\ell = 10.1\ell$	
BB_k	element of tri-diagonal matrix	
b	defined by equation 4.53	$[K^{-1}]$
β	thermal expansion coefficient (= $1/\langle\theta_v\rangle$ in one-dimension)	$[K^{-1}]$
c	mixing coefficient parameter	
C_D	drag coefficient	
C_{DN}	neutral drag coefficient	
C_E	transfer coefficient for moisture	
C_{EN}	neutral transfer coefficient for moisture	
CC_k	element of tri-diagonal matrix	
C_T	transfer coefficient for heat	
C_{TN}	neutral transfer coefficient for heat	
c_p	specific heat of air	$[JK^{-1}kg^{-1}]$
χ	fraction of above inversion air mixed into cloud during entrainment	
D	ratio of densities in CTEI (after Siems et al. 1990)	
DD_k	element of tri-diagonal matrix	
D/Dt	total derivative	

∂	partial derivative	
$\delta_i b$	buoyancy difference across the inversion	[K]
Δt	time step	[s]
Δz	grid spacing	[m]
Δz_+	grid spacing between levels k and k+1	[m]
Δz_-	grid spacing between levels k and k-1	[m]
$\Delta_i X$	change in X across inversion	
δ_{ij}	Kronecker delta	
E	evaporation rate	$[s^{-1}]$
EE_k	coefficient in solution of tri-diagonal matrix	
e	turbulent kinetic energy	$[m^2s^{-2}]$
ε	TKE dissipation rate	$[m^2s^{-3}]$
$\in_{ijk}$	alternating direction tensor	
FF_k	coefficient in solution of tri-diagonal matrix	
f	Coriolis parameter	$[s^{-1}]$
Φ_k^n	model prognostic variable at time step n and level k	
ϕ_m	dimensionless gradient of momentum	
ϕ_q	dimensionless gradient of humidity	
ϕ_t	dimensionless gradient of temperature	
G	Gaussian distribution	
Γ	model dissipation term	$[s^{-1}]$
g	acceleration due to gravity	$[ms^{-2}]$
γ	mixing coefficient parameter, equation 4.44	
γ_s	defined by equation 3.17	
H	Heaviside function	
H_{lat}	latent heat flux	$[Wm^{-2}]$
H_{sen}	sensible heat flux	$[Wm^{-2}]$
K_e	eddy mixing coefficient for TKE	$[m^2s^{-1}]$
K_h	eddy mixing coefficient for heat	$[m^2s^{-1}]$

K_m	eddy mixing coefficient for momentum	$[m^2s^{-1}]$
K_q	eddy mixing coefficient for humidity	$[m^2s^{-1}]$
K_z	K_e, K_h, K_m or K_q as appropriate	$[m^2s^{-1}]$
k	entrainment parameter in equation 3.15	
κ	von Karman constant	0.4
L	latent heat of evaporation of water	$[J\ kg^{-1}]$
L_O	Obukhov length	[m]
lw	longwave heating rate	$[K\ s^{-1}]$
ℓ	mixing length	[m]
l_1	$=A_1\ell = 0.92\ell$	[m]
l_2	$=A_2\ell = 0.74\ell$	[m]
Λ_1	$=B_1\ell = 16.6\ell$	[m]
Λ_2	$=B_2\ell = 10.1\ell$	[m]
λ	mixing length parameter	[m]
λ_b	lengthscale in Blackadar mixing length formulation, equation 4.35	[m]
ν	kinematic molecular viscosity	$[m^2s^{-1}]$
ν_θ	molecular thermal diffusivity	$[m^2s^{-1}]$
ν_q	molecular diffusivity of water vapour	$[m^2s^{-1}]$
Pr_t	turbulent Prandtl number	
Π	model forcing term	[various]
p	pressure	[mb]
q	specific humidity	$[kg\ kg^{-1}]$
q_0	sea surface specific humidity	$[kg\ kg^{-1}]$
q_l	normalised saturation deficit, equation 4.51	
q_*	humidity scale	$[kg\ kg^{-1}]$
q_l	liquid water content	$[kg\ kg^{-1}]$
$q_{liq\ max}$	maximum in-cloud liquid water content	$[kg\ kg^{-1}]$
q_{sat}	saturation specific humidity	$[kg\ kg^{-1}]$
q_t	total water content	$[kg\ kg^{-1}]$

θ	potential temperature	[K]
θ_0	surface potential temperature	[K]
θ_e	equivalent potential temperature	[K]
θ_l	liquid water potential temperature	[K]
θ_v	virtual potential temperature	[K]
θ_*	potential temperature scale	[K]
R_j	net radiation in jth direction	[Wm^{-2}]
R_{diss}	ratio of normalised tke to temperature variance dissipation	
r	cloud fraction	
ρ	density of air	[kg m^{-3}]
$\Re$	dry gas constant	[$JK^{-1}kg^{-1}$]
$\tilde{S}_e$	stability parameter	
S_{qt}	source term for total water	[kg $m^{-2}s^{-1}$]
sw	shortwave heating rate	[K s^{-1}]
σ_r	radiative heating rate	[K s^{-1}]
σ_s	variance of liquid water content from saturation	[K^{-1}]
T	temperature	[°C, K]
T_v	virtual temperature	[K]
t	time	[s]
τ	wind stress	[Nm^{-2}]
U	total wind speed	[ms^{-1}]
u	north component of wind speed	[ms^{-1}]
u_g	north component of geostrophic wind speed	[ms^{-1}]
u_i	component of velocity	[ms^{-1}]
u_*	friction velocity (surface velocity scale)	[ms^{-1}]
v	east component of wind speed	[ms^{-1}]
v_g	east component of geostrophic wind speed	[ms^{-1}]
w	vertical velocity	[ms^{-1}]
x_i	distance component	[m]

Ψ_m	dimensionless wind profile	
Ψ_q	dimensionless humidity profile	
Ψ_t	dimensionless temperature profile	
z	height above surface	[m]
z_0	roughness length	[m]
z_c	cloud depth	[m]
z_{ml}	mixed layer depth	[m]
z_q	roughness length for humidity	[m]
z_t	roughness length for temperature	[m]
ζ	dimensionless characteristic of turbulence, $=z/L_O$	

APPENDIX 2: FLUXES INVOLVING θ_v

This appendix follows Yamada and Mellor (1979) and is included here for completeness. Firstly we approximate liquid water potential temperature by:

$$\theta_l = \theta - \frac{\theta}{T}\frac{L}{c_p} q_l \tag{A2.1}$$

Thus the mean or instantaneous values of θ_v can be calculated:

$$\begin{aligned} \theta_v &= (1 + 0.61 q_t - 1.61 q_l)\theta \\ &= (1 + 0.61 q_t - 1.61 q_l)\left(\theta_l + \frac{\theta}{T}\frac{L}{c_p} q_l\right) \end{aligned} \tag{A2.2}$$

Subtracting A2.2 calculated using the mean values from that calculated using instantaneous values yields the fluctuation of virtual potential temperature which can be written in the form of A2.3 following the neglect of second order terms:

$$\beta' \theta_v' \approx \beta_T' \theta_l' + \beta_l' q_l' + \beta_{qt}' q_t' \tag{A2.3}$$

where

$$\begin{aligned} \beta_T' &= \beta(1 + 0.61 q_t' - 1.61 q_l') \\ \beta_l' &= \beta\left\{(1 + 0.61 q_t' - 3.22 q_l)\frac{\theta}{T}\frac{L}{c_p} - 1.61\theta_l'\right\} \\ \beta_{qt}' &= 0.61\beta\left(\theta_l' + \frac{\theta}{T}\frac{L}{c_p} q_l'\right) \end{aligned} \tag{A2.4}$$

To calculate the flux of θ_v we multiply both sides of equation A2.3 by u_j and take an ensemble average:

$$\beta \overline{u_j' \theta_v'} = \beta_T' \overline{u_j' \theta_l'} + \beta_{qt}' \overline{u_j' q_t'} \tag{A2.5}$$

where

$$\beta'_T = \beta_T - b\beta_l R'$$
$$\beta'_{qt} = \beta_{qt} - a\beta_l R' \qquad \text{(A2.6)}$$

and

$$R' = R - \frac{q'_l}{2\sigma_s}\frac{1}{2\pi}e^{-\frac{1}{2}q_l^2} \qquad \text{(A2.7)}$$

The covariance of θ_v with θ_l is parameterised as:

$$\beta\overline{\theta'_v\theta'_l} = -\frac{B_2\ell}{2e^{1/2}}\left\{\left(\beta'_T\frac{\partial\theta_l}{\partial z} + S\right)\overline{w'\theta'_l} + \beta'_{qt}\frac{\partial\theta_l}{\partial z}\overline{w'q'_t}\right\} \qquad \text{(A2.8)}$$

$$\tilde{S} = \beta'_T\frac{\partial\theta_l}{\partial z} + \beta'_{qt}\frac{\partial q_t}{\partial z} \qquad \text{(A2.9)}$$

and the covariance of θ_v with q_t as:

$$\beta\overline{\theta'_v q'_t} = -\frac{B_2\ell}{2e^{1/2}}\left\{\left(\beta'_T\frac{\partial q_t}{\partial z}\right)\overline{w'\theta'_l} + \left(\beta'_{qt}\frac{\partial q_t}{\partial z} + \tilde{S}\right)\overline{w'q'_t}\right\} \qquad \text{(A2.10)}$$

REFERENCES

Ackerman, A. S., O. B. Toon and P. V. Hobbs, 1995: A Model for Particle Microphysics, Turbulent Mixing, and Radiative Transfer in the Stratocumulus-Topped Marine Boundary Layer and Comparisons with Measurements. Journal of the Atmospheric Sciences, 52(8), 1204-1236.

Albrecht, B. A., 1984: A Model Study of the Downstream Variations of the Thermodynamic Structure of the Trade Winds. Tellus, 36A, 187-202.

Albrecht, B. A., 1989: Aerosols, Cloud Microphysics, and Fractional Cloudiness. Science, 245, 1227-1230.

Albrecht, B. A., C. S. Bretherton, D. Johnson, W. H. Schubert and A. S. Frisch, 1995a: The Atlantic Stratocumulus Transition Experiment - ASTEX. Bulletin of the American Meteorological Society, 76(6), 889-904.

Albrecht, B. A., M. P. Jensen and W. J. Syrett, 1995b: Marine Boundary Layer Structure and Fractional Cloudiness. Journal of Geophysical Research, 100(D7), 14209-14222.

Albrecht, B. A., R. S. Penc and W. H. Schubert, 1985: An Observational Study of Cloud-Topped Mixed Layers. Journal of the Atmospheric Sciences, 42(8), 800-822.

Albrecht, B. A., D. A. Randall and S. Nicholls, 1988: Observations of Marine Stratocumulus during FIRE. Bulletin of the American Meteorological Society, 69, 618-626.

Alekseev, V., V. Dymnikov, V. Galin, E. M. Volodin, H. W. Barker, R. D. Cess, M. H. Zhang, E. CohenSolal, H. LeTreut, R. A. Colman, J. R. Fraser, B. J. McAvaney, D. A. Dazlich, L. D. Fowler, D. A. Randall, A. D. DelGenio, K. K. W. Lo, M. R. Dix, M. Esch, E. Roeckner, W. L. Gates, G. L. Potter, K. E. Taylor, J. J. Hack, W. J. Ingram, J. T. Kiehl, J. F. Royer, B. Timbal, V. P. Meleshko, P. V. Sporyshev, J. J. Morcrette, M. E. Schlesinger, W. Wang and R. T. Wetherald, 1996: Cloud feedback in atmospheric general circulation models: An update. Journal of Geophysical Research Atmospheres, 101(D8), 12791-12794.

Anderson, G. P., S. A. Clough, F. X. Kneizys, J. H. Chetwynd and E. P. Shettle, 1986: AFGL Atmospheric Constituent Profiles (0-120 km). AFGL-TR-86-0110, Air Force Geophysics Laboratory, Hascom AFB, MA, 48 pp.

Ball, F. K., 1960: Control of Inversion Height by Surface Heating. Quarterly Journal of the Royal Meteorological Society, 86(370), 483-494.

Bechtold, P., J. W. M. Cuijpers, P. Mascart and P. Trouilhet, 1995: Modelling of Trade Wind Cumuli with a Low-Order Turbulence Model: Toward a Unified Description of Cu and Sc Clouds in Meteorological Models. Journal of the Atmospheric Sciences, 52(4), 455-463.

Bechtold, P., S. K. Krueger, W. S. Lewellen, E. vanMeijgaard, C.-H. Moeng, D. A. Randall, A. vanUlden and S. Wang, 1996: Modelling a Stratocumulus-Topped PBL: Intercomparisons Among Different One-Dimensional Codes and with Large Eddy Simulation. Bulletin of the American Meteorological Society, 77(9), 2033-2042.

Bechtold, P. and P. Siebesma, 1998: Organisation and Representation of Boundary Layer Clouds. Journal of the Atmospheric Sciences, 55(5), 888-895.

Betts, A. K., 1989: Mean Inversion Strength of the Convective Boundary Layer over the Oceans. Quarterly Journal of the Royal Meteorological Society, 115, 997-998.

Betts, A. K. and R. Boers, 1990: A Cloudiness Transition in a Marine Boundary Layer. Journal of the Atmospheric Sciences, 47(12), 1480-1497.

Betts, A. K., C. S. Bretherton and E. Klinker, 1995: Relation Between Mean Boundary-Layer Structure And Cloudiness at the RV Valdivia During ASTEX. Journal of the Atmospheric Sciences, 52(16), 2752-2762.

Blackadar, A. K., 1962: The vertical distribution of wind and turbulent exchange in a Neutral Atmosphere. Journal of Geophysical Research, 67(8), 3095-3102.

Bougeault, P., 1985: The diurnal cycle of the marine stratocumulus layer: A higher order model study. Journal of the Atmospheric Sciences, 42, 2826-2843.

Bretherton, C. S., 1993: Understanding Albrecht's Model of Trade Cumulus Cloud Fields. Journal of the Atmospheric Sciences, 50, 2264-2283.

Bretherton, C. S., P. Austin and S. T. Siems, 1995: Cloudiness and Marine Boundary Layer Dynamics in the ASTEX Lagrangian Experiments. Part II: Cloudiness, Drizzle, Surface Fluxes and Entrainment. Journal of the Atmospheric Sciences, 52(16), 2724-2735.

Bretherton, C. S., S. K. Krueger, M. C. Wyant, P. Bechtold, D. vanMeijgaard, B. Stevens and J. Texeira, 1999: A GCSS Boundary Layer Cloud Model Intercomparison Study of the First ASTEX Lagrangian Experiment. Boundary-Layer Meteorology, Submitted.

Bretherton, C. S. and R. Pincus, 1995: Cloudiness and Marine Boundary Layer Dynamics in the ASTEX Lagrangian Experiments. Part I: Synoptic Setting and Vertical Structure. Journal of the Atmospheric Sciences, 52(16), 2707-2723.

Bretherton, C. S. and M. C. Wyant, 1997: Moisture Transport, Lower-Tropospheric Stability, and Decoupling of Cloud-Topped Boundary Layers. Journal of the Atmospheric Sciences, 54, 148-167.

Brost, R. A., D. H. Lenschow and J. C. Wyngaard, 1982: Marine Stratocumulus Layers. Part I: Mean Conditions. Journal of the Atmospheric Sciences, 39, 800-817.

Busch, N. E., 1973: On the Mechanics of atmospheric turbulence. Workshop on Micrometeorology, D. A. Haugen, Ed., American Meteorological Society, 1-65.

Bushell, A. C. and G. M. Martin, 1999: The impact of vertical resolution upon GCM simulations of marine stratocumulus. Climate Dynamics, 15(4), 293-318.

Businger, J. A., 1973: Turbulent transfer in the atmospheric surface layer. Workshop on Micrometeorology, D. A. Haugen, Ed., American Meteorological Society, 67-100.

Businger, J. A. and W. J. Shaw, 1984: The Response of the Marine Boundary Layer to the Mesoscale Variations in Sea-surface Temperature. Dynamics of Atmospheres and Oceans, 8, 267-281.

Businger, J. A., J. C. Wyngaard, Y. Izumi and E. F. Bradley, 1971: Flux Profile Relationships in the Atmospheric Surface Layer. Journal of Atmospheric Sciences, 28, 181 - 189.

Chen, C. and W. R. Cotton, 1987: The Physics of the Marine Stratocumulus-Capped Mixed Layer. Journal of the Atmospheric Sciences, 44(20), 2951-2977.

Cuijpers, J. W. M. and P. Bechtold, 1995: A Simple Parameterisation of Cloud Water Related Variables for Use in Boundary Layer Models. Journal of the Atmospheric Sciences, 52(13), 2486-2490.

Cuzzi, J. N., T. P. Ackerman and L. C. Helmle, 1982: The Delta-Four-Stream Approximation for Radiative Flux Transfer. Journal of the Atmospheric Sciences, 39, 917-925.

Deardorff, J. W., 1976: On the entrainment rate of a stratocumulus-topped mixed layer. Quarterly Journal of the Royal Meteorological Society, 102, 563-582.

Deardorff, J. W., 1980: Cloud Top Entrainment Instability. Journal of the Atmospheric Sciences, 37, 131-147.

Deardorff, J. W. and J. A. Businger, 1980: Comments on "Marine Stratocumulus Convection. Part 1: Governing Equations and Horizontally Homogeneous Solutions". Journal of the Atmospheric Sciences, 37, 481-482.

Derbyshire, S. H. and R. Kershaw, 1993: Turbulence simulation in the Meteorological Office. Meteorological Magazine, 122(1447), 25-34.

deRoode, S. R. and P. G. Duynkerke, 1996: Dynamics of Cumulus Rising into Stratocumulus as Observed during the First 'Lagrangian' Experiment of ASTEX. Quarterly Journal of the Royal Meteorological Society, 122, 1597-1623.

deRoode, S. R. and P. G. Duynkerke, 1997: Observed Lagrangian Transition of Stratocumulus in Cumulus during ASTEX: Mean State and Turbulence Structure. Journal of the Atmospheric Sciences, 54(17), 2157-2173.

Donaldson, C. D., 1973: Construction of a Dynamic Model of the Production of Atmospheric Turbulence and the Dispersal of Atmospheric Pollutants. Workshop on Micrometeorology, D. A. Haugen, Ed., American Meteorological Society, 313-392.

Driedonks, A. G. M. and P. G. Duynkerke, 1989: Current problems in the stratocumulus-topped atmospheric boundary layer. Boundary-Layer Meteorology, 46(3), 275-303.

Duynkerke, P. G., 1989: The Diurnal Variation of a Marine Stratocumulus Layer: A Model Sensitivity Study. Monthly Weather Review, 117, 1710-1725.

Duynkerke, P. G. and A. G. M. Driedonks, 1988: Turbulent Structure of a Shear-Driven Stratus-Topped Atmospheric Boundary Layer: A Comparison of Model Results with Observations. Journal of the Atmospheric Sciences, 45(16), 2343-2351.

Duynkerke, P. G. and P. Hignett, 1993: Simulation of Diurnal Variation in a Stratocumulus-capped Marine Boundary Layer during FIRE. Monthly Weather Review, 121, 3291-3300.

Dyer, A. J., 1974: A Review of Flux-Profile Relationships. Boundary-Layer Meteorology, 7, 363-372.

Fu, Q. (1991) Parameterisation of Radiative Processes in Vertically Non-homogeneous Multiple Scattering Atmospheres. PhD Thesis, University of Utah, 259pp.

Garratt, J. R., 1992: The Atmospheric Boundary Layer. Cambridge University Press, Cambridge, 316 pp.

Guymer, T. H., J. A. Businger, K. B. Katsaros, W. J. Shaw, P. K. Taylor, W. G. Large and R. E. Payne, 1983: Transfer processes at the air-sea interface. Philosophical Transactions of the Royal Society of London, A308, 253-272.

Hanson, H. P., 1987: Response of Marine Atmospheric Boundary Layer Height to Sea Surface Temperature Changes: Mixed-Layer Theory. Journal of Geophysical Research, 92(C8), 8226-8230.

Hanson, H. P., 1991: Marine Stratocumulus Climatologies. International Journal of Climatology, 11, 147-164.

Hanson, H. P. and V. E. Derr, 1987: Parameterisation of Radiative Flux Profiles Within Layer Clouds. Journal of Climate and Applied Meteorology, 26, 1511-1521.

Hanson, H. P. and P. L. Gruber, 1982: Effect of Marine Stratocumulus Clouds on the Ocean-Surface Heat Budget. Journal of the Atmospheric Sciences, 39(4), 897-908.

Hartmann, D. L., M. E. Ockert-Bell and M. L. Michelsen, 1992: The Effect of Cloud Type on Earth's Energy Balance: Global Analysis. Journal of Climate, 5, 1281-1304.

Hinze, J. O., 1975: Turbulence. McGraw-Hill, New York, 709 pp.

Holtslag, A. A. M. and F. T. M. Nieuwstadt, 1986: Scaling the Atmospheric Boundary Layer. Boundary-Layer Meteorology, 36, 201-209.

JASIN Field Summary, 1979: Air-Sea Interaction Project: Summary of the 1978 Field Experiment (JASIN 1978). 139 pp.

Josey, S. A., E. C. Kent and P. K. Taylor, 1999: New Insights into the Ocean Heat Budget Closure Problem from Analysis of the SOC Air-sea Flux Climatology. Journal of Climate, 12(9), 2856 - 2880.

Kahn, P. H. and J. A. Businger, 1979: The effect of radiative flux divergence on entrainment of a saturated convective boundary layer. Quarterly Journal of the Royal Meteorological Society, 105, 303-306.

Kaimal, J. C., J. C. Wyngaard, D. A. Haugen, O. R. Cote, Y. Izumi, S. J. Caughey and C. J. Readings, 1976: Turbulence Structure in the Convective Boundary Layer. Journal of the Atmospheric Sciences, 33, 2152-2169.

Kalnay, E., M. Kanamitsu, R. Kistler, W. Collins, D. Deaven, L. Gandin, M. Iredell, S. Saha, G. White, J. Woollen, Y. Zhu, A. Leetmaa, R. Reynolds, M. Chelliah, W. Ebisuzaki, W.Higgins, J. Janowiak, K. C. Mo, C. Ropelewski, J. Wang, R. Jenne and D. Joseph, 1996: The NCEP/NCAR 40-Year Reanalysis Project. Bulletin of the American Meteorological Society, 77(3), 437-471.

Kawa, S. R. and R. Pearson, 1989: An Observational Study of Stratocumulus Entrainment and Thermodynamics. Journal of the Atmospheric Sciences, 46(17), 2649-2661.

Kent, E. C., P. G. Challenor and P. K. Taylor, 1999a: A Statistical Determination of the Random Observational Errors Present in Voluntary Observing Ships Meteorological Reports. Journal of Atmospheric and Oceanic Technology, 16(7), 905-914.

Kent, E. C. and P. K. Taylor, 1995: A comparison of sensible and latent heat flux estimates for the North Atlantic Ocean. Journal of Physical Oceanography, 25(6), 1530-1549.

Kent, E. C., P. K. Taylor and P. G. Challenor, 1999b: The Effect of Successive Correction on Variability Estimates for Climatological Datasets. Journal of Climate, accepted.

Klein, S. A., 1997: Synoptic Variability of Low-Cloud Properties and Meteorological Parameters in the Subtropical Trade Wind Boundary Layer. Journal of Climate, 10, 2018-2039.

Klein, S. A. and D. L. Hartmann, 1993: The Seasonal Cycle of Low Stratiform Clouds. Journal of Climate, 6, 1587-1606.

Klein, S. A., D. L. Hartmann and J. R. Norris, 1995: On the Relationships among Low-Cloud Structure, Sea Surface Temperature, and Atmospheric Circulation in the Summertime Northeast Pacific. Journal of Climate, 8, 1140-1155.

Kloesel, K. A., 1992: Marine Stratocumulus Cloud Clearing Episodes Observed during FIRE. Monthly Weather Review, 120, 565-578.

Kolmogorov, A. N., 1942: Equations of turbulent motion in an incompressible fluid. Iav. Akad. Nauk, SSSR, Ser. Fiz, VI(1-2), 56-58.

Koracin, D. and D. P. Rogers, 1990: Numerical simulations of the response of the marine atmosphere to ocean forcing. Journal of the Atmospheric Sciences, 47(5), 592-611.

Kraus, E. B. and J. A. Businger, 1994: Atmosphere-ocean interaction. Clarendon Press, Oxford, 362 pp.

Kraus, H. and E. Schaller, 1978: Steady-State Characteristics of Inversions of a Well-Mixed Planetary Boundary Layer. Boundary-Layer Meteorology, 14, 83-104.

Krueger, S. K., G. T. McLean and Q. Fu, 1995a: Numerical Simulation of the Stratus-to-Cumulus Transition in the Subtropical Marine Boundary Layer. Part I: Boundary-Layer Structure. Journal of the Atmospheric Sciences, 52(16), 2839-2850.

Krueger, S. K., G. T. McLean and Q. Fu, 1995b: Numerical Simulation of the Stratus-to-Cumulus Transition in the Subtropical Marine Boundary Layer. Part II: Boundary-Layer Circulation. Journal of the Atmospheric Sciences, 52(16), 2851-2868.

Kuo, H. and W. H. Schubert, 1988: Stability of Cloud-topped Boundary Layers. Quarterly Journal of the Royal Meteorological Society, 114, 1232-1240.

Lacis, A. A. and V. Olinas, 1991: A Description of the Correlated k-distribution Method for Modelling Non-grey Gaseous Absorption, Thermal Emission and Multiple Scattering in Vertically Inhomogeneous Atmospheres. Journal of Geophysical Research, 96, 9027-9063.

Large, W. G. and S. Pond, 1981: Open ocean momentum flux measurements in moderate to strong winds. Journal of Physical Oceanography, 11, 324-336.

Large, W. G. and S. Pond, 1982: Sensible and Latent Heat Flux Measurements over the Ocean. Journal of Physical Oceanography, 12, 464-482.

Lean, J., 1992: A Guide to the UK Meteorological Office Single Column Model. Hadley Centre for Climate Prediction and Research., Unpublished Document, 43 pp.

Lesieur, M. and O. Métais, 1996: New Trends in Large-eddy Simulations of Turbulence. Annual Review of Fluid Mechanics, 28, 45-82.

Lewellen, D. C. and W. S. Lewellen, 1998: Large-Eddy Boundary Layer Entrainment. Journal of the Atmospheric Sciences, 55, 2645-2665.

Lilly, D. K., 1968: Models of cloud-topped mixed layers under a strong inversion. Quarterly Journal of the Royal Meteorological Society, 94, 292-309.

Liou, K.-N., Q. Fu and T. P. Ackerman, 1988: A Simple Formulation of the Delta-Four-Stream Approximation for Radiative Transfer Parameterizations. Journal of the Atmospheric Sciences, 45(13), 1940-1947.

Liou, K. N., 1992: Radiative and Cloud Processes in the Atmosphere: Theory, Observation and Parameterisation. Oxford University Press, New York, 487 pp.

Liu, W. T., K. B. Katsaros and J. A. Businger, 1979: Bulk Parameterisation of Air-Sea Exchanges of Heat and Water Vapour Including the Molecular Constraints at the Interface. Journal of the Atmospheric Sciences, 36, 1722-1735.

Lock, A. P., 1998: The Parametrization of Entrainment in Cloudy Boundary Layers. Quarterly Journal of the Royal Meteorological Society, 124(552), 2729-2753.

Lock, A. P. and M. K. MacVean, 1999a: The Generation of Turbulence and Entrainment by Buoyancy Reversal. Quarterly Journal of the Royal Meteorological Society, 125(555), 1017-1038.

Lock, A. P. and M. K. MacVean, 1999b: The Parameterisation of Entrainment Driven by Surface Heating and Cloud-top Cooling. Quarterly Journal of the Royal Meteorological Society, 125(553), 271-299.

MacVean, M. K. and P. J. Mason, 1990: Cloud-top Entrainment Instability through Small-scale Mixing and its Parametrization in Numerical Models. Journal of the Atmospheric Sciences, 47, 1012-1030.

Mann, J. and D. H. Lenschow, 1994: Errors in airborne flux measurements. Journal of Geophysical Research, 99(D7), 14,519-14526.

Martin, G. M., D. W. Johnson, P. R. Jonas, I. M. Brooks and R. W. Barlow, 1997: Effects of Airmass Type on the Interaction between Warm Stratocumulus and Underlying Cumulus Clouds in the Marine Boundary Layer. Quarterly Journal of the Royal Meteorological Society, 123, 849-882.

Martin, G. M., D. W. Johnson, D. P. Rogers, P. R. Jonas, P. Minnis and D. A. Hegg, 1995: Observations of the Interaction between Cumulus Clouds and Warm Stratocumulus Clouds in the Marine Boundary Layer during ASTEX. Journal of the Atmospheric Sciences, 52(16), 2902-2929.

Mason, P. J., 1994: Large-eddy simulation: A critical review of the technique. Quarterly Journal of the Royal Meteorological Society, 120, 1-26.

Mellor, G. L., 1973: Analytic prediction of the stratified planetary surface layers. Journal of the Atmospheric Sciences, 30, 1061-1069.

Mellor, G. L., 1977: The Gaussian Cloud Model Relations. Journal of the Atmospheric Sciences, 34(2), 356-358.

Mellor, G. L. and T. Yamada, 1974: A Hierarchy of Turbulence Closure Models for Planetary Boundary Layers. Journal of the Atmospheric Sciences, 31, 1791-1806.

Mellor, G. L. and T. Yamada, 1977: A Turbulence Model Applied to Geophysical Fluid Problems. Proceedings of the Symposium on Turbulent Shear Flows, 18-20 April, Penn. State University, PA, 14pp.

Mellor, G. L. and T. Yamada, 1982: Development of a Turbulence Closure Model for Geophysical Fluid Problems. Reviews of Geophysics and Space Physics, 20(4), 851-875.

The Meteorological Office, 1982: Cloud Types for Observers. Met.O.716, 37 pp.

Miller, M. A. and B. A. Albrecht, 1995: Surface-Based Observations of Mesoscale Cumulus-Stratocumulus Interaction during ASTEX. Journal of the Atmospheric Sciences, 52(16), 2809-2826.

Moeng, C.-H. and A. Arakawa, 1980: A Numerical Study of a Marine Subtropical Stratus Cloud Layer and its Stability. Journal of the Atmospheric Sciences, 37, 2661-2676.

Moeng, C.-H., W. R. Cotton, C. Bretherton, A. Chlond, M. Khairoutdinov, S. Krueger, W. S. Lewellen, M. K. MacVean, J. R. M. Pasquier, H. A. Rand, A. P. Siebesma, B. Stevens and R. I. Sykes, 1996: Simulation of a Stratocumulus-topped Planetary Boundary Layer: Comparison among Different Numerical Codes. Bulletin of the American Meteorological Society, 77(2), 261-278.

Moeng, C. H., P. P. Sullivan and B. Stevens, 1999: Including Radiative Effects in an Entrainment Rate Formula for Buoyancy-driven PBLs. Journal of the Atmospheric Sciences, 56(8), 1031-1049.

Monin, A. S. and A. M. Obukhov, 1954: Basic laws of turbulent mixing in the atmosphere near the ground. Tr. Akad. Nauk SSSR Geofiz. Inst., 24(151), 163-187.

Neiburger, M., 1944: Temperature Changes during Formation and Dissipation of West Coast Stratus. Journal of Meteorology, 1(1), 19-41.

Neiburger, M., D. S. Johnson and C.-W. Chien, 1961: Studies of the Structure of the Atmosphere over the Eastern Pacific Ocean in Summer. I. The Inversion of the Eastern North Pacific Ocean. University of California Publications in Meteorology Volume 1, No. 1, University of California Press, Berkeley and Los Angeles, 94 pp.

Nicholls, S., 1983: An observational study of the mid-latitude, marine, atmospheric boundary layer. PhD Thesis, Department of Oceanography, University of Southampton. , 307pp.

Nicholls, S., 1984: The dynamics of stratocumulus: Aircraft observations and comparisons with a mixed-layer model. Quarterly Journal of the Royal Meteorological Society, 110, 783-820.

Nicholls, S., B. Brümmer, F. Fiedler, A. Grant, T. Hauf, G. Jenkins, C. Readings and W. Shaw, 1983: The structure of the turbulent atmospheric boundary layer. Philosophical Transactions of the Royal Society of London, A308, 291-309.

Nicholls, S. and J. Leighton, 1986: An observational study of the structure of stratiform cloud sheets: Part I. Structure. Quarterly Journal of the Royal Meteorological Society, 112, 431-460.

Nicholls, S., M. A. LeMone and G. Sommeria, 1982: The Simulation of a Fair Weather Marine Boundary Layer in GATE using a Three-dimensional Model. Quarterly Journal of the Royal Meteorological Society, 108, 167-190.

Nicholls, S. and J. D. Turton, 1986: An observational study of the structure of stratiform cloud sheets: Part II. Entrainment. Quarterly Journal of the Royal Meteorological Society, 112, 461-480.

Norris, J. R., 1998: Low Cloud Type of the Ocean from Surface Observations. Part I: Relationship to Surface Meteorology and the Vertical Distribution of Temperature and Moisture. Journal of Climate, 11, 369-382.

Norris, J. R. and C. B. Leovy, 1994: Interannual variability in stratiform cloudiness and sea surface temperature. Journal of Climate, 7, 1915-1925.

Nurser, A. J. G., 1996: A review of models and observations of the oceanic mixed layer. Southampton Oceanography Centre, 247 pp.

Paulson, C. A., 1970: The mathematical representation of wind speed and temperature profiles in the unstable atmospheric surface layer. Journal of Applied Meteorology, 9, 857-861.

Payne, R. E., 1972: Albedo of the sea surface. Journal of the Atmospheric Sciences, 29, 959-970.

Pincus, R., M. B. Baker and C. S. Bretherton, 1997: What Controls Stratocumulus Radiative Properties? Lagrangian Observations of Cloud Evolution. Journal of the Atmospheric Sciences, 54, 2215-2236.

Pollard, R. T., 1978: The Joint Air-Sea Interaction Experiment - JASIN 1978. Bulletin of the American Meteorological Society, 59, 1310-1318.

Pollard, R. T., T. H. Guymer and P. K. Taylor, 1983: Summary of the JASIN 1978 field experiment. Philosophical Transactions of the Royal Society of London, A308, 221-230.

Price, J. D., 1999: Observations of Stratocumulus Cloud Break-up over Land. Quarterly Journal of the Royal Meteorological Society, 125(554), 441-468.

Randall, D. A., 1980: Entrainment into a Stratocumulus Layer with Distributed Radiative Cooling. Journal of the Atmospheric Sciences, 37, 148-159.

Randall, D. A., 1984: Stratocumulus cloud deepening through entrainment. Tellus, 36A, 446-457.

Richtmyer, R. D. and K. W. Morton, 1967: Difference Methods for Initial-value Problems. 2nd Edition. Interscience Publishers, J. Wiley and Sons, New York, London, Sydney, 405 pp.

Riehl, H., 1979: Climate and Weather in the Tropics. Academic Press, London, 611 pp.

Roach, W. T., R. Brown, S. J. Caughey, B. A. Crease and A. Slingo, 1982: A Field Study of Stratocumulus. I. Mean Structure and Budgets. Quarterly Journal of the Royal Meteorological Society., 108(455), 103-124.

Rogers, D. P., 1983: A Numerical Model of the Cloudy Marine Boundary Layer. PhD Thesis, Department of Oceanography, University of Southampton. Department of Oceanography, 209 pp.

Rogers, D. P., J. A. Businger and H. Charnock, 1984: A Numerical Investigation of the JASIN Atmospheric Boundary Layer. Boundary-Layer Meteorology, 32, 373-399.

Rogers, D. P. and D. Koracin, 1992: Radiative Transfer and Turbulence in the Cloud-topped Marine Atmospheric Boundary Layer. Journal of the Atmospheric Sciences, 49(16), 1473-1486.

Rotta, J., 1951: Statistische Theorie nichthomogener Turbulenz. Z. Phys., 129, 547-572.

Salby, M. L., 1996: Fundamentals of Atmospheric Physics. Academic Press, San Diego, 627 pp.

Sasamori, T., 1968: The Radiative Cooling Calculation for Application to General Circulation Experiment. Journal of Applied Meteorology, 7, 721-729.

Schmetz, J., A. Slingo, S. Nicholls and E. Raschke, 1983: Case studies of radiation in the cloud-capped atmospheric boundary layer. Philosophical Transactions of the Royal Society of London, A308, 377-388.

Schubert, W. H., 1976: Experiments with Lilly's Cloud-Topped Mixed Layer Model. Journal of the Atmospheric Sciences, 33, 436-446.

Schubert, W. H., P. E. Cielsielski, C. Lu and R. H. Johnson, 1995: Dynamical Adjustment of the Trade Wind Inversion Layer. Journal of the Atmospheric Sciences, 52(16), 2941-2952.

Schubert, W. H., J. S. Wakefield, E. J. Steiner and S. K. Cox, 1979: Marine Stratocumulus Convection Part 1: Governing Equations and Horizontally Homogeneous Solutions. Journal of the Atmospheric Sciences, 36, 1286-1307.

Shaw, W. J., 1990: Theory and Scaling of Lower Atmospheric Turbulence: Surface Waves and Fluxes, Volume 1. , G. L. Geernaert and W. J. Plant, Ed., Kluwer Academic Publishers, 63-90.

Siems, S. T., C. S. Bretherton, M. B. Baker, S. Shy and R. E. Breidenthal, 1990: Buoyancy Reversal and Cloud Top Entrainment Instability. Quarterly Journal of the Royal Meteorological Society, 116(493), 705-739.

Simpson, J. H., W. R. Crawford, T. P. Rippeth, A. R. Campbell and J. V. S. Cheok, 1996: The Vertical Structure of Turbulent Dissipation in Shelf Seas. Journal of Physical Oceanography, 26, 1579-1590.

Slingo, A., R. Brown and C. L. Wrench, 1982a: A Field Study of Stratocumulus. III. High Resolution Radiative and Microphysical Observations. Quarterly Journal of the Royal Meteorological Society, 108(455), 145-165.

Slingo, A., S. Nicholls and J. Schmetz, 1982b: Aircraft Observations of Marine Stratocumulus during JASIN. Quarterly Journal of the Royal Meteorological Society, 108, 833-856.

Smith, S. D., 1980: Wind Stress and Heat Flux over the Ocean in Gale Force Winds. Journal of Physical Oceanography, 10, 709-726.

Smith, S. D., 1988: Coefficients for Sea Surface Wind Stress, Heat Flux and Wind Profiles as a Function of Wind Speed and Temperature. Journal of Geophysical Research, 93, 15,467-15,474.

Smith, S. D., R. J. Anderson, W. A. Oost, C. Kraan, N. Maat, J. DeCosmo, K. B. Katsaros, K. L. Davidson, K. Bumke, L. Hasse and H. M. Chadwick, 1992: Sea Surface Wind Stress and Drag Coefficients: The HEXOS Results. Boundary-Layer Meteorology, 60, 109-142.

Smith, W. S. and C.-Y. J. Kao, 1996: Numerical Simulations of the Marine Stratocumulus-Capped Boundary Layer and Its Diurnal Variation. Monthly Weather Review, 124, 1803-1816.

Sommeria, G. and J. W. Deardorff, 1977: Subgrid-scale Condensation in Models of Non-precipitating Clouds. Journal of the Atmospheric Sciences, 34, 344-355.

Stage, S. A. and J. A. Businger, 1981a: A model for Entrainment into a Cloud-Topped Marine Boundary Layer. Part I: Model Description and Application to a Cold-Air Outbreak Episode. Journal of the Atmospheric Sciences, 38, 2213-2229.

Stage, S. A. and J. A. Businger, 1981b: A Model for Entrainment into a Cloud-Topped Marine Boundary Layer. Part II: Discussion of Model Behaviour and Comparison with Other Models. Journal of Atmospheric Sciences, 38, 2230-2242.

Stephens, G. L., 1978: Radiation Profiles in Extended Water Clouds. II: Parameterisation Schemes. Journal of the Atmospheric Sciences, 35, 2123-2132.

Stephens, G. L., S. Ackerman and E. A. Smith, 1984: A Shortwave Parameterisation Revised to Improve Cloud Absorption. Journal of the Atmospheric Sciences, 41(4), 687-690.

Stevens, B., W. R. Cotton, G. Feingold and C.-H. Moeng, 1997: Large-eddy Simulations of Strongly Precipitating, Shallow, Stratocumulus-topped Boundary Layers. Journal of the Atmospheric Sciences, 55(24), 3616-2638.

Stevens, D. E. and C. S. Bretherton, 1999: Effects of Resolution of the Simulation of Stratocumulus Entrainment. Quarterly Journal of the Royal Meteorological Society., 125(554), 425-439.

Stull, R. B., 1988: An Introduction to Boundary Layer Meteorology. Kluwer Academic Publishers, Dordrecht, 666 pp.

Sullivan, P. P., C.-H. Moeng, B. Stevens, D. H. Lenschow and S. D. Mayor, 1998: Structure of the Entrainment Zone Capping the Convective Boundary Layer. Journal of the Atmospheric Sciences, 55, 3042-3068.

Taylor, P. K., A. L. M. Grant, H. Gunther and G. Olbruck, 1983: Mass, momentum, sensible heat and latent heat budgets for the lower atmosphere. Philosophical Transactions of the Royal Society of London, A308, 275-290.

Taylor, P. K. and T. H. Guymer, 1983: The structure of an atmospheric warm front and its interaction with the boundary layer. Philosophical Transactions of the Royal Society of London, A308, 341-357.

Tennekes, H., 1973: Similarity laws and scale relations in planetary boundary layers. American Meteorological Society, 177-216 pp.

Thorpe, S. A., 1969: Experiments on the Stability of Stratified Shear Flows. Radio Science, 4, 1327-1331.

Tjernström, M. and D. Koracin, 1995: Modelling the Impact of Marine Stratocumulus in Boundary Layer Structure. Journal of the Atmospheric Sciences, 52(7), 863-878.

Turner, J. S., 1968: The Influence of Molecular Diffusivity on Turbulent Entrainment Across and Density Interface. Journal of Fluid Mechanics, 33(4), 639-656.

Turton, J. D. and S. Nicholls, 1987: A study of the diurnal variation of stratocumulus using a multiple mixed layer model. Quarterly Journal of the Royal Meteorological Society, 113, 969-1009.

vanZanten, M. C., P. G. Duynkerke and J. W. M. Cuijpers, 1999: Entrainment Parameterisations in Convective Boundary Layers. Journal of the Atmospheric Sciences, 56(6), 813-828.

Wang, Q. and D. H. Lenschow, 1995: An Observational Study of the Role of Penetrating Cumulus in a Marine Stratocumulus-Topped Boundary Layer. Journal of the Atmospheric Sciences, 52(16), 2778-2787.

Wang, S., 1993: Modelling Marine Boundary-layer Clouds with a Two-layer Model: A One-dimensional Simulation. Journal of the Atmospheric Sciences, 50, 4001-4021.

Warren, S. G., C. J. Hahn, J. London, R. M. Chervin and R. L. Jenne, 1988: Global Distribution of Total Cloud Cover and Cloud Type over the Ocean. NCAR Technical Note, NCAR/TN-317+STR, 42 (plus 170 maps), pp.

Weaver, C. J. and R. Pearson, 1990: Entrainment Instability and Vertical Motion as Causes of Stratocumulus Breakup. Quarterly Journal of the Royal Meteorological Society, 116, 1359-1388.

Weaver, C. P. and V. Ramanathan, 1997: Relationships between Large-scale Vertical Velocity, Static Stability and Cloud Radiative Forcing over Northern Hemisphere Extratropical Oceans. Journal of Climate, 10, 2871-2887.

Woodruff, S. D., S. J. Lubker, K. Wolter, S. J. Worley and J. D. Elms, 1993: Comprehensive Ocean-Atmosphere Data Set (COADS) Release 1a: 1980-92. Earth System Monitor, 4(1), 4-8.

Wyant, M. C., C. S. Bretherton, H. A. Rand and D. E. Stevens, 1997: Numerical Simulations and a Conceptual Model of the Stratocumulus to Trade Cumulus Transition. Journal of the Atmospheric Sciences, 54, 168-192.

Wyngaard, J. C., 1973: On Surface Layer Turbulence. Workshop on Micrometeorology, D. A. Haugen, Ed., American Meteorological Society, 101-149.

Yamada, T., 1978: A Three-dimensional, Second-order Closure Numerical Model of Mesoscale Circulations in the Lower Atmosphere: Description of the Basic model and an Application to the Simulation of the Environmental Effects of a Large Cooling Pond. Argonne National Laboratory, 67 pp.

Yamada, T., 1979: An Application of a Three-Dimensional, Simplified Second-Moment Closure Numerical Model to Study Atmospheric Effects of a Large Cooling Pond. Atmospheric Environment, 13, 693-704.

Yamada, T. and C.-Y. J. Kao, 1986: A Modelling Study on the Fair Weather Marine Boundary Layer of the GATE. Journal of the Atmospheric Sciences, 43(24), 3186-3199.

Yamada, T. and G. L. Mellor, 1979: A Numerical Simulation of BOMEX Data using a Turbulence Closure Model Coupled with Ensemble Cloud Relations. Quarterly Journal of the Royal Meteorological Society, 105(446), 915-944.

Yamamoto, G., 1952: On a Radiation Chart. Scientific Reports of Tohoku University, Series 5, Geophysics Vol. 4, 9-23.

SOUTHAMPTON UNIVERSITY LIBRARY

USER'S DECLARATION

AUTHOR: KENT, ELIZABETH C. TITLE: A NUMERICAL MODEL STUDY OF THE STRATOCUMULUS-TOPPED MARINE BOUNDARY LAYER

DATE: 1999

I undertake not to reproduce this thesis, or any substantial portion of it, or to quote extensively from it without first obtaining the permission, in writing, of the Librarian of the University of Southampton.

To be signed by each user of this thesis

DATE	SIGNATURE	ADDRESS